UNIVERSITE JOSEPH FOURIER – GRENOBLE I

**Discipline : Sciences de la Planète**

Mémoire pour l'obtention du diplôme

**HABILITATION A DIRIGER LES RECHERCHES**

# Contribution à l'étude des systèmes convectifs en régions tropicales

Henri LAURENT

Soutenue le 29 juin 2005

Jury

| | | |
|---|---|---|
| Jean Pierre Cholet | Professeur à l'Université Joseph Fourier | Président |
| Maria Assunção F. Silva Dias | Professeur à l'Université de São Paulo | Rapporteur |
| Jean-Philippe Duvel | Directeur de Recherche au CNRS | Rapporteur |
| Jean-Philippe Lafore | Ingénieur à Météo-France | Rapporteur |
| Pierre de Félice | Professeur émérite à l'Université Paris 12 | Examinateur |
| Thierry Lebel | Directeur de Recherche à l'IRD | Examinateur |

# Table des matières

convection observed during TRMM-WET AMC/LBA. *J. Geophys. Res*., **107** (D18), 8064, doi:10.1029/2001JD000338.

- Laurent H., L. A. T. Machado, C. A. Morales and L. Durieux, 2002: Characteristics of the Amazonian mesoscale convective systems observed from satellite and radar during the WETAMC/LBA experiment. *J. Geophys. Res*., **107** (D18), 8054, doi:10.1029/2001JD000337. **135**
- Mathon V., H. Laurent and T. Lebel, 2002: Mesoscale convective system rainfall in the Sahel. *J. Applied Meteorology*, **41**, 1081-1092. **155**
- Machado L. A. T. and H. Laurent, 2004: The convective system area expansion over Amazonia and its relationships with convective system life duration and high-level wind divergence, 2004. *Monthly Weather Review*, **132**, 714-725. **167**

## PARTIE I - CURRICULUM VITAE

**Henri LAURENT**

Date de naissance : 20/07/1958

*Adresse professionnelle :*
LTHE
BP 53 - Domaine Universitaire
38041 Grenoble Cedex 9 - France
Tel : 33 (0)4 76 82 70 35
Fax : 33 (0)4 76 82 50 01

*E-mail* : Henri.Laurent@hmg.inpg.fr *ou* Henri.Laurent@ird.fr

*Adresse personnelle :*
687 chemin du Pré de l'Achard
38330 St Nazaire les Eymes

**Fonction**

Chargé de Recherche à l'IRD (Institut de Recherche pour le Développement)
Unité de Recherche : Laboratoire d'Etude des Transferts en Hydrologie et Environnement (LTHE), Unité Mixte de Recherche CNRS/ INPG /IRD/UJF (UMR 5564).

**Formation-diplômes**

1988 Thèse de Doctorat de l'Université Paris 6 en Sciences Physiques - Météorologie.
1983 DEA de Géophysique Externe - Météorologie, Université Paris 6.
1982 Maitrise de Physique, Université Paris 6.

**Parcours professionnel**

- Depuis 1991 : Chargé de Recherche à l'IRD, anciennement ORSTOM.
  *Affectations :*
  - depuis juin 2003 : LTHE, Grenoble, France
  - mai 1999-mai 2003 : CTA/IAE/ACA, São José dos Campos/SP, Brésil
  - janvier 1993-mai 1999 : Laboratoire d'Hydrologie, Centre IRD de Montpellier, France
  - juin 1992-décembre 1992 : AGRHYMET/ORSTOM, Niamey, Niger
  - octobre 1991-juin 1992 : Laboratoire d'Hydrologie, Centre ORSTOM de Montpellier, France

- 1990/1991 : Visiteur scientifique (Post-doc) en Allemagne à l'ESOC (European Space Operation Centre of ESA - European Space Agency), sur bourse EUMETSAT (European Organisation for the exploitation of Meteorological Satellites). Recherches sur la mesure du vent par satellite en utilisant les canaux visible et vapeur d'eau du satellite Meteosat.

- 1988/1990 : Post-Doc au Laboratoire de Météorologique Dynamique (LMD) du CNRS sur contrat avec l'ESOC : Etude de faisabilité sur les techniques d'extraction du vent à partir d'images Meteosat, dans le canal vapeur d'eau.

- 1985/1988 : Thèse effectuée au LMD : Etude de la qualité de prévision, sur l'Afrique boréale, du

modèle du centre européen de prévision météorologique à moyen terme (ECMWF). Directeur de thèse : A. Viltard.
Assistant vacataire à l'Université Paris Val-de-Marne : travaux dirigés de physique, de télédétection et de météorologie.

- 1983/1985 : Service National effectué en coopération comme enseignant à Dakar, Sénégal.

- 1983 : Stage de DEA sur l'utilisation de l'analyse spectrale pour l'étude des ondes d'Est en Afrique de l'ouest.

**Principales activités de recherche**

Etude des systèmes convectifs :
Cycle de vie des systèmes convectifs à partir d'images satellitales.
Précipitations associées aux systèmes convectifs de méso-échelle en région sahélienne.
Interactions surface/systèmes convectifs.

Estimation des précipitations par satellite :
Estimation et validation de précipitation par satellite et données de surface.
Erreurs d'échantillonnage des estimations de précipitation par satellite.

Mesure du vent dans la troposphère à partir d'images des satellites géostationnaires :
Mesure du vent par le canal vapeur d'eau.
Estimation de la divergence en altitude à partir des vents vapeur d'eau.

Dynamique de la circulation atmosphérique et convection tropicale :
Qualité des analyses et des prévisions des modèles de circulation générale en régions tropicales.
Etude des ondes d'Est et des interactions entre la circulation atmosphérique et les systèmes convectifs.

**Encadrement**

*Thèses*

Direction de la thèse de Vincent Mathon, soutenue le 16 mai 2001 : Etude climatologique des systèmes convectifs de méso-échelle en Afrique de l'ouest. Thèse de l'Université Paris 7. Directeur de thèse habilité Thierry Lebel.

Codirection de la thèse de Laurent Durieux, soutenue le 11/10/2002 : Etude des relations entre les caractéristiques géographiques de la surface et les nuages convectifs dans la région de l'arc de déforestation en Amazonie. Thèse en Géographie de l'Université d'Aix-Marseille, directeur de thèse J.-P. Ferrier.

Codirection de la thèse de Nadine Dessay, soutenance prévue fin 2005. Le sujet porte sur la caractérisation de la végétation et de son évolution au Brésil, et ses interactions avec le climat. Thèse en géographie de l'université Paris X, directeur de thèse H. Théry.

Participation à la direction de la thèse de Christophe Lavaysse, dont le directeur de thèse Arona Diedhiou est en affectation au Niger depuis juillet 2003. Le sujet porte sur les mécanismes multi-échelles de la variabilité de la convection dans la mousson en Afrique de l'Ouest, principalement en ce qui concerne les ondes d'est et les variations intra-saisonnières.

Participation à l'encadrement de thésards de l'INPE (Instituto Nacional de Pesquisas Espacias, Brésil) sous la responsabilité de Luiz Machado :

- José Ricardo Siqueira, thèse soutenue en décembre 2003 : Propagações meridionais da convecção: incursões de ar de latitudes médias nos trópicos.
- Luiz Fernando Sapucci, thèse en cours : Estimativo do atraso troposférico utilizando GNSS para suporte à meteorologia brasileira.

*DEA, Master*

Philippe Lopez, Mastère de Météorologie Tropicale, Ecole Nationale de la Météorologie : Etude de la représentation des lignes de grains africaines dans les analyses du modèle du Centre Européen. Mémoire soutenu le 15 décembre 1993 à l'ENM à Toulouse.

Stage de DEA (Méthodes physiques en télédétection, université Paris 7) de Vincent Mathon, juin-août 1996. Echantillonnage des nuages convectifs observés par satellite.

Participation à l'encadrement d'étudiants de l'INPE sous la responsabilité de Luiz Machado :
- Alexandra Amaro Lima, Mestrado (Master) soutenu en juillet 2001 : A variabilidade da precipitação e suas relações com medidas por satélite, radar e divergência do vento em altos níveis durante o LBA-WETAMC.
- Robson Lopes Barbosa, Mestrado, en cours : Linhas de instabilidade na região Nordeste.

*Autres*

José Almeida, stage du CRTO (Centre Régional de Télédétection de Ouagadougou) effectué à Niamey en 1992 : Identification des nuages précipitants sur images METEOSAT à partir d'informations exogènes du type prévisions locales et modèles globaux. Rapport soutenu le 22 octobre 1992.

Séjour de V. Mathon comme CSN à l'UTIS (Unité ORSTOM/ISRA de Traitement d'Images Satellitaires, Dakar, Sénégal), novembre 1996-février 1998. Mise en place d'un algorithme de suivi des systèmes convectifs à partir d'images Meteosat.

Séjour scientifique de Meiry Sakamato de la FUNCEME (Fortaleza, Brésil), de août à novembre 1997. Développement d'une méthode de mesure de la divergence au sommet des nuages convectifs à partir d'images « vapeur d'eau ».

Stage ISTOM de M. Delgado, août-septembre 1997. Le climat du Bénin.

Bruno Durand, CSN au Brésil dans le cadre du programme ESCALA, de mai 2001 à août 2002. Constitution d'une base de données pour l'étude des relations entre les flux de chaleur de l'océan Atlantique et les systèmes convectifs en Amérique du Sud.

**Autres activités scientifiques**

Responsable français du projet de coopération bilatérale IRD/CNPq (Conselho Nacional de Pesquisas, Brasil) intitulé ESCALA : Etude des systèmes convectifs et de leurs interactions avec le climat en Amérique latine et Atlantique. Responsable brésilien : Luiz Machado. 1999-2001 puis 2002-2004.

Animateur du projet de coopération CAPES/COFECUB entre l'Université de São Paulo et l'Université de Grenoble, intitulé : Convection et Précipitation en Amazonie. 2002-2003 puis 2004-2005.

Coordinateur de la participation IRD au programme européen WAMP (West African Monsoon Project). 1998-2000.

Coordinateur du projet PNEDC : Etude du cycle de vie des systèmes convectifs en Afrique de l'Ouest et de leur impact hydrologique. 1999 et 2000.

Participation à plusieurs projets nationaux ou internationaux :
- LBA (Large scale Biosphere-Atmosphere experiment), campagnes WETAMC (Amazon Mesoscale Campaign - wet season) et DRY-TO-WET Atmospheric Mesoscale Campaign.
- TRMM : Appel d'offre NASA-NASDA. Améliorations et validations d'algorithmes de restitution de la pluie, et combinaison de capteurs et de satellites. Participation française à TRMM, coordonnée par M. Desbois, regroupant le LMD, le CETP et l'ORSTOM.
- PNTS : Demande de financement pour le projet TRMM ci-dessus, qui n'est pas financé par les agences spatiales. Proposition acceptée en 1997 et 1998.
- TROPIQUES : Projet de satellite Franco-Indien dédié à l'étude des systèmes précipitants dans la bande tropicale, coordonné par M. Desbois (LMD). Les études scientifiques sont proches de celles de TRMM.
- AMIP : Intercomparaison de modèles climatiques en ce qui concerne la mousson d'Afrique de l'Ouest. Projet LMD/ORSTOM.
- PNEDC : participation à différents projets, coordonnés par M. Desbois, T. Lebel ou A. Diedhiou.

Participation à l'organisation de deux ateliers sur l'estimation et la validation des précipitations par satellite, organisés à l'AGRHYMET (Niamey, Niger) en décembre 1993 (publication AGRHYMET) et en décembre 1994 (publication ORSTOM).

Révision d'articles pour des revues à comité de lecture : Bulletin of American Meteorology Society, Journal of Applied Meteorology, Sécheresse, Physics and Chemistry of the Earth, International Journal of Remote Sensing, Revista Brasileira de Meteorologia.

## PARTIE II - PUBLICATIONS ET CONFÉRENCES

### Articles


Durand B., J. Servain, **H. Laurent** and L. A . T. Machado, 2005. Tropical Atlantic moisture flux, convection over Northeastern Brazil and pertinence of the PIRATA network. *Journal of Climate*, **18**, 2093-2101.

Machado L. A. T. and **H. Laurent**. The convective system area expansion over Amazonia and its relationships with convective system life duration and high-level wind divergence, 2004. *Monthly Weather Review*, **132**, 714-725.

Dessay N, **Laurent H.**, Machado L.A.T., Shimabukuro Y. E., Batista G. T., Diedhiou A., Ronchail J., 2004. Comparative study of 1982-1983 and 1997-1998 El Niño events over different types of vegetation in South America. *International Journal of Remote Sen*sing, **25**, 4063-4077.

Machado L. A. T., **H. Laurent**, N. Dessay and I. Miranda, 2004. Seasonal and diurnal variability of convection over the Amazon basin: a comparison of different vegetation types. *Theoretical and Applied Climatology*, **78**, 61-77.

Lima A. A., Machado L. A. T. e **H. Laurent**, 2003. Divergência do vento em altos níveis e sua relação com a cobertura de nuvens e a precipitação durante o WETAMC/LBA. *Revista Brasileira de Meteorologia*, **18**, 105-117.

Durieux L., L. A. T. Machado and **H. Laurent**, 2003. The impact of deforestation on cloud cover over the Amazon arc of deforestation. *Remote Sensing of Environment*, **86**, 132-140.

Lebel T., A. Diedhiou and **H. Laurent**, 2003. Seasonal cycle and interannual variability of the Sahelian rainfall at hydrological scales. *Journal of Geophysical Research*, **108** (D8), 8389, doi:10.1029/2001JD001580.

Mathon V., **H. Laurent** and T. Lebel, 2002. Mesoscale convective system rainfall in the Sahel. *Journal of Applied Meteorology*, **41**, 1081-1092.

**Laurent H.**, L. A. T. Machado, C. A. Morales and L. Durieux, 2002. Characteristics of the Amazonian mesoscale convective systems observed from satellite and radar during the WETAMC/LBA experiment. *Journal of Geophysical Research*, **107** (D18), 8054, doi:10.1029/2001JD000337.

Machado L. A. T., **H. Laurent** and A. A. Lima, 2002. The diurnal march of the convection observed during TRMM-WET AMC/LBA. *Journal Geophysical Research*, **107** (D18), 8064, doi:10.1029/2001JD000338.

**Laurent H.**, N. Arai, B. Fomin, L. A. T. Machado e M. A. Gondim, 2002. Extração do vento utilizando imagens de satélite no CPTEC: Nova versão e avaliação com dados do LBA e dados operacionais da DSA/CPTEC. *Revista Brasileira de Meteorologia*, **17**, 113-123.

Mathon V., A. Diedhiou and **H. Laurent**, 2002. Relationship between easterly waves and mesoscale convective systems over the Sahel. *Geophysical Research Letter*, **29** (8), 1216, doi:10.1029/2001GL014371.

Bonazzola M., L. Picon, **H. Laurent**, F. Hourdin, G. Sèze, H. Pawlowska and R. Sadourny, 2001. Retrieval of large-scale wind divergences from infrared Meteosat-5 brightness temperatures over the Indian Ocean. *Journal of Geophysical Research*, **106**, 28113-28128.

Mathon V. and **H. Laurent**, 2001. Life cycle of the Sahelian mesoscale convective cloud systems. *Quarterly Journal of Royal Meteorological Society.*, **127**, 377-406.

Diedhiou A., S. Janicot, A. Viltard, P. de Félice and **H. Laurent**, 1999. Easterly wave regimes and associated convection over West Africa and the tropical Atlantic : Results from NCEP/NCAR and ECMWF reanalyses. *Climate Dynamics,* **15**, 795-822.

Diedhiou A., S. Janicot, A. Viltard, P. de Félice and **H. Laurent**, 1998. A fast eastern wave in West Africa troposphere. *Meteorological and Atmospheric Physics.*, **69**, 39-47.

**Laurent H.**, N. D'Amato and T. Lebel, 1998 : How important is the contribution of the Mesoscale Convective Complexes to the Sahelian rainfall ? *Physic and Chemistry of the Earth*, **23**, 629-633.

Viltard A., J. Oubuih, P. de Félice and **H. Laurent**, 1998. Rainfall and the 6-9 day wave-like disturbance in West Africa during summer 1989, *Meteorological and Atmospheric Physics.*, **66**, 229-234.

**Laurent H.**, I. Jobard and A. Toma, 1998 : Validation of satellite and ground based estimates of precipitation over the Sahel. *Atmospheric Research*, **47-48**, 651-670.

**Laurent H.**, 1993 : Wind extraction from METEOSAT water vapor channel image data. *Journal of Applied Meteorology*, **32**, 1124-1133.

**Laurent H.** and M. Desbois, 1992 : Measurement and validation of atmospheric motions detected on water

vapor Meteosat imagery. *Adances in. Space Research*, **12,** (7), 105-114.

**Laurent H.**, 1990 : Estimation et correction de l'erreur systématique d'un modèle de prévision sur l'Afrique. *La Météorologie*, **34**, 13-26.

Viltard A., **H. Laurent** and P. de Félice, 1990 : Lower-tropospheric cyclonic vortices in Northern Africa in summer. *Monthly Weather Review*, **118**, 818-823.

**Laurent H.**, A. Viltard and P. de Félice, 1989 : Performance evaluation and local adaptation of the ECMWF system forecasts over Northern Africa for summer 1985. *Monthly Weather Review*,, **117**, 1999-2009.

*Rapports, thèse*

Dessay N., Shimabukuro Y. E., **Laurent H**., Machado L. A. T., Durieux L., Arai E., Rudorf B. Dados, 2001. Dados GAC 1981-2000. Relatório Técnico, INPE/CTA/IRD, São José dos Campos SP.

Thorncroft C. D., Arpe K., Fink A., Gregory D., Hodges K., Janicot S., **Laurent H**., Parker D., Redelsperger J.-L., Rowell D. P., Speth P., 2001. West African Monsoon Projet (WAMP). Final report, 260 pp., available from http://www.atmos.albany.edu/facstaff/chris/.

Desbois M., **H. Laurent**, L. Picon and A. Szantai, 1996. The use of Meteosat water vapour wind vectors in clear areas. Final report, EUMETSAT, 100 pp.

**Laurent H.**, 1990 : Feasibility study on water vapor wind extraction techniques. Final report, European Space Agency, September 1990, 80 pp. ESA Publications, ESTEC, BP 299, 2200 AG Noordwijk, The Nederlands.

**Laurent H.**, 1988 : Evaluation de la qualité de prévision, sur l'Afrique boréale, du modèle du Centre Européen de Prévision Météorologique à Moyen Terme. Thèse d'Université, Paris VI, octobre 1988.

*Conférences publiées*

Durand B., J. Servain, **H. Laurent**, and L. A. T. Machado, 2004. Fluxo de calor latente no Atlântico tropical, convecção sobre o Nordeste e a rede PIRATA. XIII Congresso Brasileiro de Meteorologia, Fortaleza, 29 August-3 September 2004.

Macedo S. R., Machado L.A.T., Vila D.A., Morales C.A., **Laurent H**. Monitoramento dos sistemas convectivos de mesoescala atuantes no Brasil utilizando o FORTRACC (Forecast and Tracking of Active and Convective Cells). XIII Congresso Brasileiro de Meteorologia, Fortaleza, 29 August-3 September 2004.

Machado L. A. T. and **H. Laurent**, 2004. Convective system area expansion and its relationship with precipitation intensity. 14th International Conference on Clouds and Precipitation, Bologna, Italy, 18-23 July 2004.

Sakamoto M., **H. Laurent** and L. A. T. Machado, 2004. The upper level winds and their relationship with convective systems – a case study. Seventh International Wind Workshop, Helsinki, Finland, 14-17 June 2004. Eumetsat Publ.

Sakamoto M. and **H. Laurent**, 2003. Wind estimation – the studies made at FUNCEME. EUMETSAT meteorological satellite conference, Weimar, Germany, 29 September–3 October 2003. Eumetsat Publ. EUM P40, available from www.eumetsat.de.

**Laurent H.**, N. Arai, B. Fomin, L. A. T. Machado e M. A. Gondim, 2002. Wind extraction using satellite images in CPTEC : New version and evaluation with WETAMC/LBA and operational DSA/CPTEC data. Sixth International wind workshop, Madison, USA, 7-10 May 2002. Eumetsat publication EUM P35, available from www.eumetsat.de.

Sakamoto M. e **H. Laurent**, 2002. Estimativa de vento na alta troposfera através de imagens do canal de vapor d´água do satélite Goes. XII Congresso Brasileiro de Meteorologia, Foz do Iguaçu, 4-9 agosto 2002. SBMET, 3187-3196.

Morales C. A., L. A. T. Machado and **H. Laurent**, 2002. Preliminary results of 3d rainfall structure characteristics of the MCS observed in the Amazon during the LBA field campaign. XII Congresso Brasileiro de Meteorologia, Foz do Iguaçu, 4-9 agosto 2002. SBMET, 3287-3305.

**Laurent H.** e L. A. T. Machado, 2002. Comparação das características dos sistemas convectivos observados na Amazônia e na África. XII Congresso Brasileiro de Meteorologia, Foz do Iguaçu, 4-9 agosto 2002. SBMET, 3018-3026.

Durand B., **H. Laurent**, L. A. T. Machado and J. Servain, 2002. Relações entre os fluxos de calor na superficie do Atlântico tropical e a cobertura de nuvens. XII Congresso Brasileiro de Meteorologia, Foz do Iguaçu, 4-9 agosto 2002. SBMET, 1749-1760.

Dessay N., **H. Laurent**, L. A. T. Machado,Y. E. Shimabukuro, A. Diedhiou e J. Ronchail, 2002. Uma análise das diferenças de comportamentos da vegetação na América do Sul durante os dois eventos El Niño de

1982-1983 e 1997-1998. XII Congresso Brasileiro de Meteorologia, Foz do Iguaçu, 4-9 agosto 2002. SBMET, 1011-1026.

Machado L. A. T. e **H. Laurent**, 2002. Relações entre a divergência do vento em altos níveis e a expansão da área dos sistemas convectivos: uma aplicação a previsão imediata. XII Congresso Brasileiro de Meteorologia, Foz do Iguaçu, 4-9 agosto 2002. SBMET, 2988-3006.

Diedhiou A., J. Ronchail, N. Dessay, L. A. T. Machado, **H. Laurent** and J. F. Royer, 2002. Climate Change over South America in relation with the Increase of Global Greenhouse Gases: a numerical study. XII Congresso Brasileiro de Meteorologia, Foz do Iguaçu, 4-9 agosto 2002. SBMET, 992-1002.

**Laurent H.**, A. Aria, B. Fomin, L. A. T. Machado e M. A. Gondim, 2002. Wind extraction using satellite images in cptec: new version and evaluation with WETAMC/LBA and operational DAS/CPTEC data. Sixth International Wind Workshop, Madison, USA, 7-10 May 2002. Eumetsat Publ., in press.

Dessay N., **Laurent H.**, Shimabukuro Y. E., Durieux L., Batista G. T., 2001. Dados NOAA-AVHRR para a avaliação do impacto El Niño sobre a vegetação. X Simpósium Brasileiro de Sensoriamento Remoto, 21 - 26 abril 2001, Foz d'Iguaçu, PR Brasil. Arq. 173, 4 pp.

**Laurent H.**, L. A. T. Machado, B. Fomin e M. A. Gondim, 2000. Extração do vento utilizando imagens de satélite no CPTEC : Nova versão e avaliação com dados do WET AMC/LBA. XI Congresso Brasileiro de Meteorologia, Rio de Janeiro, 16-20 out. 2000. SBMET, 3731-3739.

**Laurent H.**, L. A. T. Machado, D. Herdies e Carlos Morales, 2000. Características dos sistemas convectivos observados por satélite durante o experimento WET AMC/LBA. XI Congresso Brasileiro de Meteorologia, Rio de Janeiro, 16-20 out. 2000. SBMET, 3740-3747.

Dessay N., Y. S. Shimabukuro, **H. Laurent**, L. A. T. Machado e L. Durieux, 2000. Relações entre a vegetação e a cobertura de nuvens a partir dos dados NDVI NOAA GAC e ISCCP no Brasil para o período 1984 – 1993. XI Congresso Brasileiro de Meteorologia, Rio de Janeiro, 16-20 out. 2000. SBMET, 3883-3891.

Lima A. A., L. A. T. Machado e **H. Laurent**, 2000. Análise da Cobertura de Nuvens e suas relações com a Divergência do Vento em altos níveis durante o WETAMC/LBA. XI Congresso Brasileiro de Meteorologia, Rio de Janeiro, 16-20 out. 2000. SBMET, 3936-3942.

Durieux L., **H. Laurent**, L. A. T. Machado and N. Dessay, 2000. Relationship between surface and spatial distribution of deep convective systems over the Brazil during WET AMC/LBA. XI Congresso Brasileiro de Meteorologia, Rio de Janeiro, 16-20 out. 2000. SBMET, 3748-3757.

Machado L. A. T., G. Fisch, **H. Laurent**, L. C. Castro, N. Dessay e L. Durieux, 2000. Experimento Meteorológico de Mesoescala nos Lençóis Maranhenses – ESCALA. XI Congresso Brasileiro de Meteorologia, Rio de Janeiro, 16-20 out. 2000. SBMET, 1753-1761.

Machado L. A. T. e **H. Laurent**, 2000. Características Dinâmicas e Termodinâmica da Convecção Observadas na Amazônia durante o WETAMC/LBA. XI Congresso Brasileiro de Meteorologia, Rio de Janeiro, 16-20 out. 2000. SBMET, 1560-1568.

**Laurent H.**, L. A. T. Machado, D. Herdies and V. Mathon, 2000. Cloud cluster life cycle over the Amazonia during the Wet AMC/LBA campaign. 6th Conf. on Southern Hemisphere Meteorology and Oceanography, Santiago, Chile, 3-7 April 2000. AMS Publ., 326-327.

Machado L. A. T., **H. Laurent**, J. P. Duvel and J. R. Siqueira, 2000. Meridional propagation of the convection in South America. 6th Conf. on Southern Hemisphere Meteorology and Oceanography, Santiago, Chile, 3-7 April 2000. AMS Publ., 398-399.

Mathon V. and **H. Laurent**, 1999 : Inter annual variability of convective systems over West Africa. 23rd Conf. on Hurricanes and Tropical Meteorology, Dallas, 10-15 January 1999. AMS Publ., 965-968.

Diedhiou, A., **H. Laurent**, S. Janicot et A. Viltard, 1998. Approche composite de la variabilité synoptique en Afrique de l'Ouest et relation avec les précipitations. Conférence "Water Resources Variability in Africa during the XX Century, Abidjan, November 98, Vol.1, 3-10.

Diedhiou, A., V. Mathon, **H. Laurent**, et S. Janicot, 1998. Suivi de systèmes convectifs dans un flux d'Est perturbé en Afrique de l'Ouest. Conférence "Water Resources Variability in Africa during the XX Century, Abidjan, November 98, vol.2, 57-60.

**Laurent H.** and M. Sakamoto, 1998. Measure of divergence at the top of tropical convective systems from water vapor winds. Fourth International Wind Workshop, Saanenmoser, Switzerland, 20-23 October 1998. Eumetsat Publ., P24, 155-161.

Sakamoto M. S. e **H. Laurent**, 1998. Estimativa de vento a partir de imagens do canal de vapor d'agua do satélitte Meteosat. *X Congresso Brasileiro de Meteorologia*, Brasilia-DF, 26 a 30 de outubro 1998.

Sakamoto M. S. e **H. Laurent**, 1998. Medida da divergência no topo de sistemas convectivos tropicais utilizando campos de vento derivados a partir de imagens do canal de vapor d'àgua. *X Congresso Brasileiro de Meteorologia*, Brasilia-DF, 26 a 30 de outubro 1998

Sakamoto M. S. and **H. Laurent**, 1998. Measure of divergence at the top of tropical convective systems using

wind fields derived from water vapour images. 9th Conference on Satellite Meteorology and Oceanography, Paris, France, 25-29 May 1998. AMS Publ., 356-359.

Szantai A., L. Picon, M. Desbois and **H. Laurent**, 1997. Height assignment of Meteosat water vapour wind vectors in clear sky areas. Meteorological Satellite Data Users' Conference, 29 Sept-3 Oct 1997, Brussels, Belgium. EUMETSAT Publ., 21, 363-370.

**Laurent H.**, T. Lebel and J. Polcher, 1997 : Rainfall variability in Soudano-Sahelian Africa studied from raingauges, satellite and GCM. 13th Conference on Hydrology, 77th AMS annual meeting, 2-7 February, Long Beach, Ca. AMS Publ., 17-20.

**Laurent H.**, 1996 : Life distribution of mesoscale convective clouds over Africa. 7th Conference on Mesoscale Processes, Reading, United Kingdom, 9-13 September 1996. AMS Publ., 178-180.

Jobard I., **H. Laurent**, A. Maia and A. Toma, 1996 : Validation of satellite estimation of precipitation using sparse ground truth dataset in tropical Africa. 12th International Conference on Clouds and Precipitation, Zurich, Switzerland, 19-23 August 1996, 390-393.

Szantai A., M. Desbois, L. Picon, **H. Laurent** and F. Desalmand, 1996. Construction of cloud trajectories and motion of cirrus clouds and water vapour structures. Third International Wind Workshop, Ascona, Switzerland, 10-12 June 1996. EUMETSAT Publ., 221-230.

Lebel T., A. Amani, F. Cazenave, J. Lecocq, J.D. Taupin, E. Elguero, M. Greard, L. Le Barbé, **H. Laurent**, N. d'Amato et J. Robin, 1996 : La distribution spatio-temporelle des pluies au Sahel : apports de l'expérience EPSAT-Niger. Actes de la conférence à Paris, 2-4 mai 1995- L'hydrologie tropicale : géoscience et outil pour le développement. IAHS publ. no 238, 77-92.

**Laurent H**., 1996 : Validation des estimations de précipitation à grande échelle. Actes de l'atelier : Problèmes de validation des méthodes d'estimation des précipitations par satellite en Afrique intertropicale, Niamey, 1-3 décembre 1994. ORSTOM Editions, 129-138.

Arnaud Y., J.D. Taupin et **H. Laurent**, 1996. Validation de deux méthodes d'estimation des pluies à l'aide du réseau ds pluviographes. Atelier de l'Atelier : Problèmes de validation des methodes d'estimation des precipitations par satellite en Afrique intertropicale. Niamey, 1-3 décembre 1994. ORSTOM editions, 163-168.

**Laurent H.** e L. A. Machado, 1994 : Extração do vento através de imagens de satélite meteorológico. *Anais do VIII Congresso Brasileiro de Meteorologia*, Belo Horizonte (MG), 18 a 25 de outubro 1994, vol. 1, 410-413.

Arnaud Y., J.D. Taupin et **H. Laurent**, 1994 : Validation d'estimations de precipitation par satellite avec le reseau dense d'Epsat-Niger. Xe Journées Hydrologiques de l'ORSTOM, Montpellier, 13-14 septembre 1994. ORSTOM Editions, 521-532.

**Laurent H.**, 1994 : Tracking of convective cloud clusters from METEOSAT data. 10th METEOSAT Scientific Users' Conference, Cascais, Portugal, 5-9 September 1994. EUMETSAT Publ. EUM P15, 273-278.

**Laurent H.** et Y. Arnaud, 1993 : Evaluation d'estimations de pluie par satellite sur l'Afrique de l'ouest. Atelier sur l'estimation de la pluie par satellite, AGRHYMET, Niamey, 2-4 décembre 1993, Publ. AGRHYMET, 140-146.

**Laurent H.**, 1992 : Wind extraction from multiple METEOSAT channels. First workshop on wind extraction from operational meteorological satellite data, Washington D.C., September 1991. EUMETSAT Publ. EUM P10, 71-76.

*Conférences non publiées*

Machado L. A. T., C. A. Morales, **H. Laurent** and C. F. Angelis, 2004. Dry to Wet Season: cloud cover, precipitation and thermodynamics features. Third LBA scientific conference, Brasilia, 27-29 July 2004.

Macedo S. R., L. A. T. Machado, C. A. Morales, D. Vila and **H. Laurent**, 2004. Características dos sistemas convectivos de mesoescala observados sobre a Amazônia durante o experimento RACCI/LBA. Third LBA scientific conference, Brasilia, 27-29 July 2004.

**Laurent H.**, L. A. T. Machado and D. Vila, 2003. Analise do ciclo de vida dos sistemas convectivos. Primeiro workshop de analise de dados do projeto RACCI/LBA. Cachoeira Paulista, 13-15 agosto 2003.

Machado L. A. T., **H. Laurent** and C Morales : O impacto da expansão da área de sistemas convectivos no ciclo de vida e na intensidade da atividade convectiva. Primeiro workshop de analise de dados do projeto RACCI/LBA. Cachoeira Paulista, 13-15 agosto 2003.

Morales C., L. A. T. Machado, **H. Laurent** and D. Vila : Características tridimensionais dos sistemas convectivos. Primeiro workshop de analise de dados do projeto RACCI/LBA. Cachoeira Paulista, 13-15 agosto 2003.

**Laurent H.** and L. A. T. Machado, 2002. Characteristics of the convective cloud system organization during

WETAMC/LBA – Comparison with West African convective systems. Second international LBA science conference, Manaus, 7-10 July 2002.

Machado, L. A. T and **H. Laurent**, 2002. The convective system area expansion and its relation to the life cycle duration and the upper tropospheric wind divergence: an analysis using WETAMC/LBA. Second international LBA science conference, Manaus, 7-10 July 2002.

Machado, L. A. T, **H. Laurent** and A. A. Lima, 2002. The diurnal march of the convection observed during TRMM-WETAMC/LBA. Second international LBA science conference, Manaus, 7-10 July 2002.

Dessay N., **H. Laurent**, L. A. Machado, J. Ronchail and Y. E. Shimabukuro. Detecting deforested areas from NDVI series in Amazonia. Second international LBA scientific conference, Manaus, 7-10 July 2002.

**Laurent H.**, L. A. T. Machado and V. Mathon, 2001. A first comparison of convective cloud system characteristics over West Africa and Amazonia. 4th Int. Scientific Conference GEWEX, Paris, 10-14 Septembre 2001.

Machado, L. A. T and **H. Laurent**, 2001. The Amazon Energy Budget Using Field Experiment Data. 4th Int. Scientific Conference GEWEX, Paris, 10-14 Septembre 2001.

**Laurent H.**, L. A. T. Machado, D. Herdies and Carlos Morales, 2000. Characteristics of the convective cloud systems during the WET AMC/LBA experiment. First LBA Science Conference, Belem, 26-30 June 2000.

Machado L. A. T., **H. Laurent**, P. L. Silva Dias, L. D. A. Sá and G. Fisch, 2000. The Variability of the Energy Budget Using LBA -Wet Season Data. First LBA Science Conference, Belem, 26-30 June 2000.

Mathon V., **H. Laurent** and T. Lebel, 2000. Objective identification of the Squall Lines over the Sahel. European Geophysical Society, 25th General Assembly, Nice, 25-29 April 2000.

Machado, L. A. T., **H. Laurent**, D. Herdies, C. Morales and M. A F. Silva Dias, 1999. Cloud cluster characteristics and life cycle over the Amazonia during the LBA campaign. Data analysis workshop on the Wet AMC/LBA and TRMM/LBA, Cachoeira-Paulista, SP, Brasil, 8-9 November 1999.

**Laurent H.** and L. A. T. Machado, 1999. High level wind divergence during LBA/AMC. Data analysis workshop on the Wet AMC/LBA and TRMM/LBA, Cachoeira-Paulista, SP, Brasil, 8-9 November 1999.

Machado, L. A. T., **H. Laurent**, P. L. Silva Dias and L. D. A Sa, 1999. The variability of the energy budget using LBA wet season data. Data analysis workshop on the Wet AMC/LBA and TRMM/LBA, Cachoeira-Paulista, SP, Brasil, 8-9 November 1999.

Mathon V. and **H. Laurent**, 1999. Interannual variability of Sahelian convective system. European Geophysical Society, 24th General Assembly, La Haye, 19-23 April 1999.

Diedhiou A., S. Janicot, A. Viltard, P. de Félice and **H. Laurent**, 1998. Different regimes of easterly waves over West Africa and the tropical Atlantic (1979-1995). European Geophysical Society, 23th General Assembly, Nice, France, 20-24 April 1998.

Mathon V. and **H. Laurent**, 1998 : Automatic tracking of West African cloud clusters. European Geophysical Society, 23th General Assembly, Nice, France, 20-24 April 1998.

Toma A., **H. Laurent** and I. Jobard, 1996 : Estimation of rainfall from satellite data : quality assessment in a tropical region. European Geophysical Society, 21th General Assembly, The Hague, The Netherlands, 6-10 May 1996.

**Laurent H.**, 1994 : Suivi des systèmes convectifs à partir d'images METEOSAT. Séminaire EPSAT, Dakar, 21-25 novembre 1994.

**Laurent H.**, 1994 : Tropical convective cloud cluster tracking over West Africa from METEOSAT data. European conference on the Global Energy and Water Cycle, London, 18-22 July 1994.

**Laurent H.** and Y. Arnaud, 1993 : Evaluation of satellite rain estimates over Africa. International symposium on precipitation and evaporation, Bratislava, 20-24 September 1993.

**Laurent H.**, 1991 : Water vapor wind extraction. European Geophysical Society, XVI General Assembly, Wiesbaden, 22-26 April 1991.

**Laurent H.**, 1990 : Mid-tropospheric motions measured by METEOSAT-4 water vapour channel. 8th METEOSAT Scientific Users' Conference, Norrkoping, Sweden, 28-31 August 1990.

de Félice P., **H. Laurent** and A. Viltard, 1990 : Use of the ECMWF model analyses to investigate summer circulations over Northern Africa. European Geophysical Society, XV General Assembly, Copenhagen, 23-27 April 1990.

**Laurent H.**, P. de Félice and A. Viltard, 1990 : A study of the ECMWF forecasts over Northern Africa in summer. European Geophysical Society, XV General Assembly, Copenhagen, 23-27 April 1990.

# PARTIE III - ACTIVITES DE RECHERCHE

## 1. Introduction

La pluie est le paramètre clé du climat en zone tropicale habitée. D'un point de vue impacts les risques liés au froid ou au manque d'insolation ne sont généralement pas de mise dans ces régions et hormis certaines zones côtières subissant les cyclones les risques liés au vent ne sont pas fréquents. La pluie conditionne la végétation et la production agricole, le ruissellement et l'érosion, et bien sûr la ressource en eau. Une caractéristique essentielle des précipitations en zone tropicale continentale est qu'elles sont d'origine convective.

Outre qu'elle génère la pluie, la convection est capitale dans le fonctionnement de la météorologie tropicale car elle est le principal processus de transport vertical d'eau et d'énergie dans la troposphère. La vapeur d'eau des basses couches se condense en s'élevant, libérant ainsi l'énergie de chaleur latente dans la moyenne et haute troposphère. Globalement, le bilan de la convection tropicale est que le surplus d'énergie solaire reçu près de l'équateur est transporté verticalement de la basse vers la haute troposphère où il sera exporté vers les pôles : la convection tropicale est le moteur de la circulation de Hadley. On parle implicitement ici de convection profonde c'est-à-dire des nuages convectifs à fort développement vertical (cumulonimbus) par opposition aux nuages convectifs peu épais (cumulus) qui ne donnent pas ou peu de précipitation, n'atteignent pas la partie supérieure de la troposphère et ont par conséquent un rôle bien moindre pour la circulation atmosphérique. La convection profonde s'organise à diverses échelles spatiales. Les nuages convectifs tendent souvent à s'agglomérer, formant des amas nuageux qu'on appelle systèmes convectifs de méso-échelle. Ces systèmes peuvent atteindre plusieurs centaines, voire plusieurs milliers de km d'extension.

Etant intégré dans une équipe d'hydrologues de l'IRD, mon apport se devait de porter sur les précipitations. J'ai donc choisi d'axer mes recherches sur les systèmes convectifs. Ceci est justifié par la volonté d'étudier les précipitations avec une approche atmosphérique, et par le fait que d'un point de vue processus le système convectif est l'élément clé permettant de faire le lien entre la circulation générale à grande échelle associée au climat et les impacts à petite échelle qui régissent l'hydrologie.

Mes travaux peuvent être synthétisés autour de 4 thèmes reflétant les approches entreprises pour étudier la convection à travers l'objet central qu'est le système convectif et ses liens avec différents aspects du système tropical. Ces thèmes qui composent les chapitres de ce mémoire sont la caractérisation des systèmes convectifs, leurs précipitations associées, leurs liens avec la circulation générale atmosphérique, et leurs interactions avec la surface

NB : Les références soulignées dans cette synthèse correspondent aux articles annexés.

## 2. Caractéristiques des systèmes convectifs

Mes travaux de recherches se sont développés autour de l'étude des systèmes convectifs. Ceci a nécessité des développements méthodologiques afin d'être en mesure de les définir, les observer puis les analyser. Seule l'observation satellitale permet un suivi continu et sur de grandes étendues des systèmes nuageux. En effet les satellites météorologiques géostationnaires permettent une fréquence d'échantillonnage de 30 minutes et couvrent parfaitement les régions tropicales. C'est le cas pour les satellites que nous avons utilisés : le satellite européen Meteosat qui couvre l'Afrique et le satellite américain GOES qui couvre les Amériques.

On s'intéresse aux amas convectifs d'une certaine taille, les orages isolés ne sont pas considérés pour deux raisons.

Premièrement les petits systèmes de convection isolée jouent un rôle relativement négligeable pour les pluies et les bilans d'énergie atmosphérique. Cette hypothèse a pu être confirmée. Par exemple les systèmes de taille inférieure à 4200 $km^2$ représentent moins de 7 % de la couverture convective au seuil 233 K (Mathon and Laurent 2001).

Deuxièmement il existe une limitation instrumentale. La taille du pixel des satellites utilisés, d'environ 5 km, ne donne pas accès à ce qui se passe à une résolution spatiale inférieure. La résolution temporelle est de 30 minutes ce qui est l'ordre de grandeur de la durée de vie des "petits" nuages convectifs. Pour pouvoir objectivement ou même subjectivement (c'est-à-dire « à vue ») suivre un nuage d'une image à l'autre il faut qu'il ait une certaine taille, que je situerais subjectivement entre 1000 et 2000 $km^2$ pour une résolution temporelle de 30 minutes. De plus l'identification d'un système d'une image à l'autre est d'autant plus complexe que ce système est petit, ce qui nécessite une expertise de l'observateur ou sa traduction en un nombre croissant de règles dans l'algorithme. A l'inverse les systèmes d'une certaine taille sont facilement identifiables et ne requièrent que des méthodes simples.

La taille minimum choisie varie selon les auteurs et la résolution. Ainsi avec des données de satellites géostationnaires à pleine résolution nous avons choisi d'utiliser un seuil de 200 pixels, soit selon la résolution du satellite utilisé et la région étudiée environ 4200 $km^2$ sur le Sahel ou 3500 $km^2$ sur l'Amazonie. Le choix d'un seuil relativement grand se justifie pour ne pas compliquer outre mesure la méthodologie pour les petits systèmes jouant un rôle très mineur dans nos zones d'étude. Avec le même type de données mais sur l'Europe, Morel and Senezi (2002) choisissent généralement un seuil de 1000 $km^2$ en ajoutant des critères additionnels pour la sélection et l'estimation de déplacement des nuages. Avec des données à résolution spatiale et temporelle dégradée (30 km et 3 h) le seuil est généralement plus grand et peut atteindre 100000 $km^2$ dans le cas du suivi des Mesoscale Convective Complexes définis par Maddox (1980).

Un amas de nuages convectifs est appelé système convectif. On distingue parfois une partie convective et une partie stratiforme, mais l'ensemble forme le système convectif. Nous utiliserons souvent la terminologie de Système Convectif de Méso-échelle (SCM, ou MCS en Anglais), ce qui peut générer des ambiguïtés notamment avec la communauté du radar météorologique ayant un usage

différent de certaines terminologies. En effet un SCM observé par un radar représente les structures précipitantes de méso-échelle. Le terme SCM se réfère ici à un amas nuageux convectif vu du haut, c'est-à-dire toute l'enclume d'altitude, d'une taille minimum de 4200 $km^2$ (un peu moins dans le cas de l'Amérique du Sud) ayant persisté pendant au moins 1 heure.

L'identification des systèmes convectifs se fait uniquement à l'aide de la température de brillance du canal infrarouge thermique (10-12 μm). Cela repose sur le fait qu'un nuage de convection profonde possède à la fois un sommet élevé (température basse) et une forte épaisseur (émissivité proche de 1) ; par conséquent sa température de brillance égale la température de son sommet et est donc très faible. Comme déjà mentionné, cette approche ne permet pas de distinguer entre la partie réellement convective et la partie stratiforme. Cela ne pose pas de problème tant que l'on s'intéresse au comportement du système dans son ensemble et non à sa structure interne. Plusieurs seuils en température de brillance ont été retenus, afin d'une part de couvrir la gamme de couverture nuageuse convective ($T < 255$ K environ) et d'autre part de pouvoir combiner les informations obtenues à différents seuils, ce qui permet d'accéder à une description tridimensionnelle des systèmes convectifs.

Le suivi d'un système convectif d'une image à l'autre se fait à l'aide d'une méthode de recouvrement similaire à celle développée par Williams and Houze (1987) puis par Arnaud et al. (1992) et adaptée également par Morel and Sénési (2002).

Les premières versions de l'algorithme ont permis de valider la méthode (Laurent 1994) puis de commencer à étudier le cycle de vie des systèmes convectifs en Afrique de l'Ouest (Laurent 1996) et son potentiel pour étudier les systèmes précipitants (Laurent et al. 1997 ; Laurent et al. 1998b).

L'algorithme a été amélioré par Vincent Mathon dans son travail de thèse (Mathon 2001) en incorporant une procédure d'interpolation dans le cas d'images manquantes. Nous avons alors finalisé une climatologie détaillée des systèmes convectifs en Afrique de l'Ouest (Mathon and Laurent 2001). Ce travail a permis de montrer qu'en utilisant une méthode objective il est possible de suivre à partir d'images satellitales les systèmes convectifs de méso-échelle tout au long de leur cycle de vie. Leurs initiations et disparitions sont déterminées avec une bonne précision temporelle (< 1 h). Les fusions et séparations de systèmes à un seuil donné ont pu être interprétées, montrant que les séparations sont en fait représentatives de l'affaiblissement de la convection, tandis que les fusions peuvent traduire soit le développement vertical d'un système, soit l'agrégation de systèmes distincts.

Nous possédons maintenant les distributions spatiales et temporelles précises des systèmes convectifs sur l'Afrique de l'Ouest. Elles sont utiles pour l'analyse des processus liés à la convection et à son organisation ainsi que pour la validation des modèles météorologiques ou climatiques. Un résultat marquant est que la majorité de la couverture convective et par suite de la pluie est due à quelques systèmes dont le rôle s'explique par une grande durée de vie et une taille importante. Dans le cas du Sahel, ces systèmes ont de plus la caractéristique de se propager rapidement d'est en ouest.

Cette notion d'événements convectifs observés à partir du suivi des nuages rejoint celle d'événements pluvieux qui s'est imposée à partir des observations de précipitation à la surface

(LeBarbé and Lebel 1997, d'Amato and Lebel 1998, Lebel et al. 2003). Ces événements définis à partir de sources d'observations différentes ne coïncident pas exactement mais ils offrent une approche très intéressante pour étudier les précipitations tropicales. C'est ainsi qu'ont pu être mis en évidence les principaux systèmes convectifs pluviogènes sur le Sahel appelés SCO pour Systèmes Convectifs Organisés (Mathon et al. 2002b) dont il sera question au paragraphe 3. On peut également retrouver la notion d'événements convectifs dans les modèles de circulation générale (Polcher 1995). Il convient cependant d'être prudent car un événement défini dans un tel modèle n'est pas directement comparable aux événements observés. Néanmoins cette approche d'analyse par événements dans les modèles de circulation générale face aux événements observables offre des perspectives de recherche séduisantes qui n'ont été qu'effleurées jusqu'à présent (Laurent et al. 1997).

La méthodologie de suivi des systèmes convectifs a été adaptée et appliquée sur l'Amérique du Sud en utilisant les données du satellite géostationnaire GOES dont les caractéristiques sont proches de celles du satellite Meteosat. Nous nous sommes focalisés sur l'Amazonie et sur deux périodes de 2 mois correspondant à deux campagnes du projet LBA (Large-scale Biosphere Atmosphere experiment in Amazonia ; Nobre et al. 2001), la première en saison humide en janvier-février 1999 (WET-AMC/LBA : Wet season Atmospheric Mesoscale campaign ; Silva Dias et al. 2002) et la seconde en fin de saison sèche en septembre-octobre 2002 (DRYTOWET-AMC/LBA, appelée également RACCI : Radiation, Cloud and Climate Interactions). L'objectif est d'étudier le comportement de la convection durant une période clé de la mousson en Amazonie du sud-est, en exploitant l'information apportée par le suivi des systèmes convectifs conjuguée aux autres observations de la campagne, soit principalement radiosondages, pluviographes et radars.

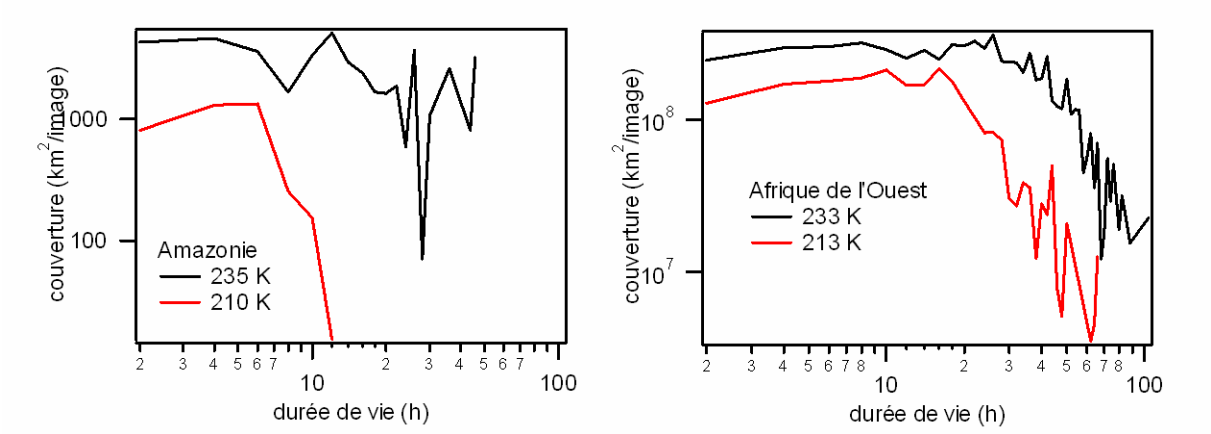


**Figure 1.** Couverture nuageuse convective (unités arbitraires) en fonction de la durée de vie des systèmes convectifs, pour l'Amazonie et pour l'Afrique de l'Ouest. (Laurent and Machado, 2002)

Les distributions des systèmes convectifs pendant WET-AMC/LBA sont décrites dans Laurent et al. (2002a). L'analyse des systèmes convectifs à partir de cette courte période ne permet bien évidemment pas d'établir une climatologie comme cela est le cas en Afrique de l'Ouest. On peut cependant comparer qualitativement les systèmes convectifs en Amazonie du sud-est, pendant la saison humide, aux systèmes convectifs bien documentés de l'Afrique de l'Ouest pendant la saison des pluies. La Figure 1 permet de faire ressortir un résultat marquant, à savoir que les systèmes convectifs

amazoniens sont de plus courte durée de vie que ceux observés sur le Sahel. Ceci est particulièrement visible en considérant les systèmes convectifs très profonds (seuil à 213 ou 210 K) : sur l'Afrique ces systèmes très actifs peuvent durer plus d'une journée et le maximum de contribution à la couverture nuageuse provient des systèmes durant entre 8 et 20 h ; sur l'Amazonie ces systèmes ne durent jamais plus de 12 h et le maximum de contribution à la couverture nuageuse provient des systèmes ayant une durée de vie entre 4 et 6 h.

D'un point de vue méthodologique j'ai développé une version adaptée aux images de radar météorologique de l'algorithme de suivi des systèmes convectifs. Il est alors possible de comparer le déplacement des masses nuageuses, observées par satellite, avec les zones de précipitations observées par radar. Les données utilisées ont été acquises par le radar bande C de la NASA appelé TOGA depuis sa participation à l'expérimentation TOGA-COARE[1] dans le Pacifique ouest. Le radar faisait des acquisitions toutes les 10 minutes, avec 11 élévations de 0.5 a 6.2 degrés. Cette stratégie a permis de calculer un indicateur de précipitation à l'altitude constante de 2 km, le CAPPI (Constant Altitude Plan Position Indicator, Anagnostou and Krajewski 1997). Cet indicateur est projeté sur une grille de 5 km x 5 km pour être compatible avec la résolution des données satellitales. Nous avons choisi d'utiliser les seuils de 20 et 35 dBZ correspondant grossièrement aux zones de précipitations faibles et fortes, à un taux de pluie de l'ordre de 0.5 et 5 $mm.h^{-1}$ respectivement. Le seuil de taille pour le suivi des systèmes a été ajusté dans ce cas à 1000 $km^2$.

La Figure 2 illustre le comportement des cellules de pluie dans les basses couches (traits noirs ou jaunes) qui sont observées sous la couverture des systèmes convectifs (en bleu ou rouge suivant le seuil) pendant deux séquences temporelles distinctes durant la campagne WET-AMC/LBA. Cette représentation permet de visualiser les évolutions des systèmes précipitants qui existent sous l'enclume d'altitude des systèmes convectifs. On peut voir que le comportement des systèmes est bien différent entre ces deux séquences caractérisées par différents régimes de vent dans la basse troposphère, appelés régime d'Est et régime d'Ouest (Laurent et al. 2002a). Ces régimes qui apparaissent dans la Figure 4 sont explicités dans la partie 4.

[1] Tropical Ocean Global Atmosphere – Coupled Ocean Atmosphere Response Experiment

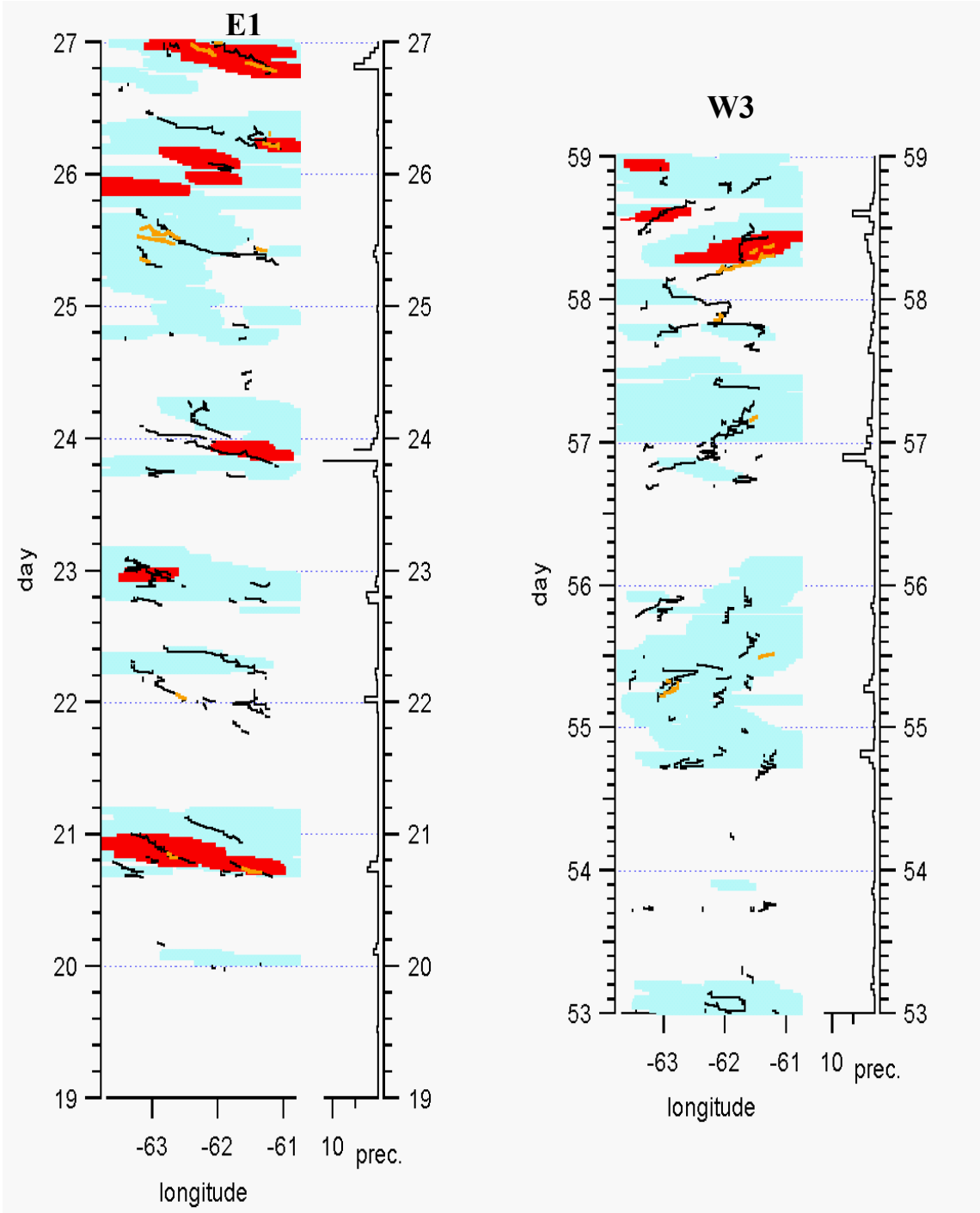


**Figure 2.** Diagramme Hovmöller des trajectoires de cellules de pluie observées par radar aux seuils de 20 dBZ (noir) et 35 dBZ (jaune) superposées à la couverture nuageuse associée aux SCM aux seuils de 235 K (bleu) et 210 K (rouge), pour deux périodes correspondant à un régime d'Est (E1) et d'Ouest (W3) pendant l'expérimentation WETAMC/LBA (l'ordonnée indique les jours depuis le 1er janvier 1999). La précipitation horaire moyenne (mm) du réseau de pluviographes est également indiquée à droite. (Adapté de Laurent et al., 2002a).

## 3. Systèmes convectifs et précipitation

Les systèmes convectifs apportent l'essentiel des pluies en zone tropicale. Pour étudier les précipitations tropicales il est donc naturel de s'intéresser aux systèmes convectifs, mais cela suppose de connaître les relations qui les unissent.

La première difficulté est d'obtenir une mesure des précipitations. Dans les régions tropicales il n'existe que peu de données conventionnelles, ou plus précisément de réseaux de données suffisamment denses pour estimer avec une bonne précision les précipitations. Les mesures par radar hydrométéorologique n'ont pas de couverture suffisante et ne permettent pas une estimation quantitative fiable. La seule option restante consiste à utiliser l'information satellitale qui fournit une couverture complète, une bonne résolution spatiale et une très bonne résolution temporelle dans le cas des satellites géostationnaires. Malheureusement l'imagerie des satellites géostationnaire permet seulement d'observer le sommet des nuages et non pas la précipitation elle-même. Il existe une corrélation entre la couverture de nuage convectifs et la précipitation en surface, mais ce genre de relation n'est valable que statistiquement ou autrement dit en moyenne spatiale ou temporelle. Nous avons mené une étude pour connaître la précision qu'on peut attendre d'une estimation de précipitation par satellite (Laurent et al. 1998a). Le but était d'évaluer la qualité des estimations de précipitation opérationnelles (c'est-à-dire produites rapidement et utilisables pour des applications telles que l'estimation des récoltes, la gestion de la ressource en eau, etc) disponibles sur le long terme. Les résultats montrent que les méthodes utilisant le satellite ou le réseau synoptique conduisent à des estimations de qualité comparable, meilleures que la climatologie. Les méthodes combinant données satellitales et de surface fournissent des estimations un peu meilleures. Toutefois les estimations de pluie opérationnelles nécessitent des données disponibles très rapidement, ce qui réduit sensiblement le jeu de données de surface disponible. Elles restent donc peu satisfaisantes en regard de la précision nécessaire en général pour des applications en hydrologie et agriculture. De telles estimations sont valables sur des moyennes spatio-temporelles qui dépendent de la précision souhaitée mais dont la limite acceptable avec les données disponibles actuellement serait typiquement 0.5° et 10 jours (Laurent et al. 1998a). A ces échelles les apports de chaque système convectif sont cumulés et, au premier ordre, on peut se passer de l'information propre aux systèmes convectifs et se contenter de l'information sur la couverture totale en nuages convectifs.

Dans le travail cité ci-dessus les données de surface étaient utilisées de manière classique, à l'aide de moyenne ou de krigeage simple. Des travaux récents (Ali 2004, Ali et al. 2005) montrent qu'une utilisation plus pertinente des données de surface peut mener à des estimations de pluie plus précises, au point d'égaler voire de faire mieux que les estimations combinant satellite et donnée sol. Ceci montre que les méthodes actuelles ne sont pas optimales pour tirer le meilleur parti des informations fournies par les observations sol d'une part, et les observations satellitales d'autre part.

On sait depuis longtemps que les systèmes convectifs fournissent une part importante des pluies en zone tropicale (cf. par exemple Houze 1981), mais peu d'études ont cherché à préciser ce point. Ces études se sont généralement restreintes aux MCC (Mesoscale Convective Complexes). Définis par Maddox (1980), les MCC sont en fait les systèmes convectifs les plus importants en taille, avec une

forme plus ou moins circulaire afin de ne pas inclure les systèmes linéaires. Etudiés initialement sur les grandes plaines des Etats-Unis, ils ont également été beaucoup étudiés sur d'autres régions (par exemple Velasco and Fritsch 1987 pour l'ensemble des Amériques Miller and Fritsch 1991 pour le Pacifique, Laing and Fritsch 1993 pour l'Afrique) car ils sont peu nombreux et contribuent à une part importante de la couverture nuageuse convective, et donc de la pluie totale. Leur faible nombre et leur grande taille permettent de les suivre manuellement à partir de données satellitales de résolution dégradée. L'exclusion des systèmes linéaires n'est pas très bien adaptée pour le cas de l'Afrique de l'Ouest car il élimine une partie des lignes de grains qui jouent pourtant un rôle essentiel dans cette région. Certaines études ont cherché à évaluer la contribution des MCC à la pluie totale. Par exemple, Fritsch et al. (1986) estimaient que 20 à 50 % de pluie sur les grandes plaines des Etats-Unis provenait des MCC. Pour l'Afrique de l'Ouest, Laing et al. (1999) estimaient cette contribution à 22 %, ce qui semblait montrer qu'on ne pouvait se limiter aux MCC pour étudier les précipitations associées aux systèmes convectifs.

Pour étudier la pluie associée aux systèmes convectifs il faut un réseau très fin d'observation des précipitations : le seul existant en Afrique de l'Ouest est celui du degré carré de Niamey de l'expérience EPSAT-Niger (Lebel et al. 1992). Une première étude (Laurent et al. 1998b) a montré que la plupart des événements pluvieux intenses sur Niamey, produisant 80% du total pluviométrique annuel, étaient associés à des systèmes convectifs importants en termes de taille, de développement vertical et de durée de vie, facilement observables par satellite. Ce résultat incitait à rechercher une identification objective des systèmes convectifs efficaces en terme de pluie.

En travaillant sur une période de 10 années de précipitations observées finement sur le degré carré de Niamey, et avec le suivi objectif et exhaustif des systèmes convectifs de méso-échelle ayant traversé cette région, nous avons pu préciser les pluies associées aux systèmes convectifs (Mathon et al. 2002b). Le principal résultat de cette étude est l'identification à partir des images satellitales de systèmes convectifs très actifs, représentant 80% de la couverture convective sur le Sahel et apportant 90% du total pluviométrique sur la région de Niamey (Sahel central). Ces systèmes que nous avons appelés SCO (Systèmes Convectifs Organisés) en raison de leurs caractéristiques de taille, de durée de vie, de développement vertical et de propagation, correspondent aux lignes de grains au sens large.
Un autre résultat de cette étude a été de quantifier la contribution des MCC à la couverture convective et la pluie en Afrique de l'Ouest, soit respectivement 16% et 19%. Les MCC sont davantage pluviogènes que la moyenne des systèmes convectifs mais sont relativement rares. Bien que l'Afrique de l'Ouest soit une région où les MCC soient plutôt nombreux comparativement à l'ensemble du globe (Mohr and Zipster 1996), ils sont loin d'expliquer l'essentiel de la précipitation.

La convection tropicale sur les continents est initiée par le réchauffement de la surface et se déclenche donc dans l'après-midi. Cependant la pluie observée peut avoir un cycle diurne très différent suivant l'organisation de la convection ou autrement dit suivant les caractéristiques des systèmes convectifs. Ainsi les observations EPSAT-Niger ont révélé que contrairement à ce à quoi on pouvait s'attendre, les précipitations montrent pour cette région du Sahel un maximum en fin de nuit !

Pour illustrer ce point nous allons comparer le cas du Sahel central et le cas de l'Amazonie du sud-ouest.

La Figure 3 montre que les SCM naissent très majoritairement en début ou milieu d'après-midi (vers 13 h locale dans le cas de l'Amazonie, vers 16 h locale dans le cas du Sahel). Ils se développent ensuite et génèrent un maximum de couverture nuageuse convective en début de nuit (entre 16 h et 20 h dans le cas amazonien, entre 19 h et 1 h dans le cas sahélien). Cependant le cycle diurne des précipitations est totalement différent. Dans le cas amazonien les systèmes convectifs sont majoritairement brefs et explosifs, la précipitation intervient très rapidement, au cours de la phase de croissance des systèmes (Machado et al. 2002, Laurent et al. 2002a). On observe donc un net maximum de pluie vers 13 h. Un maximum secondaire vers 2 h du matin est attribué à des systèmes de convection plus organisée.

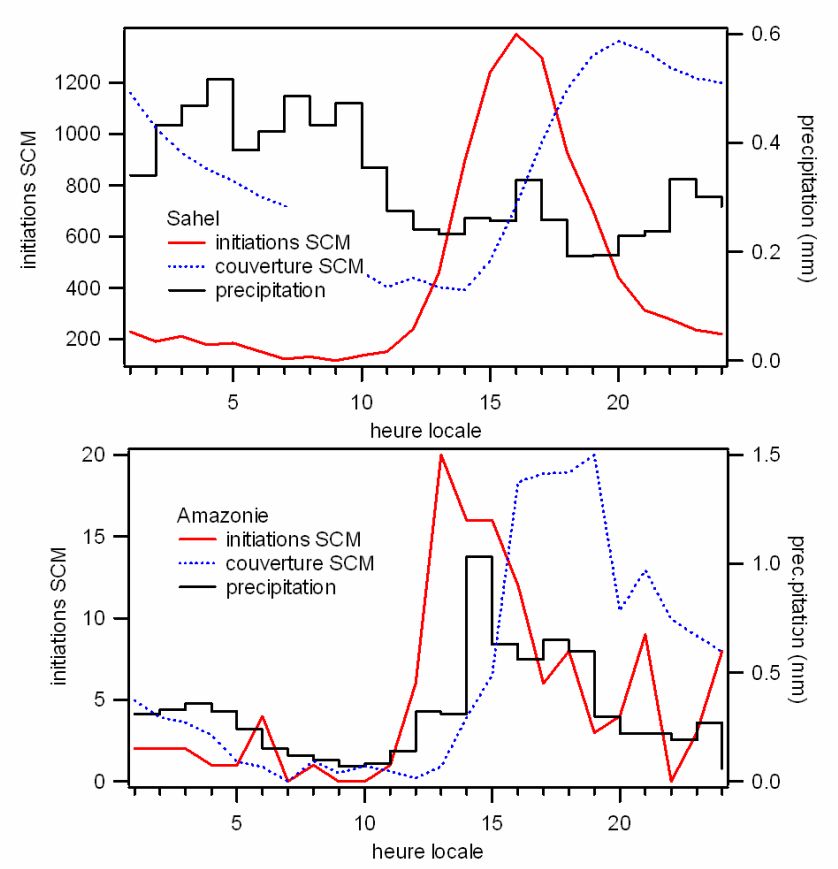


**Figure 3.** Cycle diurne du nombre d'initiations de systèmes convectifs de méso-échelle (SCM), de la couverture nuageuse convective (unité arbitraire) et des précipitations sur l'Afrique de l'Ouest (région de Niamey, en haut) et l'Amazonie du sud-est (Rondônia, en bas).

A l'inverse en zone sahélienne les systèmes convectifs qui comptent réellement pour la pluie sont de grande durée de vie et peuvent donner des précipitations sur de longues périodes. Dans le cas de Niamey, les systèmes qui génèrent le plus de pluie sont des lignes de grains qui naissent 500 ou 1000 km plus à l'est et qui survolent la région bien après leur heure d'initiation (Mathon et al. 2002b). Ceci explique le cycle diurne apparemment paradoxal des pluies à Niamey.

## 4. Systèmes convectifs et circulation générale

Les systèmes convectifs sont un élément majeur de l'atmosphère tropicale avec laquelle ils interagissent fortement. L'existence d'un système convectif dépend bien évidemment de l'état de l'atmosphère : instabilité, énergie et eau disponibles, etc., et de sa dynamique, champs de vents moyens et transitoires notamment. En retour le système convectif modifie l'atmosphère, principalement en redistribuant verticalement de l'eau et de l'énergie.

Parmi les questions scientifiques sur lesquelles on aimerait avancer on peut citer :
- quels sont les paramètres météorologiques déterminants pour le cycle de vie des systèmes convectifs ? Peut-on identifier les facteurs qui agissent sur la formation d'un système, sur son développement ou son affaissement, sur sa propagation ?
- quelles sont les conséquences d'un système convectif sur l'atmosphère, non seulement en termes de profils verticaux de température et d'humidité mais également en termes de modification de la circulation générale ?
- quels sont les feedbacks entre systèmes convectifs et circulation générale ?

Au fur et à mesure des avancées effectuées sur les questions précédentes, les modèles de prévisions météorologiques seront améliorés et permettront de prévoir de mieux en mieux les systèmes convectifs, et par conséquent la pluie, en régions tropicales. Les implications dans ces régions sont évidentes pour l'hydrologie, l'agronomie, la gestion du risque, et même la santé (cf. le projet AMMA[2]). Ces avancées profiteront également à la prévision climatique dont les implications sont planétaires. Mieux comprendre les interactions entre systèmes convectifs tropicaux et circulation générale permet (entre autres !) de mieux prévoir l'impact de l'augmentation des gaz à effet de serre sur l'Europe…

Ma contribution dans ce vaste champ d'investigation a porté principalement sur trois points :
- le comportement des systèmes convectifs en fonction du vent dans la basse à moyenne troposphère ;
- les liens existants ou non entre les ondes d'est et les systèmes convectifs ;
- l'effet des systèmes convectifs sur la divergence du vent dans la haute troposphère.

### *4.1 Régime de vent d'est ou d'ouest en Amazonie*

Durant l'expérimentation WETAMC/LBA les observations du vent ont montré une alternance de périodes de vents de nord-ouest et de vents de nord-est dans la basse et moyenne troposphère. Ainsi ont été définis des « régimes » d'ouest et d'est associés à des caractéristiques différentes de la convection (Silva Dias et al. 2002, Rickenbach et al. 2002, Laurent et al., 2002a). Cette alternance de régimes d'est et d'ouest est montrée dans la Figure 4. La Figure 2 illustre le comportement différent des systèmes convectifs, et des cellules de pluie associées, durant ces deux régimes.

[2] Analyses Multidisciplinaires de la Mousson Africaine - http://amma.mediasfrance.org/

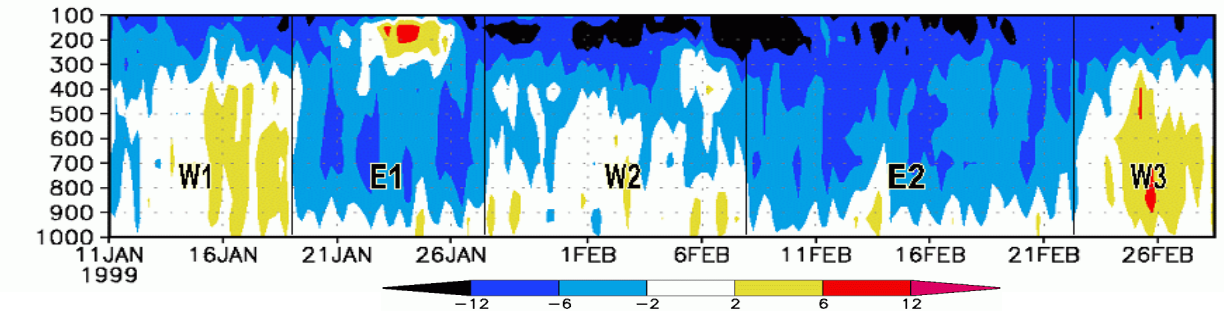


**Figure 4.** Coupe verticale de la composante zonale du vent ($ms^{-1}$) dans la troposphère sur la zone de l'expérience WETAMC/LBA, d'après les réanalyses NCEP. Les périodes des régimes d'ouest (W) et d'est (E) sont indiquées. (Laurent et al 2002a).

Différentes études (Silva Dias et al. 2002, Rickenbach et al. 2002, Laurent et al. 2002a, Peterson et al. 2002, Machado et al. 2002) ont montré que la convection en Amazonie durant le régime d'ouest produit des pluies moins intenses mais plus durables, en d'autre terme les systèmes convectifs sont plus étendus. A l'inverse, en régime d'est la convection est plus explosive, avec d'avantages d'éclairs, ce qui est probablement conséquent à une inhibition de la convection. La propagation des systèmes convectifs est également différente comme on peut le voir sur la Figure 2. Bien marquée et généralement associée avec le vent vers 700 hPa pendant le régime d'est, la propagation des SCM mais surtout celle des cellules de pluie est plus erratique durant le régime d'ouest. A noter également que la propagation des systèmes peut être opposée à l'écoulement dans la haute troposphère, comme on peut le voir autour du 24 janvier dans les Figures 2 et 4 et comme fréquemment observé en régime d'ouest. Ces situations conduisent à des cisaillements verticaux importants qui jouent un rôle dans le comportement des systèmes convectifs, notamment en éloignant les particules condensées en altitude des lieux de formation de nouvelles cellules convectives. Ceci apparaît dans le comportement des cellules de pluie pendant le régime d'ouest (figure 2).

*4.2 Ondes d'est*

En Afrique de l'Ouest le phénomène transitoire le plus remarquable de la circulation générale est une oscillation du champ de vent dans la basse à moyenne troposphère (850 à 600 hPa). Cette oscillation se traduit par une onde d'échelle synoptique, de période entre 3 et 5 jours, appelée onde d'est africaine bien qu'elle se propage sur tout l'Atlantique (Diedhiou et al. 2004). Les ondes d'est ont été bien étudiées depuis l'expérience GATE en 1974 (par exemple Reed et al. 1977) et plus récemment (pour une synthèse complète voir la thèse de Arona Diedhiou, 1998). Plusieurs travaux ont montré que les ondes d'est peuvent moduler les précipitations. Cependant les liens entre ondes d'est et systèmes convectifs ne sont pas élucidés. L'observation montre que les ondes d'est se propagent vers l'ouest à une vitesse d'environ 8 $ms^{-1}$. Les lignes de grains (ou les SCO) qui sont les systèmes convectifs prédominants en termes de pluviométrie sur le Sahel se déplacent également vers l'ouest mais à une vitesse de 12 à 15 $ms^{-1}$. Les lignes de grains ne peuvent donc pas rester longtemps dans une même phase d'onde. Or les modèles de circulation générale ont tendance à produire des systèmes convectifs phasés dans les ondes d'est. Les modèles de circulation générale ont une bonne représentation des

ondes d'est depuis longtemps (Laurent et al. 1989) tandis que leur représentation de systèmes tels que les lignes de grains est encore embryonnaire (Lopez 1993).

Comme déjà mentionné, divers travaux ont mis en évidence la modulation de la pluie et de la convection par les ondes d'est africaines. De même on a pu montrer que les ondes de période 6-9 jours, qui ne sont pas exactement ce qu'on appelle les ondes d'est « classiques » mais qui font partie de la même famille, peuvent également moduler la pluie (Viltard et al. 1998). L'étape suivante a été d'analyser le lien entre les ondes d'est, 3-5 jours et 6-9 jours, et la convection (Diedhiou et al. 1999). Cette étude a permis de clarifier comment les ondes d'est modulent la convection et la pluie et de montrer que la modulation est différente selon qu'il s'agit d'une onde de période 3-5 jours ou 6-9 jours.

Lorsque nous avons disposé du suivi des systèmes convectifs sur une assez grande période nous avons abordé l'étude du lien entre les ondes d'est et les systèmes convectifs (Mathon et al. 2002a). Dans cette étude qui s'intéresse plus particulièrement au Sahel, seuls sont considérés les SCO qui, pour mémoire, représentent 80% de la couverture nuageuse convective et apportent 90% de la pluie totale. Les résultats sont ambigus. D'une part on retrouve ce qui avait déjà été observé pour la convection en général ou pour la pluie, à savoir que les SCO se situent en moyenne préférentiellement dans et à l'avant du thalweg de l'onde (dans et à l'arrière du thalweg dans le nord du Sahel et dans le cas des ondes 6-9 jours). D'autre part, contrairement à ce qu'on aurait pu attendre, le nombre ou la couverture nuageuse des SCO ne semblent pas significativement influencés par l'occurrence des ondes d'est à l'échelle saisonnière.

Le comportement des systèmes convectifs par rapport aux ondes d'est est illustré par la Figure 5 qui présente une série chronologique du champ de vent à 700 hPa sur 48 heures. Sur ce champ de vent (non filtré) ont été superposés les SCM suivis à partir d'images satellitales pour 3 seuils en température de brillance (253, 233 et 213 K). A noter que ce suivi n'a été effectué que sur une fenêtre (0 N-20 N ; 20 E-20 W) qui ne couvre pas la zone océanique. Le 23 juin à 00 TU on observe une onde d'est typique (période 3-5 jours) dont le thalweg se situe à 15 E. De petits systèmes convectifs se développent dans et à l'avant de ce thalweg, entre 10 et 20 E. Ces systèmes se développent en se propageant vers l'ouest avec l'onde et vont se regrouper en un gros système le 23 juin à 18 TU, en accord avec le développement diurne des SCM. Une seconde onde 3-5 j apparaît le 24 juin à 00 TU vers 30 E. Six heures plus tard le thalweg associé est situé vers 25 E, avec également des systèmes convectifs qui se développent à l'avant de ce thalweg. Cet exemple illustre bien que l'onde d'est, lorsqu'elle existe, influe sur la localisation des systèmes convectifs, tout au moins dans leur phase de croissance. Ensuite les systèmes convectifs se propageant plus vite que l'onde leur relation avec les ondes pendant le reste de leur cycle de vie n'est plus évidente.

Dans l'exemple pédagogique présenté dans la Figure 5 apparaît également une onde caractérisée par une circulation anticyclonique entre deux thalwegs situés à 15 W et 60 W le 23 juin à 00 TU. Il s'agit d'une onde 6-9 jours. On note de nombreux petits SCM entre 5 et 15 W, c'est-à-dire dans et à l'arrière du thalweg. Ces systèmes vont se propager vers l'ouest, restant dans la même phase de l'onde

pendant leur phase de développement. Ceci illustre avec les systèmes convectifs le résultat obtenu par Diedhiou et al. (1999), à savoir que dans le cas des ondes 6-9 j le maximum de convection se situe dans et à l'arrière du thalweg, dans le flux de sud, alors que dans le cas des ondes 3-5 j il se situe dans et à l'avant du thalweg, dans le flux de nord.

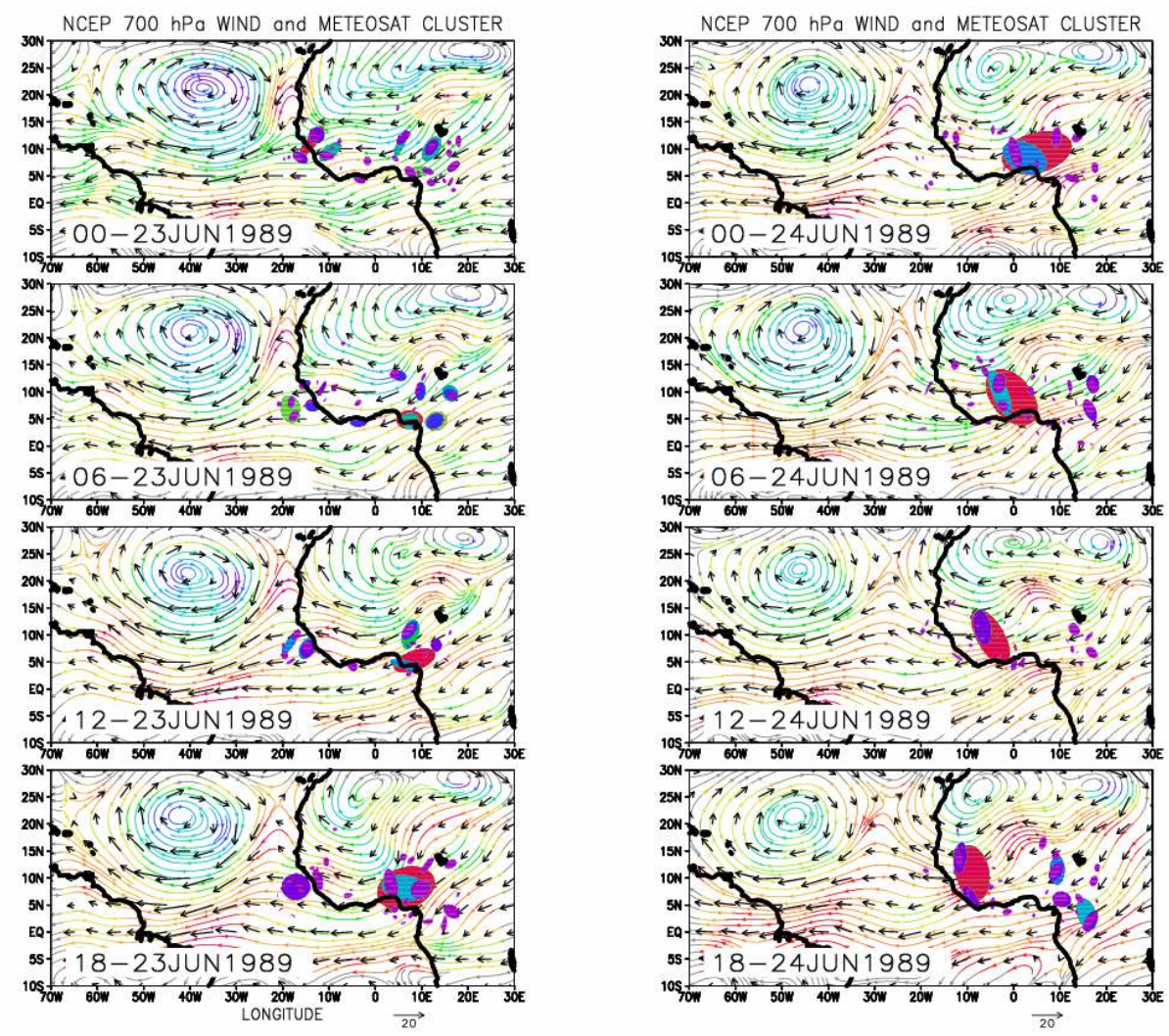


**Figure 5.** Systèmes convectifs de méso-échelle suivis par satellite aux seuils 253 K (rouge), 233 K (bleu) et 213 K (violet), superposés au champ de vent à 700 hPa ($ms^{-1}$) d'après les réanalyses NCEP. Séquence toutes les 6 h du 23 et 24 juin 1989. Les SCM sont suivis uniquement sur la fenêtre 0N-20 N et 20W-20E. (Adapté de Lebel et al. 2003).

Un autre aspect est de savoir si l'existence ou l'absence d'ondes d'est a une importance pour l'occurrence de systèmes convectifs. Comparant les périodes avec ou sans onde d'est établie, les résultats montrent que les SCO ne sont pas sensibles à la présence d'ondes (Mathon et al. 2002a). En synthèse, quand une onde d'est existe elle module la localisation des systèmes convectifs et par conséquent celle de la pluie, mais l'existence, le nombre et la taille des SCO ne semblent pas dépendre de l'activité des ondes d'est.

*4.3 Divergence en altitude*

La convection profonde et les mouvements atmosphériques horizontaux sont intimement liés. A l'échelle de la circulation de Hadley, la convection fournit l'énergie nécessaire pour forcer des mouvements de grande échelle qui vont en retour produire la convergence d'humidité dans les basses couches nécessaire pour alimenter la convection. Cet ensemble se traduit par des mouvements ascendants dans les systèmes convectifs et de la divergence dans les hautes couches par respect de l'équation de continuité. Ce schéma peut se retrouver à l'échelle d'un système convectif : il s'agit de la théorie de l'instabilité convective de second ordre (CISK), cf. par exemple Smith (1997). D'autres schémas plus complexes sont observés, cependant la partie supérieure d'un système convectif est a-priori associée à de la divergence, tout au moins dans les phases de développement et de maturité.

Malheureusement les observations conventionnelles en altitude sont rares dans les tropiques et hormis quelques expérimentations ciblées et de courte durée on ne dispose que de données satellitales pour étudier les circulations atmosphériques associées à la convection. Depuis la mise en opération des satellites géostationnaires météorologiques, leurs opérateurs ont développé des techniques d'estimation du vent par suivi de nuages d'une image à l'autre. Les petits nuages choisis à cette fin en utilisant le canal infrarouge thermique (~ 12 μm) sont censés se comporter comme des traceurs passifs entre deux images, soit 30 min. Cette technique donne des résultats satisfaisants et alimente les modèles météorologiques depuis longtemps, mais le nombre d'observations obtenues est insuffisant pour en déduire une valeur dérivée telle que la divergence horizontale du vent.

Ces dernières années de nouvelles techniques se sont développées en utilisant d'autres canaux des satellites géostationnaires. Il se trouve que c'est un domaine qui m'est familier pour en avoir été un des instigateurs en développant la mesure du vent à partir du canal vapeur d'eau (~ 6 μm) (Laurent, 1993). Cette technique allait bientôt devenir un produit opérationnel en Europe, puis aux Etats-Unis (Velden et al. 1997) et dans les autres centres de production opérationnelle de produits dérivés des satellites météorologiques (Japon, Inde, Russie, et plus récemment Brésil).

Les estimations de vent à partir d'images successives du canal vapeur d'eau des satellites géostationnaires sont nombreuses, concentrées dans la moyenne et surtout la haute troposphère, et fournissent des champs de vents denses et cohérents. Outre leur vocation première qui est d'alimenter en temps réel les modèles de prévision météorologique, ces observations peuvent également être utiles pour des études climatologiques (Schmetz et al. 1995) ou pour étudier les systèmes convectifs. Nous avons ainsi développé une estimation de la divergence du vent horizontal dans la haute troposphère à partir des vents "vapeur d'eau" (Laurent and Sakamoto 1998), en utilisant une méthode d'interpolation sur une grille régulière adaptée de Barnes (1964). Ce travail préliminaire montrait que les zones de convection profonde étaient bien corrélées avec une divergence en altitude. Cette approche a ensuite été utilisée en complément avec d'autres observations et un modèle de circulation générale dans une étude de la divergence associée à la convection sur l'océan indien (Bonazzola et al. 2001). Dans cette étude la divergence déduite des vents "vapeur d'eau" a été utilisée pour valider une reconstruction de la divergence à partir de la température de brillance et de l'activité convective. L'objectif de ce type

d'approche est de forcer un modèle atmosphérique afin d'améliorer la prévision du transport vertical et de la divergence qui ne sont actuellement pas suffisamment bien décrits dans les modèles globaux.

Une étude approfondie de la divergence associée aux systèmes convectifs a été menée sur l'Amérique du Sud sur la période de l'expérimentation WETAMC/LBA du 10 janvier au 28 février 1999. Les techniques d'estimation du vent à partir d'images du canal vapeur d'eau ont été adaptées et optimisées pour les satellites GOES et Meteosat (Laurent et al. 2002b, Sakamoto and Laurent 2002, 2003, Sakamoto et al. 2004). La figure 6 montre un exemple du vent observé dans la haute troposphère (vers 200 hPa), ainsi que le champ de vent interpolé sur une grille régulière et la divergence horizontale qui s'en déduit par différences finies. Les structures suivies correspondent ici à des nuages hauts ou à des structures de vapeur d'eau dans le voisinage des nuages hauts, dans la couche 250-150 hPa. Les structures vapeur d'eau de ciel clair, qui sont plus difficiles à interpréter en terme de vent et qui se situent à des altitudes plus basses, n'ont pas été prises en compte.

Afin d'effectuer des tests sur le calcul de la divergence qui se révèle très sensible aux résolutions spatiales et temporelles, j'ai calculé les vents "vapeur d'eau" à très haute résolution spatiale et toutes les 30 min sur la période WETAMC/LBA. (résultats non publiés). En valeur moyenne le champ de vent observé est excellent et le champ de divergence associé, très cohérent, montre des maxima qui correspondent très bien avec les zones de convection : on peut le voir en comparant la Figure 9 dans Machado and Laurent (2004) et la Figure 4 dans Laurent et al. (2002a). A des échelles de temps plus fines comme dans l'exemple de la Figure 6, on observe des champs de divergence consistants qui évoluent de façon cohérente au cours du temps, mais dont l'interprétation et le lien avec les systèmes convectifs ne sont pas triviaux. Ceci est fortement lié à la grande sensibilité de l'estimation de la divergence à l'échelle considérée. Une approche spectrale est à l'étude afin de mieux séparer les échelles.

Sur le site principal de l'expérimentation WETAMC/LBA où nous disposons de nombreuses observations in-situ (radiosondages, précipitations, radar) en complément des observations satellitales, nous avons mené une analyse détaillée des relations entre la divergence en altitude, les systèmes convectifs et la précipitation (Lima et al. 2003). Dans ce cas particulier, on observe d'une part un bon accord entre la divergence dérivée des vents "vapeur d'eau" et celle calculée à partir d'un réseau de radiosondages, et d'autre part une correspondance entre le maximum de divergence et le maximum d'activité convective (voir la Figure 10 dans Machado and Laurent 2004). Malheureusement ce résultat n'a pu encore être confirmé ailleurs, en grande partie à cause du manque d'observations adéquates. Ce sera un point qui sera étudié sur l'Afrique de l'Ouest grâce aux données de l'expérimentation AMMA en 2006.

La relation entre les systèmes convectifs et la divergence dans la haute troposphère a été étudiée dans Machado and Laurent (2004). Le point de départ de cette étude était de savoir si on pouvait relier simplement la divergence du vent induite au sommet d'un système convectif avec son taux d'expansion. Les résultats montrent qu'une telle simplification n'est pas valable : il faut tenir compte également du taux d'expansion du système dû à la condensation de l'eau. Les résultats montrent que :

- une anomalie positive de divergence s'observe au sommet des systèmes convectifs ;
- cette anomalie augmente avec l'importance du système (indiquée par sa durée de vie ou sa taille) ;
- cette anomalie est faible lors de l'initiation du système et devient importante dans la phase de croissance et de maturation du système, puis redevient faible en fin de cycle ;
- l'anomalie de divergence est en valeur absolue relativement faible comparée au taux d'expansion du système convectif.

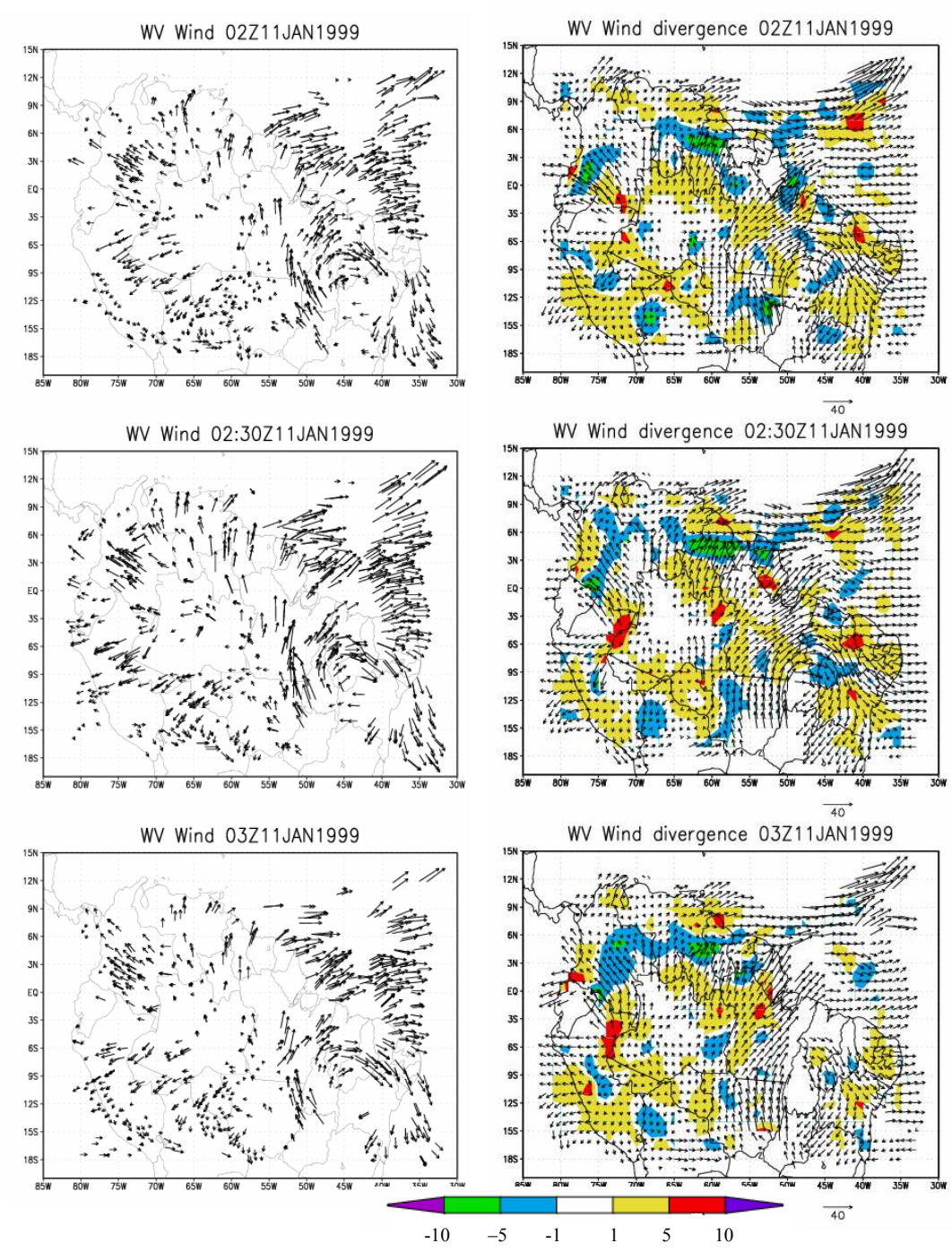


**Figure 6.** Vent dans la couche 150-250 hPa observé à partir d'images du canal vapeur d'eau du satellite GOES à 30 min d'intervalle (gauche). Champ de vent ($ms^{-1}$) calculé par interpolation spatio-temporelle des champs observés sur une grille régulière et divergence associée ($10^{-5}$ $s^{-1}$) (droite).

## 5. Systèmes convectifs et surface

L'atmosphère tropicale continentale pendant la saison humide est le plus souvent conditionnellement instable. Cela veut dire qu'une particule d'air des basses couches élevée jusqu'à un certain niveau voit sa flottabilité devenir positive et se met donc à s'élever spontanément : c'est le début de la convection. Ainsi pour déclencher la convection il faut un mécanisme qui suscite l'élévation initiale des basses couches ou bien des facteurs qui diminuent la couche d'inhibition. Dans les deux cas les conditions de surface jouent généralement un rôle.

Le relief est un paramètre important pour la convection. D'une part, la couche d'inhibition est réduite pour des masses d'air dont la base est surélevée, par exemple dans le cas d'un plateau par rapport à des bas-fonds. D'autre part, les variations du relief dévient l'écoulement du vent des basses couches et peuvent dans certains cas amener l'air à son niveau de convection libre.

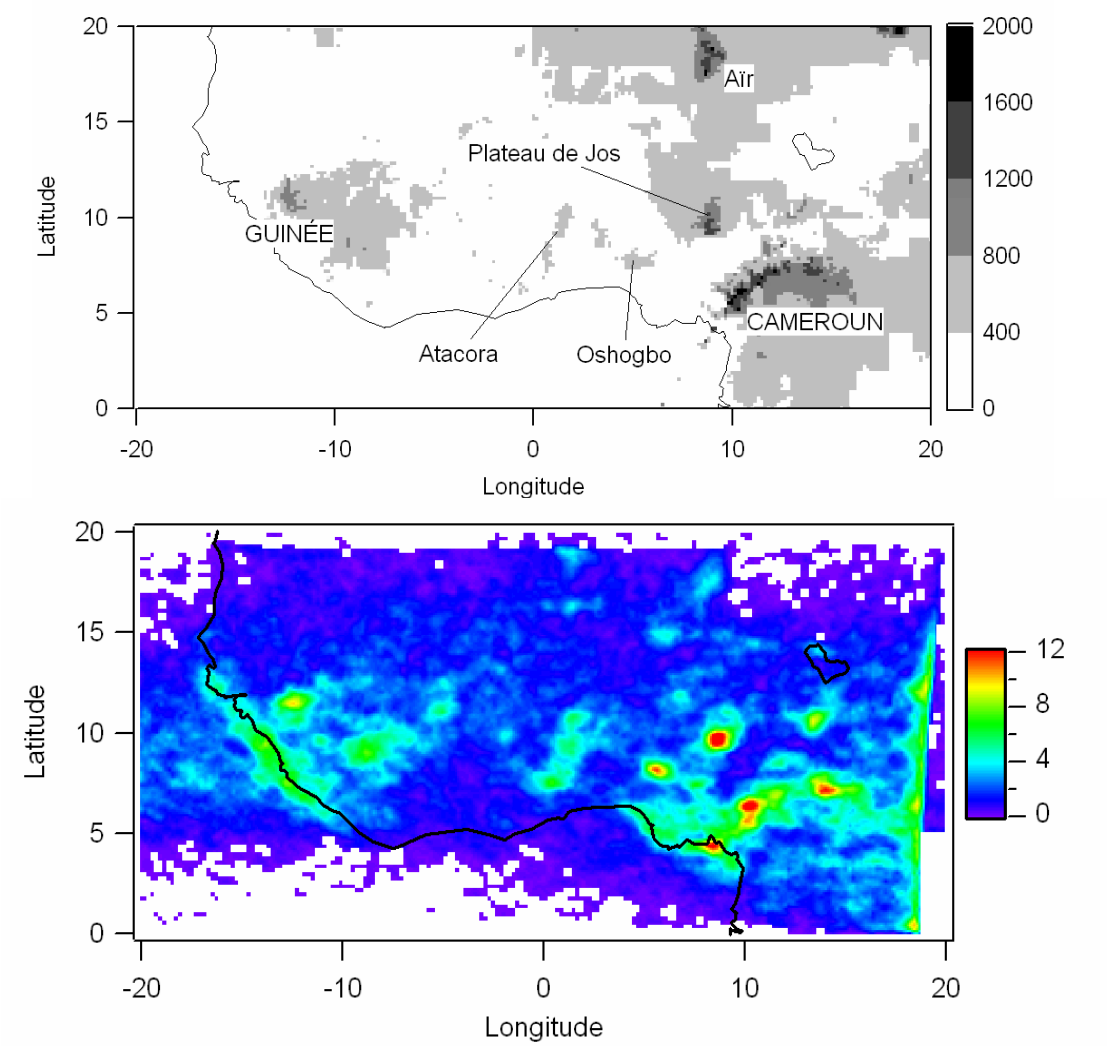


**Figure 7.** Relief (m) de l'Afrique de l'Ouest (haut) et nombre d'initiations de systèmes convectifs de méso-échelle par an (bas). Le maximum vers 19 E est un artefact dû au bord des images utilisées.

La Figure 7 montre le relief et les lieux de naissance des systèmes convectifs sur l'Afrique de l'Ouest. On peut reconnaître dans les lieux de naissance les reliefs tels que les montagnes du Cameroun, le plateau de Jos, l'Aïr, l'Atacora, les montagnes guinéennes. A noter également sur la Figure 7 les lieux de naissance privilégiés sur la cote guinéenne et sur la côte du Nigeria, zones qui combinent plusieurs effets favorables à la convection : flux d'humidité de l'océan vers le continent (flux de mousson), élévation des masses d'air forcée par le relief, et effets de brises côtières. Les trois principaux lieux de naissance des systèmes convectifs, à savoir les monts du Cameroun et de Guinée et le plateau de Jos, se retrouvent dans les occurrences de la convection totale (voir Figure 13 dans Mathon and Laurent 2001). Cependant les systèmes convectifs les plus importants en taille et en activité, après leur naissance sur les reliefs de l'est du Sahel (plateau de Jos, Aïr, …), ont une contribution maximale sur le centre du Sahel qui est peu élevé et sans relief notoire (voir Figure 16 dans Mathon and Laurent 2001 et Figure 6 dans Mathon et al. 2002b). Ceci montre que les systèmes convectifs qui se propagent sur le Sahel n'ont plus besoin du relief pour entretenir la convection, mais au contraire qu'ils s'auto-entretiennent en perturbant eux-mêmes les basses couches de leur environnement immédiat, comme cela a été montré à partir d'observations et de modélisations des lignes de grains tirées des expériences GATE en 1974 et COPT en 1981 (Franck 1978, Roux 1988, Redelsperger and Lafore 1988, Lafore and Moncrieff 1989, Sun et al. 1993).

Dans une étude à plus fine échelle (Laurent et al. 2002a) nous avons analysé l'influence du relief sur l'initiation des systèmes convectifs durant l'expérience WETAMC/LBA. Les résultats ont montré que les systèmes convectifs s'initient préférentiellement dans les zones relativement élevées (mais pas au sommet des montagnes) et dont l'escarpement est également relativement fort. En analysant l'initiation des systèmes en fonction du vent près de la surface, il apparaît que les conditions favorables sont situées sur les pentes du relief du coté au vent. Il n'a pas été mis en évidence de différence notoire pour le déclenchement des systèmes convectifs entre régime d'est et régime d'ouest. Dans cette étude nous avons également tenté d'analyser l'influence éventuelle du type de végétation sur le déclenchement de la convection, sans résultat significatif. Cette absence de résultat est en partie attribuée au fait que l'étude portait sur la saison humide en Amazonie. En effet, Fisch et al. (2004) montrent que les différences dans la structure de la couche limite atmosphérique entre forêt et pâturages apparaissent de manière marquante en saison sèche ou en saison de transition et non en saison humide.

Nous nous sommes également intéressés aux effets d'un changement de végétation sur la convection, et plus particulièrement aux conséquences de la déforestation en Amazonie. Le but de cette étude (Durieux et al. 2003) était d'évaluer si le changement climatique prédit par les simulations numériques en cas de déforestation majeure était déjà perceptible. Les résultats ne montrent pas de changement significatif de la couverture nuageuse attribuable à la déforestation à l'échelle interannuelle. Ceci est dû au fort impact du phénomène El Niño sur les variations interannuelles. En revanche un changement est décelable sur les distributions saisonnières et diurnes de la couverture nuageuse. La Figure 8 illustre le cycle annuel de la couverture de nuages hauts pour deux régions voisines et similaires, l'une ayant subie une forte déforestation (D3) et l'autre non (R3). On peut voir

que la région déforestée a une couverture en nuages hauts (nuages liés à la convection) renforcée en saison humide et diminuée en saison sèche. Au total, les résultats de cette étude montrent que le remplacement de la forêt primaire par des pâturages entraîne les tendances suivantes : pendant la saison sèche les zones déforestées présentent une augmentation des nuages bas en début d'après-midi et une diminution de la convection la nuit ; en saison humide la convection est augmentée en début de nuit sur les zones déforestées. Ainsi la déforestation tendrait à renforcer les différences entre les saisons.

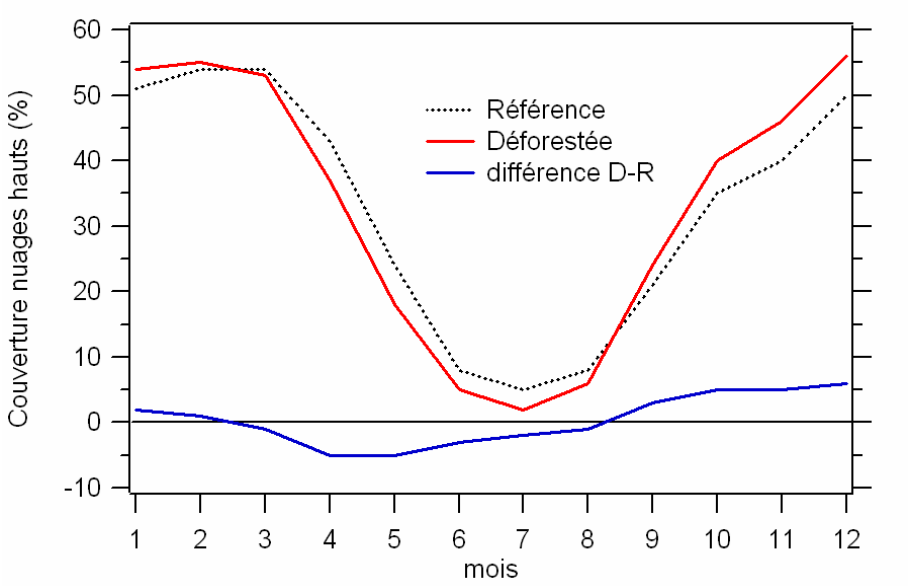


**Figure 8.** Moyenne mensuelle de la couverture de nuages hauts (P < 440 hPa) exprimée en pourcentage de la surface totale, pour une région déforestée et pour une région similaire de référence. (Adapté de Durieux et al. 2003).

Comme mentionné ci-dessus le phénomène El Niño a un fort impact sur la variabilité interannuelle du climat en Amérique du Sud. Cet impact est bien sûr différent selon les régions. En étudiant l'effet des deux principaux El Niño du siècle passé (1982-1983 et 1997-1998) sur les différents types de végétation du Brésil, nous avons montré que l'impact en un lieu donné peut être radicalement différent (Dessay et al. 2004). Cette étude suggère plusieurs pistes pour expliquer ces différences. Tout d'abord il convient de quantifier la part des problèmes qui peuvent découler d'une homogénéité insuffisante des données d'observation satellitales, ce qui dans le cas considéré ne peut expliquer à lui seul les différences d'impacts observées entre les deux épisodes El Niño. Une première explication physique serait une sensibilité de la végétation aux conditions climatiques qui ont précédé l'événement El Niño. D'autre part les températures de surface de l'Atlantique peuvent moduler les effets dans l'atmosphère des anomalies de températures de surface du Pacifique propres au phénomène El Niño.

Afin d'étudier le rôle de l'océan Atlantique sur le climat du Brésil nous avons analysé les corrélations entre les flux de chaleur latente sur l'Atlantique tropical et la convection sur le continent. Une première étude s'intéressant plus particulièrement à la couverture de nuages convectifs sur la

région du Nordeste (Durand et al. 2005), montre comment la saison des pluies pourrait être mieux prévue à partir de données d'observations de flux de surface en mer. Une autre étude en cours (non publiée) s'intéresse aux relations entre ces flux de chaleur latente de l'Atlantique et l'organisation des systèmes convectifs sur le Nordeste et l'Amazonie, en regardant en particulier la naissance des lignes de grains qui se forment sur le littoral et leur propagation jusqu'au cœur de l'Amazonie.

Dans une étude sur la variabilité saisonnière et le cycle diurne de la convection dans la région amazonienne, nous avons tenté d'analyser les différences entre des régions ayant différents types de végétation (Machado et al. 2004). Précisons que même pendant la saison dite « sèche » il y a une activité convective non négligeable dans ces régions. Il apparaît que les zones déforestées et les régions de savane réagissent de façon similaire. Les différences entre régions de forêt dense et régions de savane ou déforestées sont bien plus marquées durant la saison sèche que pendant la saison humide. Un résultat intéressant est que les sites de forêt dense équatoriale présentent un cycle saisonnier assez important pour les précipitations et la couverture nuageuse, alors que l'énergie disponible pour la convection (CAPE) varie peu. Ceci montre que de faibles changements dans les paramètres énergétiques qui régissent la convection peuvent avoir un fort impact sur la précipitation. Par conséquent l'atmosphère tropicale en Amazonie apparaît sensible à un changement climatique à travers sa sensibilité aux paramètres régissant la convection. Un autre résultat suggéré par cette étude est que les sites de forêt équatoriale montrent la capacité de stocker de l'énergie latente dans le complexe atmosphère-biosphère pendant la saison sèche, ce qui n'est pas le cas pour les régions de savane ou de déforestation (pâturages).

Dans cette étude il est aussi montré que les régions de savane présentent une fréquence d'événements orageux très importante avant et pendant la saison humide, et très faible pendant la saison sèche. Les événements pluvieux sont relativement peu fréquents mais plus violents pendant la transition entre la saison sèche et la saison humide.

Les différences observées dans l'activité de la convection et notamment les différences entre saison sèche et saison humide se retrouvent dans l'observation de la végétation, sans que l'on soit d'ailleurs en mesure de faire la part entre un effet atmosphérique et le changement de végétation. Une étude en cours (Dessay et al., article en préparation) montre que le pic de stress de la végétation qui s'observe en saison sèche pour la forêt tropicale ouverte est bien plus prononcé pour une zone déforestée, alors que les différences sont peu marquantes le reste de l'année. Une méthode de détection des zones déforestées a été développée à partir de ce résultat.

## 6. Systèmes convectifs et prévision immédiate

Les systèmes convectifs sont le vecteur principal des pluies en région tropicale. Mais ces amas de nuages orageux peuvent être extrêmement violents et causer des dégâts considérables soit par les rafales de vent associées soit par les pluies violentes qu'ils provoquent. C'est ainsi qu'une meilleure connaissance de leurs évolutions est requise non seulement pour améliorer la compréhension et la modélisation du climat, mais également comme aide à la prévision immédiate (nowcasting). A titre d'exemple, nous avons été sollicités par une société gérant la distribution d'énergie au Brésil pour développer une application de nos recherches permettant de mieux anticiper les trajectoires des systèmes convectifs qui causent d'importants dommages aux lignes électriques.

L'identification de paramètres prédictifs pour l'évolution d'un système convectif aurait des applications importantes pour un système d'aide à la prévision immédiate. C'est pourquoi nous avons approfondi l'étude des relations entre le développement d'un système convectif et son évolution au cours de son cycle de vie (Machado and Laurent 2004). Cette étude montre que la vigueur du développement initial d'un système, mesurée par son taux d'expansion, donne une indication sur sa durée de vie (cf. Figure 9) et sa taille.

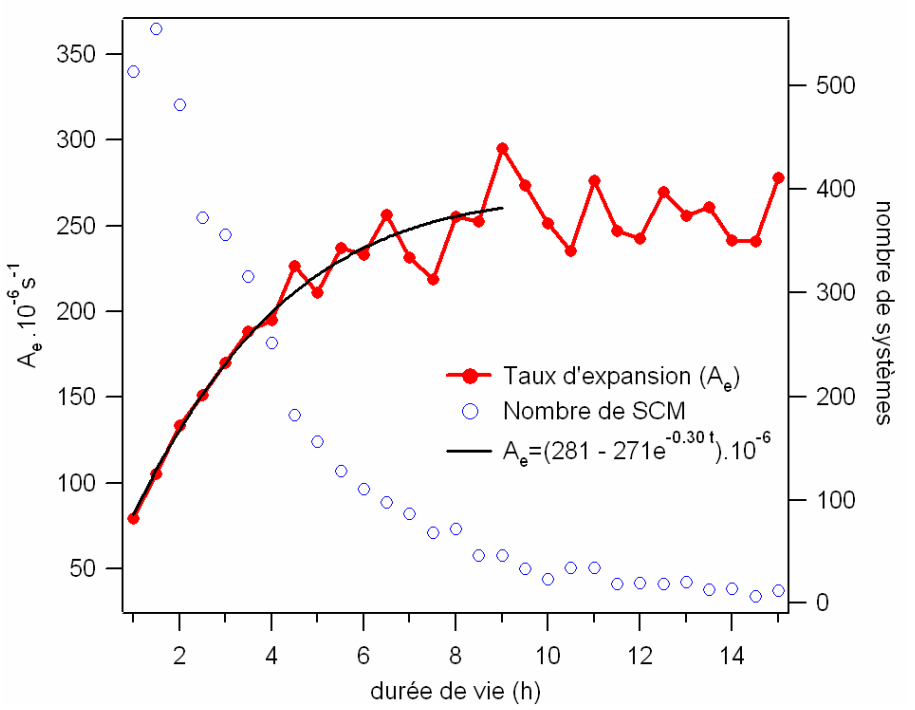


**Figure 9.** Taux d'expansion initial de la surface des SCM en fonction de leur durée de vie. Le nombre de cas est également indiqué. (Adapté de Machado and Laurent 2004).

Il apparaît donc possible de prévoir la durée de vie probable d'un système convectif en mesurant son taux d'expansion initial. La trajectoire à court terme de ce système peut être estimée à partir de sa trajectoire déjà accomplie et de la connaissance climatologique qu'on peut avoir de la région comme par exemple pour l'Afrique de l'Ouest (Mathon and Laurent 2001). De plus on dispose d'indications sur l'importance de l'écoulement atmosphérique vers 700 hPa sur le comportement des systèmes

convectifs (Laurent et al. 2002a), ce qui permet de tester des indicateurs de trajectoires probables des systèmes en fonction du vent à ce niveau.

Ces idées nous ont amenés à développer une version opérationnelle de l'algorithme de suivi des systèmes convectifs appelée FORTRACC (Forecast and tracking of active convective cells). A partir du travail de Machado and Laurent (2004), le cycle de vie des systèmes convectifs est modélisé par l'équation donnant l'aire du système en fonction du temps :

$$A(t) = \alpha.\exp(at^2 + bt + c)$$

Ce qui conduit pour l'évolution du système à :

$$1 / A * (\partial A/\partial T) = mt + b$$

Les valeurs de m et b sont ajustées sur une région donnée à partir d'une étude statistique, en classant les systèmes convectifs en trois catégories selon leur durée de vie : inférieure à 2 h, entre 2 et 6 h, ou supérieure à 6 h. A partir de ces droites ajustées, la durée de vie d'un système se déduit de son taux d'expansion observé à son initiation.

Ce produit fonctionne en opérationnel au Centre de prévision du temps et d'études climatiques (CPTEC)[3] de l'institut de recherches spatiales du Brésil (INPE). Il permet de voir les systèmes convectifs à l'instant présent sur l'Amérique du Sud, leur évolution passée et leur évolution probable dans les 2 h à venir.

[3] Voir la page du CPTEC : www.cptec.inpe.br rubrique *satélite* puis rubrique *sistemas convectivos-tempestades*.

# PARTIE IV – PERSPECTIVES

Le cycle de l'eau dans les régions tropicales est dominé par la convection. En effet à grande échelle la convection effectue le transport vertical de l'eau et de l'énergie dans la troposphère tropicale, activant l'exportation d'énergie vers les pôles et donc la redistribution globale de l'énergie reçue inégalement du soleil. Cette convection est alimentée par les flux de vapeur d'eau des basses couches et se traduit par la zone de convergence intertropicale. A plus petite échelle, la convection s'organise en amas nuageux de méso-échelle (~ 10 à 1000 km) dont les éléments les plus actifs (cyclones, tempêtes tropicales, lignes de grains) peuvent avoir des conséquences dévastatrices. Ces systèmes convectifs de méso-échelle sont les vecteurs des pluies tropicales qui sont générées par des cellules convectives internes aux systèmes de méso-échelle. On atteint ici l'échelle (~1 à 10 km) des champs de précipitations qui intéressent l'hydrologie. C'est l'échelle des impacts de la pluie sur la surface : agriculture, érosion, activités socio-économiques et santé. C'est également à petite échelle qu'ont lieu les processus de rétroactions des flux de surface sur la convection atmosphérique.

Les systèmes convectifs de mésoéchelle sont les producteurs de pluie dans les régions tropicales, ils sont également l'élément central pour étudier le couplage entre l'atmosphère et l'hydrologie. La mésoéchelle est l'échelle à laquelle on peut essayer de faire le lien entre les processus atmosphériques régionaux tels que la mousson ou les interactions entre surface et variabilité atmosphérique, et l'échelle pertinente en hydrologie qui se situe plutôt au niveau des cellules de pluie internes aux systèmes convectifs.

En s'appuyant sur les résultats obtenus récemment par les campagnes d'observation LBA en Amazonie, on peut partir de l'hypothèse qu'il existe deux types de convection :

- type 1 : forte inhibition, systèmes violents, précipitations relativement courtes mais de forte intensité donnant donc une quantité totale de précipitation équivalente, beaucoup d'éclairs, phase de glace importante, mouvements verticaux forts. Comme il y a peu de systèmes convectifs l'atmosphère contient beaucoup de noyaux de condensation (CCN).
- type 2 : système de mousson, faible inhibition, plus de systèmes, de plus grande taille (ce point reste à vérifier), précipitations assez longues mais moins intenses, moins d'éclairs, mouvements verticaux moins violents, moins de glace et phase chaude plus importante. Comme il y a un bon lessivage de l'atmosphère il y a moins de CCN.

On remarque que ces deux types de convection (ou plus exactement d'organisation de la convection), observés en un même lieu à différents moments en Amazonie, correspondent à l'idée qu'on se fait de la convection au Sahel (type 1) et au sub-Sahel (type 2) durant la mousson africaine. Cela demande à être approfondi.

L'étude de l'organisation de la convection dans la mousson africaine va être possible avec des moyens inégalés grâce au programme AMMA (Analyse Multidisciplinaire de la Mousson Africaine) dont la stratégie d'observation est organisée en trois niveaux temporels : une période d'observation longue (1990-2010) qui permet entre autres d'acquérir des observations détaillées des précipitations ; une période d'observation renforcée (2005-2007) qui va, entre autres, activer un réseau synoptique de radiosondages ; des campagnes d'observations intensives en 2006 qui vont fournir, entre autres, des données d'observation in situ des processus liés à la convection et aux flux de surface. Ces jeux de données vont permettre des études très complètes de la convection à différentes échelles, et de ses interrelations avec les autres processus atmosphériques et de surface. Au niveau des échelles spatiales, la mésoéchelle relie les processus atmosphériques régionaux tels que la mousson ou les interactions entre surface et variabilité climatique, avec les échelles pertinentes en hydrologie qui se situent plutôt au niveau des cellules de pluie internes aux systèmes convectifs..

Poursuivant l'approche systèmes convectifs de méso-échelle, plusieurs champs de recherches apparaissent pour comprendre le fonctionnement de la convection :

*1. Systèmes convectifs*

Il est avant tout nécessaire de poursuivre la climatologie des systèmes convectifs, c'est-à-dire l'étude de leur cycle de vie et de leur classification. Il s'agit de dégager différentes classes de systèmes convectifs en relation avec l'efficacité pluviométrique ou en fonction des implications dans la circulation atmosphérique. Ce travail nécessite de faire appel à différents types de données d'observation satellitales et in-situ. Les climatologies obtenues pour différents continents présentent des similitudes et des différences qu'il convient de comprendre pour espérer pouvoir les reproduire par la modélisation.

Poursuivre la climatologie des systèmes convectifs s'impose non seulement pour disposer de périodes d'observations plus longues et donc bien adaptées à l'étude de la variabilité climatique, mais également pour tirer profit des possibilités offertes par les nouveaux satellites. La nouvelle série des satellites Meteosat (MSG pour Meteosat Seconde Génération) offre 12 canaux au lieu de 3 et de meilleures résolutions spatiale (3 km) et temporelle (15 min). On s'attend à une amélioration sensible de la description des systèmes convectifs, par exemple la possibilité de discrimination entre nuage chaud et glace avec le canal 1.6 µm ou l'identification du type de glace avec le canal 3.9 µm. Il existe donc des perspectives pour relier la phase des systèmes convectifs dans leur cycle de vie à la microphysique des nuages et aux précipitations. Le satellite MEGHA-TROPIQUES, dont le lancement est prévu en 2009, sera dédié à l'étude du système tropical, permettant en particulier d'étudier l'environnement des systèmes convectifs. Les études préliminaires nécessitent une climatologie des systèmes convectifs qui doit être établie à partir du suivi des systèmes sur différentes régions : Amérique du Sud, océan Atlantique, Afrique, océan Indien.

*2. Liens avec la grande échelle et les processus de mésoéchelle*

Plusieurs voies sont possibles pour étudier les liaisons entre les systèmes convectifs et la circulation à grande échelle. Par exemple un travail fondé sur une réduction pertinente de

l'information disponible sur la circulation générale fournie par les réanalyses d'une part, et sur le catalogue des systèmes convectifs précipitants d'autre part, devrait permettre d'identifier des paramètres dérivés de la circulation à grande échelle pouvant expliquer la variabilité pluviométrique à méso-échelle. Autre exemple, les travaux sur la divergence en altitude vont être poursuivis afin de comprendre pourquoi le lien très fort entre la convection profonde et la divergence en altitude qu'on observe à grande échelle et sur une grande période ne se retrouve pas clairement à l'échelle d'un système convectif.

La convection repose sur des processus de méso-échelle qui vont être étudiés grâce aux observations de l'expérimentation AMMA mais également avec les nouveaux moyens satellitaires. Par exemple la variation de la microphysique de nuage au cours du cycle de vie des systèmes convectifs pourra être explorée à partir de données radar, des éclairs, des capteurs micro-ondes des satellites défilants (TRMM, MegaTropiques) et même avec MSG (possibilité de discrimination entre nuage chaud et glace ou identification du type de glace, comme déjà mentionné ci-dessus). Par ailleurs un sujet important est l'étude du phénomène d'inhibition de la convection, qui pourrait être à l'origine de la différence entre la convection explosive de type 1 (forte inhibition) et la convection de type 2 correspondant au régime de mousson (faible inhibition). Il s'agit d'évaluer les processus liés à l'inhibition : subsidence, advection d'air stable (plus sec ou plus froid), déficit d'énergie dans les basses couches.

*3. Précipitations*

Les précipitations sont la principale interface entre hydrologie et physique de l'atmosphère. Leur étude soulève des questions intéressantes souvent relatives aux problèmes d'échelle. Les précipitations produites par les Modèles de Circulation Générale Atmosphériques (MGCA) ou par des estimations dérivées d'observations satellitales sont des moyennes sur des mailles très grandes par rapport aux besoins d'entrée des modèles hydrologiques. Il est donc nécessaire de développer des méthodes de désagrégation. Réciproquement il existe un besoin d'agrégation lié à la conception de certains modèles. D'une manière générale la pluie est mal estimée, et rarement observée aux échelles pertinentes pour l'investigation scientifique ou pour les applications telles que la gestion de la ressource en eau. Suite aux travaux très récents d'Abdou Ali (2004) la modélisation des champs de précipitation au Sahel intègre depuis peu les caractéristiques des systèmes convectifs déduites du suivi par satellite. Ces travaux seront poursuivis pour développer de nouvelles méthodes d'estimation des précipitations, suivant trois approches :

- une approche basée sur l'expansion des systèmes convectifs dans leur phase initiale, dans la suite des travaux de Machado and Laurent (2004) ;

- une approche basée sur la microphysique en l'utilisation d'un modèle radiatif pour simuler la température de brillance en fonction de la microphysique des systèmes convectifs estimée à partir d'observations par satellite (MSG), s'appuyant en partie sur les approches dites « model to satellite ».

- une approche stochastique à développer à partir des travaux d'Abdou Ali (2004) et du suivi des systèmes convectifs. Une telle méthode qui considère les aspects statistico-dynamiques des champs de précipitations devrait mener à une meilleure combinaison de données de surface et données satellitales, en prenant en compte explicitement la notion d'événement.

Un autre aspect qui est particulièrement important pour des régions comme le Sahel ou le Nordeste brésilien est celui de l'efficacité des précipitations. Pourquoi un système convectifs apparemment très actif peut parfois ne donner que peu ou pas de précipitation en surface ? Il semble que l'explication relève de l'évaporation de la pluie dans les basses couches. Une approche spécifique pour étudier ce phénomène doit être développée lors de l'expérimentation AMMA.

*4. Impacts et liens avec la surface*

Dans le cas de l'Amazonie, les observations ont montré que la couche limite est sensiblement différente entre zone de forêt et zone de pâturage pendant la saison sèche alors que la différence s'estompe pendant la saison humide (Fisch et al. 2004), et nous avons montré que la couverture nuageuse était modifiée par la déforestation au niveau du cycle diurne et saisonnier (Durieux et al. 2003). Ces différents résultats demandent à être approfondis dans le cadre de la mousson africaine ; ils ouvrent des pistes de recherche pour comprendre le rôle de la surface dans la variabilité climatique, ce qui est un thème important du projet AMMA.

Par ailleurs l'analyse des systèmes convectifs fourni un moyen d'investigation de la variabilité climatique en région tropicale, et par suite de ses impacts sur la surface. Les principaux domaines concernés sont l'agriculture, les ressources en eau et la santé. Des travaux commencent à être menés au LTHE dans les deux premiers domaines (thèses de M. Balme et T. Vishel, respectivement). Les impacts dans le domaine de la santé seront abordés dans le cadre du programme AMMA.

Parallèlement à ces études axées sur des processus ou des objets particuliers, des approches intégratives sont également souhaitables. Ainsi la comparaison des systèmes convectifs sur deux continents tropicaux différents tels que l'Amérique Latine et l'Afrique doit permettre d'améliorer notre compréhension de la convection en général. On s'efforcera de répondre aux questions non exhaustives suivantes :

- Les deux types de convection observés sur l'Amazonie ont-ils un lien avec ceux observés entre le Sahel et le sub-Sahel ?
- Peut-on unifier la notion d'événement entre ce qui est perçu à partir des champs de précipitations, les systèmes convectifs observés par satellite, et les événements convectifs représentés dans les modèles de circulation générale atmosphérique ?

Des avancées sur ces questions permettront d'améliorer la modélisation et par suite la prévision.

Un autre aspect important est l'application de la recherche. A cet égard tout progrès sur l'estimation des précipitations par satellite devra se traduire rapidement dans les algorithmes opérationnels. C'est pourquoi ces travaux sont et seront menés en partenariat avec l'AGRHYMET[4]. L'algorithme de suivi des systèmes convectifs, développé initialement à des fins de recherche, existe déjà dans une version opérationnelle au Brésil. De nombreux développements sont prévus dans les années à venir dans ce partenariat franco-brésilien. Par ailleurs, une perspective actuellement à l'étude est de transférer ce savoir-faire en Afrique, en développant ainsi une coopération Sud-Sud.

[4] AGRHYMET : Centre régional de formation et d'application en agrométéorologie, hydrologie et météorologie, regroupant les pays du Sahel.

**Références bibliographiques citées dans le texte**


Ali A., 2004. Modélisation de l'invariance d'échelle des champs de pluie sahéliens - application aux algorithmes d'estimation et aux études de variabilité climatique. Thèse d'Université, Institut National Polytechnique de Grenoble, 21 décembre 2004, 170 pp.

Ali A., A. Amani, A. Diedhiou, and T. Lebel, 2005. Evaluation of CILSS countries raingauge networks and objective intercomparison of satellite rainfall products. Submitted to J. Appl. Meteor.

Anagnostou, E. N., and W. F. Krajewski, 1997: Simulation of radar reflectivity fields: Algorithm formulation and evaluation. *Water Resour. Res.,* **33,** 1419–1428.

Arnaud, Y., M. Desbois, and J. Maizi, 1992: Automatic tracking and characterization of African convective systems on Meteosat pictures. *J. Appl. Meteor*., **31**, 443-453.

Barnes, S. L., 1964: A technique for maximizing details in numerical weather map analysis. *J. Appl. Meteor.*, **3**, 396–409

Bonazzola M., L. Picon, H. Laurent, F. Hourdin, G. Sèze, H. Pawlowska and R. Sadourny, 2001. Retrieval of large-scale wind divergences from infrared Meteosat-5 brightness temperatures over the Indian Ocean. *J. Geophys. Res*., **106**, 28113-28128.

D'Amato, N., and T. Lebel, 1998: On the characteristics of the rainfall events in the Sahel with a view to the analysis of climatic variability. *Int. J. Climatol.,* **18,** 955–974.

Dessay N, Laurent H., Machado L.A.T., Shimabukuro Y. E., Batista G. T., Diedhiou A., Ronchail J., 2004. Comparative study of 1982-1983 and 1997-1998 El Niño events over different types of vegetation in South America. *Int. J. Remote Sen*sing, **25**, 4063-4077.

Diedhiou A., 1998. Etude des régimes d'ondes d'est et de leurs interactions avec la convection en Afrique de l'Ouest et sur l'Atlantique tropical. Thèse de l'Université Paris 12, 220 pp.

Diedhiou A., S. Janicot, A. Viltard, P. de Félice and H. Laurent, 1999. Easterly wave regimes and associated convection over West Africa and the tropical Atlantic : Results from NCEP/NCAR and ECMWF reanalyses. *Climate Dynamics,* **15**, 795-822.

Diedhiou A., L. A. T. Machado and H. Laurent, 2004. Climatology of African easterly disturbances over the tropical Atlantic ocean. Submitted to J. Climate.

Durand B., J. Servain, H. Laurent and L. A . T. Machado, 2005. Tropical Atlantic moisture flux, convection over Northeastern Brazil and pertinence of the PIRATA network. *J. Climate*, **18**, 2093-2101..

Durieux L., L. A. T. Machado and H. Laurent, 2003. The impact of deforestation on cloud cover over the Amazon arc of deforestation. *Remote Sensing of Environment*, **86**, 132-140.

Fisch G, Tota J, Machado LAT, Silva Dias MAF, Lyra RFD, Nobre CA, Dolman AJ, Gash JHC. The convective boundary layer over pasture and forest in Amazonia. *Theor. Appl. Climatology*, **78**, 47-59.

Fritsch, J. M., R. J. Kane, and C. R. Chelius, 1986: The contribution of mesoscale convective weather systems to the warm-season precipitation in the United States. *J. Climate Appl. Meteor*., **25**, 1333-1345.

Frank, W. M., 1978: The life cycles of GATE convective systems. *J. Atmos. Sci*., **35**, 1256–1264.

Houze R; A., 1981: Structure of atmospheric precipitation systems: A global survey. *Radio Sci.,* **16,** 671–689.

Laing, A. G., and J. M. Fritsch, 1993: Mesoscale convective complexes in Africa. *Mon. Wea. Rev.,* **121,** 2254–2263.

Laing, A. G.,J. M. Fritsch and A. J. Negri, 1999: Contribution of mesoscale convective complexes to rainfall in Sahelian Africa: Estimates from geostationary infrared and passive microwave data. *J. Appl. Meteor.,* **38,** 957–964.

Lafore, J.-P., and M. W. Moncrieff, 1989: A numerical investigation of organization and interaction of the convective and mesoscale region of a tropical squall line. *J. Atmos. Sci.,* **46,** 521–544.

Laurent H., 1993 : Wind extraction from METEOSAT water vapor channel image data. *J. Appl. Meteor.*, **32**, 1124-1133

Laurent H., 1994 : Tracking of convective cloud clusters from METEOSAT data. 10th METEOSAT Scientific Users' Conference, Cascais, Portugal, 5-9 September 1994. EUMETSAT Publ. EUM P15, 273-278.

Laurent H., 1996 : Life distribution of mesoscale convective clouds over Africa. 7th Conference on Mesoscale Processes, Reading, United Kingdom, 9-13 September 1996. AMS Publ., 178-180.

Laurent H. and M. Sakamoto, 1998. Measure of divergence at the top of tropical convective systems from water vapor winds. Fourth International Wind Workshop, Saanenmoser, Switzerland, 20-23 October 1998. Eumetsat Publ., P24, 155-161.

Laurent H. and L. A. T. Machado, 2002. Characteristics of the convective cloud system organization during WETAMC/LBA – Comparison with West African convective systems. Second international LBA science conference, Manaus, 7-10 July 2002.

Laurent H., A. Viltard and P. de Félice, 1989 : Performance evaluation and local adaptation of the ECMWF system forecasts over Northern Africa for summer 1985. *Month. Wea. Rev.*,, **117**, 1999-2009.

Laurent H., T. Lebel and J. Polcher, 1997 : Rainfall variability in Soudano-Sahelian Africa studied from raingauges, satellite and GCM. 13th Conference on Hydrology, 77th AMS annual meeting, 2-7 February, Long Beach, Ca. AMS Publ., 17-20.

Laurent H., I. Jobard and A. Toma, 1998a : Validation of satellite and ground based estimates of precipitation over the Sahel. *Atmos. Res.*, **47-48**, 651-670.

Laurent H., N. D'Amato and T. Lebel, 1998b : How important is the contribution of the Mesoscale Convective Complexes to the Sahelian rainfall ? *Phys. Chem. Earth*, **23**, 629-633.

Laurent H., L. A. T. Machado, C. A. Morales and L. Durieux, 2002a. Characteristics of the Amazonian mesoscale convective systems observed from satellite and radar during the WETAMC/LBA experiment. *J. Geophys. Res*., **107** (D18), 8054, doi:10.1029/2001JD000337.

Laurent H., N. Arai, B. Fomin, L. A. T. Machado e M. A. Gondim, 2002b. Extração do vento utilizando imagens de satélite no CPTEC: Nova versão e avaliação com dados do LBA e dados operacionais da DSA/CPTEC. *Revista Brasileira de Meteorologia*, **17**, 113-123.

Le Barbé, L., and T. Lebel, 1997: Rainfall climatology of the HAPEX-Sahel region during the years 1950–1990. *J. Hydrol.,* **188–189,** 43–73.

Lebel T., H. Sauvageot, M. Hoepffner, M. Desbois, B. Guillot, and P. Hubert, 1992: Rainfall estimation in the Sahel: The EPSAT-Niger experiment. *Hydrol. Sci. J.*, **37**, 201–215.

Lebel T., A. Diedhiou and H. Laurent, 2003. Seasonal cycle and interannual variability of the Sahelian rainfall at hydrological scales. *J. Geophys. Res.*, **108** (D8), 8389, doi:10.1029/2001JD001580.

Lima A. A., Machado L. A. T. e H. Laurent, 2003. Divergência do vento em altos níveis e sua relação com a cobertura de nuvens e a precipitação durante o WETAMC/LBA. *Revista Brasileira de Meteorologia*, **18**, 105-117.

Lopez P, 1993. Etude de la représentation des lignes de grains africaines dans les analyses du modèle du Centre Européen. Mémoire de Mastère de Météorologie Tropicale, ENM, Toulouse, 96 pp.

Mathon V., 2001. Etude climatologique des systèmes convectifs de méso-échelle en Afrique de l'Ouest. Thèse de l'Université Paris 7, 238 pp.

Mathon V. and H. Laurent, 2001. Life cycle of the Sahelian mesoscale convective cloud systems. *Quart. J. Roy. Meteo. Soc.*, **127**, 377-406.

Mathon V., A. Diedhiou and H. Laurent, 2002a. Relationship between easterly waves and mesoscale convective systems over the Sahel. *Geophys. Res. Let*, **29** (8), 1216, doi:10.1029/2001GL014371.

Mathon V., H. Laurent and T. Lebel, 2002b. Mesoscale convective system rainfall in the Sahel. *J. Appl. Meteor.*, **41**, 1081-1092.

Machado L. A. T. and H. Laurent. The convective system area expansion over Amazonia and its relationships with convective system life duration and high-level wind divergence, 2004. *Mon. Wea. Rev.*, **132**, 714-725.

Machado L. A. T., H. Laurent, N. Dessay and I. Miranda, 2004. Seasonal and diurnal variability of convection over the Amazon basin: a comparison of different vegetation types. *Theor. Appl. Climatology*, **78**, 61-77.

Machado L. A. T., H. Laurent and A. A. Lima, 2002. The diurnal march of the convection observed during TRMM-WET AMC/LBA. *J. Geophys. Res*., **107** (D18), 8064, doi:10.1029/2001JD000338.

Maddox, R. A., 1980: Mesoscale convective complexes. *Bull. Amer. Meteor. Soc.,* **61,** 1374–1387.

Miller, D., and J. M. Fritsch, 1991: Mesoscale convective complexes in the western Pacific region. *Mon.Wea. Rev*., **119**, 2978-2992.

Morel and Senesi, 2002. A climatology of mesoscale convective systems over Europe using satellite infrared imagery. I: Methodology. *Quart. J. Roy. Meteo. Soc.*, **128**, 1953-1971.

Mohr and Zipster 1996. Mesoscale convective systems defined by their 85-GHz ice scattering signature: size and intensity comparison over tropical oceans and continents. *Mon. Wea. Rev.,* **124**, 2417-2437.

Nobre, C.A.; Wickland, D. & Kabat, P.I. 2001. The large scale biosphere-atmosphere experiment in Amazonia (LBA). *Global Change Newsletter,* **45**, 2-4.

Petersen, W. A., S. W. Nesbitt, R. J. Blakeslee, R. Cifelli, P. Hein, and S. A. Rutledge, 2002: TRMM observations of intraseasonal variability in convective regimes over the Amazon. *J. Climate,* **15,** 1278–1294.

Polcher, J., 1995 : Sensitivity of tropical convection to land surface processes. *J. Atmos. Sci*., **52**, 3143-3161.

Redelsperger, J.-L., and J.-P. Lafore, 1988: A three-dimensional simulation of a tropical squall line: Convection, organization and thermodynamic vertical transport. *J. Atmos. Sci.,* **45,** 1334–1356.

Reed RJ, Norquist DC, Recker EE, 1977. The structure and properties of African wave disturbances as observed during phase III of GATE. *Mon Wea. Rev*, **105**, 317-333.

Rickenbach T. M., R. N. Ferreira, J. B. Halverson, D. L. Herdies, and M. A. F. Silva Dias, 2002. Modulation of convection in the southwestern Amazon basin by extratropical stationary fronts, *J. Geophys. Res*., **107** (D20), doi:10.1029/2000JD000263.

Roux, F., 1988: The West African squall line observed on 23 June 1981 during COPT 81: Kinematics and thermodynamics of the convective region. *J. Atmos. Sci.,* **45,** 406–426.

Sakamoto M. e H. Laurent, 2002. Estimativa de vento na alta troposfera através de imagens do canal de vapor d´água do satélite Goes. XII Congresso Brasileiro de Meteorologia, Foz do Iguaçu, 4-9 agosto 2002. SBMET, 3187-3196.

Sakamoto M. and H. Laurent, 2003. Wind estimation – the studies made at FUNCEME. EUMETSAT meteorological satellite conference, Weimar, Germany, 29 September–3 October 2003. Eumetsat Publ. EUM P40, available from www.eumetsat.de.

Sakamoto M., H. Laurent and L. A. T. Machado, 2004. The upper level winds and their relationship with convective systems – a case study. Seventh International Wind Workshop, Helsinki, Finland, 14-17 June 2004. Eumetsat Publ.

Schmetz, J., WP Menzel, C. Velden, XQ Wu, L. Vandeberg, S. Nieman, C. Hayden, K. Holmlund and C. Geijo, 1995: Monthly mean large-scale analyses of upper-tropospheric humidity and wind field divergence derived from three geostationary satellites. *Bull. Amer. Meteor. Soc.,* **76,** 1578–1584.

Silva Dias, M. A., and Coauthors, 2002: Cloud and rain processes in a biosphere–atmosphere interaction context in the Amazon region. *J. Geophys. Res.*, **107**, 8072, doi:10.1029/2001JD000335.

Smith, R. K., 1997 :On the theory of CISK. *Quart. J. Roy. Meteo. Soc.*,**123**, 407-418

Sun, J., S. A. Braun, M. I. Biggerstaff, R. G. Fovell and R. A. Houze, Jr., 1993. Warm upper-level downdrafts associated with a squall line. *Mon. Wea. Rev*., **121**, 2919-2927.

Thorncroft, C. D., Arpe, K., Fink., A., Gregory, D., Hodges, K., Janicot, S., Laurent, H., Parker, D., Redelsperger, J.-L., Rowell, D. P., Speth, P., 2001. West African Monsoon Projet (WAMP). Final report, 260 pp., available from http://www.atmos.albany.edu/facstaff/chris/.

Velden, C., C. M. Hayden, S. J. Nieman, W. P. Menzel, S. Wanzong, and J. S. Goerss, 1997: Upper-tropospheric winds derived from geostationary satellite water vapor observations. *Bull. Amer. Meteor. Soc.*, 78, 173–195.

Velasco and Fritsch, 1987. Mesoscale convective complexes in the America. *J. Geophys. Res*., **92**, 9591-9613.

Viltard A., J. Oubuih, P. de Félice and H. Laurent, 1998. Rainfall and the 6-9 day wave-like disturbance in West Africa during summer 1989, *Meteorol. Atmos. Phys.*, **66**, 229-234.

Williams, M., and R. A. Houze, 1987: Satellite-observed characteristics of winter monsoon cloud clusters. *Mon. Wea. Rev*., **115**, 505-519.

## PARTIE V – SELECTION D'ARTICLES

- Laurent H., 1993 : Wind extraction from METEOSAT water vapor channel image data. *J. Applied Meteorology*, **32**, 1124-1133.
- Laurent H., I. Jobard and A. Toma, 1998 : Validation of satellite and ground based estimates of precipitation over the Sahel. *Atmospheric Research*, **47-48**, 651-670.
- Laurent H., N. D'Amato and T. Lebel, 1998 : How important is the contribution of the Mesoscale Convective Complexes to the Sahelian rainfall ? *Phys. Chem. Earth*, **23**, 629-633.
- Mathon V. and H. Laurent, 2001. Life cycle of the Sahelian mesoscale convective cloud systems. *Quart. J. Roy. Meteo. Soc.*, **127**, 377-406.
- Mathon V., A. Diedhiou and H. Laurent, 2002. Relationship between easterly waves and mesoscale convective systems over the Sahel. *Geophys. Res. Let*, **29** (8), 1216, doi:10.1029/2001GL014371.
- Machado L. A. T., H. Laurent and A. A. Lima, 2002. The diurnal march of the convection observed during TRMM-WET AMC/LBA. *J. Geophys. Res.*, **107** (D18), 8064, doi:10.1029/2001JD000338.
- Laurent H., L. A. T. Machado, C. A. Morales and L. Durieux, 2002. Characteristics of the Amazonian mesoscale convective systems observed from satellite and radar during the WETAMC/LBA experiment. *J. Geophys. Res.*, **107** (D18), 8054, doi:10.1029/2001JD000337.
- Mathon V., H. Laurent and T. Lebel, 2002. Mesoscale convective system rainfall in the Sahel. *J. Applied Meteorology*, **41**, 1081-1092.
- Machado L. A. T. and H. Laurent. The convective system area expansion over Amazonia and its relationships with convective system life duration and high-level wind divergence, 2004. *Monthly Weather Review*, **132**, 714-725.

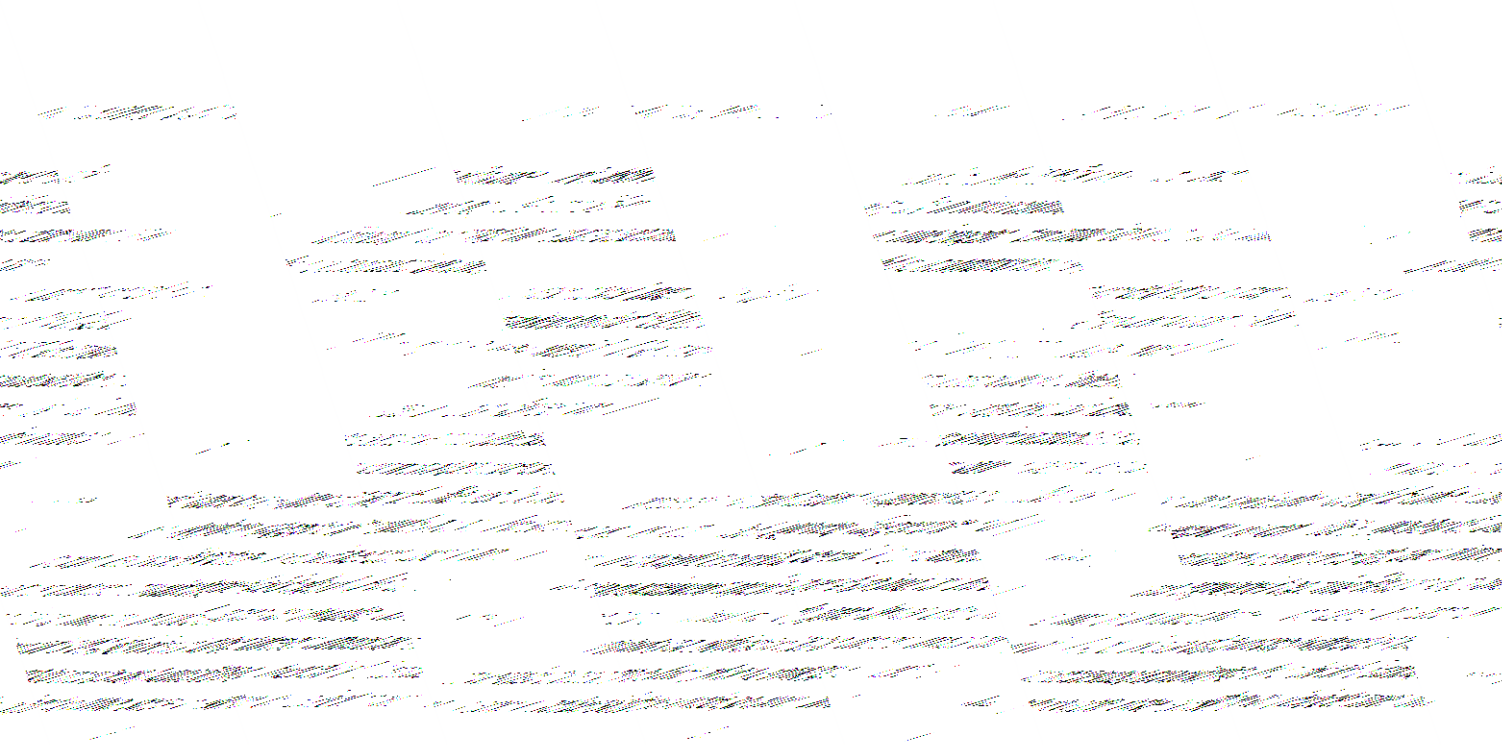

Atmospheric Research 47–48 (1998) 651–670

# Validation of satellite and ground-based estimates of precipitation over the Sahel

H. Laurent [a,*], I. Jobard [b,1], A. Toma [b,2]

[a] *ORSTOM, groupe PRAO, BP 5045, 34032 Montpellier, France*
[b] *Laboratoire de Météorologie Dynamique, CNRS, Ecole Polytechnique, 91128 Palaiseau, France*

Accepted 7 August 1997

**Abstract**

The aim of this study is to compare and discuss the validation of rainfall estimates from five methods, at various space and time scales. The studied areas are the Sahelian Africa where a network of about 580 raingauges is available and a small region covering Burkina-Faso where the raingauge network is denser, with 58 raingauges in a $2.5° \times 3°$ area. The reference estimation (i.e., the 'ground-truth' rainfall) is computed by kriging the raingauge data. Rainfall is estimated with three satellite-based operational algorithms which provide 10-day cumulated rainfall using Meteosat infrared channel data. Rainfall is also estimated from two ground-based methods, using either climatologic data or the rain gauge data of the synoptic network which are available in real-time. One of the satellite methods is calibrated using the synoptic raingauge data and is thus a satellite–gauge combined method. Comparisons are performed for 10-day and 30-day integration periods and for spatial scales from 0.20 to 1 degree. A set of validation criteria is used for quality assessment. An interesting result is that the satellite-based methods and the ground-based methods lead to similar scores. The satellite–gauge combined method leads to slightly better scores. For this method, the estimation error for the 10-day cumulated rainfall and a $0.5° \times 0.5°$ spatial resolution is about 35% of the mean rainfall amount. Other results concern the general methodology of method intercomparison. It is shown that for accurate performance assessment a single criterion is seldom sufficient and that the performance criteria are sensible to dataset partitioning.


*Keywords:* Precipitation; Validation; Satellite rainfall estimation

* Corresponding author. Fax: +33-4-6754-7106; e-mail: henri.laurent@mpl.orstom.fr
[1] Fax: +33-1-6933-3005; e-mail: jobard@lmd.polytechnique.fr
[2] Fax: +33-1-6933-3005; e-mail: toma@lmd.polytechnique.fr

0169-8095/98/$19.00 
*PII* S0169-8095(98)00051-9

## 1. Introduction

Quantitative estimation of rainfall in the tropics is a problem of major importance. At a global scale, the tropical precipitations play a significant role in the global energy budget and in the general atmospheric circulation. At a regional scale, rainfall is economically crucial for many countries, especially for agricultural and water management survey in semiarid areas. Ground measurements are generally sparse and only few data are available for real-time monitoring. Data are available from geostationary satellites with a good space and time resolution; but they do not allow for an accurate measurement of rainfall. Rainfall in tropical regions is mainly provided by large convective systems (Le Barbé and Lebel, 1997; Laurent et al., 1997); it can be estimated from the satellite infrared temperatures assuming that the convective cloudiness is estimated by the cloud top temperature. This approach, based on a statistical relationship between thermal infrared temperature and precipitation, is valid only for space and time-averaged estimates (Arkin, 1979; Jobard and Desbois, 1992). However rainfall estimates from satellite data are essential to compensate for the low density or the lack of ground-based rainfall measurements.

The aims of this paper are: to assess the quality of satellite rainfall estimations; to compare different algorithms with each other; and to compare satellite estimates with ground-based estimates. It deals with the different issues encountered in the validation procedure of any rainfall estimation method, when an areal rainfall field is to be compared with a rainfall field computed from point values provided by raingauges and considered as the 'ground-truth' or reference values. These issues mainly concern: (a) the choice of the appropriate spatial scales and time integration periods; (b) the effects of a partition of the data sets according to various characteristics, such as homogeneous climatic regions or time periods; (c) the criteria allowing performance assessment.

This study addresses the problem of rainfall estimation over the Sahelian belt; the basic spatial resolution is a $0.5° \times 0.5°$ surface and rainfall is cumulated over 10-day periods. The methodology is discussed in Section 2 and the case studies are presented in Section 3 where rainfall estimates obtained from five different methods are compared with rainfall reference values using the 10-day rainfall records from the sparse raingauge network of the Sahelian band in tropical Africa, during five rainy seasons (1989 to 1993). A better spatial resolution is investigated in Section 3.2 by focusing over Burkina-Faso where a denser raingauge network is available.

## 2. Methodology

### *2.1. Estimation of the reference rain field*

According to Creutin and Obled (1982), the validation or comparison of estimation methods needs the definitions of a set of reference values and of error criteria in order to evaluate the agreement between the estimates and the reference values. For the validation of a rainfall estimation method using satellite image data, the reference values must

represent space-averaged rainfall values. As the ground rainfall measurements are obtained from a rain gauge network, an interpolation scheme has to be used to obtain areal rainfall values from point values.

*2.1.1. Kriging interpolation*

The chosen interpolation method is ordinary kriging, which performs better than other interpolation schemes (Tabios and Salas, 1985; Lebel et al., 1987). Ordinary kriging is based on the hypothesis of stationarity of increments (also called weak stationarity by Creutin and Obled (1982)). A non-stationary kriging method would be necessary only when there is a drift. The annual rain fields over the Sahel exhibit a latitude-related gradient, but there is no characteristic structure of the rain fields for 10-day cumulated amounts. Therefore, we computed the reference values with an ordinary kriging method.

Kriging is a linear interpolation method allowing to estimate areal values as a weighted mean of the point observations. The weights attributed to the different observations depend on the variability structure of the rainfall field. This variability structure is taken into account using the variogram function which is the difference between the variance and the covariance function. Empirical variograms are calculated using the observation data sets and then a variogram model is fitted. For each grid cell, using the variogram model, a linear system yields the interpolation weights attributed to the observation points. In addition to the estimation of areal values, kriging allows for the calculation of the errors associated to these estimates, given by the kriging standard deviations which depend on the variogram and on the distribution of the observations. For a detailed presentation of theoretical and practical issues related to kriging, see for example, Isaaks and Srivastava (1989).

In order to choose the variogram model, we used the 'climatologic variogram' approximation (Bastin et al., 1984). This approximation supposes that the fields corresponding to different 10-day periods, scaled by the empirical standard deviation of the corresponding 10-day period, are realizations of the same stochastic variable. Fig. 1 shows the empirical climatologic variograms, computed for ten 10-day periods of 1990 for the whole Sahel region. In Fig. 1, also shown is the fitted spherical model which is characterized by a sill of 1, a range of 7° and a nugget of 0.35. For the Burkina-Faso study area, having a spatial extent of only 3°, the locally computed variograms show the same relative sill and nugget effect than the variogram used for the whole Sahel area (spatial extent of 20°) but a smaller range. The parameters used for the Burkina-Faso study area are a sill of 1, a range of 3° and a nugget of 0.35.

It should be noticed that the empirical variograms computed for areas of different spatial extents have a range that depends on that extent. This could be explained by the fact that the phenomenon is non-stationary, but in that case, the variograms should not present obvious sills. Hence, the dependence of the range should be explained by the fact that different variability structures appear when different spatial extents are considered. The scales of rainfall variability depend on the type of cloud structures encountered in the studied areas: for example, convective cells, convective cloud clusters, large mesoscale systems or squall lines. As an illustration of the range dependence on spatial extent, Lebel and Le Barbé (1997), using the same 'climatologic variogram' approxima-

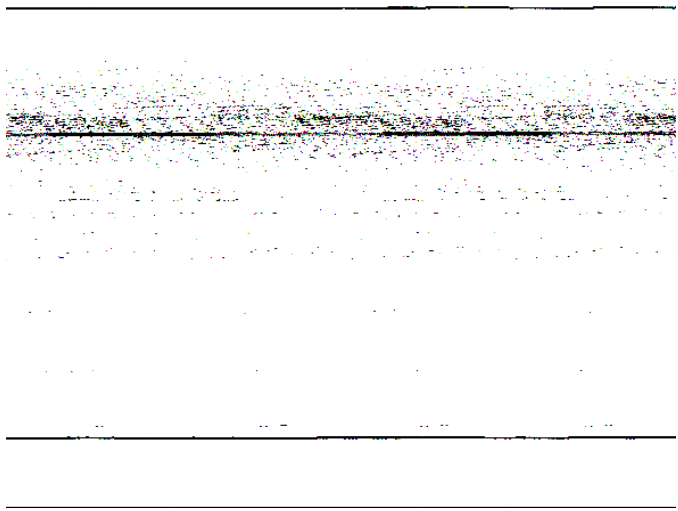

Fig. 1. Climatologic variograms for 10 different 10-day periods over the Sahel area, in summer 1990. The fitted spherical model is also plotted.

tion, found a range of approximately 0.5° for a studied area having a spatial extent of 1° (the Niamey square degree) and a nugget of 0.15.

*2.1.2. Working area*

Fig. 2 represents the study area in western Africa. In Fig. 2a, the grey region shows the distribution of the $0.5° \times 0.5°$ cells that include at least one raingauge station in their vicinity, that is to say within a distance of $0.5° \times \sqrt{2}$ from the centre of the cell. The black region shows the cells with at least five raingauge stations. The uncertainty of the areal values depends on the local density of stations. The grid cells that include a sufficient number of stations in their vicinity, allowing for an acceptable uncertainty of the areal rainfall values, are considered as reliable. Only these reliable cells are taken into account as reference values. The minimum number of stations in the cell vicinity, which is a function of the grid cell size, must be high enough to give values with a low uncertainty but the choice is also guided by the necessity to have enough values for the validation and also to cover a large enough portion of the region. Fig. 3a shows the number of grid cells in the study area for different minimum numbers of stations, taken as one, three, five or 10, as a function of the grid cell sizes ranging from 0.1° to 2.5°. Fig. 3b shows the corresponding total surface covered by the reliable cells. Taking also into account the results presented by Lebel and Le Barbé (1997) regarding the uncertainties, the compromise chosen for our study is 5 stations and a 0.5° grid cell size; this corresponds to the region represented in black in Fig. 2a, which covers actually a surface of only 65 square degrees out of the 600 square degrees of the whole window.

Fig. 2b shows the kriging standard deviations of the reference rain field; it represents another way of estimating the uncertainty of the reference areal values for each grid cell. It is noticeable that the contour of the grid cells considered as reliable (the black region

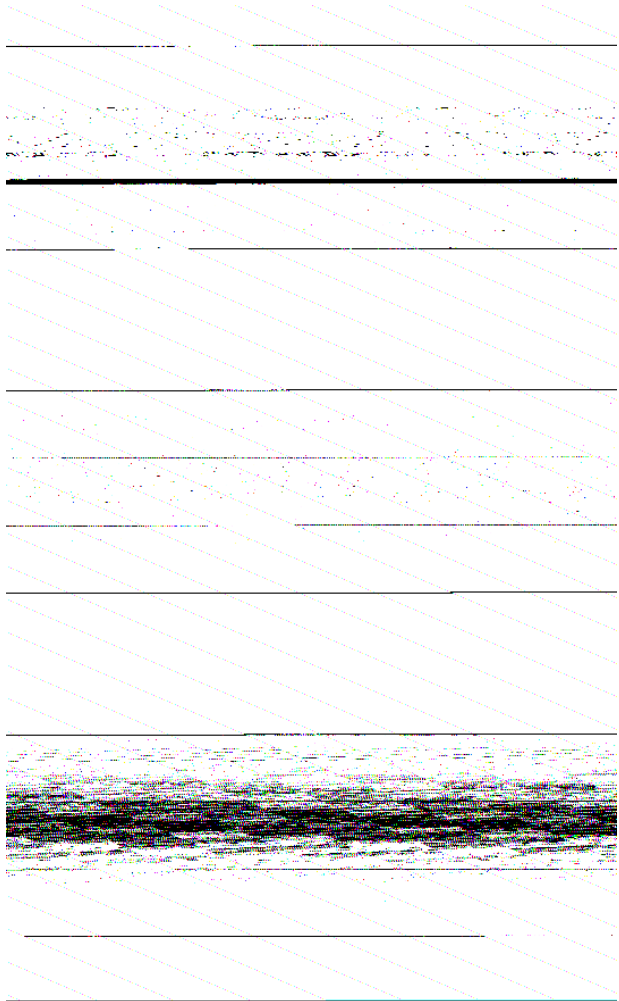

Fig. 2. (a) Study area, with the 0.5°×0.5° validation cells. Grey cells contain at least one raingauge in their vicinity, black cells contain at least five raingauges. (b) Kriging standard deviation (mm). (c) Location of zone 1 (Senegal), zone 2 (Central Sahel) and zone 3 (Chad) and location of the Burkina-Faso case study area and its extended area.

in Fig. 2a) corresponds to a kriging standard deviation value between 10 and 15 mm. The average of the kriging standard deviation for the reliable cells is 9 mm.

When the dataset corresponds to a large zone covering different climatic regions or to a long time period such as the whole rainy season, it is interesting to define separate subsets of the reference data. The dataset is partitioned in order to validate the estimation method for each rainfall regime and for homogeneous regions. For example, we delimited three geographical zones within our study area: the Chad zone, the central Sahel zone and the Senegal zone which are shown in Fig. 2c. We also used a smaller

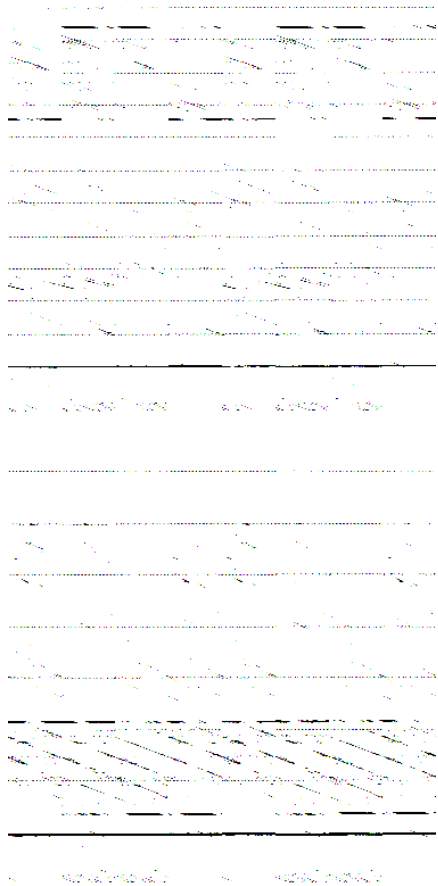

Fig. 3. (a) Number of grid cells in the study area containing at least one, three, five or 10 raingauge stations in their vicinity as a function of the grid cell size. (b) Corresponding total surface covered by the cells.

study area over the Burkina-Faso region, shown in Fig. 2c, to illustrate as well the impact of the selection of a homogeneous area for validating rainfall estimations and to investigate a better spatial resolution.

Fig. 4a shows the locations of the 594 rain gauge stations available for 1989. The network was similar for 1990, but less observations were available for 1991, 1992 and 1993. The 54 stations of the synoptic network are displayed in Fig. 4b; these stations are considered in this study as giving ‘real-time’ observations, while the other rain gauge stations are producing observations which are available only after several weeks.

### *2.1.3. Considered scales*

One must choose the spatial resolution and time integration period of the reference values by considering not only the characteristics of the available dataset but also the scales which are relevant for the type of application for which the rainfall is estimated,

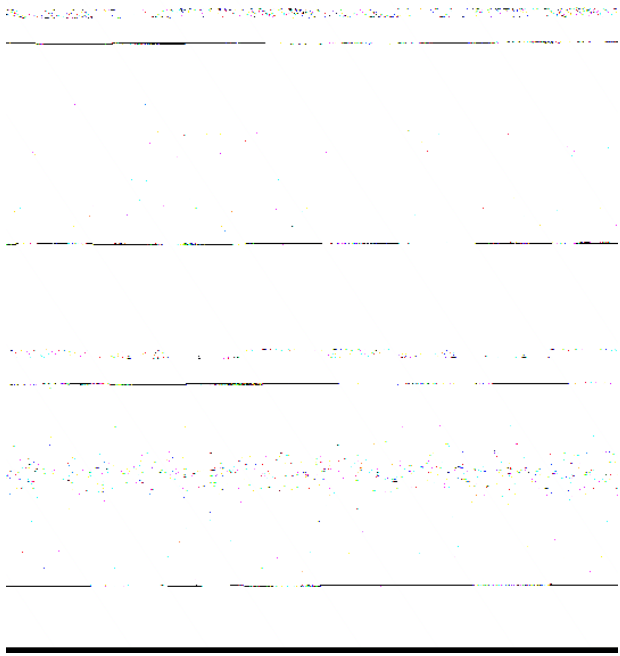

Fig. 4. Raingauge network over the Sahel. (a) All stations. (b) Synoptic stations.

such as hydrology, agrometeorology and climatology. The rainfall data were provided by AGRHYMET (Centre for Agricultural, Hydrological and Meteorological Applications in the Sahel). This centre is mainly invested in crop monitoring in the Sahelian countries and it archives the 10-day cumulated rainfall at about 580 stations. Thus, our choice for the time integration period was limited to at least a 10-day period. For the study over the whole Sahelian belt, we chose a 0.5° spatial resolution and considered also wider resolutions, up to 1° which is appropriate for climatic studies. For the study over Burkina-Faso, the basic integration time was also 10 days but we considered spatial resolution from 0.20° up to 1.0°.

### *2.2. Rainfall estimation methods*

The validation of five rainfall estimation methods was performed in order to evaluate how the results of their performance assessment depend on the different choices and on the parameters involved in the procedure discussed in Section 2.1. For this study, we have selected two simple ground-based estimation methods and three satellite methods, one of them being actually a satellite–gauge combined method. They are respectively referred to as CLM, SYN, GPI, TAM and LAN. These methods can easily be used for real-time rainfall monitoring.

The two simple ground-based estimation methods are the following: (a) CLM is the climatic estimation method computing the mean rainfall over 10-day periods from the

ORSTOM daily rainfall data-base, over the period 1970–1990; (b) SYN is a method computing a simple interpolation from the data of the neighboring synoptic stations, using weights inversely proportional to the square distance.

The three satellite methods are the following: (a) GPI is the GOES Precipitation Index method proposed by Arkin (1979); (b) TAM is a multiple infrared threshold method, developed at Reading University (UK) by the TAMSAT team (Dugdale et al., 1990); (c) LAN is developed by ORSTOM at Lannion (France) and this is an infrared method calibrated every 10 days with the real-time observations (Carn et al., 1989).

Among the numerous existing algorithms for estimating rainfall from satellite data, we chose these three simple infrared algorithms that are run in operational routines in tropical regions. Hourly or half-hourly images available from the geostationary satellites are used. The infrared channel (10–12 $\mu$m) is preferred to the visible channel because it is continuously available during day and night. The algorithms are based on the duration of the occurrence of cold cloud retrieved from the infrared brightness temperature below a temperature threshold, over each pixel, within a 10-day period.

The GPI method defines cold cloud as pixels with an infrared brightness temperature below the $-38$°C threshold. The rainfall estimate is then derived as:

$$R = \alpha F$$

where $R$ stands for rainfall (in mm), $F$ is the fractional cold cloud duration (in hours) cumulated over a period and averaged over an area, and $\alpha$ is 3 mm/h. The GPI method was designed for climatic rainfall estimates over $2.5° \times 2.5°$ areas and monthly scale (Arkin and Meisner, 1987). It was then used at smaller scales for algorithm intercomparison as it stands for the reference infrared rainfall estimation method (Arkin and Ardanuy, 1989).

An important aspect of any method based on cloud top temperature is the choice of the threshold discriminating between rain and no-rain clouds. The TAM method uses several thresholds. Western Africa is divided into nine zones considered to have a homogeneous rainfall climatology. Within each zone, the threshold is constant during 1 month. For each zone and each month, the value of the threshold is selected between $-40$°C and $-60$°C, through a regression performed against observations, to produce a calibration in the form:

$$R = aD + b \qquad \text{if } D \neq 0, \qquad R = 0 \qquad \text{if } D = 0$$

where $R$ stands for rainfall (in mm) and $D$ is the cold cloud duration (in hours). The calibration coefficients $a$ and $b$ are updated each year, taking into account the observations of the previous years.

The LAN method estimates the rainfall as:

$$R = aD + bT_s + c \qquad \text{if } D \neq 0, \qquad R = 0 \qquad \text{if } D = 0$$

where $R$ is the rainfall (in mm), $D$ is the cold cloud duration for a threshold of $-40$°C, $T_s$ is the mean of the two maximum infrared brightness temperatures within the two 5-day periods of the 10-day period. $T_s$ encounters for the relationship between the surface temperature and rainfall. For each 10-day period, the regression coefficients $a$, $b$ and $c$ are computed using the rain gauge observations available in real-time from the synoptic network. In that respect, the LAN method is a satellite–gauge combined method.

### 2.3. Validation procedure

The choice of the relevant criteria allowing performance evaluation of the estimation methods is an important issue. Various statistical parameters can be used to measure the strength of the statistical relationship between the estimated values and the reference values. Let $v_i$, $(i = 1,n)$ be the set of $n$ reference values, and $e_i$, $(i = 1,n)$ the set of estimates. Let $\bar{v}$ $(\bar{e})$ and $\sigma_v$ $(\sigma_e)$ be the mean and standard deviations of the reference (estimate) values. The most common statistical criteria are the following.

(a) The bias which is the difference between the mean estimate $\bar{e}$ and the mean reference value $\bar{v}$.

(b) The linear correlation coefficient $r$,

$$r = \frac{\sum_{i=1}^{n} (v_i - \bar{v})(e_i - \bar{e})}{n\sigma_v \sigma_e}$$

where $r$ measures the cofluctuation between estimate and reference. It is not sensitive to a bias. The associated uncertainties $\Delta r$ corresponding to a 95% confidence interval have been computed using a Fisher's transformation (Kendall and Stuart, 1963).

(c) The root mean square error:

$$\mathrm{rmse}^2 = \frac{1}{n}\sum_{i=1}^{n} (e_i - v_i)^2$$

where rmse can be considered as an absolute measure of the distance between estimate and reference.

(d) The non-dimensional skill score index or Nash index (Murphy, 1995; Obled et al., 1994):

$$I = 1 - \frac{\mathrm{rmse}^2}{\sigma_v^2}$$

where, $I$ is equal to 1 for a perfect estimate $(e_i = v_i)$ and is equal to 0 for the best constant estimate $(e_i = \bar{v})$. This non-dimensional index can be interpreted as a relative measure of the distance between estimate and reference, and thus it is convenient for the comparison of results obtained with different datasets.

(e) The scaled root mean square error:

$$\mathrm{Srmse}^2 = \frac{1}{n}\sum_{i=1}^{n} \left( \frac{e_i - v_i}{v_i} \right)^2, \qquad \text{for } v_i > 20 \text{ mm}$$

where Srmse is also a measure of the relative distance between estimate and reference. However, the scaling factors have different meanings for $I$ and Srmse. The coefficient $I$ depends on the standard deviation of the reference dataset. Srmse, scaled with respect to the values of the reference, depends on the mean of the reference dataset. For small values of $v_i$ the contribution to Srmse would be very large, hence, Srmse was computed only for $v_i$ larger than a threshold. The value of this threshold (20 mm) was chosen to

discard less than 10% of the total number of points.
(f) The coefficient $a$ of the linear regression:

$$v = ae + b$$

is also convenient to measure the cofluctuation between estimate and reference (Morissey and Janowiak, 1996).

The above criteria are not independent. Murphy (1995) shows that:

$$I = r^2 - \left( r - \frac{\sigma_e}{\sigma_v} \right)^2 - \left( \frac{\bar{v} - \bar{e}}{\sigma_e} \right)^2$$

and thus

$$I \leq r^2.$$

Another simple relationship exists between $a$ and $r$.

$$a = r \frac{\sigma_e}{\sigma_v}$$

It is also important to add to these quantitative synthetic criteria the visual and qualitative information given by the scatter plot which allows to identify some characteristics of the data distribution or limitations of the method that the statistical criteria do not reveal.

## 3. Results

### *3.1. Case study over the Sahel*

For this study, the five satellite methods described in Section 2.2 have been run to provide 10-day rainfall estimates for five rainy seasons from 1989 to 1993, for eight 10-day periods running from 21 June to 10 September of each year, over West Africa at the Meteosat pixel resolution (5 km). Then estimates have been arithmetically averaged over the $0.5° \times 0.5°$ grid cells defined for the reference data, covering the Sahel.

The error criteria presented in Section 2.3 were computed for the five estimation methods using the whole dataset at the basic resolution; the whole dataset contains an average of 250 grid cells, for each of the forty 10-day periods considered during the five studied years, that is to say more than 8000 values. Several partitions of the dataset such as the subsets for each year, for each 10-day period and for each geographical zone, and coarser space and time resolutions datasets were also used. As it is impossible to present here the whole set of results, we selected several meaningful results which are of interest for the purpose of our study.

Table 1a to e give the error criteria for the year 1990. The best score in each column appears in bold. Table 1a shows the results obtained with the basic resolution: the integration time is 10 days, the grid resolution is 0.5° and a minimum of five stations in the grid cell vicinity are used for the reference values. The best scores are obtained by the satellite–gauge combined method (LAN). The gauge method (SYN) is significantly

Table 1
Correlation coefficient ($r$) and associated uncertainty ($\Delta r$), root mean square error (rmse), mean error (bias), scaled rmse (Srmse) and skill score ($I$) for five rainfall estimates over the Sahelian belt in summer 1990. The header line of [a] to [e] indicates the /time integration period/space resolution/minimum number of stations in the vicinity of the reference grid cells/mean reference rainfall/sample size. For [b] and [d], the rainfall values are scaled to 10-day cumulated rainfall.

| Method | $r \pm \Delta r$ | rmse (mm) | bias (mm) | Srmse | $I$ |
|---|---|---|---|---|---|
| *[a] / 10-day / 0.5° / five stations / 54.1 mm / 2056 values* | | | | | |
| GPI | 0.70 ± 0.02 | 28 | 17 | 0.67 | −0.06 |
| TAM | 0.69 ± 0.02 | 21 | 0 | 0.41 | 0.44 |
| LAN | **0.79 ± 0.02** | **17** | −4 | **0.32** | **0.60** |
| CLM | 0.66 ± 0.03 | 21 | 0 | 0.44 | 0.42 |
| SYN | 0.75 ± 0.02 | 21 | −2 | 0.42 | 0.41 |
| *[b] / 30-day / 0.5° / five stations / 58.6 mm / 514 values* | | | | | |
| GPI | 0.74 ± 0.04 | 24 | 18 | 0.50 | −0.27 |
| TAM | 0.64 ± 0.05 | 17 | 1 | 0.30 | 0.36 |
| LAN | **0.83 ± 0.03** | **12** | −4 | **0.20** | **0.66** |
| CLM | 0.77 ± 0.04 | 14 | 0 | 0.25 | 0.58 |
| SYN | 0.78 ± 0.03 | 14 | −1 | 0.26 | 0.54 |
| *[c] / 10-day / 1.0° / five stations / 52.5 mm / 720 values* | | | | | |
| GPI | 0.72 ± 0.04 | 29 | 18 | 0.68 | −0.11 |
| TAM | 0.69 ± 0.04 | 21 | 1 | 0.42 | 0.43 |
| LAN | **0.80 ± 0.03** | **17** | −3 | **0.31** | **0.63** |
| CLM | 0.69 ± 0.04 | 20 | 0 | 0.42 | 0.46 |
| SYN | 0.76 ± 0.03 | 20 | −2 | 0.41 | 0.46 |
| *[d] / 30-day / 1.0° / five stations / 56.8 mm / 180 values* | | | | | |
| GPI | 0.76 ± 0.06 | 25 | 19 | 0.53 | −0.30 |
| TAM | 0.63 ± 0.09 | 18 | 1 | 0.32 | 0.32 |
| LAN | **0.84 ± 0.04** | **12** | −3 | **0.20** | **0.69** |
| CLM | 0.79 ± 0.06 | 13 | −1 | 0.25 | 0.62 |
| SYN | 0.81 ± 0.05 | 13 | −1 | 0.25 | 0.62 |
| *[e] / 10-day / 0.5° / 10 stations / 54.4 mm / 901 values* | | | | | |
| GPI | 0.69 ± 0.03 | 28 | 17 | 0.66 | −0.15 |
| TAM | 0.73 ± 0.03 | 18 | 2 | 0.38 | 0.51 |
| LAN | **0.78 ± 0.03** | **17** | −4 | **0.31** | **0.59** |
| CLM | 0.63 ± 0.04 | 21 | 1 | 0.45 | 0.39 |
| SYN | 0.77 ± 0.03 | 20 | −3 | 0.39 | 0.42 |

better than TAM and CLM according to the correlation coefficient, but this is not confirmed by other criteria. The rmse varies from 17 to 28 mm, which is significantly larger than the uncertainty of the reference rainfall, estimated by the kriging standard deviation value of 9 mm, given in Section 2.1.2. The scaled rmse (Srmse) shows that the estimate errors vary from 32 to 67% of the reference rainfall. According to the values of $r^2$, 40 to 65% of the variance of the reference dataset is explained by the estimates. As

mentioned in Section 2.3, $I$ exhibits smaller values than $r^2$. This is particularly apparent when the bias is large, as it is the case for the GPI estimates.

Table 1b shows the results obtained with a time integration of 30 days. All the rainfall values have been scaled to 10-day cumulated rainfall for the sake of comparison of the results with the others. The improvement of the coefficients is noticeable when the time integration period is increased from 10 days to 30 days. Table 1c shows that increasing the grid cell size from 0.5° to 1.0° has no impact in this case. Table 1d shows that combining both the effect of increasing the grid cell size and the integration time does not yield additional improvement. However, the analysis of the results is limited by the fact that the reference values are not identical: the 30-day cumulated rainfall makes use of only six out of the eight 10-day periods, and the 1° areal rainfall makes use of a different selection of reliable grid cells. Complementary results concerning time and space integration will be presented in Section 3.2.

Table 1e shows the results obtained when only the grid cells containing at least 10 stations in their vicinity are selected for the validation. Comparison between Table 1a and e indicates that this more stringent selection has a very large impact on the number of grid cells available for the validation (as also seen in Fig. 3), but a very small effect on the computed criteria. This result supports the fact that five stations in the grid cell vicinity are sufficient to obtain a good areal rainfall amount at the space and time scales of this study.

To test the effect of partitioning the dataset for the five methods, we compared the correlation coefficients obtained with the whole dataset to the correlation coefficients obtained for each of the forty 10-day periods (eight 10-day periods for each of the 5 years). These correlation coefficients are plotted in Fig. 5, which shows a range of different values for each 10-day period. However, for each method, the mean of the 40 correlation coefficients is roughly equivalent to the correlation coefficient obtained for the whole dataset. It could be expected that dataset partitioning according to 10-day period would yield smaller correlation coefficients; this is not observed in our results, because these coefficients are computed on an extended geographical zone insuring a large enough range of values for each subset.

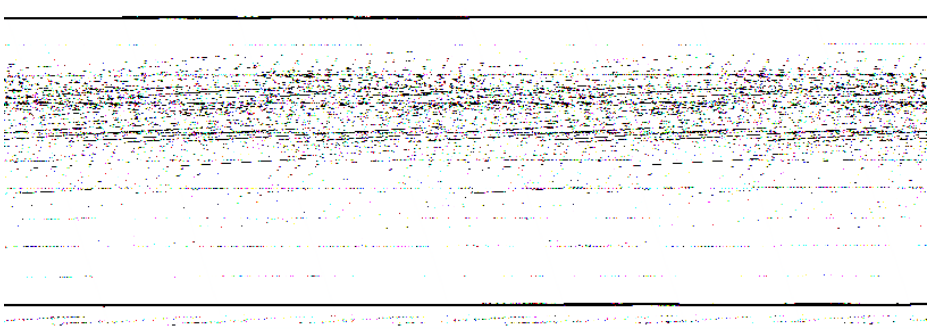

Fig. 5. Correlation coefficients for the five methods, obtained for each of the forty 10-day periods (from the last period of June to the first of September) plotted for years 1989 to 1993.

Table 2
Correlation coefficient and associated uncertainty for the five estimation methods for different datasets: for five years together over the Sahel (1989–1993), for each year over the Sahel (from 1989 to 1993), for all years together over three geographical zones: the Senegal region (zone 1), the central Sahel region (zone 2) and the Chad region (zone 3)

| Method | 1989–1993 | 1989 | 1990 | 1991 | 1992 | 1993 | Zone 1 | Zone 2 | Zone 3 |
|---|---|---|---|---|---|---|---|---|---|
| sample size | 8038 | 2056 | 2056 | 1234 | 1515 | 1177 | 621 | 6418 | 999 |
| GPI | $0.67 \pm 0.01$ | $0.65 \pm 0.03$ | $0.70 \pm 0.02$ | $0.55 \pm 0.04$ | $0.73 \pm 0.02$ | $0.70 \pm 0.03$ | $0.82 \pm 0.03$ | $0.65 \pm 0.01$ | $0.39 \pm 0.05$ |
| TAM | $0.54 \pm 0.02$ | $0.37 \pm 0.04$ | $0.69 \pm 0.02$ | $0.61 \pm 0.04$ | $0.68 \pm 0.03$ | $0.76 \pm 0.03$ | $0.51 \pm 0.06$ | $0.52 \pm 0.02$ | $0.43 \pm 0.05$ |
| LAN | $\mathbf{0.78} \pm 0.01$ | $0.74 \pm 0.02$ | $\mathbf{0.79} \pm 0.02$ | $0.74 \pm 0.03$ | $\mathbf{0.85} \pm 0.01$ | $\mathbf{0.83} \pm 0.02$ | $0.85 \pm 0.02$ | $\mathbf{0.79} \pm 0.01$ | $0.50 \pm 0.05$ |
| CLM | $0.61 \pm 0.01$ | $0.54 \pm 0.03$ | $0.66 \pm 0.03$ | $0.69 \pm 0.03$ | $0.56 \pm 0.04$ | $0.71 \pm 0.03$ | $0.69 \pm 0.04$ | $0.60 \pm 0.02$ | $0.35 \pm 0.06$ |
| SYN | $\mathbf{0.78} \pm 0.01$ | $\mathbf{0.81} \pm 0.02$ | $0.75 \pm 0.02$ | $\mathbf{0.80} \pm 0.02$ | $0.74 \pm 0.02$ | $0.79 \pm 0.02$ | $\mathbf{0.87} \pm 0.02$ | $0.78 \pm 0.01$ | $\mathbf{0.64} \pm 0.04$ |

Table 2 shows the correlation coefficients for the five 10-day estimation methods over the Sahel, for all 5 years together (1989–1993) and for each of the 5 years (from 1989 to 1993). The three right hand columns give the results obtained with the 5 year dataset for the three geographical zones displayed in Fig. 2c. Table 3 is similar to Table 2, but shows the skill scores. It should be noted that in considering subsets (i.e., for each year or geographical region), the sample size of the dataset is reduced but the values are not averaged. This is hence a different approach from integrating (averaging) in space or time.

It is noteworthy that the best criteria (in bold in the tables) are obtained for the LAN and the SYN methods. Concerning the geographical partition, it is obvious that both criteria ($r$ and $I$) are not good for zone 3. This zone is small and homogeneous, the standard deviation of the reference data is only 13.2 mm for this zone while it is, respectively, 16.2, 21.8 and 24.4 mm for zone 1, zone 2 and the whole region. Therefore, the correlation coefficient, and moreover, the skill score are likely to be smaller for zone 3. For zone 1, which has the smallest sample size, all methods yield good scores, with the exception of the TAM method, presumably because the TAM calibration coefficients were fitted considering somewhat different zones. The GPI method, calibrated with data from the GATE experiment close to this area, produces better results than anywhere else.

Fig. 6a to e display the scatterplots and the statistical coefficients for the five methods, for the 10-day periods of 1992. In addition to these five plots, the results of a sixth method are also plotted in Fig. 6f named LAN_CLIM. It is the LAN method calibrated with the climatic rainfall of each synoptic station. The features of the scatter plot and the coefficients show that LAN_CLIM is significantly worse than LAN, and actually compares with CLM. This result demonstrates that for the LAN method, replacing the actual observed rainfall at the synoptic stations by climatic values strongly degrades the method. Hence, the better scores achieved by the LAN method compared to the two other satellite methods, are mostly due to the calibration with ground observation rather than to differences in the satellite data processing. Also, the slightly better score achieved by the satellite–gauge combined method (LAN) compared to the gauge method (SYN) indicates that there is a potential for a better interpolation of gauge data using the cloud information derived from satellite data.

The scatterplots show that the method CLM does not produce neither low nor high rainfall. It is well known that climatic values cannot fit extreme precipitation. These

Table 3
Same as Table 2, but for the skill scores $I$.

| Method | 1989–1993 | 1989 | 1990 | 1991 | 1992 | 1993 | Zone 1 | Zone 2 | Zone 3 |
|---|---|---|---|---|---|---|---|---|---|
| sample size | 8038 | 2056 | 2056 | 1234 | 1515 | 1177 | 621 | 6418 | 999 |
| GPI | 0.23 | 0.26 | −0.06 | 0.03 | 0.47 | 0.34 | 0.61 | 0.24 | −1.01 |
| TAM | 0.16 | −0.54 | 0.44 | 0.33 | 0.44 | 0.49 | 0.02 | 0.14 | 0.01 |
| LAN | **0.59** | **0.52** | **0.60** | 0.50 | **0.71** | **0.58** | **0.73** | **0.61** | −0.01 |
| CLM | 0.35 | 0.19 | 0.42 | 0.45 | 0.30 | 0.50 | 0.46 | 0.33 | **0.04** |
| SYN | 0.39 | 0.26 | 0.41 | **0.54** | 0.32 | 0.48 | 0.70 | 0.38 | −0.36 |

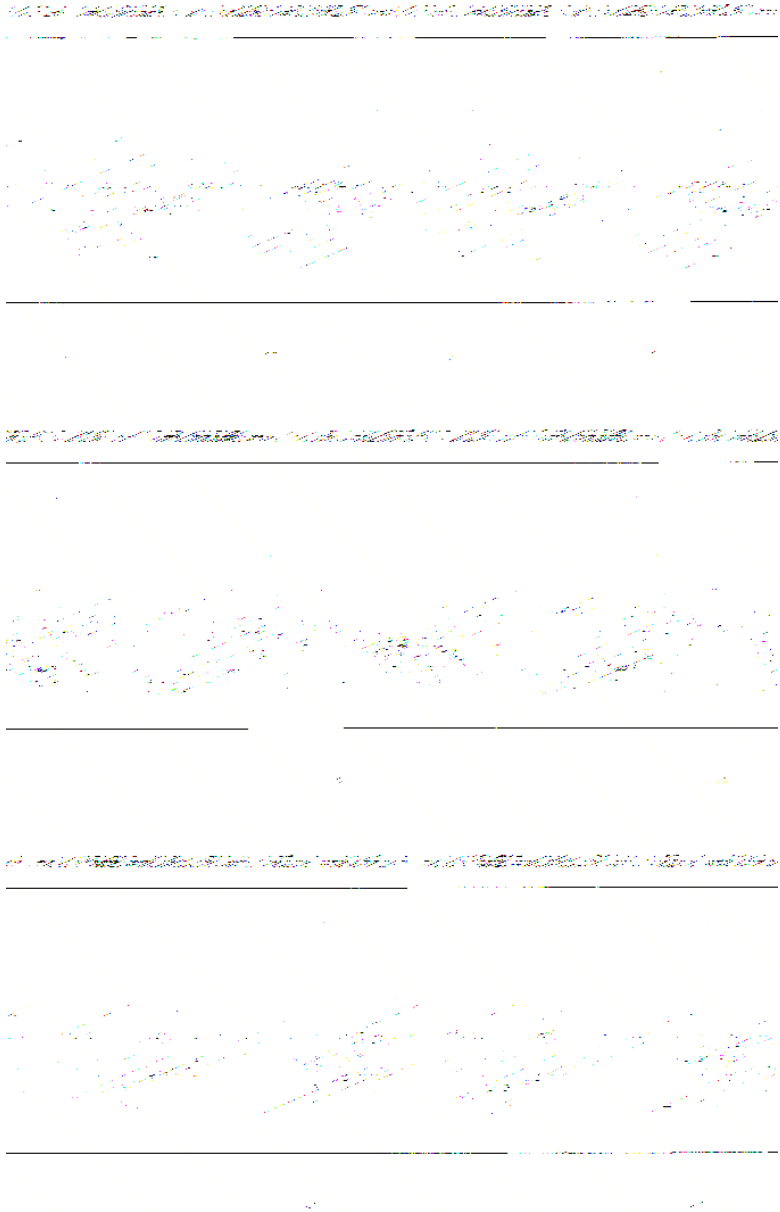

Fig. 6. Scatterplots of rainfall estimates vs. reference values (mm), for six rainfall estimation methods for summer 1992. Sample size: 1515 (about 190 grid cells for eight 10-day periods).

features can also be observed on TAM and LAN_CLIM that are indeed calibrated with climatic datasets. It is also verified on the scatterplots that the typical default of the three satellite methods is to underestimate large rainfall values.

### 3.2. Case study over Burkina-Faso

In this section different rainfall estimates are analyzed over a small region of about 750,000 km$^2$, between 11°N–13.5°N and 2.5°W–0.5°E. This area covers mainly Burkina-Faso and was chosen for the high density of the raingauge network. Results are presented for one rainy season (nine 10-day periods, from 21 June 1989 to 20 September 1989). In this area, 58 stations were available; the number of available raingauges is 65 when taking into account a slightly larger area in order to avoid border effects. These data were used to compute the areal reference values over a $0.2° \times 0.2°$ grid cell, using the kriging method described in Section 2.1.1. Due to the density of the network, it was considered that all grid cells were reliable and are to be used for computing error criteria. Hence, each 10-day period consists of 180 grid cells (i.e., a total of 1620 values for the whole dataset) for the $0.2° \times 0.2°$ resolution.

There are three synoptic stations in the area, and five in the extended area. These data were used to compute the SYN estimates, using weight inversely proportional to the square distance. Additionally, two other methods were tested for the computation of a ground-based rainfall estimate using the synoptic stations: (a) KRG: the kriging method, with the same parameters as for the computation of the reference values, but using only the synoptic stations; (b) ARM: the arithmetic mean of the synoptic observations, using a moving neighborhood of 150 km. Two out of the three satellite methods already described, GPI and LAN, are used in this section.

The results for the basic resolution ($0.2° \times 0.2°$ grid cells and 10-day periods) are presented in Table 4. Columns 1 (correlation coefficient), 3 (skill score), 5 (slope of the regression) and 6 (rmse) are computed using all 1620 values for each method. Additionally, we computed the correlation coefficient and the skill score for each of the nine 10-day periods; their mean values are presented in columns 2 and 4.

The first observation is that all methods perform in a similar way, especially with respect to the correlation coefficient. Concerning the ground-based methods, the similar results indicate that the network is too sparse for the sophisticated interpolation methods like kriging to show their superiority. The LAN method produces rmse criteria 15% smaller than the other estimates. Concerning the slope of the regression between the estimates and the reference values, both satellite methods yielded weaker regression slopes than the ground-based methods. This can be explained by the fact that the satellite

Table 4
Correlation coefficient $r$, mean 10-day correlation coefficient, skill score $I$, mean 10-day skill score, slope of the linear regression $a$ and root mean square error rmse for five rainfall estimation methods over the Burkina-Faso area for summer 1989. Grid cell size of 0.2°, time integration of 10 days. For each 10-day period, 180 values were available (1620 for the whole dataset).

| Method | $r$ | Mean $r$ | $I$ | Mean $I$ | $a$ | rmse (mm) |
|---|---|---|---|---|---|---|
| ARM | **0.69** | 0.37 | 0.37 | **−0.70** | 0.66 | 30 |
| SYN | 0.67 | 0.41 | 0.29 | −0.93 | **0.68** | 30 |
| KRG | 0.68 | **0.42** | 0.33 | −0.83 | 0.67 | 29 |
| LAN | **0.69** | 0.41 | **0.46** | −0.86 | 0.54 | **26** |
| GPI | 0.68 | 0.18 | 0.36 | −0.97 | 0.58 | 28 |

estimates tend to saturate, as it is also shown in Fig. 6. These observations regarding the distance criteria and the slope show that it is important to study more performance criteria than only the correlation coefficient.

It is also worth noting that the mean criteria, computed using a partition of the dataset according to the nine 10-day periods, are considerably worse than the criteria computed using the whole dataset. A similar partitioning for the previous case study over the Sahel, indicated that the correlation coefficients for each 10-day period tend to show some variability (Fig. 5) but are not dramatically smaller than the correlation coefficient for the whole dataset. We explain the different behavior obtained from the Burkina-Faso dataset by the different space extent of the studied area. If one computes correlation coefficients (or skill scores) either for a large area (spatial inhomogeneity) or for long periods (time inhomogeneity), one obtains better results than the results obtained over a limited area and a single 10-day period, since rainfall is then likely to be more homogeneous. This effect of the range of variables has also been noticed by Kessler and Neas (1994) and shows that in our case the tested methods simply estimate a large scale trend of rainfall but cannot estimate the shorter scale fluctuations neither in time nor space.

As it was performed in Section 3.1 over the Sahel area, we tested the behavior of the performance criteria to space and time averaging over the Burkina-Faso area. The results shown in Table 5a to c include only one ground-based method (SYN) as all these methods perform similarly. The mean 10-day values of criteria were not included, because the number of values for each 10-day is not large enough to insure statistical significance.

Table 5a and b and Fig. 7 show the effect of changing the spatial resolution from 0.2 to 1.0° grid cells. As for the case study presented in Section 3.1, there is some

Table 5
Correlation coefficient $r$, slope of the linear regression $a$, root mean square error rmse and skill score $I$, for three rainfall estimation methods over the Burkina-Faso area for summer 1989 for: (a) grid cell size of 0.5°, integration time of 10 days; (b) grid cell size of 1.0°, integration time of 10 days; (c) grid cell size of 0.5°, integration time of 30 days

| Method | $r \pm \Delta r$ | $a$ | rmse (mm) | $I$ |
|---|---|---|---|---|
| *[a] / 0.5° / 10-day / 270 values* | | | | |
| SYN | $0.71 \pm 0.06$ | **0.75** | 27 | 0.36 |
| LAN | **0.73** $\pm 0.06$ | 0.57 | **24** | **0.51** |
| GPI | **0.73** $\pm 0.06$ | 0.63 | 26 | 0.43 |
| *[b] / 1.0° / 10-day / 54 values* | | | | |
| SYN | $0.77 \pm 0.12$ | **0.84** | 23 | 0.41 |
| LAN | **0.80** $\pm 0.10$ | 0.73 | **18** | **0.62** |
| GPI | $0.79 \pm 0.11$ | 0.78 | 22 | 0.45 |
| *[c] / 0.5° / 30-day / 90 values* | | | | |
| SYN | $0.82 \pm 0.07$ | **0.81** | 15 | 0.54 |
| LAN | **0.83** $\pm 0.07$ | 0.59 | **13** | **0.65** |
| GPI | $0.71 \pm 0.11$ | 0.49 | 18 | 0.30 |

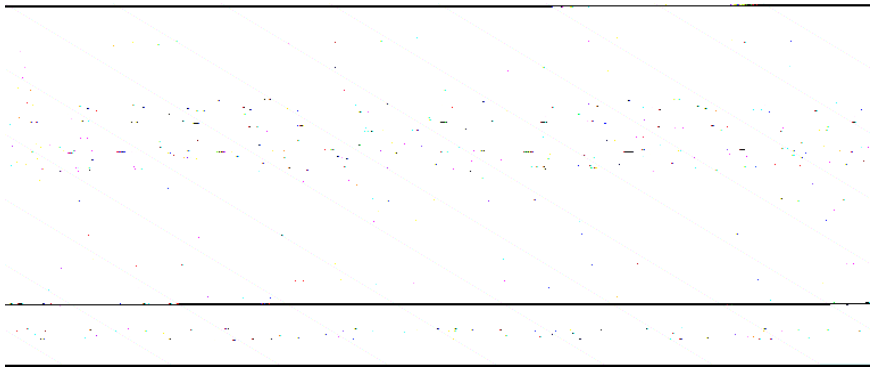

Fig. 7. Correlation coefficient (a) and skill score (b) as function of grid cell size for three estimation methods, for the Burkina-Faso dataset.

improvement in the performance criteria, but this does not change the method ranking (LAN performs always the best for correlation coefficient and skill score, as shown in Fig. 7). The regression slopes for the satellite-based methods are always weaker than for ground-based methods; this shows that space averaging does not totally remove the saturation effect of the satellite methods. Table 5c shows the results obtained using time steps of 30 days. The impact of increasing the integration time is more important than for space averaging; however, the saturation effect of the satellite methods is even more obvious. Again, LAN performs better than the other methods in terms of rmse and skill score.

## 4. Conclusion

The aims of this study concerned the following two issues: (i) the quality assessment and intercomparison of operational rainfall estimation methods, based on either satellite or on ground data; (ii) the methodology of this quality assessment and intercomparison.

(i) The results show that the satellite methods and the ground-based methods using only the sparse synoptic gauge network yield more or less similar results and, as expected, are better than the climatic estimation method. This conclusion is valid both at a continental scale (Sahel) and at a regional scale (Burkina-Faso). However, the satellite–gauge combined method (LAN) using real-time information of both types (satellite and synoptic network measurements) yields better results. The results are better concerning the distance criteria (root mean square error and skill score) but they are not better concerning the cofluctuation criteria (the correlation coefficient are similar but the slope of the linear regression is weaker than for the ground-based methods). This suggests that there is a potential for better ways of combining the two types of information.

As an example of the best scores obtained with the LAN method, here are the values of the performance criteria for 10-day cumulated rainfall over 1 year (1990) and for the spatial resolution of $0.5° \times 0.5°$ over the Sahel area: correlation coefficient $r = 0.8$; root

mean square error rmse = 17 mm; bias = −4 mm for a mean rainfall of 54 mm; root mean square error scaled by the rainfall amount Srmse = 32%; skill score $I = 0.6$; the rmse is significantly larger than the uncertainty of the reference rainfall of 9 mm.

A comparison between several ground-based methods over the Burkina-Faso area shows that using the sparse synoptic raingauge network, the choice of the interpolation method is not important; kriging does not yield better results than simple interpolation methods, because of the lack of information concerning the structure of rainfall at the considered time and space scales. Further work is needed in order to study whether it is possible to extract such information from the satellite data.

(ii) Another result of the study is to show how the quality assessment of rainfall estimates depends on the time and space integration scale, the dataset partitioning and the performance criteria.

The use of different time and space integration scales confirmed that performance generally increases with grid cell size and time step.

Partitioning the whole dataset into subsets corresponding to different periods or geographical zones shows that the values of the performance criteria strongly depend on the considered validation subset. We emphasize that partitioning does not imply any averaging or integrating and hence this dependence is not related to the law of large numbers. We noticed that: (a) computing the criteria over a small area (the Burkina-Faso case study) and one time step (10-day period) yields poor results ($r < 0.5$ and $I < -0.7$); (b) merging datasets in space or/and time (all 10-day periods, whole Sahel area) yields acceptable criteria.

The performances of rainfall estimation methods are linked to the rainfall range which in turn is related to the space and time extent of the validation dataset. An illustration was given by the very poor scores obtained by all methods over a limited area (zone 3) where the rainfall standard deviation was very low.

The use of different error criteria showed that for accurate performance assessment a single criterion is seldom sufficient. For example the ranking of the methods according to either the correlation coefficients or the skill scores are different (Tables 2 and 3). For the Burkina-Faso case study, the satellite methods yield correlation coefficients which are identical to the ground-based methods (Table 5), but the corresponding regression slopes are weaker (due to the underestimation of large rainfall values by the satellite methods). Although it is usual in validation or intercomparison exercises to use only one performance criterion (most often the correlation coefficient), it is recommended to compute several criteria: if there is a general agreement from all the criteria, the validation is strengthened; if there is no agreement, the discrepancies can help to understand the weaknesses of the estimation methods.

## Acknowledgements

The suggestions and comments of anonymous reviewers helped us to improve the manuscript. They are gratefully acknowledged. Special thanks are addressed to AGRHYMET for providing us with the datasets. This study was a joint EPSAT/AGRHYMET project, based on the recommendations of the workshop held in Niamey, Niger, in December 1994.

## References

Arkin, P.A., 1979. The relationship between fractional coverage of high cloud and rainfall accumulations during GATE over the B-scale array. Mon. Weather Rev. 107, 1382–1387.

Arkin, P.A., Ardanuy, P.E., 1989. Estimating climate-scale precipitation from space: a review. J. Climate 2, 1229–1238.

Arkin, P.A., Meisner, B.N., 1987. The relationship between large-scale convective rainfall and cold cloud over the western hemisphere during 1982–1984. Mon. Weather Rev. 115, 51–74.

Bastin, G., Lorent, B., Duqué, C., Gevers, M., 1984. Optimal estimates of the average area rainfall and optimal selection of raingauge locations. Water Resour. Res. 20, 463–470.

Carn, M., Lahuec, J.P., Dagorne, D., Guillot, B., 1989. Rainfall estimation using TIR Meteosat imagery over the Western Sahel. 4th Conf. on Satel. Meteor. and Oceanography, San Diego, AMS, pp. 126–129.

Creutin, J.D., Obled, C., 1982. Objective analysis and mapping techniques for rainfall fields: an objective comparison. Water Resour. Res. 18, 413–431.

Dugdale, G., McDouglas, V.D., Milford, J.R., 1990. Potential and limitations of rainfall estimates for Africa derived from cold cloud statistics. 8th Meteosat Scientific Users' Meeting, Norköpping, Sweden. Eumetsat Publ. EUM P08, pp. 211–220.

Isaaks, E.H., Srivastava, R.M., 1989. Applied Geostatistics. Oxford Univ. Press, Oxford, pp. 561.

Jobard, I., Desbois, M., 1992. Remote sensing of rainfall over tropical Africa using Meteosat infrared imagery: sensitivity to time and space averaging. Int. J. Remote Sensing 13 (14), 2683–2700.

Kendall, M.A., Stuart, A., 1963. The Advanced Theory of Statistics. Griffin (Ed.), p. 1730.

Kessler, E., Neas, B., 1994. On correlation, with application to the radar and raingauge measurement of rainfall. Atmos. Res. 34, 217–229.

Laurent, H., Lebel, T., Polcher, J., 1997. Rainfall variability in Soudan, Sahelian Africa studied from raingauges, satellite and GCM. Preprints, 13th Conf. Hydrology, AMS Annual Meet., 2–7 Feb. 1997, Long Beach, CA, pp. 17–10.

Le Barbé, L., Lebel, T., 1997. Rainfall climatology of the HAPEX-Sahel region during the years 1950–1990. J. Hydrol. 188–189 (1–4), 43–73.

Lebel, T., Le Barbé, L., 1997. Rainfall monitoring during HAPEX-Sahel: 2. Point and areal estimation at the event and seasonal scales. J. Hydrol. 188–189 (1–4), 97–122.

Lebel, T., Bastin, G., Obled, C., Creutin, J.D., 1987. On the accuracy of areal rainfall estimation: a case study. Water Resour. Res. 23, 2123–2134.

Morissey, M.K., Janowiak, J.E., 1996. Sampling-induced conditional biases in satellite climate scale rainfall estimates. J. Appl. Meteorol. 35, 541–548.

Murphy, A.H., 1995. The coefficients of correlation and determination as measures of performance in forecast verification. Weather and Forecasting 10, 681–688.

Obled, C., Wendling, J., Beven, K., 1994. The sensitivity of hydrological models to spatial rainfall patterns: an evaluation using observed data. J. Hydrol. 159, 305–333.

Tabios, G.Q., Salas, J.D., 1985. A comparative analysis of techniques for spatial interpolation of precipitation. Water Resour. Res. 21, 365–380.

*Q. J. R. Meteorol. Soc.* (2001), **127**, pp. 377–406

# Life cycle of Sahelian mesoscale convective cloud systems

By VINCENT MATHON* and HENRI LAURENT
*Institut de Recherche pour le Développement, France*

(Received 11 October 1999; revised 18 July 2000)

SUMMARY

This paper provides an eight-year high-resolution climatology of Sahelian mesoscale convective systems (MCSs) during the summer. MCSs are defined as convective cloud clusters larger than 5000 km$^2$. They are extensively tracked from METEOSAT full-resolution infrared images (time resolution 0.5 h and spatial resolution about 5 km). The method enables every MCS to be tracked throughout its entire lifetime. For each time step, the MCS location and its morphological and radiative characteristics are computed for three different brightness temperature thresholds. The methodology is presented, evaluated and compared with previous studies using low-resolution data.

Statistical MCS distributions, diurnal cycle and spatial variability of MCS characteristics are analysed on the basis of this high-resolution tracking. It is shown that a few large and long-lived cloud clusters contribute most of the total cloud cover. Sahelian cloud clusters propagate westward at a greater speed when very deep convection is well developed. The diurnal organization of the convection has been analysed, and has proved that the merging of MCSs is partly explained by the actual merging of independent convective entities, whereas the splitting of MCSs is mostly associated with weakening of convection. The importance of mesoscale convective complexes for the total MCS coverage has also been studied.

KEYWORDS: Automatic tracking Climatology Mesoscale convective systems METEOSAT infrared data Sahel

## 1. INTRODUCTION

The strong interaction between deep convection and general atmospheric circulation implies that tropical convection is a key element of the global climate. Convection is central to vertical exchanges of radiative and latent energy. Tropical convective clouds generally cluster in large systems which are responsible for most tropical precipitation (Gamache and Houze 1983). For the central Sahel, D'Amato and Lebel (1998) have shown that the mesoscale convective systems (MCSs) account for more than 90% of annual rainfall.

Using satellite data, several studies have provided comprehensive statistics on annual, seasonal and diurnal variations, and size distribution of convective systems over West Africa (Desbois *et al.* 1988; Duvel 1989; Machado *et al.* 1992, 1993). Machado and Rossow (1993) studied the structural characteristics and radiative properties of tropical cloud clusters. They suggested that such studies can be improved by taking into account the development stage of convective systems. Studies of the convective systems' life cycle can also provide further insight into scale interactions from the convective-cell scale to the large scale. Thorncroft and Haile (1995) and Rowell and Milford (1993) have studied the relationships between the large-scale environment and Sahelian convective systems over limited periods. The modulation of the convection by easterly waves has been documented by Reed *et al.* (1977), Duvel (1990), Machado *et al.* (1993) and Diedhiou *et al.* (1998). These studies could be further developed by considering the life cycle of convective systems which interact with the easterly waves. Moreover, improved statistics for atmospheric model parametrizations and validations can be built from comprehensive studies of the life cycle of MCSs.

Several methods of tracking have been developed to take into account the life cycle of convective systems. Aspliden *et al.* (1976) and Martin and Schreiner (1981), using satellite images, manually tracked the main convective systems which occurred during

* Corresponding author: IRD, Laboratoire d'Hydrologie, F-34032 Montpellier, France.
e-mail: mathon@mpl.ird.fr

GATE (Global Atmospheric Research Program Atlantic Tropical Experiment). More recently, Desbois *et al.* (1988) and Rowell and Milford (1993) tracked squall lines over West Africa. Laing and Fritsch (1993) focused on very large convective systems called MCCs (mesoscale convective complexes as defined by Maddox 1980). Such manual and operator-dependent methods are, however, somewhat subjective and difficult to reproduce. Moreover, as the process is lengthy, only limited periods have been treated. As climatology and variability studies require homogeneous processing over a long period, automated methods have been developed.

Woodley *et al.* (1980) tracked convective systems for three months in the GATE area with an automated procedure based on a propagation speed criterion. Williams and Houze (1987) used another automated method based on a minimum overlapping area between MCSs in successive images. This method was later applied for three winters to the ISCCP (International Satellite Cloud Climatology Project, Rossow and Schiffer 1991) B1 images over the tropical Pacific warm pool by Mapes and Houze (1993) and the TOGA COARE (Tropical Ocean/Global Atmosphere Coupled Ocean–Atmosphere Response Experiment) area by Chen and Houze (1997). Arnaud *et al.* (1992) developed a similar method in 1989 over Africa with additional criteria for merging or splitting. Morel *et al.* (1997) used another slightly different areal overlap method over France. The area of a given cluster was extrapolated in the following image and a test applied to the overlap area with existing clusters.

With increasing availability of satellite data, periods of study have become longer. Hodges and Thorncroft (1997) provided a first short-term climatology of African convective systems by applying a new method over eight years (1983–90) using ISCCP B3 data. In their methodology the images are smoothed and convective systems are depicted using a 258 K threshold. This relatively warm threshold is used to balance out the smoothing effects. The tracking method is based on minimization of a cost function which measures the coherence in direction and speed of the minimum temperature within the cloud systems (Hodges 1998).

The different methods developed use different criteria to identify and track convective systems using satellite data. Machado *et al.* (1998), using ISCCP B3 data, have compared different match criteria to connect convective clusters: maximum areal overlap, minimum propagation speed, minimum size difference, minimum of the minimum-temperature difference, minimum of a cost function and 'subjective' choice. They concluded that "a simple (but more objective) tracking method, based on area overlap, is shown to work as well for larger convective systems as more elaborate methods which look for morphological and radiative similarities of the convective system clouds". Actually, such a method performs well as long as the propagation of the cluster in two sequential images is small compared to its size. For 3 h resolution data, Machado *et al.* (1998) consider that the areal overlap method performs well for a cluster radius larger than 100 km. With a better time resolution the minimum cluster size can be reduced.

The studies described above used sampled data or were made over limited periods. In this study, we present an eight-year (1989–92; 1995–98) high-resolution climatology of convective systems over West Africa in summer. Convective systems are tracked from full-resolution satellite images using an entirely automated method giving objective results over large datasets. The algorithm is basically an areal overlap method similar to the one described by Williams and Houze (1987), with a major improvement consisting of interpolating cluster life cycles in the case of missing data.

The methodology used to identify and track convective clusters throughout their life cycle is described in section 2. In section 3 we present cluster distributions over the Sahel in summer. Diurnal variations are investigated in section 4. The spatial variability

of some cluster characteristics over West Africa is presented in section 5. The last section summarizes the main results.

## 2. METHODOLOGY

### (*a*) *Cloud cluster characterization*

Convective clouds are detected from infrared (IR) satellite images, assuming that low brightness temperatures are strongly related to deep convection. In the tropics, cold cloud with high emissivity is generally the result of deep convection. A brightness temperature threshold depicts cold cirrus shields which may last longer than convection, i.e. cloud clusters are tracked including the dissipation stage when convection is no longer active.

Convective clouds are thus identified in METEOSAT IR channel (10.5–12.5 $\mu$m) images using a temperature threshold: cloud clusters are defined as a contiguous area of pixels with a brightness temperature lower than the threshold.

Clouds larger than 5000 km$^2$ are called MCSs and no attempt is made to identify the convective and stratiform parts within an MCS.

MCSs are delineated using three different brightness temperature thresholds: 253 K, 233 K and 213 K. The 253 K threshold was chosen as the highest cloud temperature associated with convection (Duvel 1989; Mapes and Houze 1993). The 233 K threshold is in the range of the most commonly used thresholds for identifying deep convection and accumulated convective precipitation in the tropics (Arkin 1979). The 213 K threshold aims to identify the very deep convection, the most active part of convective systems.

Maddox (1980) has defined MCCs as follows:

(i) cloud shield with IR temperature $\leqslant$241 K must have an area $\geqslant$100 000 km$^2$; and
(ii) interior cold cloud region at 221 K temperature threshold must have an area $\geqslant$50 000 km$^2$; and
(iii) conditions (i) and (ii) must be satisfied simultaneously for at least six consecutive hours; and
(iv) eccentricity (minor axis/major axis) must be $\geqslant$0.7 at time of maximum extent.

The eccentricity criterion was arbitrarily specified to preclude classification of linear-type systems as MCCs. Over West Africa, linear-type systems are of particular interest; squall lines represent about half of the major rainfall events over the central Sahel (d'Amato and Lebel 1998; Laurent *et al.* 1998). Several studies employed similar temperature thresholds, e.g. Fritsch *et al.* (1986), Miller and Fritsch (1991), Laing and Fritsch (1993, 1997), Rowell and Milford (1993). In a recent study of MCSs over the Americas, Machado *et al.* (1998) employed the 245 K threshold to define the convective systems, and the 218 K threshold to define the active deep convective cells embedded within the convective systems. They observed that the shape of the size distribution of the convective cloud systems is not very sensitive to the choice of the temperature threshold, because there is a near-linear dependency of convective system sizes with varying thresholds over a range of 10–20 K. Here we have chosen the 233 K and 213 K thresholds to cover a large range of clouds. Furthermore, as already mentioned, 233 K is a reference threshold for rainfall estimation, while the 213 K threshold leads to the best correlation with rainfall during the core of the rainy season over the central Sahel (Jobard and Desbois 1992).

Most of the above mentioned studies of convective cloud tracking employ reduced-resolution data, such as the ISCCP datasets. We use here full time and space resolution:

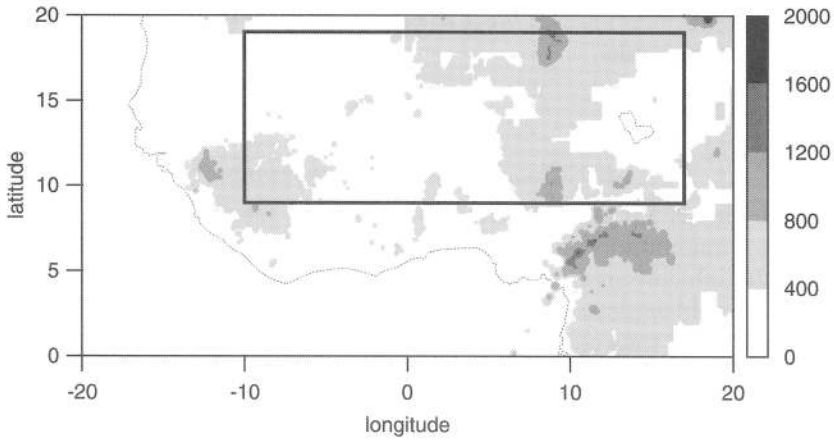


Figure 1. Map of West Africa showing the orography (m) above 400 m. The central Sahel area is shown by the box.

METEOSAT images are available every 30 min, space resolution is about 5 × 5 km at the subsatellite point. The images are windows covering West Africa, extracted from the full-disk images. Figure 1 shows the window of extraction. Orography above 400 m and the central Sahel area location are also indicated in Fig. 1. Navigation and calibration are performed using EUMETSAT (European Meteorological Satellite system) guidelines. We have processed METEOSAT data for ten summers (1989–98). However, to have the most homogeneous dataset possible, the results are confined to the period 21 June to 14 September for the years 1989, 1990, 1991, 1992, 1995, 1996, 1997 and 1998. For this period less than 10% of data are missing. The 1993 and 1994 datasets were not used here because of a systematic lack of images, leading to a great change in the distribution of the number of MCSs. For example, as the 1830 UTC image is always missing, the number of initiations is significantly increased in the early evening when the convection is at a maximum.

### (*b*) *Tracking*

Tracking of convective clouds is performed with an areal overlap method, similar to the one described by Williams and Houze (1987). This technique simply assumes that a cloud at a later time corresponds to those at an earlier time when their positions overlap. When several MCSs overlap we consider the pair with the largest overlap surface.

The tracking method is applied only to MCSs. There are two reasons for this choice: first, the propagation speed of tropical cloud does not usually exceed 80 km $h^{-1}$, so there is always a large overlap area when using successive images half-an-hour apart; second, several numerical problems are avoided. Actually, for cloud clusters smaller than 5000 $km^2$, the number of systems increases greatly whereas the overlap surface becomes limited. The probability of several clouds satisfying the maximum overlap criterion increases and, even for a human operator, it becomes difficult to keep account of all the different possible cases. The drawback is that filtering of small clusters can result in a reduction of the lifetime of the cloud system. Moreover, cases of cluster re-generation can be missed if the cluster size is temporarily smaller than 5000 $km^2$. An evaluation of the error related to small-cluster filtering is given in section 2(d).

An MCS generates spontaneously whenever there is no overlapping with any MCS in the previous image. When an MCS splits up, the largest part keeps the MCS label,

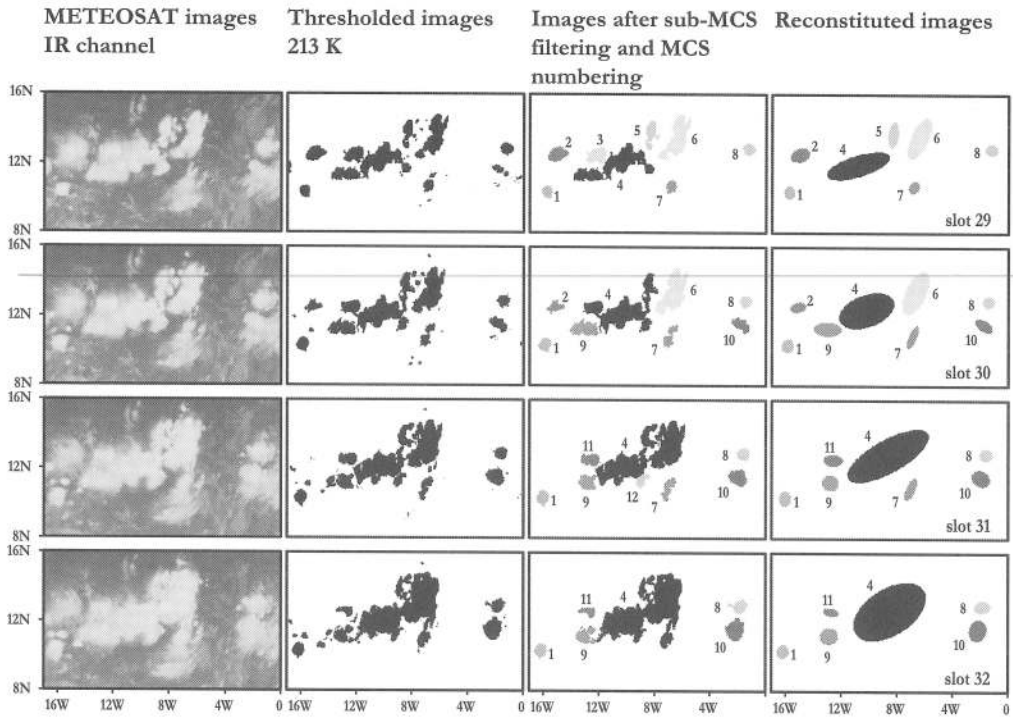


Figure 2. From top to bottom: sequence of four consecutive time steps 30 min apart, from slot 29 (approximately 1415 UTC) to slot 32 (approximately 1545 UTC). From left to right: raw METEOSAT infrared images; thresholded images (threshold = 213 K); numbered mesoscale convective systems (MCSs; cut-off of small clouds); image reconstituted from the output of the tracking process.

whereas the smaller parts are considered as 'split generations'. Similarly, an MCS life cycle comes to an end either when there is no overlapping with any MCS of the following image (cloud dissipation) or when it merges with a larger MCS (merger-end).

Figure 2 illustrates the tracking scheme over a series of four time steps, from the initial METEOSAT images to the reconstituted images obtained from information contained in the final product output, assuming an ellipsoidal shaped cloud cluster. The images are first temperature 'thresholded', then the small clouds are removed and the remaining cloud clusters (MCSs) identified and numbered. Tracking aims to connect the clusters between two successive time steps. To detect and identify the different possible cases, both 'forward' and 'backward' tracking is computed. Forward tracking consists, for a given cluster at time $t$, of searching among the clusters at time $t + 1$ for the one with the largest overlap area. Backward tracking consists, for a given cluster at time $t + 1$, of searching for the cluster at time $t$ with the largest overlap area. The various possible cases are illustrated by reference to the numbered clusters in Fig. 2.

- *Regular tracking*: cluster 6 is easily connected between slot 29 and slot 30, both by forward and backward tracking.
- *Generation*: between slot 29 and slot 30, backward tracking does not connect any cluster to the cluster 10; this cluster is therefore assumed to initiate at slot 30. Note that some clouds do exist in the non-filtered slot 29, but they are smaller than the size threshold and so are not integrated in the tracking process.

• *Dissipation*: between slot 30 and slot 31, forward tracking does not connect any cluster to the cluster 2; this cluster is therefore assumed to dissipate at that time. Note that only a few pixels of cluster 2 still exist in the non-filtered slot 31.

• *Merger*: between slot 30 and slot 31, clusters 4 and 6 merge. Unlike the dissipation case, forward tracking does connect cluster 6 with a cluster in the following image. Thus we consider that cluster 6 ends up by merging into a bigger cluster (cluster 4).

• *Split*: between slot 29 and slot 30, a part of the cluster 4 splits and gives rise to the new cluster 9. Backward tracking indicates that cluster 9 is the result of a split rather than from spontaneous generation.

Several cases can occur simultaneously. For example, between slot 29 and slot 30, clusters 3 and 5 merge into cluster 4, whereas cluster 9 is split-generated.

To our knowledge, only one case is not accounted for. This is illustrated in Fig. 2, slot 31, where the cluster 12 does not appear in the reconstituted image. This is because clusters not present in more than one image are not taken into account. This generally only applies to small MCSs. As such cases do not represent a significant amount of cloud cover, they are ignored in the current version of the tracking algorithm.

The parameters shown in Table 1 are recorded for each cluster, each temperature threshold $T0$ and each time step. Among the morphological parameters, we calculate an effective radius. This is a convenient measure of cluster size, although cloud clusters are generally not circular. Additionally, we calculate the angle and eccentricity of the cluster assuming that it has an ellipsoidal shape. Four synthetic parameters (size, geometric centre coordinates, eccentricity and orientation of the ellipse) can be used for an approximate reconstitution of the cloud coverage.

Among the radiative parameters, we calculate the temperature gradient at the western edge. Actually, it is not a true gradient since cloud tops do not constitute a planar surface. This parameter aims to detect the sharpness of the cluster's western edge. This could be a means of depicting squall lines among MCSs (Desbois *et al.* 1988). The clear-sky test is calculated for a similar reason.

### (*c*) *Interpolation of missing data*

Interpolation of missing data is particularly important for evaluating the number of systems.

There are basically three cases where images are missing.

• The 1989 to 1991 data are stored on magnetic tapes. A lot of successive images are missing (typically 12 hours, i.e. 24 images) due to deterioration of some of the tapes.

• The 1992 to 1997 data were received and archived from a METEOSAT Primary Data Users Station at UTIS*. Some IR images systematically go missing owing to acquisition of images from other channels. In 1993 and 1994 the shortfall of IR data reaches five images per day (slots 1, 13, 23, 25, 37). As already mentioned in section 2(a), this systematic lack of data has led us to exclude these two years from this study.

• A few images (up to four) are always missing around midnight towards the end of the summer period, due to the eclipse phenomenon.

If the number of missing images is high ($>10$ images) the tracking procedure is stopped and the clusters are flagged as having ended due to the end of the dataset. A

* Unité de Traitement d'Images Satellitaires, ISRA/IRD (Institut Sénégalais de Recherches Agricoles/Institut de Recherche pour le Développement), Dakar, Sénégal.

TABLE 1. LIST OF PARAMETERS CALCULATED DURING THE TRACKING PROCESS

| Morphological parameters | Radiative parameters | Additional parameters |
|---|---|---|
| Cluster size expressed in number of pixels and in km$^2$ | Minimum temperature (brightness temperature of the coldest pixel) | Universal and local time at the cluster location |
| Cluster radius (km) defined as: $r = \sqrt{surface/\pi}$ where *surface* is the size of the MCS in km$^2$ | Mean temperature | Coordinates of the weighted centre, where the weight of each pixel is defined as: $w = T0 - T + 1$ |
| Coordinates of the geometric centre | Temperature variance | Cluster speed deduced from the displacement of the weighted centre |
| Ellipsoidal cluster shape (angle and eccentricity) deduced from the inertia axis | 2 K binned-temperature histogram | Coordinates of the cluster front, computed as the mean location of the pixels constituting the western edge of the cluster (as Sahelian MCSs propagate westward, the western edge is the cluster front) |
| Number and total coverage of clusters embedded in the MCS at the immediately colder threshold if $T0 > 213$ K, or at 203 K if $T0 = 213$ K | Mean temperature of the ten biggest clusters embedded in the MCS | For the 213 K and 233 K thresholds, identification of the cluster at the 233 K and 253 K threshold respectively |
| Coordinates of the geometric centre of the ten biggest clusters embedded in the MCS | Volume index, defined as: $I = \sum(T0 - T + 1)$ | At the first time step, a flag indicates whether it is a spontaneous generation, a split-generation or a new dataset. If a split-generation, the number of the originating cluster is recorded |
| Size of the ten biggest clusters embedded in the MCS | Clear-sky test defined as $Igrd = T1 - T2$ where $T1$ is the maximum temperature encountered ten pixels westward of the west front, and $T2$ is the minimum encountered three pixels eastward of the west front | At the last time step, a flag indicates whether it is a cloud dissipation, a merger into a bigger cluster or a dataset end. If a merger, the number of the destination cluster is recorded |
| | West edge temperature gradient computed over a 21 line × 11 column window fitted to the shape of the west cluster edge and centred around the gravity centre | |

$T0$ is the brightness temperature threshold value; $T$ is the brightness temperature of a given pixel.

new process is started on the following dataset, and no attempt is made to have time continuity between the clusters of the two datasets.

If only a few images are missing, a recovery process is run to connect the clusters before and after the missing images, and to interpolate their size and location during this gap. This is effected by generating virtual images, and running the tracking process as if there were no missing images. These virtual images are generated by extrapolating the displacement of each MCS present in the last actual image. This approach provides a means to connect the clusters before and after the gap. A connection is rejected if:

$$\mathrm{Min}(Rb, Ra) < d/(N + 1),$$

where $Rb$ and $Ra$ are the radii of the cluster involved before and after the gap, $d$ is the cluster displacement during the gap, and $N$ is the number of missing images. Additionally, the minimum cluster radius is increased from 40 to 100 km if the number of missing images is greater than five. If a cluster confirms these tests, its characteristics during the gap are interpolated linearly.

### (*d*) *Impact of size cut-off on the MCS life cycle*

An extension of tracking at 233 K (213 K) for cluster sizes smaller than 5000 km$^2$ can be carried out by using the information recorded on the ten biggest clusters at 233 K (213 K) embedded in the 253 K (233 K) MCSs. Extending tracking before MCS generation or after MCS dissipation makes it possible to estimate the error in the cluster lifetime related to size cut-off. Cases of clusters that 'regenerate' at small scale can also be depicted. The technique used to track small clusters is similar to that described in section 2(b), except that the criterion is no longer maximum areal overlap but minimum geometric-centre displacement. Additionally, the displacement must be less than 75% of $\{R(t) + R(t+1)\}$ where $R(t)$ is the effective radius of the cluster at time step $t$.

To extend tracking of an MCS at 233 K before its initiation it is assumed that the corresponding MCS at 253 K was the same at previous time steps. If initiation is the result of a split, there is no doubt about the initiation time. If initiation is spontaneous, the cluster that corresponds to the MCS at 233 K is tracked at previous time steps amongst the ten biggest clusters at 233 K embedded in the MCS at 253 K. The same technique is applied to extend the tracking after MCS dissipation.

This objective method makes it possible to extend the life cycle of the MCS to a size of one pixel in most cases. One can calculate that in 75% (90%) of cases at 253 K (233 K), the tenth biggest embedded cluster is smaller than or equal to one pixel during the 3 h preceding initiation or the 3 h following dissipation at the next coldest threshold. The difference between MCS tracking and extended tracking gives an estimation of the maximum error in the initiation (or dissipation) time. This methodology of life extension was applied to the most complete dataset (1998). 8158 (3761) MCSs were tracked at 233 K (213 K). After life extension, 2.4% (4.2%) of the MCSs correspond to regeneration and most of them are short-lived MCSs. The error in the number of systems is less than 1.3% (2.1%).

Figure 3 shows the frequency of error in MCS initiation time. At 233 K the error is very small: 0 h in 73% of cases, $\leqslant$1 h in 92% of cases. At 213 K the frequency of the 0 h error is smaller, however, the total of errors $\leqslant$1 h is almost 85%. Similar results (not shown) are obtained for the dissipation time. With a subjective manual tracking, it is often not possible to connect a cloud cluster of a size as small as one pixel. It should therefore be noted that the error presented in Fig. 3 stands as an overestimation of the actual (subjective) cut-off error.

In conclusion, the size cut-off of 5000 km$^2$ does not significantly affect the total number of tracked MCSs and the time of initiation or dissipation is close to what could be achieved by manual tracking.

### (*e*) *Comparison of tracked cloud coverage with total cloud coverage*

Cloud clusters not included in the results of the tracking algorithm are small and very short-lived, not persisting in two successive images. Figure 4(a) shows the cloud coverage fraction of the total cloud cover (up to the pixel) over the continental Sahel for the 233 K threshold and over eight years (1989–92 and 1995–98), and the cloud cover reconstituted after the tracking process with and without taking into account

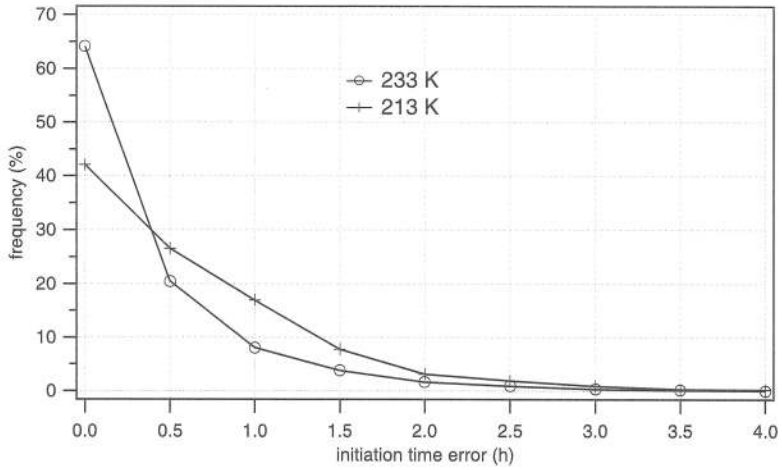


Figure 3. Frequency (%) of the error made in convective system initiation time (h) at thresholds 233 K (line and circles) and 213 K (line and crosses). This error is related to the cluster size cut-off of 5000 km$^2$.

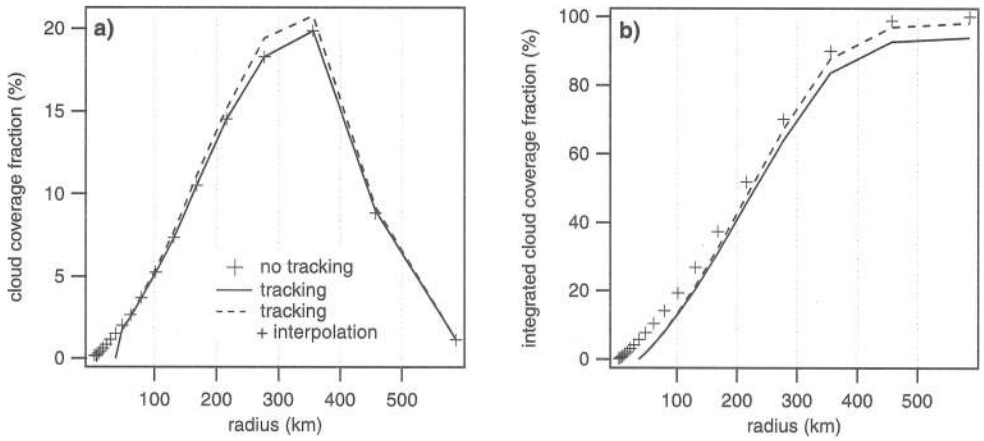


Figure 4. (a) Cloud coverage fraction (%) over the central Sahel versus cloud radius (km), at a threshold of 233 K. The real distribution of the whole convective system population (no tracking, crosses) is compared with tracked mesoscale convective system distributions using the interpolation scheme (dashed line) or not (solid line). (b) Same as (a) but for the integrated cloud coverage fraction (%), calculated using clusters which crossed the central Sahel during summer over eight years.

interpolations. One can see that up to 60 km the distribution of the total cloud cover is equal to the reconstituted coverage when interpolations are not taken into account. Figure 4(b) corresponds to the integration of Fig. 4(a). The contribution to total cloud cover of sub-MCS clouds represents about 7% of total cloud coverage (9% for the 213 K threshold). However, as some of the missing data are interpolated, some additional cloud cover is recovered during the tracking process. This effect, which mainly concerns medium to large clusters (Fig. 4(b)) induces a slight shift in distributions.

The ability of the tracking algorithm to represent actual cloud occurrences has been investigated. Actual cloud occurrences (233 K) are directly computed from IR satellite images and sampled into a $0.2° \times 0.2°$ grid for the period 1 June to 31 August 1998.

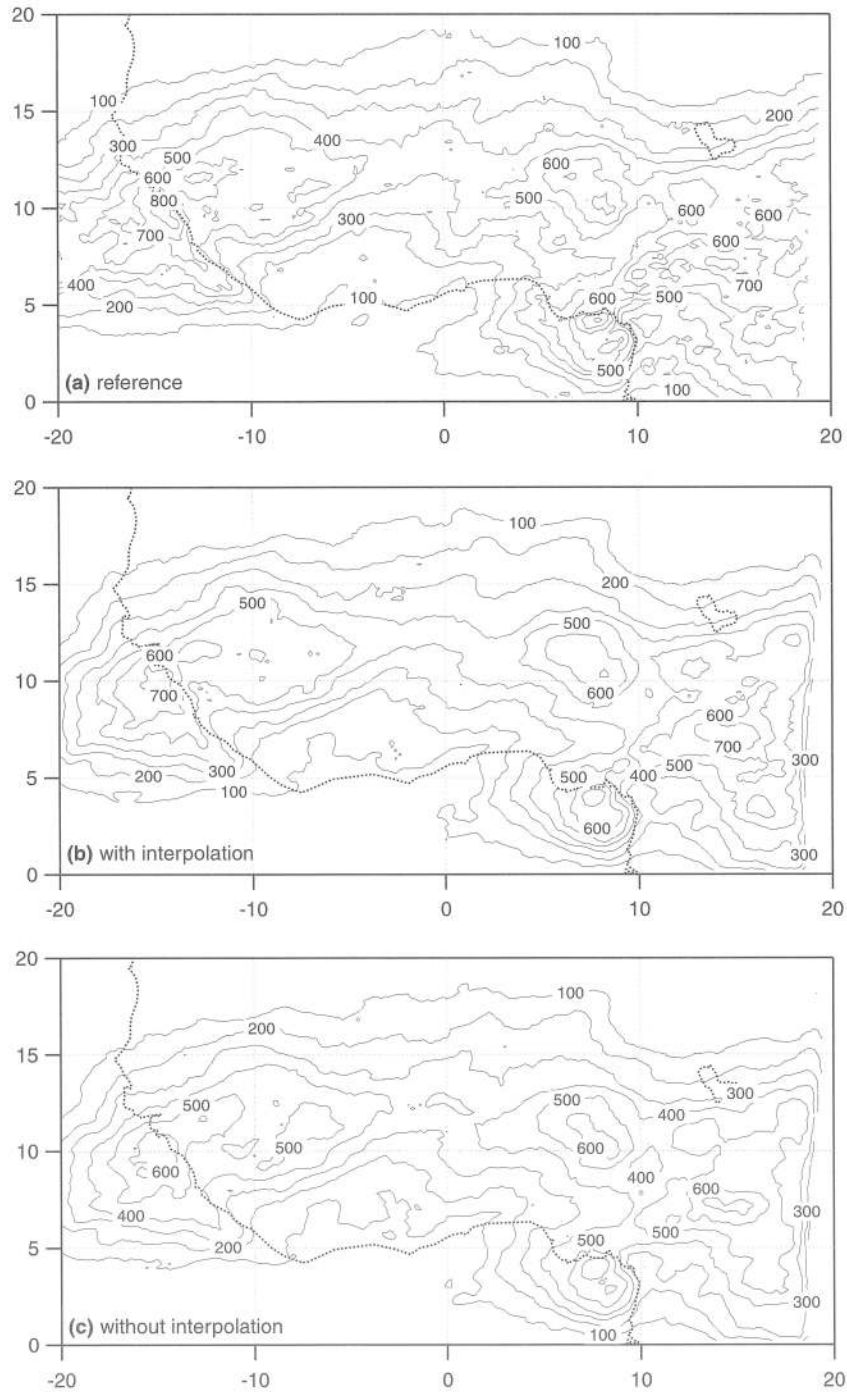


Figure 5. Occurrences of convective cloud from 1 June to 31 August 1998 at a threshold of 233 K. (a) Reference calculated from the images of the entire dataset. (b) Calculated from the tracking outputs obtained with an incomplete dataset (see text) using the interpolation scheme. (c) Same as (b) but without the interpolation scheme.

This period was selected because the dataset was almost complete (only six missing images out of a total of 4416).

MCS occurrences after tracking are computed on the basis of the most unfavourable conditions encountered in the 10-year dataset, i.e. removing five images per day in the 1998 dataset, as described in section 2(c).

MCS occurrences after tracking are reconstituted using ellipsoidal approximations and sampled into a $0.2° \times 0.2°$ grid. As the time resolution is 0.5 h, local MCS cloudiness duration (h) can be derived by dividing MCC occurrences by two. The results are presented in Fig. 5 and show the actual cloud occurrences (Fig. 5(a)) and MCS occurrences calculated after tracking (Fig. 5(b) and (c)). The interpolation scheme (Fig. 5(b)) makes it possible to obtain a spatial distribution of cloud occurrences very close to the actual one. There is a slight smoothing due to the ellipsoidal approximation. Not using the interpolation scheme (Fig. 5(c)) results in significant underestimation of the cloud occurrences related to the missing images. However, simple scaling by proportion of removed images leads to results similar to those obtained in Fig. 5(b) (not shown). Actually, the interpolation scheme is particularly useful for studies of distributions depending on MCS duration. For instance, the error in the number of long-lived MCSs (life $>$ 24 h) drops from 150% or more to less than 10% when using the interpolation scheme (not shown).

When applying cluster tracking to ISCCP B2 data (time resolution 3 h, one pixel every 30 km) the associated minimum trackable cluster radius is about 100 km (Machado *et al.* 1998). It can be seen in Fig. 4(b) that the contribution of tracked convective clouds to total cloud cover drops from 93% to 80% when the minimum radius rises from 40 to 100 km. For the clusters as defined by the first Maddox (1980) criterion (radius larger than 160 km at 233 K) this percentage drops to 65%. The first Maddox criterion at threshold 233 K is obtained using linear interpolation.

## 3. MCS DISTRIBUTIONS

In this section we present MCS distributions over the central Sahel. Figure 6 shows the distributions of MCS characteristics according to their lifetime, with values binned into 2 h classes, for the three temperature thresholds. For example, the first class (2 h) contains clusters with a duration of 1, 1.5, 2 and 2.5 h. The longest lifetimes recorded were 133 h, 88.5 h and 50.5 h at the 253 K, 233 K and 213 K thresholds, respectively. The total number of clusters by class of lifetime (Fig. 6(a)) displays a similar decrease for the three populations. With the exception of the very long lifetime, the plot is roughly linear, which means that the relationship follows a power law: $N(life) \approx life^{-\alpha}$, where $\alpha$ is between 1.6 and 1.8.

The number of clusters is not relevant to what can be observed in a given image: long-lived clouds are observed over more images then short-lived ones but are less numerous. The cluster frequency (Fig. 6(b)) is computed by multiplying the number of clusters per given lifetime by the lifetime itself, and dividing by the total number of images. This is proportional to the probability of observing a cloud with a duration belonging to a given lifetime class. Again, this plot is dominated by short-lived MCSs. The duration of long-lived MCSs does not compensate their very low number.

Figure 6(c) shows that the mean MCS radius increases with the lifetime. Machado *et al.* (1998) found a roughly linear relationship in the 6–27 h range, with a slope of about 6 km $h^{-1}$ at threshold 245 K for MCSs over the Americas. Within the same range of lifetimes we have found a roughly linear relationship with a slope of about 6.5 km $h^{-1}$ (5 and 4.2 km $h^{-1}$) at threshold 253 K (233 K and 213 K), consistent with the finding of

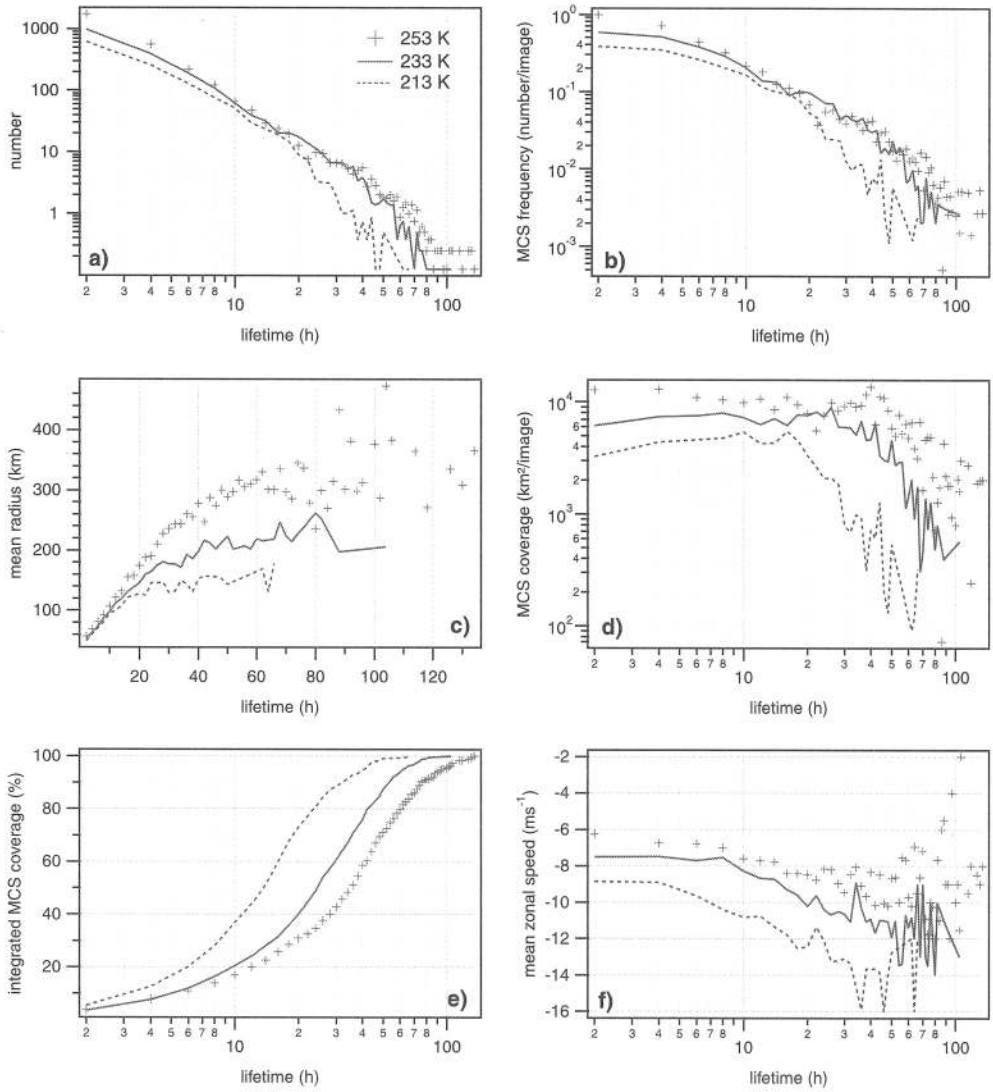


Figure 6. Mean annual distributions versus lifetime (h) at thresholds 253 K (crosses), 233 K (solid line) and 213 K (dashed line). (a) Number of mesoscale convective systems (MCSs). (b) MCS frequency (number per image). (c) Mean MCS radius (km) calculated by averaging the effective radius over the whole life cycle. (d) MCS coverage ($km^2$ per image). (e) Integrated MCS coverage fraction (%). (f) Mean MCS zonal speed ($m\ s^{-1}$). Results were obtained using clusters which crossed the central Sahel during summer over eight years.

Machado *et al.* (1998). However, they found that the relation between size and lifetime was not sensitive to the temperature threshold used. This difference may result from a better accuracy in determining the duration of MCSs with full resolution. Sahelian MCSs may also have different characteristics compared to those over the Americas where both continental and oceanic MCSs are studied.

The cloud cover (Fig. 6(d)) gives the surface area of each MCS class, expressed in $km^2$ per image. This distribution is no longer driven by short-lived clusters. The contribution from each class is roughly constant for shorter lifetimes, up to at least 24 h (16 h for the coldest threshold). The cumulative cloud cover (Fig. 6(e)), deduced from

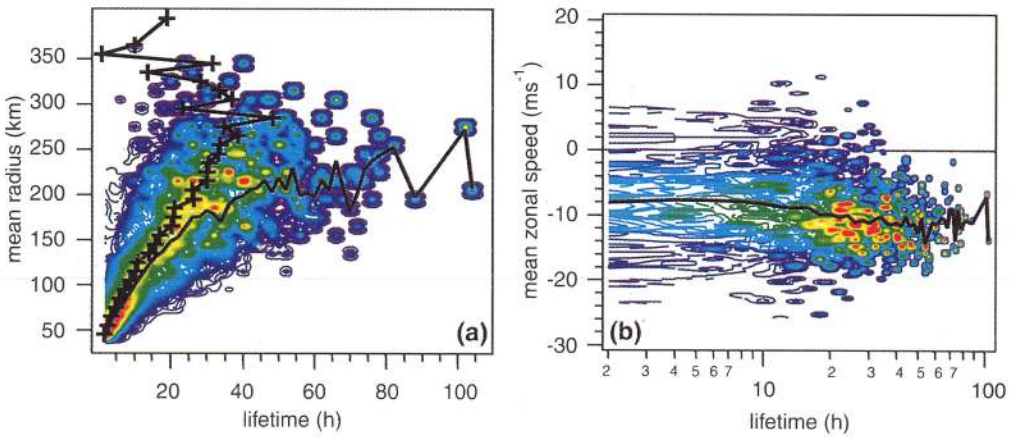


Figure 7. (a) Averaged mean mesoscale convective system (MCS) radius (km) versus lifetime (h; solid line) and averaged lifetime (h) versus mean MCS radius (km; line and + symbols) at threshold 233 K. The corresponding scatter plot is illustrated by contours. The colour wavelength is proportional to the cloud coverage contribution of each class. (b) Averaged mean MCS zonal speed (m $s^{-1}$) versus lifetime (h; solid line). The corresponding scatter plot is illustrated by contours. The colour wavelength is proportional to the cloud coverage contribution of each class. Results were obtained using clusters which crossed the central Sahel during summer over eight years.

the integration and the normalization of Fig. 6(d), shows that for threshold 253 K (233 K and 213 K), half the total MCS coverage is due to MCSs lasting longer than 35 h (24 h and 14 h). This result demonstrates the importance of very long-lived MCSs, whose very small number (Fig. 6(a) and (b)) is compensated for by their duration and their mean size (Fig. 6(c)).

Convective cloud clusters propagate westward over the Sahel, as shown by the plot of the mean zonal speed (Fig. 6(f)). The mean zonal speed is defined as the mean zonal displacement between the beginning and end of the MCS life cycle. The velocity is generally larger for long-lived than for short-lived clusters, and for the coldest threshold. For very long-lived clusters the speed is around 14 m $s^{-1}$ for the 213 K threshold, 12 m $s^{-1}$ for the 233 K threshold and 10 m $s^{-1}$ for the 253 K threshold. As clusters at a given threshold include all those at a colder threshold, this result shows that the convective cloud clusters with a large active area of convection propagate faster than those with little or no active area of convection. Another interpretation is that squall lines seen in the cold threshold propagate west, leaving behind them a region of slower stratiform cloud which is included in the warmer threshold MCSs. All in all, MCSs are likely to propagate faster during their mature stage when convection is deeper.

As already shown in Fig. 6(c), there is a close relationship between the mean lifetime and the mean radius of MCSs. The significance of this relationship is questionable because the values are widely scattered. Figure 7 displays the scatter plot of the mean MCS radius (Fig. 7(a)) and mean zonal speed (Fig. 7(b)) versus their lifetime, for the 233 K threshold. In these plots, each radius/lifetime class is represented by a marker whose colour wavelength is proportional to the cloud coverage of the MCSs in this class (arbitrary scale). The superimposed curves give the average radius (or zonal speed) in the lifetime class, and the average lifetime in the radius class. This representation shows qualitatively that, with the exception of extreme values, the mean relationship as plotted in Fig. 6 is reasonably representative of the behaviour of the MCSs that contribute most to cloud coverage.

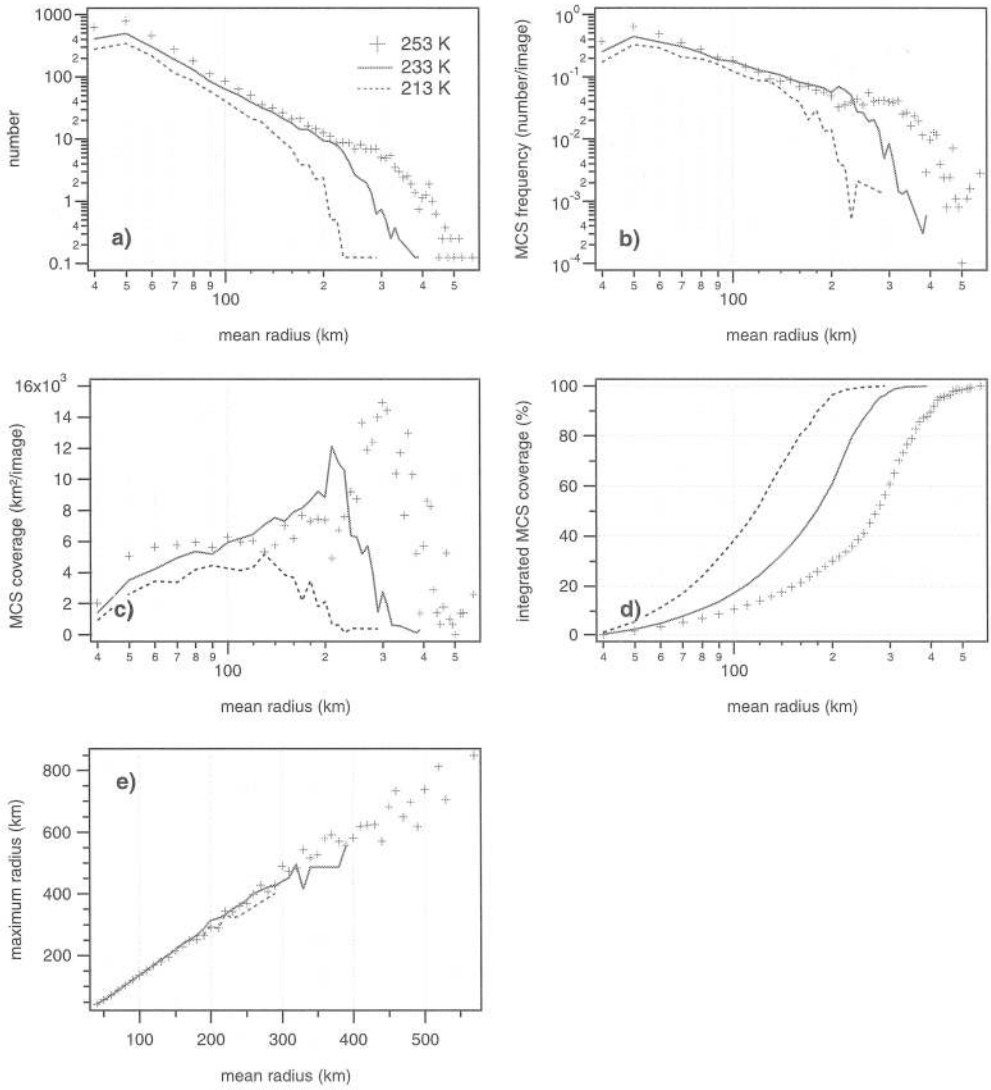


Figure 8. Mean annual distributions versus mean effective radius (km) at thresholds 253 K (+ symbols), 233 K (solid line) and 213 K (dashed line). (a) Number of mesoscale convective systems (MCSs). (b) MCS frequency per image. (c) MCS coverage (km$^2$ per image). (d) Accumulated MCS coverage fraction (%). (e) Maximum effective radius (km). Results were obtained using clusters which crossed the central Sahel during summer over eight years.

Figure 8 shows MCS characteristics according to their mean radius, binned into 10 km classes. The number of MCSs in the first class (40 km, i.e. radius between 35 km and 45 km) is diminished by the sub-MCS cut-off.

The number of MCSs (Fig. 8(a)) exhibits a regular decrease, almost linear for $R > 50$ km and $R < Rc$, where $Rc$ is a critical radius of 300 km (210 and 140 km) for the 253 K threshold (233 and 213 K). This can be expressed as a power law according to the radius: $n(R) \approx R^{-\alpha}$. A fitting on the linear part of the graphs gives a value of $\alpha = 2.9 \pm 0.2$.

The cluster frequency $n(R)life/N$, where $N$ is the number of images, is plotted in Fig. 8(b). It gives the probability of observing a cloud with a mean radius within a given

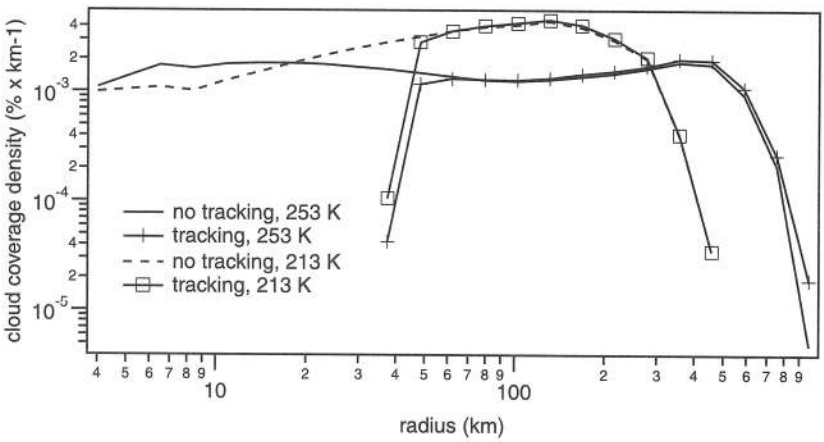


Figure 9. Cloud coverage density (% $km^{-1}$) versus instantaneous effective radius (km) at thresholds 253 K and 213 K. Real distributions (all clouds, no tracking) are compared with tracked mesoscale convective system distributions using the interpolation scheme (tracking). Calculations are based on clusters which crossed the central Sahel during summer over eight years.

radius class. For the same range of radii as in Fig. 8(a), the distribution in Fig. 8(b) can also be approximated in a power law: $n(R)life/N \approx R^{-\alpha}$, with $\alpha = 1.6 \pm 0.2$. Cloud cover increases according to the mean cluster size (Fig. 8(c)), up to the critical radii already mentioned. This result shows that the small number of large clusters is more than compensated for, in terms of cloud coverage, by their size and lifetime.

Cumulative cloud cover (Fig. 8(d)) shows that consideration of cloud clusters with a mean size larger than 100 km will explain between 60% and 90% of the total cloud cover, depending on the relevant threshold.

The result presented here according to the MCS mean radius would have been very similar if presented according to their maximum radius. There is a very strong relationship between the mean MCS radius and its radius at the time of maximal extent, as shown in Fig. 8(e). The maximum radius $Rmax$ can be expressed as: $Rmax = 1.5R$, where $R$ is the mean MCS radius during its lifetime. One may notice that this relationship is verified by a cluster with a linear radius increase, from the beginning to the maximum extent, followed by a linear decrease up to the end.

The behaviour of cluster coverage shown in Fig. 8(c) is consistent with results obtained by Machado *et al.* (1992, 1993). Note that over continental West Africa cloud cover is mostly driven by large clusters whereas the reverse is true over the ocean. Note also that there is a change in the slope between warm and cold thresholds. Machado *et al.* (1992, 1993) did not track cloud clusters, and therefore calculated cluster density according to the instantaneous cluster radius rather than the radius averaged over the life cycle. Applying the same method we have computed the cluster fraction density $S(\Delta R)$ as defined by Machado *et al.* (1992). $S(\Delta R)$ is the cluster coverage density expressed as a fraction of the total cloud cover at the relevant threshold, and computed over radius intervals varying logarithmically with the radius, in order to obtain a similar number of clusters in each interval. Figure 9 shows $S(\Delta R)$ computed for full-resolution images over the eight years as well as for the clusters reconstituted after tracking. It can be compared to Fig. 8 of Machado *et al.* (1992) obtained from low-resolution images. Two main results can be derived: firstly, the results obtained with the mean radius are close

to those obtained with the instantaneous radius; secondly, it is noticeable that our results at full resolution confirm and extend the results obtained at low resolution.

## 4. Diurnal cycle

### (*a*) *Overall MCS diurnal cycle*

The diurnal cycle of the relative cloud cover (up to the pixel size) over the central Sahel zone is shown in Fig. 10(a). As expected (see, e.g. Desbois *et al.* 1988; Duvel 1989), convective activity in the central Sahel is maximum in the early evening and minimum at noon. The amplitude of the diurnal cycle is larger for the coldest temperature thresholds according to the results of Duvel (1989) and Machado *et al.* (1993). There is a relative minimum around 2400 LST explained by the missing images associated with the eclipse phenomenon.

The total cloud cover is plotted in Fig. 10(b), as well as the cloud cover of the MCSs, i.e. the tracked cloud clusters. 'After tracking' curves correspond closely to 'before tracking' curves, except around 2400 LST. This is a result of interpolation of missing data. This result shows that the tracking procedure (filtering of sub-MCS, interpolation of missing data) does not induce any systematic bias in the diurnal cycle of cloud coverage, but has a smoothing effect where data are missing. Further analysis will only describe the tracked cloud clusters (MCS) characteristics.

Behaviours of the MCS diurnal cycle for the 233 K threshold are displayed in Figs. 11 and 12. As these behaviours are very similar for the other two thresholds, only the differences will be mentioned. Figure 11(a) shows the number of MCS appearances and disappearances. Spontaneous generations are more modulated by the diurnal cycle than are split-generations. The extent of split-generated MCSs is similar to that of spontaneous-generated MCSs during the period of weak convective activity, but becomes more negligible during high convective activity. The number of split-generated MCSs is proportionally smaller (larger) for the 213 K threshold (253 K), with weak diurnal amplitude. The diurnal cycle of MCS generations is similar for the three thresholds, with a high maximum between 1600 and 1700 LST.

In Fig. 11(a), the number of dissipations and the number of mergers are also plotted. Dissipations are more modulated by the diurnal cycle than are the mergers. The extent of dissipations is greater than merger disappearances, however, mergers significantly increase the number of MCS ends during the afternoon, just after the generation maximum. The same behaviour is observed for the other two thresholds with maximum dissipation around 2100 LST and maximum merging around 1800 LST.

Figure 11(b) displays total MCS numbers and coverage for the 233 K threshold. The number of MCSs decreases after 1900 LST when there are less initiations than dissipations. There is a lag of about 1 h between the maximum number (1900 LST) and the maximum coverage (2000 LST). The rate of decrease is lower for coverage than number, because the mean MCS size is larger at night than during the day. Number variations are very similar for the 213 K and 253 K thresholds. For the 213 K threshold, corresponding to very active convection, coverage variation is almost in phase with number variation, with a minimum at 1100 LST and a maximum at 1900 LST. For the 253 K threshold, corresponding to the whole cluster anvil, coverage reaches its minimum at 1400 LST and its maximum at between 2000 LST and 2400 LST. These features are consistent with a vertical, explosive development of convection at the beginning of the cloud cluster life cycle and with horizontal expansion later.

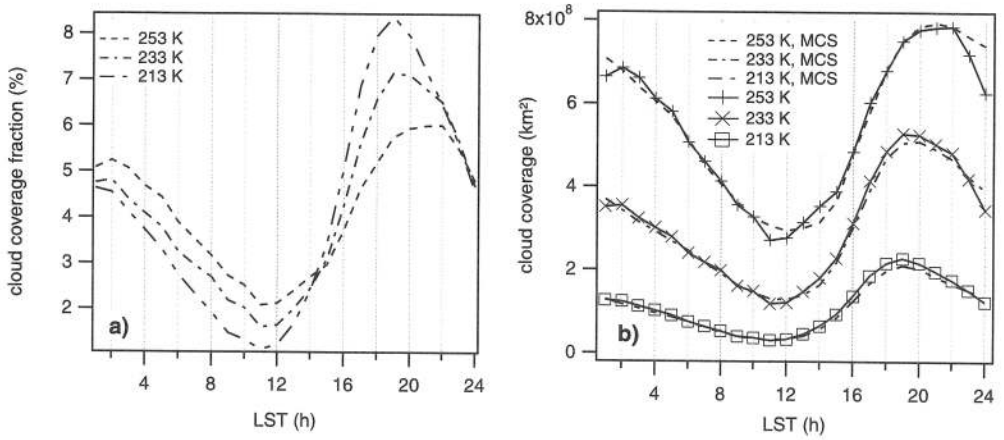


Figure 10. (a) Fraction of mesoscale convective system (MCS) cloud coverage at a given threshold (%) according to local time (h), for thresholds 253 K, 233 K and 213 K. (b) Total cloud coverage ($km^2$) according to local time (h), for thresholds 253 K, 233 K and 213 K. Real distributions are compared with the MCS distributions obtained after tracking with the interpolation scheme. Results were obtained using clusters which crossed the central Sahel during summer over eight years.

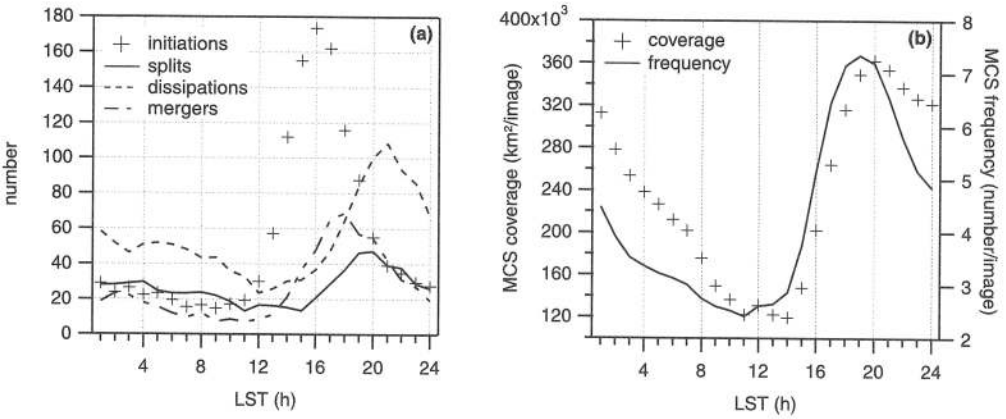


Figure 11. (a) Mean annual number of initiations (crosses), splits (solid line), dissipations (dashed line) and mergers (dot-dashed) according to local time (h), at threshold 233 K. (b) Mesoscale convective system (MCS) cloud frequency ($km^2$ per image; solid line) and MCS coverage (number per image; plus signs) according to local time (h), at threshold 233 K. Results were obtained using clusters which crossed the central Sahel during summer over eight years.

### (*b*) *Splits and mergers*

In Fig. 11(a) we distinguish split-generation from spontaneous generation and merger-end from dissipation. However, the significance of these splits and mergers is questionable because they are highly dependent on the temperature threshold. Split-generation may be associated with weakening of convection or with actual division of a cluster into two (or more) convective entities. Similarly, a merger-end may be the result of convection strengthening or actual merging of two different entities. To study these different cases, mergers and splits are further analysed by considering what is going on at a warmer temperature threshold. The methodology is as follows.

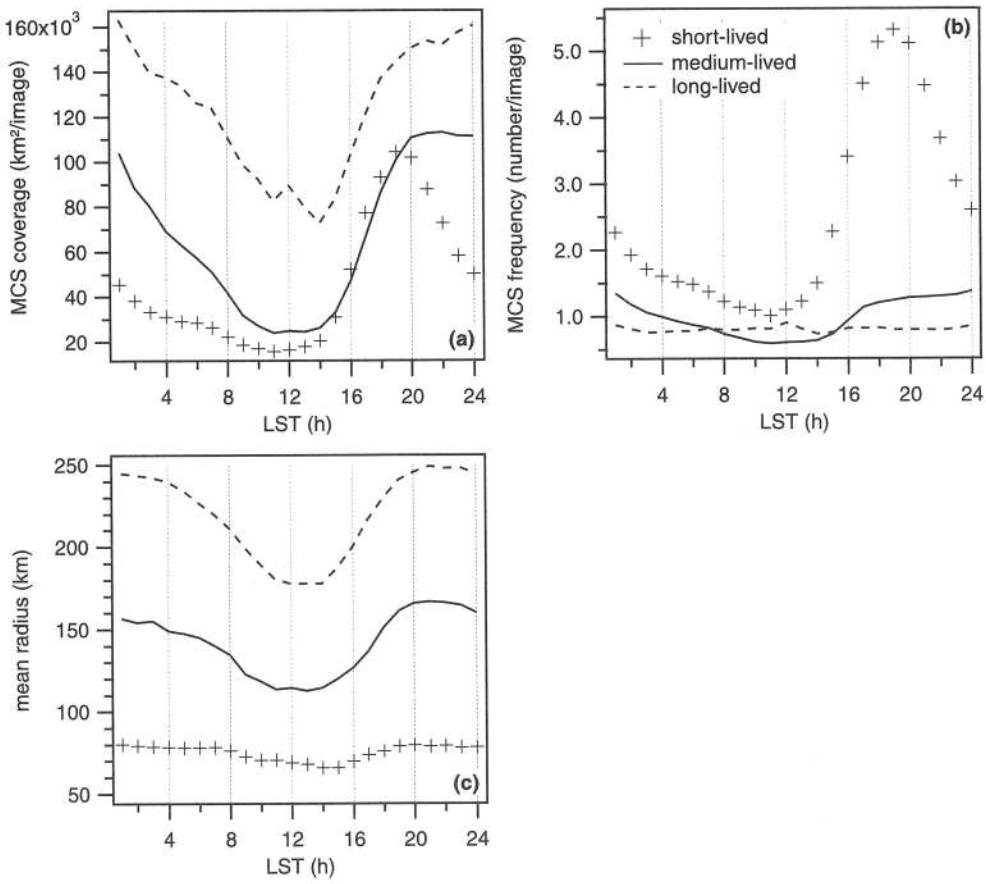


Figure 12. (a) Diurnal variations of mesoscale convective system (MCS) coverage (km$^2$ per image) for short-lived (duration $\leqslant$10 h; crosses), medium-lived (10 h < duration $\leqslant$ 24 h; solid line) and long-lived (duration > 24 h; dashed line) MCSs, at threshold 233 K. (b) Same as (a) but for MCS frequency (number per image). (c) Same as (a) but for the mean MCS radius (km). Results were obtained using clusters which crossed the central Sahel during summer over eight years.

• Hypothesis: the limit of convection corresponds to the 253 K threshold, therefore splits and mergers are actual at this threshold.

• Splits at 233 K or 213 K: suppose MCS1 is a cluster which splits into MCS1 and MCS2 at time $t0$. The earliest of the disappearances of MCS1 and MCS2 occurs at $t1$. If, between $t0$ and $t1$, the corresponding MCS at 253 K remains the same for MCS1 and MCS2, then we consider the split is due to weakening of convection. Otherwise, it is an actual split of different convective entities. Therefore we take into account the fact that MCS splits can occur at multiple levels but not simultaneously.

• Mergers at 233 K or 213 K: these are treated the same as splits at 233 K or 213 K.

In other words, convective entities are defined here by their anvils at 253 K. Splits or mergers of MCSs at a colder threshold are considered as actual only if they belong to different convective entities.

Table 2 shows the number of splits and mergers for different thresholds taking into account this classification. The number of splits or mergers due to variations in convective intensity (artificial mergers or splits) is much greater than actual splits or

TABLE 2. DIVISION (%) OF CLUSTER (a) MERGERS AND (b) SPLITS INTO ARTIFICIAL AND ACTUAL CLASSES

| | | 233 K | 213 K |
|---|---|---|---|
| (a) mergers | artificial | 49 | 79 |
| | actual | 51 | 21 |
| (b) splits | artificial | 79 | 93 |
| | actual | 21 | 7 |

Artificial mergers: the variation of convective activity within a single convective entity. Actual mergers: the actual merging of different convective entities. Results obtained using clusters which crossed the Sahel during summer over eight years.

mergers for the two thresholds. The proportion of actual mergers is much greater than the proportion of actual splits for the two thresholds. An interesting result is that at the coldest threshold, representative of very active convection, 21% of all mergers are due to actual mergers of convective entities defined at 253 K. This is not true for the splitting process, where only 7% of very active convective clusters can split into different entities. The same behaviour can be observed for the 233 K threshold, showing that splits are mostly associated with weakening of convection and that convective organization is not a negligible process. The diurnal cycle of the actual mergers is much more pronounced than that of artificial mergers (not shown), with a maximum around 1700–1800 LST. The maximum of actual splits (not shown) occurs around 1800–2000 LST, whereas the maximum of artificial splits occurs slightly later, around 1900–2100 LST.

### (*c*) *MCS diurnal cycle and lifetime*

Three classes of MCS lifetimes are defined: short-lived (duration $< 10$ h), medium-lived ($10$ h $\leqslant$ duration $\leqslant 24$ h) and long-lived (duration $> 24$ h). The diurnal cycle of MCS cover, number and radius has been computed for the three classes of lifetime. Figure 12(a) shows that the diurnal cycle of the cloud coverage is comparable for all three classes, with the exception of maximum coverage time. Due to number distribution and the interdependence of size and duration, short-lived MCSs are much more numerous (Fig. 12(b)) and have a smaller size (Fig. 12(c)) than long-lived MCSs. The diurnal cycle of short-lived MCS number is very close to that of the total MCS number (Fig. 11(b)), with a wide amplitude, whereas their mean size is small and varies little during the day. For long-lived MCSs, the number is smaller in comparison, whereas the size has a pronounced diurnal cycle which explains coverage variations. For medium-lived MCSs, variations in cloud coverage are explained by variations in both number and size. The number of splits and mergers of medium- and long-lived MCSs is small (typically 5% of the total) and does not show any significant diurnal cycle (not shown). The number of spontaneous generations of long-lived MCSs has a well-marked peak around 1400 LST, whereas the short-lived MCS generation peak is around 1600 or 1700 LST (not shown). This result shows that the probability of a developing convective cloud evolving into a long-lived cluster is less in the case of late generation. The general diurnal cycle of the convective systems can be summarized as follows: the maximum generation at 1600 LST produces a maximum of systems at 1900 LST; the clusters aggregate (maximum of actual mergers at 1700–1800 LST), leading to a reduced number and a larger mean size; irrespective of actual mergers, the development of convection also leads to a reduced number (artificial mergers) and a larger mean

size; the maximum of convective cloud cover occurs at 2000 LST; at midnight, the small clusters have vanished, either by dissipation or by merging into larger clusters, and cloud cover is due to the large and long-lived clusters.

## 5. Spatial variability

In this section we present spatial distributions of some MCS characteristics over West Africa, averaged over the same time period as in the previous sections (21 June to 14 September for the years 1989–92 and 1995–98).

As already mentioned, convective cloud occurrences are worth studying as they are, to a first approximation, statistically linked to accumulated rainfall; this is the basis of most satellite rainfall estimation methods using the IR channel, such as the GOES Precipitation Index (Arkin 1979). Figure 13 shows for the three thresholds the mean annual MCS occurrences sampled into a $0.2° \times 0.2°$ grid. Actually, each MCS area is reconstituted from its ellipsoidal shape and, as already discussed in section 2(e), these maps are representative of actual cloud occurrences.

The maximum of very intense convective clouds (threshold 213 K) of the intertropical convergence zone is almost zonally distributed over the central Sahel at 12.5°N. At warmer temperature thresholds, the maximum of convective cloud is located further south; it is at about 10.5°N for the 253 K threshold.

Figures 14(a) and 14(b) show the mean annual number of initiations for long-lived MCSs (duration 24 h) and for short- and medium-lived MCSs (duration <24 h) for the 233 K threshold. Actually, for each spontaneous generation (split-generated MCSs have not been taken into account here), an area of 5000 $km^2$ (i.e. 9 grid points) centred on the MCS's location has been considered. Therefore the maps of Fig. 14 give MCS occurrences at the time of generation. Long-lived MCS initiations (Fig. 14(a)) are rare and proportionally greater to the north of 9°N. There is a noticeable generation maximum over the Jos plateau (9°N, 8°E) and another over the Guinea coast. On the right-hand side of the map one can observe an anomaly corresponding to the edge of the images used for most of the years. Figure 14(b) is very close to the total number of initiations, since short- and medium-lived MCSs account for most of the total number. It can be seen in Fig. 14(b) that MCSs tend to be orographically triggered (see Fig. 1), as already noted for instance by Rowell and Milford (1993) and Hodges and Thorncroft (1997). Over the central Sahel 55% of initiations occur above 400 m, corresponding to 20% of the area. Note that 45% of initiations occur below 400 m, which means that large-scale orography is not the only trigger of convection. There is again a generation maximum over the Jos plateau and some weaker maxima over other highlands: Cameroon mountains (7°N, 12°E), Fouta Djalon (10°N, 10°W), Air mountains (18°N, 8°E), Atakora mounts (9°N, 1°E). There are also high maxima of initiation around the Guinea and Nigerian coasts. These regions are both characterized by a maximum of low-level humidity convergence and a relatively high sea surface temperature.

Figure 15 shows cluster dissipations (merger-ended MCSs not being taken into account), computed as in Fig. 14. Again, total dissipations are driven by short-lived clusters. Maxima are in regions of high total-cloud coverage (see Fig. 13). They are in the same locations as generation maxima, or westward-shifted as in the example of the Jos plateau maximum. For long-lived MCSs (Fig. 15(a)), dissipation maxima are not very well marked. One can note that many long-lived MCSs dissipate over the ocean, west of the Guinea coast. Although there are no clearly preferential regions of dissipation from a latitudinal point of view over the continental Sahel, one can observe

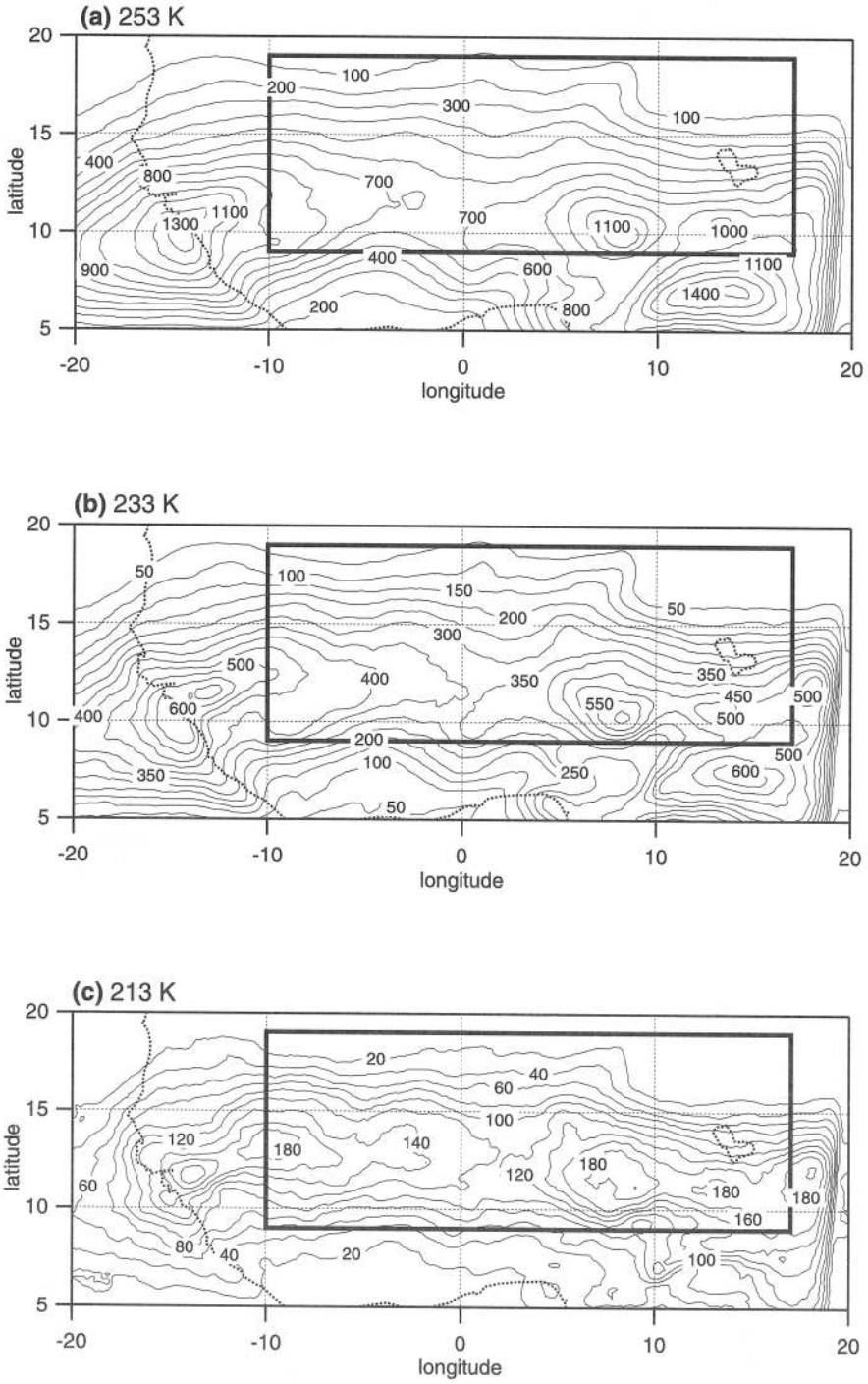


Figure 13. (a) Mean annual mesoscale convective system occurrences at threshold 253 K. (b) Same as (a) but for the 233 K threshold. (c) Same as (a) but for the 213 K threshold. Results obtained during summer over eight years. The central Sahel area is shown by the boxes.

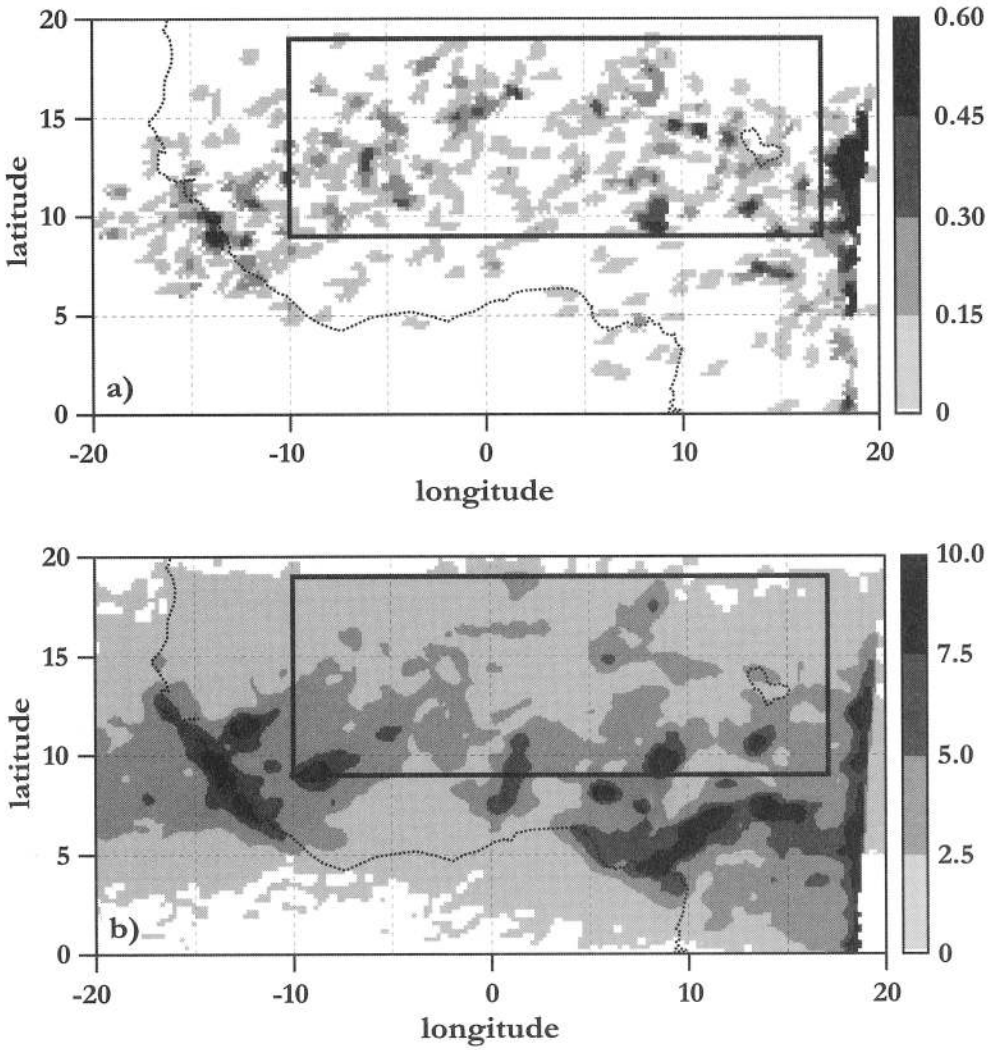


Figure 14. (a) Long-lived annual mesoscale convective system (MCS) occurrences at initiation time, at threshold 233 K. Only spontaneous initiations of MCSs with a lifetime of more than 24 h are considered. (b) Same as (a) but for the MCSs with a lifetime of less than 24 h. Results were obtained using clusters which crossed the central Sahel during summer over eight years. The central Sahel is shown by boxes.

that dissipations are more concentrated to the south of 15°N. Actually we have observed many long-lived MCSs with south-westward trajectories. Desbois *et al.* (1988) and d'Amato and Lebel (1998) observed similar behaviour. Such trajectories can explain the southward shift between long-lived MCS initiations and dissipations.

Figure 16(a) displays the contribution of long-lived MCSs (duration $\geqslant$24 h) to the total MCS occurrences (Fig. 13) for the 233 K threshold. Over the continental Sahel, about 50% of all MCS occurrences are related to long-lived MCSs, and the largest contributions are concentrated to the south of 15°N. Moreover, long-lived MCSs defined at 233 K account for 60% of the Sahelian deep convective coverage (213 K, not shown). Another way to demonstrate the importance of long-lived clusters with regard to total cloud cover is to compute the mean lifetime of the convective pixels. The methodology

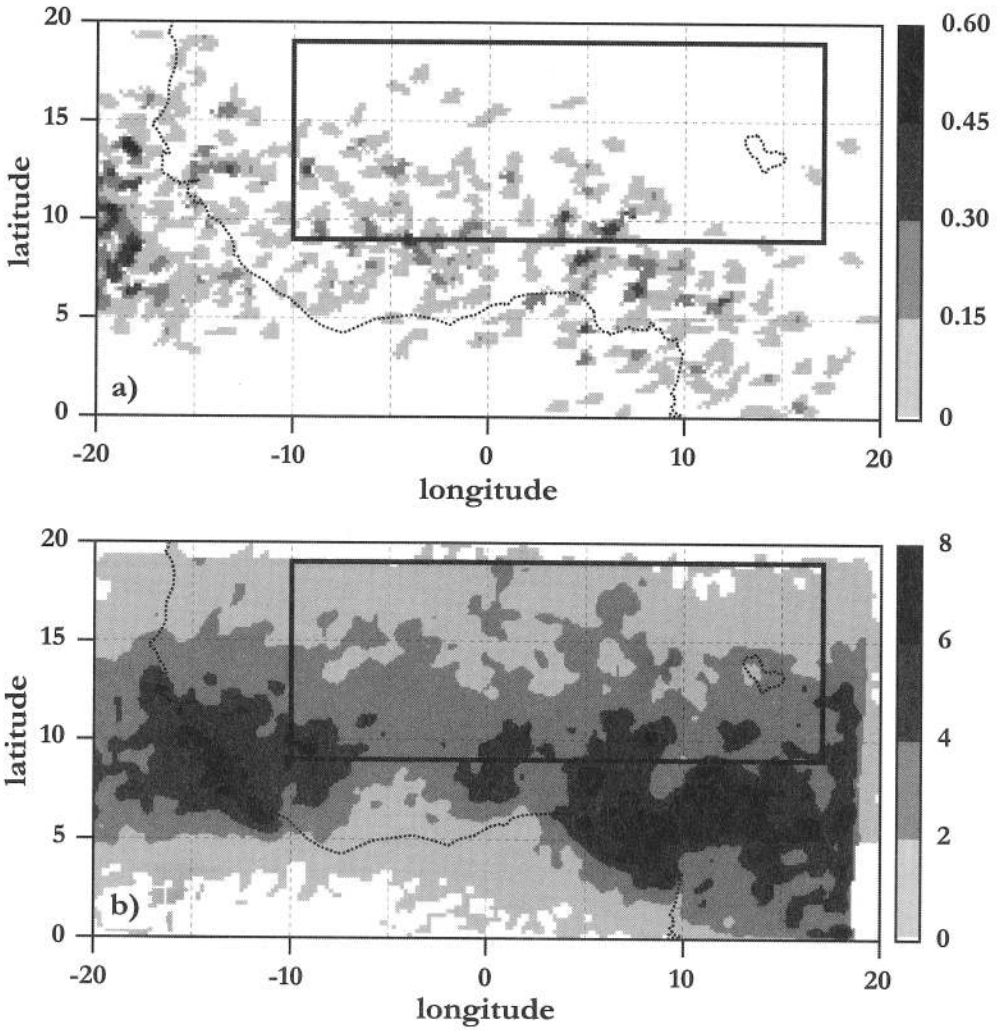


Figure 15. As Fig. (14) but at dissipation time.

is the same as for calculation of mean annual MCS occurrences (Fig. 13), however, each cloudy grid cell is given the value of the lifetime of the corresponding MCS, rather than unity. The results in Fig. 16(b) show long mean lifetimes, up to 30 h over the continental Sahel. This result is quite different from the direct average of the MCS lifetime (figure not shown). The latter reflects the behaviour of very short-lived clusters which are most numerous, and is therefore closely related to the time resolution of the dataset used.

Figure 16(c) shows the mean zonal speed modulus. It is calculated here as the mean westward displacement between the beginning and the end of the cluster, because half-hourly speed is too dependent on cluster shape change, particularly in the case of merging or splitting. The result displayed has been computed with the same methodology as for mean duration, for the purpose of representing the mean speed of the convective pixels. The MCS speed is a maximum over the central Sahel.

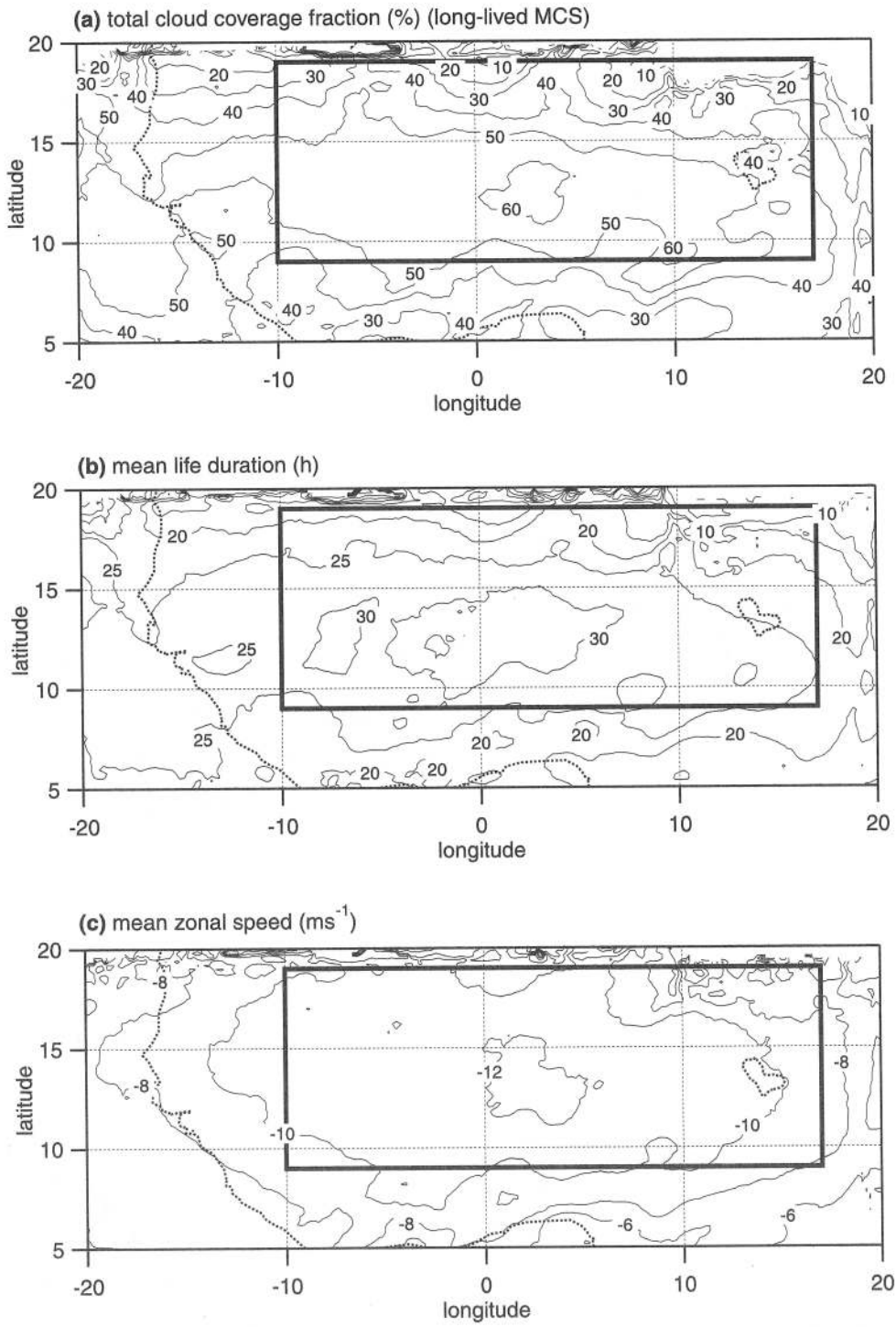


Figure 16. (a) Fraction (%) of total mesoscale convective system (MCS) occurrences corresponding to those with a lifetime greater than 24 h. (b) Mean MCS lifetime (h). (c) Mean MCS zonal speed (m $s^{-1}$). Results were obtained using clusters which crossed the central Sahel during summer over eight years for the threshold 233 K. The central Sahel is shown by boxes.

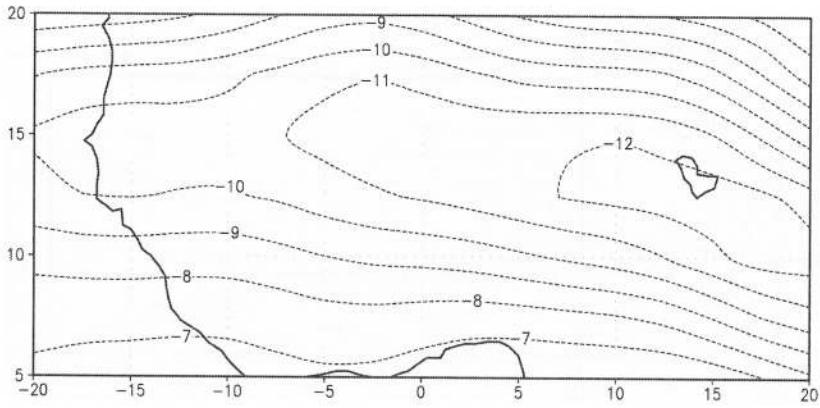


Figure 17. Mean zonal wind (m $s^{-1}$) over West Africa at 600 hPa computed from the National Centers for Environmental Prediction re-analysis over the period 21 June to 14 September over eight years (1989–92 and 1995–98).

The mean zonal speed of squall lines over the Sahel obtained by Desbois *et al.* (1988) was between 12 and 19 m $s^{-1}$. The mean speed presented in Fig. 16(c) is smaller, which is not surprising as the squall lines are known to be the fastest among the MCSs. Desbois *et al.* (1988) also computed the speed as the mean of three-hourly displacements, which can lead to slightly greater values than those shown in Figure 16(c). Figure 17 shows the mean zonal wind speed at the 600 hPa level where the African easterly jet (AEJ) is a maximum, computed from the National Centers for Environmental Prediction (NCEP) re-analysis over the corresponding time period. It can be seen that the magnitude of the AEJ is similar to the MCS speed. Note that the MCS mean speed is lower than the AEJ over the eastern Sahel, where the AEJ is a maximum.

Results shown in Fig. 16(b) and (c) at threshold 233 K were computed at threshold 213 K (not shown). The mean duration is a maximum (8 h) over the central Sahel between 12 and 16°N. Within the 12–16°N belt, the mean speed is larger by about 2 m $s^{-1}$ than that at threshold 233 K. Consequently, over the central Sahel the mean speed at threshold 213 K is very similar to the mean AEJ magnitude, where the AEJ is a maximum and slightly greater to the west of 5°E.

The importance of the MCCs as defined by Maddox (1980) has been evaluated. The Maddox definition of a MCC (see section 2(a)) was adapted to our temperature thresholds: MCCs are defined here as MCSs satisfying the following conditions:

(i) area $\geqslant$80 000 $km^2$ at the 233 K threshold; and

(ii) interior cold cloud region at the 213 K threshold must have an area $\geqslant$30 000 $km^2$; and

(iii) conditions (i) and (ii) must be satisfied simultaneously for at least six consecutive hours; and

(iv) eccentricity (minor axis/major axis) must be $\geqslant$0.7 at the time of maximum extent.

This selection gives a total of 255 MCCs for the eight years. Figure 18(a) shows that MCC occurrences tend to be located between 10 and 15°N, where they account for roughly 15% of the MCS coverage (Fig. 18(b)). Figure 18(c) shows the spatial distribution of mean MCC zonal speed. One may notice that MCCs move faster to the west of 5°E than to the east of 5°E and over the ocean. Compared to the spatial

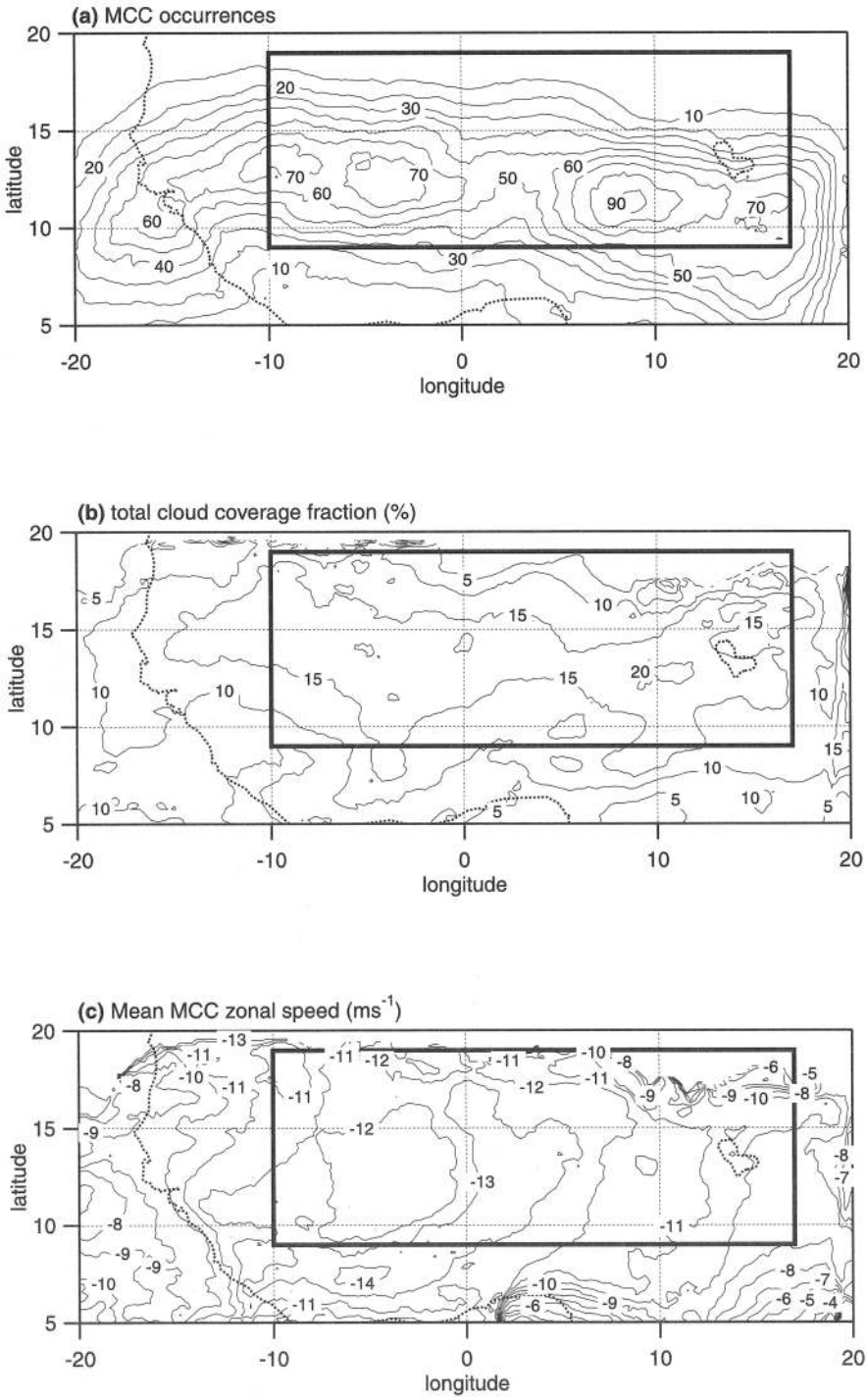


Figure 18. (a) Mean annual mesoscale convective complex (MCC) occurrences. (b) Fraction (%) of total mesoscale convective system occurrences explained by MCCs. (c) Mean MCC zonal speed (m $s^{-1}$). Results were obtained using clusters which crossed the central Sahel during summer over eight years for threshold 233 K. The central Sahel is shown by boxes.

distribution of the mean MCS zonal speed (Fig. 16(c)), the MCC mean speed is greater by about 1 m $s^{-1}$, which is consistent with the fact that the speed of long-lived MCSs is greater than average. Note that mean MCC zonal speed is slightly greater than the AEJ to the west of 5°E and slightly less to the east.

A comparison between long-lived MCS occurrences (Fig. 16(a)) and MCC occurrences, shows that the MCC classification does not represent all organized MCSs over the Sahel. Long-lived MCSs (*life* > 24 h) account for 50% of the total MCS cloud coverage at threshold 233 K, whereas MCCs account for less than 15%.

## 6. Summary

An automated method for tracking mesoscale convective systems is an important tool for characterizing the behaviour of convection using comprehensive satellite observations. A tracking algorithm has been presented, demonstrating that it is possible to track MCSs with an overlap method through almost their entire life cycle. For example, 93% of the total cloud coverage at threshold 233 K can be tracked from full-resolution images. Despite an MCS cut-off of 5000 $km^2$ and with a long time resolution, it is possible to evaluate most MCS lifetimes with an error margin of less than 2 h (this error is obtained by extending the tracking to a few pixels). Such precision gives good determination (<1 h) of MCS initiation and dissipation times. Cases of regeneration related to size cut-off are rare. As an MCS life cycle is interpolated when data are missing, the number of systems tracked can be determined with high accuracy. This point is important for future studies on interannual variability in convective activity. By combining the three thresholds, and assuming that threshold 253 K corresponds to the limit of convection (Duvel 1989; Mapes and Houze 1993), one can provide an interpretation of observed splits and mergers. It has been shown that the merging of different active convective entities is not a negligible process.

An eight-year high-resolution climatology of Sahelian MCSs has been derived using this tracking methodology. As shown by Machado *et al.* (1998), we found a power law relationship between the number of MCSs and their lifetime. The mean MCS radius is related to the lifetime, with a roughly linear relationship in the 6–27 h range. This relationship is sensitive to the temperature threshold.

It was also found that a few long-lived MCS mostly explain the total cloud coverage. For example, MCSs with a lifetime greater than 24 h contribute to half the total cloud coverage at threshold 233 K. With the relationship between mean radius and lifetime, comparable results are obtained versus mean radius. At 253 K the anvil of cloud clusters larger than 10 000 $km^2$ accounts for 90% of the total cloud coverage; at 213 K the very active convective MCSs larger than 10 000 $km^2$ account for 60% of the total cloud coverage. This kind of result is interesting, because 10 000 $km^2$ lies within the typical range of horizontal resolution in general circulation models.

Diurnal variations of cloud coverage are similar to those obtained by Desbois *et al.* (1988), Duvel (1989) or Machado *et al.* (1993) with a maximum of convective activity in the early evening and a minimum at noon. For short-lived MCS (duration <10 h) diurnal variations of the number of systems explain the diurnal variations of cloud coverage, whereas for long-lived MCS, diurnal variations of the cloud coverage are related to the diurnal variations of the systems size. MCS initiations exhibit large diurnal variations with a maximum between 1600 and 1700 LST. Maximum generation of long-lived MCS occurs earlier, around 1400 LST. This result is consistent with results obtained by Rowell and Milford (1993) with short-lived and long-lived squall lines. Further analysis on split-generations and merger-ends shows that most splits are related to a weakening

of convection. Actual splits of two MCSs are rare for deep convection. Similarly, a large part of cluster mergers is related to intensification of convection. However, actual mergers are not negligible. This type of merging exhibits a large diurnal cycle with a maximum in the afternoon around 1700 LST.

Spatial variability of convective cloud clusters has also been investigated. As already shown by Rowell and Milford (1993), Thorncroft and Haile (1995), and Hodges and Thorncroft (1997), most initiations are orographically determined. Coastal regions associated with high sea surface temperature (Guinea and Nigerian coasts) are also preferred regions for initiations. Dissipation maxima are also determined by orography and the ocean. In fact, most MCSs are short-lived, so their dissipation location is close to their initiation location.

Hodges and Thorncroft (1997) and Hodges (1998) discussed the conditions required for convective activity to develop. The requisite convective available potential energy (CAPE) is built up through low-level advection of warm moist air (i.e. a high value of low-level equivalent potential temperature) associated with an unstable vertical thermodynamic profile. Additionally, the vertical wind shear associated with the AEJ favours the organization of convective systems into long-lived propagating systems such as squall lines.

MCSs generally propagate westwards, and their speed increases when their lifetime is long. Additionally, MCSs are likely to propagate faster during the mature stage when convection is stronger. Mean MCS zonal speed roughly corresponds to the AEJ. At threshold 213 K and to the west of 5°E, mean MCS zonal speed is slightly greater than the mean AEJ zonal component.

The importance of MCCs, as defined by Maddox (1980), has been also investigated. MCCs explain 10% to 15% of total MCS coverage at threshold 233 K. One can observe a relatively good agreement between mean MCC zonal speed and the mid-level mean zonal wind to the east of 5°E. To the west of 5°E, as observed at threshold 213 K, the mean MCC zonal speed becomes slightly greater than the mean AEJ zonal component.

High-resolution tracking provides results that generally confirm and extend those obtained by previous authors with low resolution. This is particularly noticeable for spatial variability. Results depending on cloud coverage should not be very different whether one uses full or low resolution, since it has been demonstrated that MCSs contributing to most of the cloud cover are long-lived and large clusters. Over the Sahel up to 60% of the total cloud cover is due to long-lived ($\geqslant$24 h) MCSs. However, statistical distributions of lifetime, as well as statistics on the number of MCSs, could be somewhat different since the accurate measurement of lifetimes and determination of cases of re-generation, are difficult to obtain with low resolution.

It was beyond the scope of this study to address all the issues mentioned in the introduction, such as scale interactions from the convective cell to the largest scale, interactions of convective systems with easterly waves or statistics for model parametrizations. However, results presented here document the convective systems' life-cycle, and show that a small number of major convective events explain most of the total convective cloud cover. Based on these results further studies are foreseen in order to address some of the remaining mentioned issues.

## ACKNOWLEDGEMENT

This study was supported by the European WAMP (West African Monsoon Project) programme.

## REFERENCES


Arkin, P. A. 1979 The relationship between fractional coverage of high cloud and rainfall accumulations during GATE over the B-scale array. *Mon. Weather Rev.*, **107,** 1382–1387

Arnaud, Y., Desbois, M. and Maizi, J. 1992 Automatic tracking and characterization of African convective systems on Meteosat pictures. *J. Appl. Meteorol.*, **31,** 443–453

Aspliden, C. I., Tourre, Y. and Sabine, J. B. 1976 Some climatological aspects of West African disturbance lines during GATE. *Mon. Weather Rev.*, **104,** 1029–1035

Chen, S. S. and Houze, R. A. 1997 Diurnal variation and life cycle of deep convective systems over the tropical Pacific warm pool. *Q. J. R. Meteorol. Soc.*, **123,** 357–388

D'Amato, N. and Lebel, T. 1998 On the characteristics of the rainfall events in the Sahel with a view to the analysis of climatic variability. *Int. J. Climatol.*, **18,** 955–974

Desbois, M., Kayiranga, T., Gnamien, B., Guessous, S. and Picon, L. 1988 Characterization of some elements of the Sahelian climate and their interannual variations for July 1983, 1984 and 1985 from the analysis of METEOSAT ISCCP data. *J. Climate*, **1,** 867–904

Diedhiou, A., Janicot, S., Viltard, A., de Félice, P. and Duvel, J. P. 1998 Easterly wave regimes and associated convection over West Africa and the tropical Atlantic: results from NCEP/NCAR and ECMWF reanalyses. *Clim. Dyn.*, 15795–15822

Duvel, J. P. 1989 Convection over tropical Africa and the Atlantic Ocean during northern summer. Part I: Interannual and diurnal variations. *Mon. Weather Rev.*, **117,** 2782–2799

1990 Convection over tropical Africa and the Atlantic Ocean during northern summer. Part II: Modulation by easterly waves. *Mon. Weather Rev.*, **118,** 1855–1868

Fritsch, J. M., Kane, R. J. and Chelius, C. R. 1986 The contribution of mesoscale convective weather systems to the warm-season precipitation in the United States. *J. Clim. Appl. Meteorol.*, **25,** 1333–1345

Gamache, J. F. and Houze, R. A. 1983 Water budget of a mesoscale convective system in the tropics. *J. Atmos. Sci.*, **40,** 1835–1850

Hodges, K. I. 1998 Feature-point detection using distance transforms: application to tracking tropical convective complexes. *Mon. Weather Rev.*, **126,** 785–795

Hodges, K. I. and Thorncroft, C. D. 1997 Distribution and statistics of African mesoscale convective weather systems based on the ISCCP METEOSAT imagery. *Mon. Weather Rev.*, **125,** 2821–2837

Jobard, I. and Desbois, M. 1992 Remote sensing of rainfall over tropical Africa using METEOSAT infrared imagery: sensitivity to time and space averaging. *Int. J. Remote Sensing*, **13–14,** 2683–2700

Laing, A. G. and Fritsch, J. M. 1993 Mesoscale convective complexes in Africa. *Mon. Weather Rev.*, **121,** 2254–2263

1997 The global population of mesoscale convective complexes. *Q. J. R. Meteorol. Soc.*, **123,** 389–405

Laurent, N. D'Amato, and Lebel, T. 1998 How important is the contribution of the mesoscale convective complexes to the Sahelian rainfall? *Phys. Chem. Earth*, **23,** 629–633

Machado, L. A. T. and Rossow, W. B. 1993 Structural characteristics and radiative properties of tropical cloud clusters. *Mon. Weather Rev.*, **121,** 3234–3260

Machado, L. A. T., Desbois, M. and Duvel, J. P. 1992 Structural characteristics of deep convective systems over tropical Africa and the Atlantic Ocean. *Mon. Weather Rev.*, **120,** 392–406

Machado, L. A. T., Duvel, J. P. and Desbois, M. 1993 Diurnal variations and modulation by easterly waves of the size distribution of convective cloud clusters over West Africa and the Atlantic Ocean. *Mon. Weather Rev.*, **121,** 37–49

Machado, L. A. T., Rossow, W. B., Guedes, R. L. and Walker, A. W. 1998 Life cycle variations of mesoscale convective systems over the Americas. *Mon. Weather Rev.*, **126,** 1630–1654

Maddox, R. A. 1980 Mesoscale convective complexes. *Bull. Am. Meteorol. Soc.*, **61,** 1374–1387

Mapes, B. E. and Houze, R. A. 1993 Cloud clusters and superclusters over the oceanic warm pool. *Mon. Weather Rev.*, **121,** 1398–1415

Martin, D. W. and Schreiner, A. J. 1981 Characteristics of West African and east Atlantic cloud clusters: a survey from GATE. *Mon. Weather Rev.*, **109,** 1671–1688

Miller, D. and Fritsch, J. M. 1991 Mesoscale convective complexes in the western Pacific region. *Mon. Weather Rev.*, **119,** 2978–2992

Morel, C., Orain, F. and Senesi, S. 1997 'Automated detection and characterization of MCS using the METEOSAT infrared channel'. Pp. 213–220 of Proceedings of the 1997 meteorological satellite data users conference, EUMETSAT, Brussels, Belgium

Reed, R. J., Norquist, D. C. and Recker, E. E. 1977 The structure and properties of African wave disturbances as observed during Phase III of GATE. *Mon. Weather Rev.*, **105,** 317–333

Rossow, W. B. and Schiffer, R. A. 1991 ISCCP cloud data products. *Bull. Am. Meteorol. Soc.*, **72,** 2–20

Rowell, D. P. and Milford, J. R. 1993 On the generation of African squall lines. *J. Climate*, **6,** 1181–1193

Thorncroft, C. D. and Haile, M. 1995 The mean dynamic and thermodynamic fields for July 1989 over tropical North Africa and their relationship to convective storm activity. *Mon. Weather Rev.*, **123,** 3016–3031

Williams, M. and Houze, R. A. 1987 Satellite-observed characteristics of winter monsoon cloud clusters. *Mon. Weather Rev.*, **115,** 505–519

Woodley, W. L., Griffith, C. G., Griffin, J. S. and Stromatt, S. C. 1980 The inference of GATE convective rainfall from SMS-1 imagery. *J. Appl. Meteorol.*, **19,** 388–408

# Relationship between easterly waves and mesoscale convective systems over the Sahel

Vincent Mathon
MSE, IRD, BP 5045, 34032 Montpellier Cedex, France

Arona Diedhiou
LTHE, IRD, BP 53, 38041 Grenoble Cedex 9, France

Henri Laurent
CTA-IAE-ACA, 12228-904 - São José dos Campos/SP, Brazil

Received 12 November 2001; revised 23 January 2002; accepted 28 January 2002; published XX Month 2002.

[1] Relationship between Sahelian mesoscale convective systems and easterly waves is studied at various time and space scales during 5 rainy seasons (1st July–15th September 1990–1994). This study focuses on a sub-population of MCSs called organised convective systems (OCS) which account for most of the rainfall. Wave activity periods are detected by spectral analyses on the 700 hPa meridional wind component, information on the convective systems is derived from an automatic tracking algorithm and rainfall data of the EPSAT-Niger experiment. We observe a modulation of OCS cloud cover at synoptic-scale during easterly wave activity, with an increase of the cloud cover in and ahead of the trough but OCS rainfall efficiency is maximum behind of the wave trough. At seasonal scale, OCS number and cloud cover distributions are not significantly affected by easterly wave occurrences, which means that the latter are not directly associated to the interannual variability of rainfall. *INDEX TERMS:* 3314 Meteorology and Atmospheric Dynamics: Convective processes; 3364 Meteorology and Atmospheric Dynamics: Synoptic-scale meteorology; 3374 Meteorology and Atmospheric Dynamics: Tropical meteorology

## 1. Introduction

[2] Easterly waves are an important component of the West African climate as they modulate rainfall and convection [e.g. *Burpee*, 1972; *Reed et al.*, 1977; *Duvel*, 1990; *Diedhiou et al.*, 1998; *Diedhiou et al.*, 1999]. Typically they have a period of 3–5 days and propagate westward with a phase velocity of about 7–8 degrees longitude per day. Although easterly waves are known to modulate rainfall and convection, the relationships between easterly waves and MCSs are not well documented. This paper aims to analyse the relationship between MCS and easterly waves from the seasonal scale to the mesoscale. Three datasets have been used. The NCEP/NCAR dataset [*Kalnay et al.*, 1996] consists of a reanalysis of the global observational network of meteorological variables (wind, temperature, geopotential height, humidity) with a single version of the forecast model of the NCEP (National Center for Environmental Prediction). In this study we use the 700 hPa wind reported on a 2.5° × 2.5° grid every 6 hours (00:00, 06:00, 12:00 and 18:00 UTC) on the periods 1 June–30 September from 1990 to 1994. The second dataset consists of information on MCS life-cycles obtained from an automatic tracking algorithm applied on METEOSAT full resolution images (ie. time resolution of 30 minutes and spatial resolution of about 5 km, see *Mathon and Laurent* [2001] for a detailed description and evaluation of the method). MCSs are here defined as cloud clusters with a size larger than 5000 km$^2$ at the brightness temperature threshold 233 K. The tracking technique yields MCS size, speed, location and vertical development during the life-cycle. The third dataset is rainfall data from the EPSAT-Niger experiment [*Lebel et al.*, 1992]. The experiment started in 1990 with a hundred recording raingauges covering a 160 * 110 km$^2$ area hereafter referred to as the E-N study area. In 1994, the network was reduced to 30 gauges. *Lebel and Amani* [1999] have shown that such a network is able to estimate precisely the average rainfall over the E-N study area at the event scale and beyond. In the following we will make use of homogeneous 5′ rainfall series recorded by the 30 gauges network between 1990 and 1994. These 5′ rainfall data are accumulated in order to produce event rainfall at each gauge, according to the criteria given in section 1-c. In order to have an homogeneous dataset combining these three different sources of information, the period of study has been limited to the 1st July to the 15th September over 5 years (1990–1994).

## 2. Methodology

### 2.1. Easterly Waves Detection

[3] Easterly waves are detected using wavelet analysis on the meridional wind component at 700 hPa. This level is in the range of those commonly used to study synoptic-scale easterly waves. The wavelet analysis is performed for the NCEP grid point closest to the EPSAT-Niger area (2.5E–12.5N), see *Diedhiou et al.* [1999] for more details on the methodology. Periods characterised by a maximum of the wavelet modulus in the 3–10 day band periods are retained. In a second step we verify that an easterly wave disturbance at synoptic-scale does exist. In such a case, we use the 3–10-day filtered wind field at 700 hPa to determine in which wave sector the EPSAT-Niger area and the convective systems are located. This methodology may not allow us to detect every easterly wave but it makes us confident that the selected dates correspond to actual easterly wave disturbances at synoptic scale.

### 2.2. MCS Classification

[4] In this paper we use a classification that attempts to depict objectively MCSs that account for most of rainfall over the central Sahel. The so-called Organized Convective Systems (OCSs) are defined at 233 K but they must contain at least one cluster at 213 K with a size larger than 5000 km$^2$, a lifetime greater than 3 hours and a mean speed greater than 10 m.s$^{-1}$ [*Mathon*, 2001]. Over the Sahel, OCSs are associated with approximately 80% of the cloud cover at threshold 233 K while accounting for only 12% of the total MCS number. Figure 1 shows that the OCS contribution in


0094-8276/02/2001GL014371$05.00

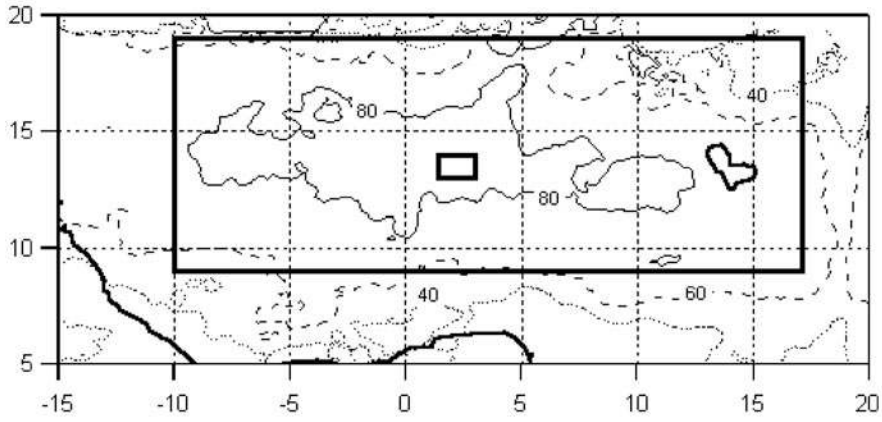


**Figure 1.** OCS contribution (%) to the total MCS cloud coverage (233 K). The central Sahel and the EPSAT-Niger area are outlined. 80%, 60% and 40% isolines are drawn in full, dashed and dotted lines respectively.

term of cloud cover at threshold 233 K is generally larger than 80% in the 12°N–16°N belt and larger than 60% almost everywhere in the central Sahel. Over the EN-area, OCSs contribute to 93% of the total rainfall [*Mathon*, 2001].

### 2.3. OCS Rainfall Characterisation

[5] In order to study OCS rainfall characteristics we use a concept of rainfall event derived from the one of *Amani et al.* [1996]. The most efficient E-N rain events can be defined as follow:
at least 80% of the gauges must record a rain depth equal or greater than 1 mm during the event;
there should not be a rainfall interruption of more than 30 minutes over the whole network. If all 30 gauges do not report any rain during a continuous 30-minute period then this is the end of the rain event.

[6] The major rain events as defined above explain approximately 75% of the total rainfall recorded over the EN-area [*D'Amato and Lebel*, 1998].

[7] To study rainfall characteristics of the satellite observed OCSs we have to deal with window-effects which are unavoidable when comparing a window-limited (16,000 km$^2$) measurement of a convective cloud which may only partly cover the instrumented area. Our approach to reduce this effect consists of selecting OCSs according to their overlapping surface with the instrumented area. We have tested several overlapping surface thresholds at different temperature thresholds (253 K, 233 K and 213 K) so as to explain most of the major rain events defined above while eliminating most of the other cases. The best compromise was found with OCSs covering more than 80% of the EN-area at threshold 233 K. These criteria allow us to select 45% of the OCSs that correspond to 78% of the total rainfall over the EN-area. Hereafter, only OCSs which satisfy the 80% overlapping criterion are considered for rainfall characterisation.

## 3. OCSs and Easterly Waves Relationships

### 3.1. Relationships at Synoptic Scale

[8] Figure 2a shows the distribution of the OCS cloud cover according to the wave sector over the central Sahel. As expected, OCSs are more frequently located at and ahead of the trough. However, when considering separately the southern (9°N–14°N) and the northern (14°N–19°N, Figure 2b) part of the central Sahel, one observes a radical change of the easterly wave modulation. As shown by *Duvel* [1990], OCSs are less frequently located in the northern flux sector compared to the other sectors. He suspected that humidity advection by easterly waves could play a significant role over the northern part of the Sahel where the humidity transport by the monsoon flux is less important than that observed to the south.

[9] Figure 2c documents the relationships between easterly waves and OCSs at the genesis and the termination of their life-cycle. Note that initiations and separations (resp. dissipations and mergings) exhibit similar behaviours (not shown). Genesis occur preferentially at and ahead of the trough whereas terminations are more frequently observed ahead of the trough. Keeping in mind that we consider only four sectors, results of Figure 2c are consistent with those of *Payne and McGarry* [1977]. However, the amplitude of the modulation is significantly weaker in our study. This may be due to differences in the definition of the genesis or the termination of a life-cycle. Note also that their study is limited to the phase III of GATE and includes the adjacent Atlantic ocean.

### 3.2. Relationships at Seasonal Scale

[10] The previous section confirmed that easterly waves modulate OCS cloud cover. One might ask whether or not easterly wave occurrences modify the global OCS statistics over the whole Sahel and at the scale of the rainy season. Table 1 shows the OCS number and cloud cover during periods of wave activity and inactivity. A simple scaling by proportion of the duration of wave activity and inactivity indicates that easterly waves do not have any significant impact on parameters at such time and space scale. As OCSs provide most of the rainfall over the Sahel, this suggests that easterly waves are not

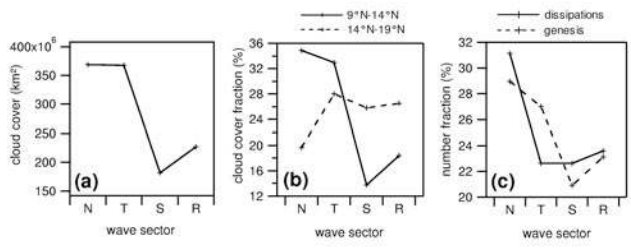


**Figure 2.** a) OCS cloud cover distribution (km$^2$, 233 K) versus wave sector (Northerly flux, Trough, Southerly flux and Ridge). b) Easterly waves modulation of OCS cloud cover (%) over the southern and the northern part of the central Sahel. c) Frequency (%) distribution of the location of OCSs versus wave sector at their genesis and their dissipation. A total of 411 OCSs was observed over the central Sahel during the 5 summers studied.

**Table 1.** OCS Number and Cloud Cover (233K, km$^2$) Over the Central Sahel During Five Summers (1$^{st}$ July–15$^{th}$ September) for Periods of Wave Activity and Inactivity are Considered Separately

| | OCS number | | OCA cloud cover ($10^9$ km$^2$) | |
|---|---|---|---|---|
| | Wave activity | Wave inactivity | Wave activity | Wave inactivity |
| **Observed** | **411** | **729** | **1.15** | **1.94** |
| **Scaled** | **742** | **729** | **2.06** | **1.94** |

Also indicated are the number and the cloud cover after scaling by proportion of the accumulated duration of wave activity and wave inactivity.

the main factor in the interannual variability of rainfall for this region.

[11] Figure 3 shows the distributions of the OCS number and cloud cover versus lifetime after scaling by proportion of the duration of easterly waves activity and inactivity. There are no significant differences between the distributions. Thus, long-lived OCS occurrences are not specially favoured by the presence of easterly waves.

### 3.3. Relationships at Mesoscale

[12] The results shown in Figure 4 are obtained using the methodology explained previously. Thus, window-effects are limited and we can then expect to relate rainfall variability to physical processes. It can be reminded that only the most energetic waves and the most rain producing OCSs are considered here.

[13] Figure 4a shows the accumulated rain yield and cloud cover associated with OCSs during periods of wave activity. Over the EN-area, both the cloud cover and the rain yield are modulated by easterly waves with a preferential location at the trough. The modulation of rainfall is primarily correlated to the modulation of cloud occurrences. However, more detailed investigations indicate that easterly waves also modulate OCS rainfall efficiency. Indeed, as shown in Figure 4b, the mean rain yield per OCS over the EN-area is larger behind the trough, in the southerly flux sector than in the other sectors. Also shown in Figure 4b is the ratio between the accumulated cloud cover over the EN-area and the accumulated rainfall. Again, OCS occurrences are associated with more rainfall when they are located in the southerly flux sector. This suggests that easterly waves may affect results obtained using satellite-derived rainfall estimation methods such as the GPI [*Arkin*, 1979]. Humidity advection by easterly waves, which appears to be a significant process (Figure 2b), might also affect OCS rainfall efficiency. However results in

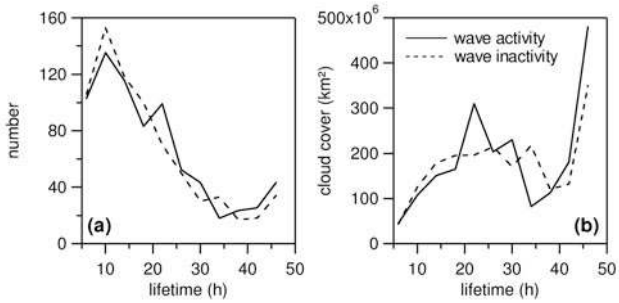


**Figure 3.** a) OCS number and b) cloud cover (km$^2$, 233 K) versus lifetime during periods of wave activity and inactivity. The distributions have been scaled by proportion of the accumulated duration of wave activity and inactivity and only OCSs which have crossed the central Sahel have been considered.

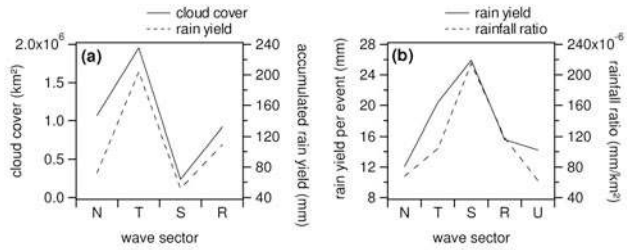


**Figure 4.** Characteristics of the OCS cloud cover and rainfall versus wave sectors (N, T, S, R). a) OCS 233 K cloud cover (km$^2$) and rain yield (mm) over the E-N area cumulated during the periods of wave activity observed during 5 years. b) OCS averaged rain yield (mm) and mean ratio between OCS rainfall and cloud cover (mm/km$^2$). Results obtained during wave inactivity are referred to the U sector.

Figure 4b have to be moderated. Cases satisfying criteria defined in section 1-c during easterly wave activity are relatively rare (only 25 cases over 5 summers).

## 4. Conclusion

[14] This paper documents the relationship between African easterly waves and OCSs over the central Sahel at different space and time scales. OCSs are very rain-efficient systems which provide 93% of rainfall over the EN-area and 80% of the 233 K cloud cover over the central Sahel [*Mathon*, 2001].

[15] At synoptic scale, results obtained by previous studies are confirmed. OCSs are located preferentially at and ahead of the trough in the southern part of the Sahel and at and behind the trough in the north. However, we have shown that OCS initiations and dissipations are only slightly modulated by easterly waves compared to the *Payne and McGarry* [1977] study. We suspect that it is primarily due to differences in the definition of the genesis or the termination of a life-cycle or to the fact that their study is limited to phase III of GATE and includes the adjacent Atlantic ocean.

[16] The study at larger scales (over the whole Sahel and for the core of the Sahelian rainy season), shows that easterly wave occurrences during the season do not significantly modify the OCS number or the OCS cloud cover distributions. These results suggest that easterly waves are not the main factor in the interannual variability of rainfall over the region. However, at the scale of the EN-area, we have found that OCS rain efficiency is maximum in the southerly flux sector. Despite the small number of cases available for this study, it can be argued that humidity advection by the southerly flux favours rainfall production.

[17] **Acknowledgments.** The authors are very thankful to Climate Diagnostics Center (NOAA, BOULDER, CO) for providing the reanalyses dataset, to Jean Louis Monge for his efficiency in managing the CLIMSERV data base at LMD and to Thierry Lebel for discussion on the observed rainfall data over Niamey.

## References

Amani, A., T. Lebel, J. Rousselle, and J. D. Taupin, Typology of rainfall fields to improve rainfall estimation in the Sahel by the area threshold method, *Water Resour. Res.*, *32*, 2473–2487, 1996.

Burpee, R. W., The origin and structure of easterly waves in the lower troposphere of north Africa, *J. Atmos. Sci.*, *29*, 77–90, 1972.

D'Amato, N., and T. Lebel, On the characteristics of the rainfall events in the Sahel with a view to the analysis of climatic variability, *Int. J. Climatol.*, *18*, 955–974, 1998.

Diedhiou, A., S. Janicot, A. Viltard, P. de Felice, and H. Laurent, Easterly waves regimes and associated convection over West Africa and the tro-

pical Atlantic: Results from the NCEP/NCAR and ECMWF reanalyses, *Clim. Dynamics*, *15*, 795–822, 1999.

Diedhiou, A., S. Janicot, A. Viltard, and P. de Felice, Evidence of two regimes of easterly waves over West Africa and the tropical Atlantic, *Geophys. Res. Let*, *25*, 2805–2808, 1998.

Duvel, J. P., Convection over tropical Africa and the Atlantic ocean during northern summer. Part II: Modulation by easterly waves, *Mon. Wea. Rev.*, *118*, 1855–1868, 1990.

Kalnay, E., M. Kanamitsu, R. Kistler, and W. Collins, et al., The NCEP/NCAR 40-years reanalysis project, *Bull. Amer. Meteor. Soc.*, *77*, 437–471, 1996.

Lebel, T., and A. Amani, Rainfall estimation in the Sahel: what is the ground truth?, *J. Appl. Meteor.*, *38*, 555–568, 1999.

Lebel, T., H. Sauvageot, M. Hoepffner, M. Desbois, B. Guillot, and P. Hubert, Rainfall estimation in the Sahel: The EPSAT-Niger experiment, *Hydrol. Sci. J.*, *37*, 201–215, 1992.

Mathon, V., Etude climatologique des systèmes convectifs de méso-échelle en Afrique de l'ouest., PhD thesis, Paris VII, 250 pp., 2001.

Mathon, V., and H. Laurent, Life cycle of the Sahelian mesoscale convective cloud systems, *Quart. J. Roy. Meteor. Soc.*, *127*, 377–406, 2001.

Payne, S., and M. M. McGarry, The relationships of satellite inferred convective activity to easterly waves over West Africa and the adjacent ocean during phase III of GATE, *Mon. Wea. Rev.*, *105*, 413–420, 1977.

Reed, R. J., D. C. Norquist, and E. E. Recker, The structure and properties of African wave disturbances as observed during Phase III of GATE, *Mon. Wea. Rev.*, *105*, 317–333, 1977.

Arona Diedhiou, LTHE, IRD, BP 53, 38041 Grenoble Cedex 9, France. (diedhiou@hmg.inpg.fr)

Henri Laurent, CTA-IAE-ACA, 12228-904 - São José dos Campos/SP, Brazil.

Vincent Mathon, MSE, IRD, BP 5045, 34032 Montpellier Cedex, France.

# Diurnal march of the convection observed during TRMM-WETAMC/LBA

Luiz A. T. Machado, Henri Laurent,[1] and Alexandra A. Lima

Divisão de Ciências Atmosféricas, Instituto de Aeronáutica e Espaço, Centro Técnico Aeroespacial, São José dos Campos, SP, Brazil

Received 8 January 2001; revised 16 July 2001; accepted 11 September 2001; published 6 September 2002.

[1] Radiosonde, satellite data, Tropical Ocean–Global Atmosphere (TOGA) radar 2 km constant altitude plan position indicator (CAPPI), and rainfall collected from the TRMM-Wet Season Atmospheric Mesoscale Campaign (WETAMC)/Large-Scale Biosphere-Atmosphere (LBA) Experiment in Amazonia have been used to investigate the diurnal cycle of the tropical convection. Geostationary Operational Environmental Satellite (GOES 8) images were used to describe the diurnal modulation of the total/high/convective cloud fraction and the diurnal evolution of the size spectrum and initiation/dissipation of the convective systems. Radar 2 km CAPPI were used to describe the diurnal cycle of the rain fraction for different thresholds and the diurnal evolution of the size spectrum and initiation/dissipation of the rain cells. An average over the four rain gauge networks was applied to describe the average hourly rainfall. The upper air network data set was used to compute the thermodynamic variables: equivalent potential temperature ($\theta_e$), convective available potential energy (CAPE), thickness of positive buoyancy, instability, and convective inhibition. High and convective cloud area fractions reach their maximum some hours after the maximum rainfall detected by rain gauge and radar 2 km CAPPI. The minimum cloud cover occurs only a few hours before the maximum precipitation and the maximum cloud cover occurs during the night. The maximum rainfall takes place at the time of the maximum initiation of the convective systems observed by satellite and rain cells. At the time of maximum precipitation the majority of the convective systems and rain cells are small sized and present the maximum increasing area fraction rate. The diurnal evolution of $\theta_e$ also presents a very clear diurnal variation, with maximum occurring in the early afternoon. The CAPE is well related to $\theta_e$. When $\theta_e$ is high CAPE is high; the atmosphere is unstable and has a deep layer of positive buoyancy and small convective inhibition. These results suggest the following mechanism controlling the diurnal of convection: In the morning, cloud cover decreases as the solar flux reaching the surface increases and consequently increases $\theta_e$. In the early afternoon, convection rapidly develops, high and convective cloud fractions increase rapidly, and the maximum precipitation and initiation is observed. After convection is developed the atmosphere profile is modified, reaching a nearly saturated state; the water vapor flux decreases in the boundary layer which becomes very stable, thereby inhibiting surface fluxes and consequently extinguishing the convection. *INDEX TERMS:* 3314 Meteorology and Atmospheric Dynamics: Convective processes; 3329 Meteorology and Atmospheric Dynamics: Mesoscale meteorology; 3360 Meteorology and Atmospheric Dynamics: Remote sensing; 3374 Meteorology and Atmospheric Dynamics: Tropical meteorology; *KEYWORDS:* convection, cloud cover, diurnal cycle, convective systems

**Citation:** Machado, L. A. T., H. Laurent, and A. A. Lima, Diurnal march of the convection observed during TRMM-WETAMC/LBA, *J. Geophys. Res.*, *107*(D20), 8064, doi:10.1029/2001JD000338, 2002.

## 1. Introduction

[2] One of the main characteristics of tropical convection is its strong reaction to diurnal forcing [e.g., *Minnis and Harrison*, 1984; *Duvel and Kandel*, 1985] among others). Knowledge of the diurnal modulation of convection is very useful to verify the diurnal cycle described by general circulation models. Furthermore, this modulation has an important influence on the radiative forcing of cloud cover,

[1]Institut de Recherche pour le Developpement (IRD), France, Cooperation Conselho Nacional de Desenvolvimento Cientifico e Tecnólogico (CNPq), Grenoble, Brazil/IRD.


0148-0227/02/2001JD000338$09.00

and thus constitutes a relevant factor for the Earth radiation balance.

[3] The first field campaign of the Large-Scale Biosphere-Atmosphere (LBA) Experiment in Amazonia was held in the Brazilian state of Rondônia in January–February 1999. The campaign known as the Wet Season Atmospheric Mesoscale Campaign (WETAMC/LBA) and the LBA-TRMM was focused on the dynamical, microphysical, electrical, and diabatic heating characteristics of tropical convection in the Amazon region (for a detailed description, see *Silva Dias et al.* [2002]).

[4] The TRMM-WETAMC/LBA experiment combining different measurements allows to describe the diurnal cycle of the clouds, precipitation, and thermodynamics variables. The understanding of the relationships among these parameters and their response to the diurnal cycle is the key question to understand the physical mechanisms and the feedbacks that control the daily variability of the convection.

[5] Infrared radiation in the atmospheric window is very sensitive to both surface temperature and cloud cover, especially deep convective clouds. Many properties of the diurnal cycle of the convection over South America have been described by geostationary satellites data. *Minnis and Harrison* [1984] examined the diurnal cloud variability for one month (November 1978) from hourly Geostationary Operational Environmental Satellite (GOES 8) high-resolution image, documenting regionally the diurnal variations in low, middle, and high cloudiness. *Hendon and Woodberry* [1993] investigated the diurnal cycle from one-year global imagery constructed from infrared channel; they analyzed the brightness temperature and deep convective activity describing the global distribution of amplitude and phase of the diurnal cycle. *Janowiak et al.* [1994] described the diurnal character of cold cloudiness in oceanic tropics during the period 1986–1990 using fractional coverage of cold clouds for three different temperature thresholds. *Guedes and Machado* [1997] using ISCCP (International Satellite Cloud Climatology Project) data described the diurnal variation of the cloud cover over the South America. *Garreaud and Wallace* [1997] studied the diurnal cycle over the Americas using ISCCP data and rainfall estimates based on microwave SSM/I imagery. They concluded that in general way cloudiness over land tends to occur in the late afternoon.

[6] *Silva Dias and Bonatti* [1985] and *Silva Dias et al.* [1987] examined the diurnal variation in the thermodynamic structure and the divergence fields using a numerical weather model over the Amazon region. These studies showed the importance of diurnal variations, especially to relate large-scale fields to the tropical troposphere response to diurnal forcing in the Amazon. Near coastlines the land-sea-breeze circulation can explain much of the diurnal cycle of clouds and precipitation. The diurnal cycle of convective cloudiness, in the North of Brazilian coast and parts of the Central Amazon Basin, is related to the activity of squall lines generated by coastal region sea breeze. *Garstang et al.* [1994] and *Cohen et al.* [1995] pointed out the importance of squall line activity to the total precipitation over the rain forest of the central Amazon basin and its relation to the sea-land-breeze. The Rondônia state is far away from the coast and consequently the action of these squall lines is reduced, solar heating and large-scale features mainly modulate the diurnal cycle.

[7] *Machado* [2000], analyzing data from ABLE-2B and FluAmazon experiments, suggested that the solar flux absorbed by the surface is always smaller than the total surface flux supplied to the atmosphere during convective events and always larger during nonconvective events. This means that the surface loses more energy than it receives during convective events and vice versa. The surface energy never seems to be in equilibrium. However, the quantity of energy stored at the surface seems to be limited, defining a timescale, that determines when surface and atmosphere need to export or receive energy in order to balance their deficit or excess of energy. The process that controls this deficit/excess of energy within the diurnal timescale will be discussed here based on the thermodynamic variables and the different characteristics of the cloud cover variability.

[8] The main goal of this study is to describe the diurnal cycle of the different cloud types, of the rain observed by the radar (reflectivity) and of the thermodynamics variables. The relationships between those parameters would allow understanding the physical mechanisms that control the cloud cover variability.

[9] In section 2 we present the data and methodology used. Section 3 presents the diurnal cycle of the cloud cover and radar reflectivities. Section 4 deals with the structural and morphological characteristics of the diurnal organization of the convective cloud cover. In section 5 we discuss the behavior of the thermodynamic parameters and their diurnal variation. Section 6 summarizes the results.

## 2. Data and Methodology

[10] This study uses four sources of data: GOES 8 infrared brightness temperature images, the 2 km constant altitude plan position indicator (CAPPI) from NASA-C Band Doppler weather radar, known as Tropical Ocean–Global Atmosphere (TOGA) radar, precipitation measurements from a rain gauge network and radiosondes released at Rebio Jarú, Rolim de Moura, and Abracos during the TRMM-WETAMC/LBA experiment.

[11] GOES 8 images were preprocessed by NASA-GSFC. The raw data were converted to brightness temperature and later to count and stored in 8 bit TIFF images. Navigation files were created periodically during the experiment period. The horizontal resolution is 4 km × 4 km at the nadir. During the LBA experiment the images were available every half hour, according to NOAA-GOES scanning strategy. Continuous series of cloud fraction were built using these images, for different brightness temperature thresholds, over a 2.3° × 2.3° area covering the WETAMC/LBA region (longitude: −63.3° and −61.0° and latitude: −12.1° and −9.8°). Cloud Fraction was computed for the following infrared GOES channel 4: brightness temperature (Tir) thresholds: Tir < 284 K, Tir < 273 K, Tir < 265 K, Tir < 245 K, Tir, 235 K, Tir < 225 K, Tir < 210 K, and Tir < 200 K. These thresholds were chosen based in the general histogram of the Tir over the TRMM-WETAMC region (Figure 1a). These thresholds intend to describe a measure ranging from the total cloud cover (warmer thresholds) to the convective cloud cover (colder thresholds).

[12] Figure 1 shows the histogram of the Tir for different hours. The thresholds used in this study are also indicated in the figure. We can see two different patterns: One is mainly

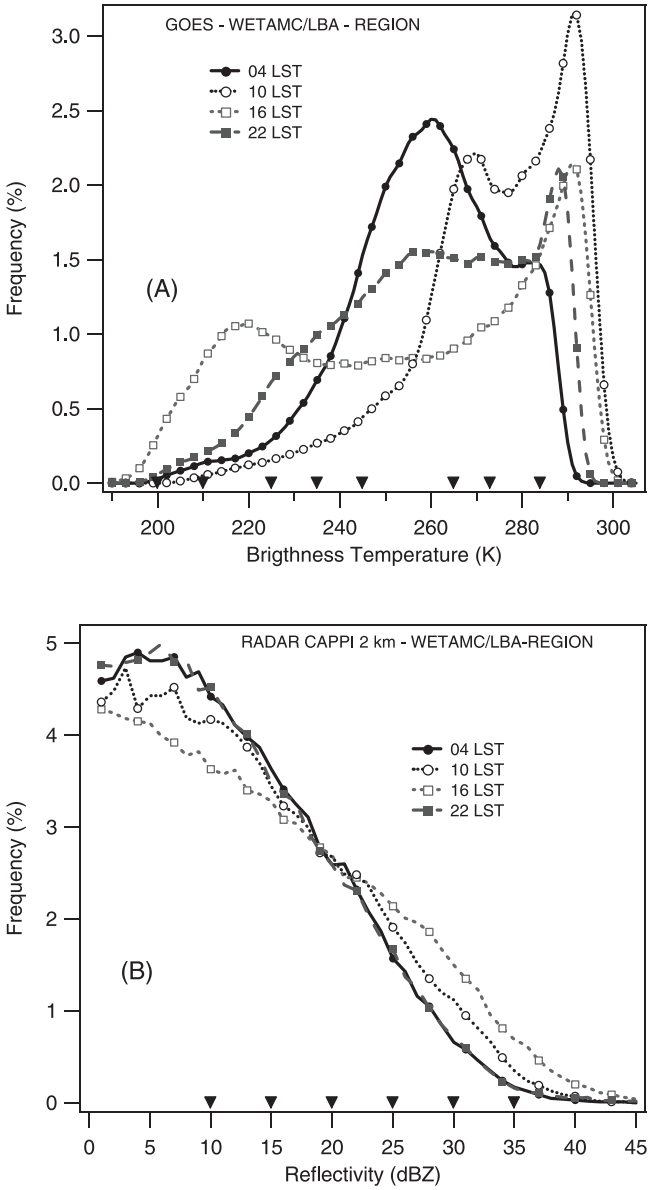


**Figure 1.** Histogram of the brightness temperature (a) from GOES 8 images and the reflectivity from 2 km CAPPI TOGA radar (b). The histogram was computed for the TRMM WETAMC/LBA region (longitude: −63.3° and −61.0° and latitude: −12.2° and −9.8°) for the period from 9 January to 27 February 1999. The histograms are presented for 0400, 1000, 1600, and 2200 LST.

associated with clear sky emission (Tir warmer than about 284 K) and another with cloud emission (Tir colder than about 284 K). The limit between the clear sky distribution and the cloud distribution is not obvious. The atmospheric mixed layer temperature, during the experiment, was always larger than 287 K. Due to the large amount of water vapor close to the surface the absorption of infrared radiance by this gas was strong, thus clear sky brightness temperature measured by the satellite is more associated to the mixed layer brightness temperature than to the surface brightness temperature. Thus, the threshold of 284 K, slightly colder than the atmospheric mixed layer temperature, was the one chosen to estimate the total cloud cover. We also used the thresholds of 273 K and 265 K to have a detailed description of the cloud cover.

[13] The coldest part of the histogram, below 245 K, is likely to be associated with convective cloud cover, including thick Cirrus, high levels thick stratiform clouds and Cumulus Nimbus. *Rickenbach* [1999] and *Wu and LeMone* [1999] studied the cloud top evolution of tropical squall lines during TOGA-COARE. They found that the coldest clouds were more closely associated with weaker surface precipitation because cold cloud shield became spatially decoupled from the source convection. They concluded that cold brightness temperature cloudiness implies that deep convection is or recently was active. Cold brightness temperature threshold is more related to the convective part of the cloud cover in the time/space-averaged sense than for instantaneous images. The size distribution of the coldest part of the convective systems obtained from instantaneous image should not be interpreted as the precipitation portions but as the higher and deeper portions of the convective system. *Machado and Rossow* [1993] discussed the thresholds suitable to describe the convective clouds over the whole globe. They concluded that, in general, image pixels containing high level clouds are identified by brightness temperature smaller than 245 K and convective parts by brightness temperature smaller than 215 K. *Maddox* [1980], *Miller and Fritsch* [1991], and *Machado et al.* [1998] identified mesoscale convective systems as clouds with thresholds of Tir between 241 K and 245 K, and the most active convective parts, embedded inside the convective systems, by thresholds of Tir between 221 K and 215 K. In this study we have used 4 thresholds to identify the different convective parts of the total cloud cover by the thresholds 245 K, 235 K, 225 K, 210 K, and 200 K. Continuous hourly series of the different cloud fractions were constructed by averaging the cloud fractions observed each hour as representative of the observation of the middle of the hour. These series were used to determine the average hourly variation of the cloud fraction.

[14] The TOGA radar has a wavelength of 5.4 cm, a beam width of 1.65 degrees and a peak power of 250 kW. It is operated with a pulse width of 2.0 μs and gate width of 250 m covering a region of 150 km radius. Complete volume scans were performed every 10 minute intervals (sometimes more frequently) accomplishing elevations from 0.5 up to 30.0 degrees or higher. In this study we have used the 2 km CAPPI based on weight beam volumes. The weight and the 3-D position are precomputed based on the elevation/range of the radar. The horizontal resolution of the CAPPI was set to 5 km × 5 km in order to have nearly the same spatial resolution of GOES images.

[15] Figure 1b presents the histogram of the reflectivity (REF) of the CAPPI over the same region used for satellite cloud fraction. Reflectivity fraction was calculated for different thresholds (REF > 10, REF > 15, REF > 20, REF > 25, REF > 30, and REF > 35 dBZ). Thresholds bellow 10 dBZ were not considered due to very small signal/noise relationship. We can note that the reflectivity distribution fits a section of Gaussian function. The distribution is very smoothed and the selection of the six thresholds was defined linearly (5 dBZ interval) up to 35 dBZ. The upper limit of 35 dBZ is a little smaller than some authors have used to describe convection but it was defined to have a

significant statistical population of pixels, the average diurnal peak of the 35 dBZ area fraction is not larger than 1.5%, the histogram in Figure 1b shows the population of values larger than 35 dBZ. The reflectivity fraction intends to describe the rain distribution at 2 km height for different rain intensities. It will be called *rain fraction* hereafter. A continuous hourly series was constructed averaging the rain fraction inside one hour as representative of this hour.

[16] Cloud fraction and rain fraction were computed from 9 January to 27 February as:

$$F_S = \frac{100}{N}\sum_{i=1}^{N}\partial_i \rightarrow \left\{\begin{array}{l}\partial_i = 1, Tir < Threshold\\ \partial_i = 0, Tir \geq Threshold\end{array}\right\}$$
$$F_R = \frac{100}{N}\sum_{i=1}^{N}\partial_i \rightarrow \left\{\begin{array}{l}\partial_i = 1, REF > Threshold\\ \partial_i = 0, REF \leq Threshold\end{array}\right\} \quad (1)$$

where $F_s$ and $F_r$ are the cloud fraction and the rain fraction from satellite radiances and from CAPPI 2 km TOGA radar reflectivity respectively.

[17] The rain gauge network was distributed in four clusters. The rain gauge tipping buckets have a sampling resolution of 0.254 mm and maximum temporal resolution of 10 s. We used in this study the hourly cumulated rain gauge data from the Goddard DAAC (Distributed Active Archive Center). An average over the 4 networks was applied to describe the average hourly rainfall over the TRMM-WETAMC region.

[18] To compute the thermodynamic parameters we have used the upper air network data set operating during the WETAMC/LBA. The radiosondes were released every three hours at (0000 UTC to 2100 UTC) and data collection was conducted from 9 January (only Abracos) to 28 February. The simultaneous radiosonde releases, for the three sites, cover only the period from 24 January to 20 February. The data used in this study has passed a preliminary quality control. The data vertical resolution employed in this work is 40 hPa. Due to the strong influence of the surface observation in the computation of the thermodynamic parameters and some uncertainties in surface observation data we have computed the thermodynamic variable first level using an average of the first 40-hPa layer. Differences between Vaisalla and VIZ system and uncertainties in the radiosonde measures in TRMM-WETAMC/LBA are discussed by G. Fisch et al. (The convective boundary layer over pasture and forest in Amazonia, submitted to *Journal of Geophysical Research*, 2001, hereinafter referred to as Fisch et al., submitted manuscript, 2001).

## 3. The Diurnal Cycle of Cloud and Rain Fraction

[19] The average hourly cloud fraction was computed, for the different thresholds, in order to present the typical diurnal variation of the different cloud types. Figure 2a shows the hourly average cloud fraction for the thresholds 284 K (close to total cloud cover), 235 K (high cloud cover), and 210 K (clouds associated with the deep convection as seens by satellite). Three different scales are presented in this figure, because of the large variations among the different cloud fraction. Indeed, the total cloud cover varies from 56% to 94%, the high cloud fraction from

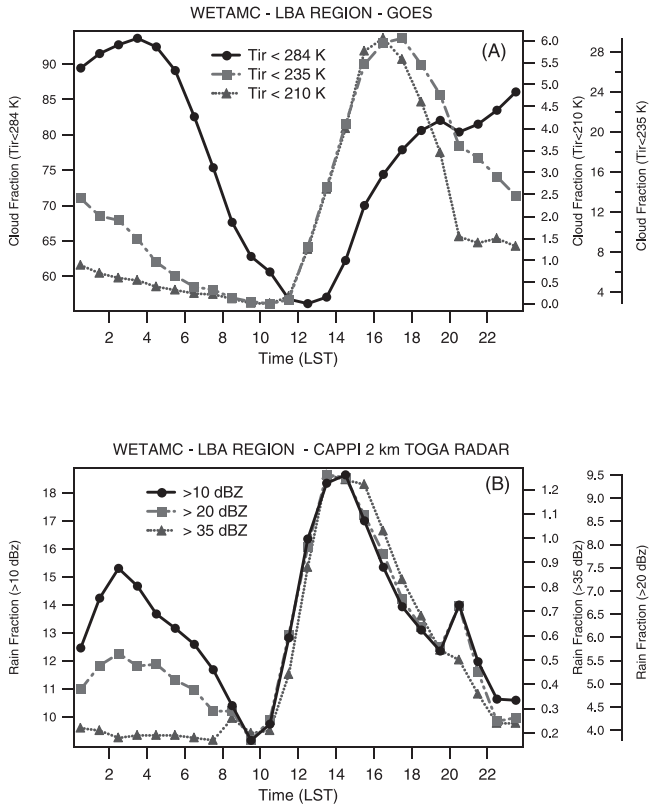


**Figure 2.** Hourly average cloud fraction (a) for the brightness temperature threshold of 284 K, 235 K, and 210 K, and for rain fraction (b) defined as the fraction larger than 10 dBZ, 20 dBZ, and 35 dBZ, for the period from 9 January to 27 February 1999. Each cloud fraction is presented in a specific scale.

3% to 29% and the deep convective cloud fraction from 0% to 6%.

[20] The 210 K cloud fraction peaks at 1630 LST and the 235 K cloud fraction at 1730 LST, i.e., deep convective cloud fraction peaks one hour earlier than high cloud fraction. A similar short time phase lag from very cold to warmer cloud top was also found in some other studies [e.g., *Chen and Houze*, 1997; *Garreaud and Wallace*, 1997]. We observe for both cloud fraction (convective and high clouds) a strong increase after 1130 LST with a maximum cloud fraction increase rate around 1330 LST. After the maximum, deep convective fraction shows a fast decrease between 1630 and 2030 LST, with a maximum decrease rate at 1930 LST. After 2030 LST we observe a break and the coldest cloud fraction decreases slowly during the night presenting a very small average convective cloud fraction. For high cloud fraction we observe nearly the same behavior, however, it does not decrease as fast as convective cloud fraction. After 2030 LST high cloud fraction shows a slow decrease from 18% to almost 0% at 1130 LST, in the next day morning. For the total cloud fraction [284 K] a completely different behavior is observed. The total cloud fraction peaks at 0330 LST with an average of 94%. During nighttime the total cloud fraction is always larger than 80% on average. *Minnis and Harrison* [1984] studying the diurnal variability of regional cloud distributions show a

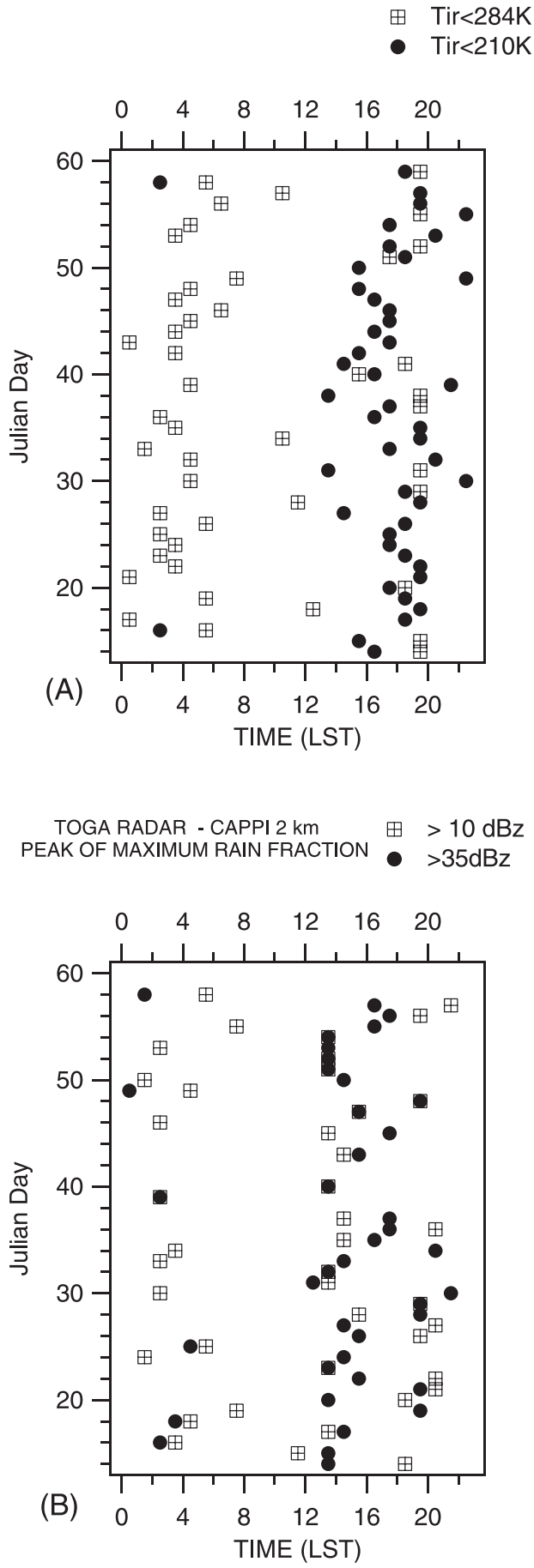


nocturnal maximum in the total cloudiness over Rondônia region. *Duvel* [1989] studying the diurnal variation of low and midlevel cloud over tropical Africa found the same feature, a very strong diurnal modulation with maximum coverage between 0300 LST and 0600 LST. After the maximum, the total cloud fraction decreases slowly up to 1230 LST. Minimum total cloud fraction happens at the time when high and convective cloud fraction have the maximum increase rate; it means that convection starts to develop when the total cloud cover is minimum and solar flux is around the maximum, at the time when the maximum solar radiation reaches the surface. The total cloud fraction, that accounts for a much larger amount of cloud cover than the high and convective fraction (around 3.5 times the high cloud fraction and 12.0 times the convective cloud fraction) has a secondary peak at 1930 LST when high and convective clouds have the maximum decreasing rate. This result suggests that high clouds might evolve to middle and low-level clouds and/or become thinner, with a smaller emissivity. One hour after the secondary maximum, around 2030 LST, the total cloud fraction increases again to reach the night maximum at 0330 LST as mentioned before. The nighttime cloud cover has an important impact in the energy radiation budget by reducing the outgoing longwave radiation and increasing the energy stored in the subcloud layer.

[21] The histogram in Figure 1a clearly presents the diurnal evolution of the different cloud covers. We can see at 1600 LST a large number of pixels around 220 K followed by an increased population of pixels between 240 K to 260 K at 2200 LST. At 0400 LST this large population of pixels moved around 260 K and around 270 K at 1000 LST. These behaviors reveal the change in the cloud cover during the day from deep convective clouds at 1600 LST to middle and low clouds during the night and early morning. Due to the semitransparent clouds (mainly thin Cirrus clouds) that bias the cloud cover classification, at 2200 LST the large population of pixels between 240 K and 260 K is, probably related to a mixing of clouds with different emissivities and cloud tops. The relative humidity profiles presented later in Figure 5 will clarify the diurnal evolution of the cloud types.

[22] Some nocturnal mesoscale convective systems crossed the WETAMC/LBA region during the experiment (for a complete discussion about mesoscale convective systems, see *Laurent et al.* 2002). One can question whether the average nighttime maximum in the total cloud cover is a consequence of these sporadic nocturnal squall lines or not. Figure 3a presents the time of maximum cloud fraction, for each day, for the thresholds 284 K and 210 K. For the majority of the days, the total cloud fraction peaks during night (around 0200–0400 LST) and the convective cloud fraction peaks during the afternoon (around 1600–1900 LST). For some days only the total cloud fraction occurs in the afternoon, probably associated with stronger convective activity, but in such cases a secondary peak is also observed during the night. The convective cloud fraction shows an almost systematic maximum in the late afternoon. The maximum convective fraction occurs during the night for

**Figure 3.** (opposite) Diagram day versus local time showing the moment of the maximum 284 K and 210 K cloud fraction (a) and 10 dBZ and 35-dBZ-rain fraction (b).

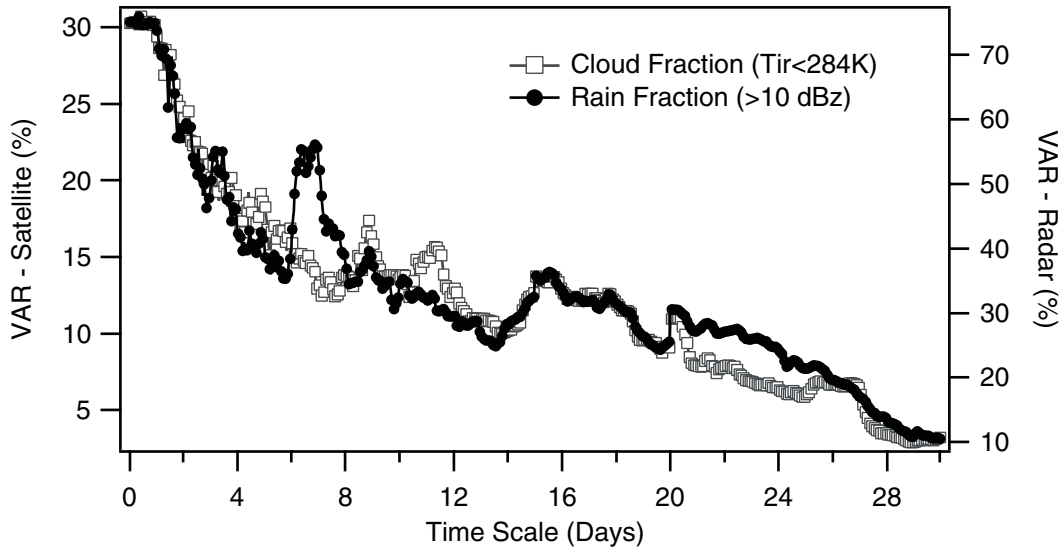


**Figure 4.** Average difference, expressed in percentages, between hourly distributions obtained from the timescale (days) and the hourly distribution obtained for the whole period. For timescale equal 1, VAR correspond to the difference between each day and the average distribution. The distributions are presented for total cloud fraction (284 K) and rain fraction (10 dBZ).

only a few days. The convective cloud fraction for situations of nocturnal maximum is not larger than the average afternoon convective cloud fraction, thus the results from Figure 3a show that the sporadic nocturnal convection does not bias the average distributions.

[23] The average hourly rain fraction was computed for the different thresholds, in order to present the typical diurnal variation in the rain-reflectivity intensity field. Figure 2b shows the hourly average rain fraction for the thresholds: REF > 10 dBZ (any type of rain - close to the total rain fraction at 2 km height), REF > 20 dBZ (weak to moderate rain at 2 km height) and REF > 35 dBZ (more intense rain at 2 km height). Three different scales are presented due to the amplitude that varies from 18% to 9% for the total rain fraction, from 3% to 10% for the moderate rainfall area fraction and from 0% to 1.5% for the intense rain area fraction.

[24] The three rain fraction peak in the early afternoon, at the same time, around 1330–1530 LST. Differently from the cloud fraction, the total, moderate, and intense rain fractions have their maxima at the same time. They present a rapid increase between 1030 to 1430 LST, at the time of minimum total cloud cover, and a slow decrease from 1430 to 2230 LST. A secondary peak for moderate and light rainfall was noted around 2030 LST, probably associated to the late occurrence of some diurnal convection. During the night a secondary peak is observed associated with light to moderate rainfall in agreement with the results obtained for cloud fraction. The minimum rain fraction occurred, for all thresholds, around 0930 LST. It can be seen in the histogram showed in Figure 1b that the shape of the curves do not change during the diurnal cycle. Nevertheless, the slope of the histograms change during the time evolution where 20 dBZ level remains constant during the entire day.

[25] Figure 3b presents the time of the maximum rain fraction, for each day, for REF > 10 dBZ and REF > 35 dBZ. The hour of maximum occurrence is more variable for the total rain fraction than for the total cloud fraction. Sometimes the daily maximum happens in the afternoon sometimes during the night. However, as it was discussed for the cloud fraction, a maximum total rain fraction in the afternoon does not mean that a secondary maximum was not observed during the night. Although for the majority of the days the maximum intense rain fraction (REF > 35 dBZ) occurred in the afternoon, around 1430 LST, for some days it occurs during the night. Rain fraction has a much larger variability than cloud fraction.

[26] To have an idea about how representative is the average diurnal variation of the cloud cover and of the rain fraction showed in Figure 2, we have computed the variability of these distributions as follows:

$$VAR(k) = \frac{\left\{\frac{1}{M}\sum_{i=1}^{m=N/k}\left\{\frac{1}{24}\sum_{h=1}^{24}\left(f_i^k(h) - F(h)\right)^2\right\}\right\}}{\frac{1}{24}\sum_{i=1}^{24}F(h)} * 100 \quad (2)$$

where, N is the number of days, F(h) is the average hourly cloud or rain fraction obtained for the N days (the whole period), $f_i^k(h)$ is the average hourly cloud or rain fraction over the period of k days (k varies from 1 to N/2) computed in the $i^{eme}$ part of the data set. VAR (k), corresponds to the average difference, expressed in percentage, between the hourly distribution obtained over k days and the hourly distribution obtained for the whole period. For example, VAR(1) corresponds to the difference between each day and the average distribution.

[27] We can see in Figure 4 that for k varying from 1 to 5 days, VAR(k) decreases exponentially from 30% to 13% for the cloud fraction, and from 70% to 35% for the rain fraction. As mentioned before, the rain fraction has a larger variability

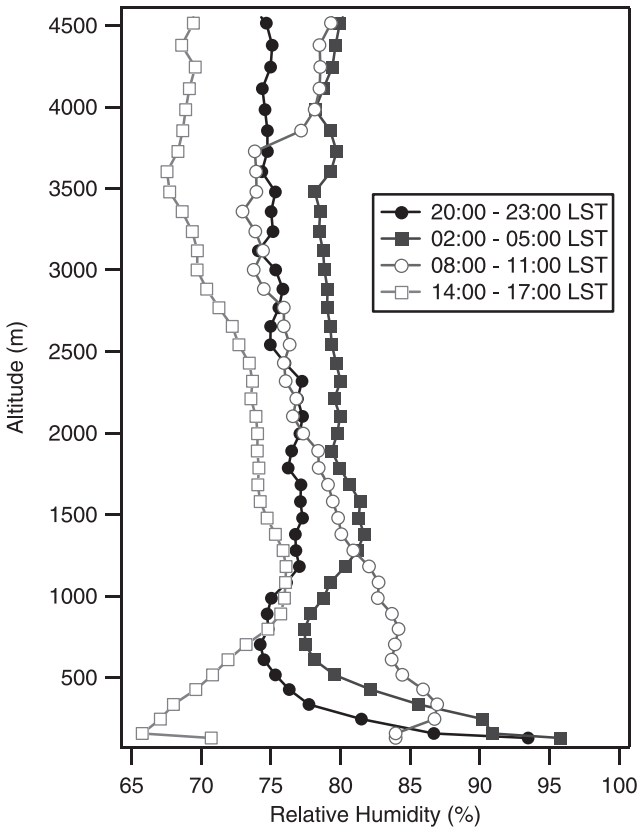


**Figure 5.** Relative humidity average profile for 2000–2300 LST, 0200–0500 LST, 0800–1100 LST, and 1400–1700 LST for Rebio Jaru station from surface to 4500 m.

than the cloud fraction and the average distribution should be interpreted carefully. Larger rain fraction variability is expected because rain is an internal feature of the total cloud cover, having a shorter time/space scale than the cloud top. For k > 5 days, the error slowly decreases linearly with the timescale. This result shows that the variability of the diurnal cycle of cloud and rain fraction is very high but decreases rapidly up to 5 days; for timescale larger than 5 days this variability decreases slowly and the diurnal cycle is very close to that one described by 30 days average.

[28] To describe the diurnal variation of cloud fraction and rain fraction better, we have computed the hourly averaged relative humidity profiles measured in the Rebio Jaru site. Figure 5 shows large diurnal variation of the relative humidity profile from surface to 4500 m. We notice a very high average relative humidity near the surface during the nighttime, probably related to the shallow nocturnal boundary layer height. From around 1000 m up to 4500 m the average relative humidity profile for 0200–0500 LST presents the largest values around 82%. Its likely to corresponds to low-level clouds that systematically form in this layer in agreement with the total cloud cover fraction observation. High average relative humidity values, at these levels, are probably due to a systematic cloud layer. During the morning (0800–1100 LST), at the same time as the Sun rising and insolation increases, low level clouds beginning to dissipate. Figure 5 shows, at this time, the largest average relative humidity at the layer from around 300 m to 1000 m. The specific humidity profile (not shown) reveals that the atmosphere, in the early afternoon, is dryer in the boundary layer and becomes wetter in the following hours showing the typical behavior of the diurnal convection. *Machado* [2000] described the energy stored in the atmosphere after convection in the Amazon Basin; he showed that a large amount of latent energy is stored in the middle atmosphere as a consequence of the vertical water vapor flux due to the convective towers.

## 4. The Spatial Organization of Clouds and Reflectivities

[29] *Miller and Fritsch* [1991] and *Machado et al.* [1992] described the structural properties of the tropical cloud clusters, observed from satellites images. They show a nearly equal contribution of all cloud cluster sizes to the mean high cloud cover, when data is integrated over a long period. However, for specific analysis such as different times of the day and different phase of synoptic perturbation, the cloud cluster size distribution can be very useful. *Machado et al.* [1993] describe the typical behavior of the cloud organization for the diurnal cycle over the Atlantic Ocean and West Africa using the cloud cluster size distribution. *Machado and Rossow* [1993] have used the 245 K threshold to describe high level clouds over the whole globe. In the present work we have defined high level clouds as the area covered by adjacent pixels (in GOES image) having Tir smaller than 235 K. This threshold is colder than former used because higher spatial resolution images is being used and the Tir average histogram shows that 235 K is more adapted to describe the high level clouds at this specific region. We computed the location of the center and the area covered by the convective system. Because of the large range of convective system shapes observed, we compute an effective radius (called as radius hereafter), assuming a circular shape. What we call radius is then only a convenient linear measure of the convective system area. In the present study we have taken into account only the convective system whose center crossed the LBA region, as defined in the data section.

[30] The same procedure was applied to the radar data, using the CAPPI 2 km and the threshold of 20 dBZ. The adjacent pixels in the CAPPI image with reflectivity larger than 20 dBZ will be called rain cell. Studies based on ground and aircraft-based meteorological measurements define a convective cell as a region of high speed updraft within cumulonimbus clouds; the size of these cells is less than equal to 20 km [*Cotton and Anthes*, 1989], larger than the typical size of individual satellite pixels. Radars detect only the precipitation sized particles, not the smaller particles composing the clouds. The radar echoes of these systems, defined by radar reflectivities greater than 35 dBZ are commonly defined as convective core or convective cells. The spatial organization of the rain cells corresponds to the organization of moderate to intense rain at 2 km height.

[31] Convective system describes the cloudiness mesoscale organization and the rain cell defines the rain feature as an intimate part of the convective systems, which will be called hereafter as only convective system and rain cell. The distributions of convective systems and rain cells area fraction as function of the radius were computed for each

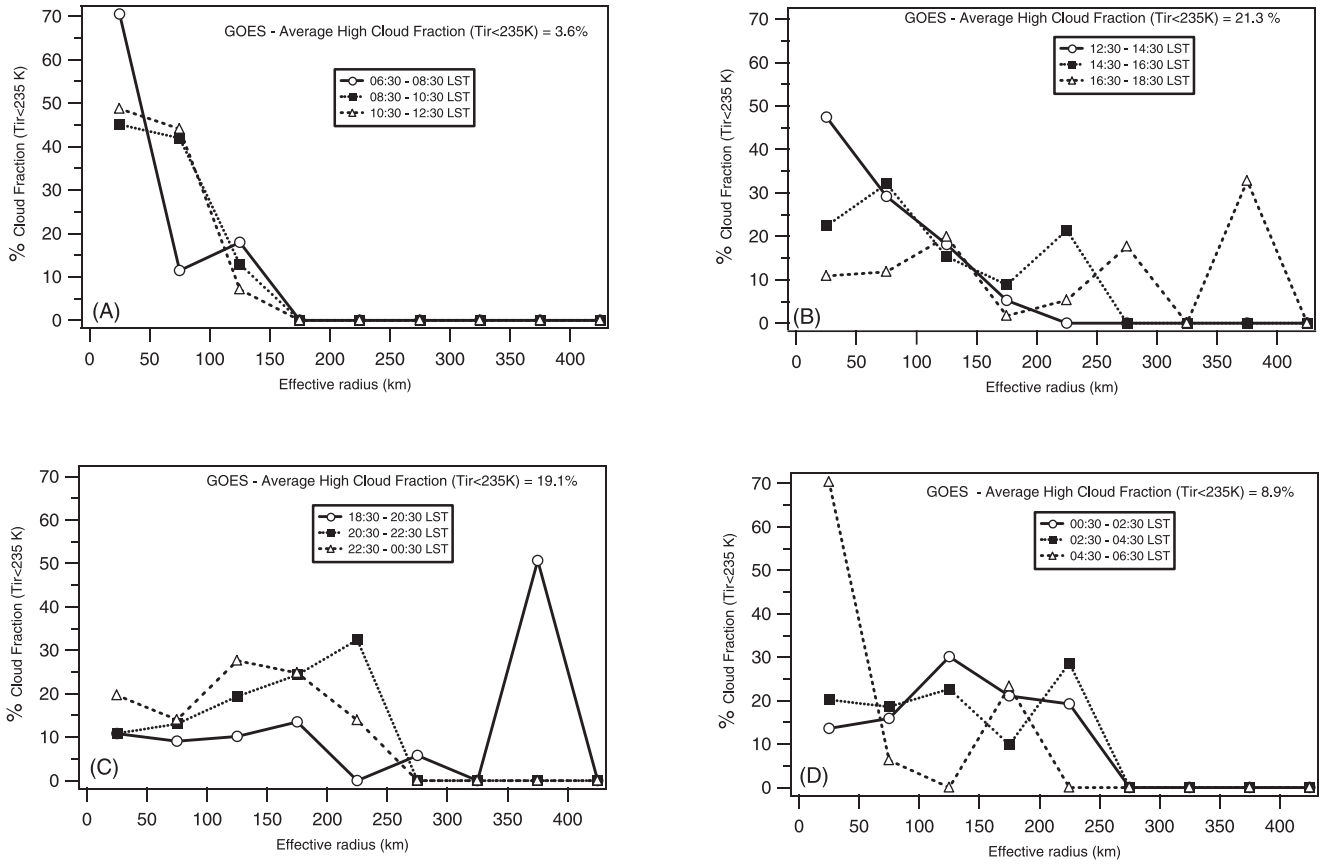


**Figure 6.** Convective system size distribution as function of the diurnal cycle. Convective system were defined using the threshold of 235 K. Distributions are presented as the two-hours average. The curves show the contribution to the total cloud cover at specific time by different convective system radius size.

two-hour. It describes the relative contribution of high cloud cover (moderate rain fraction) for a given radius class as follows:

$$S(\Delta r) = \frac{1}{s_t} \sum_{r=r1}^{r2} s(r) \qquad (3)$$

where S($\Delta$r) is the contribution to the total high cloud cover ($S_t$) of the convective systems having a radius in the $\Delta$r size interval (from $r_1$ to $r_2$); s(r) is the area of the system with radius r. The distributions are normalized by the total fraction ($S_t$) therefore, do not take into account the diurnal variability of the cloud fraction.

[32] Figure 6 shows the size distributions of the convective system for different hours. This figure presents the spatial scale involved in the diurnal evolution showed in Figure 2. In the early morning the majority of the high cloud cover is organized in small-scale systems, during the period 0630–0830 LST, 70% of the convective systems have a size around 25 km. The size distribution for the period 0830–1230 LST shows that high cloud cover is also dominated by small spatial scale but with a slight increase in convective systems size. In the afternoon between 1230 and 1830 LST we observe a progressive increase in the spectrum of the cloud size. At 1430–1630 LST only 22% of the cloud cover is due to small systems, at this time two spatial scale dominate the spectrum: 75 km and 225 km. Later on, only 10% of the high cloud cover is organized in small scale and convective systems become larger with typical sizes of 250 and 375 km. Around 1830–2030 LST almost the entire high cloud cover is organized into large convective systems. During the evening the spatial scale of the convective systems decreases to around 100 to 200 km. This typical convective system size persists during the whole night. At the end of the night and at dawn the large convective systems are nearly dissipated and the high cloud cover presents a small-scale organization. A general behavior of the spatial scale diurnal variability can be described as an increase in the convective system size organization from the early afternoon to the early night. After convective systems reach the maximum spatial scale organization (an average size of 250 km), they are followed by a fast decrease to a medium size, around 140 km radius, maintaining this spatial scale up to the early morning when high cloud cover becomes organized in very small scale.

[33] Figure 7 presents for different hours the size distribution of the rain cells (REF > 20 dBZ) computed from the TOGA radar 2 km CAPPI. We note that the rain cell size distribution during the whole night and in the morning have approximately the same shape: Around 12% of the total rain fraction is from cells with radius around 5 km (except at some hours we observe a slight maximum for 15 km radius); a constant contribution of around 15% for rain cells size up to 30–40 km, followed by a nearly linear decrease. The most remarkable difference in the size spectrum during this period can be noted at night (0030 to 0630 LST) when a maximum

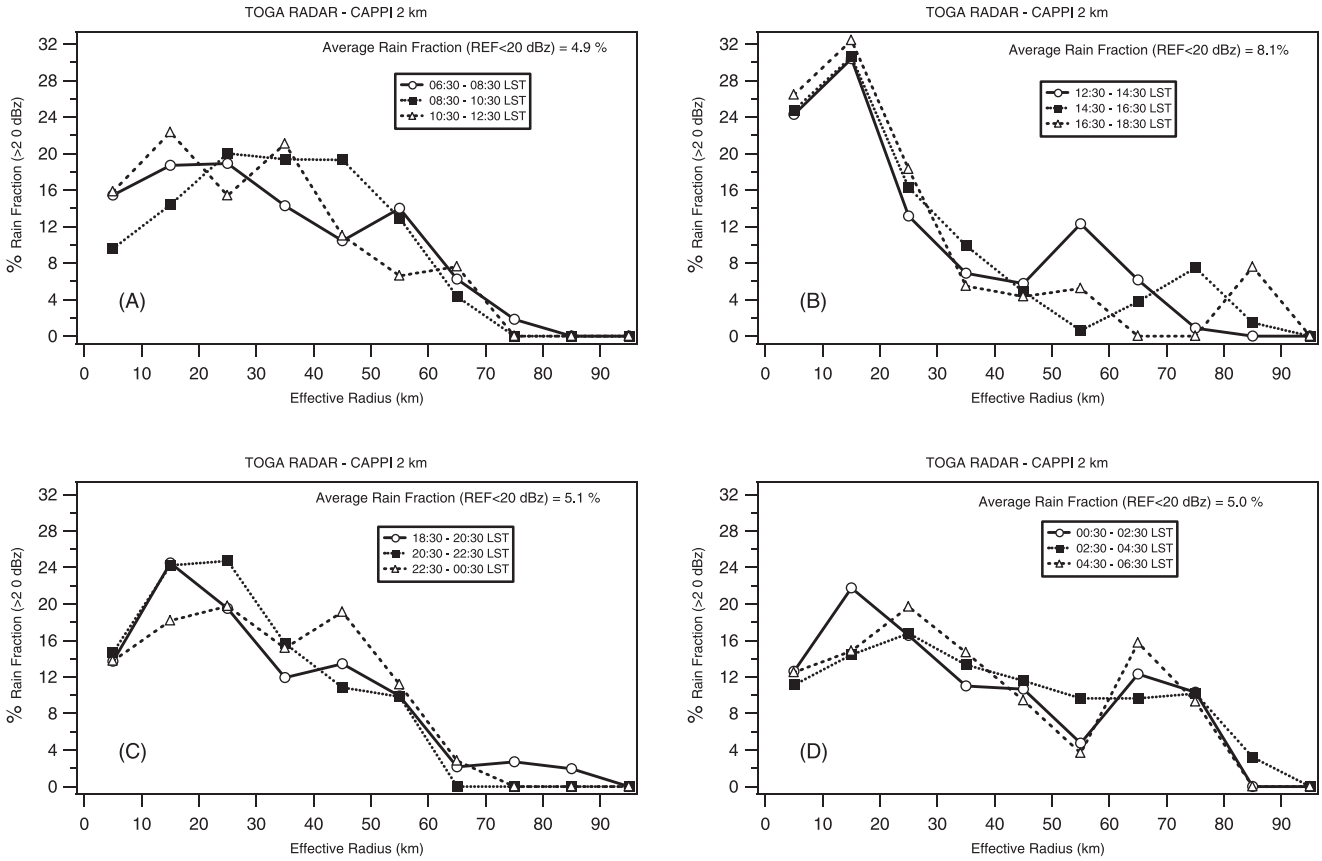


**Figure 7.** Rain cells size distribution as function of the diurnal cycle. Rain cells were defined using the threshold of 20 dBZ. Distributions are presented as the two-hours average. The curves show the contribution to the total rain fraction at specific time by different rain cells radius size.

around 70 km radius is very clear. It is related to the size organization of the nocturnal rain cells associated with low reflectivities values discussed in the previous section.

[34] In the afternoon, time of maximum convection, the size distribution has a different behavior from the other times of the day. There is a well-defined maximum for 15 km followed by an important decrease up to 40 km radius. We can also note the size evolution of large rain cells system increasing from 55 km at 1230–1430 LST to 85 km at 1630–1830 LST. The time evolution is consistent by showing the size increase of the rain cells in the afternoon. However, the contribution to the total rain fraction for these structures, larger than 50 km, is very small and probably is not a systematic feature.

[35] The convective system (Tir < 235 K) and rain cell (REF > 20 dBZ) structures were followed in time using the methodology described by *Mathon and Laurent* [2001]. This methodology permits us to describe the life cycle of the convective system and the rain cells and to establish the time and location of the spontaneous initiations and dissipations. The initiations due to split and the dissipations due to merge of convective systems or rain cells, as well as, the initiations or the dissipations due to an interval of missing images, have not been considered here. The tracking method was applied on satellite and radar images, for the convective systems and rain cells crossing the LBA region, see *Laurent et al.* [2001] for more details.

[36] Figures 8a and 8b present the hourly average of the convective system and rain cell spontaneous initiations and dissipations and the average rainfall computed from the four rain gauge networks. The maximum rain fraction (Figure 2b) occurs around 1300–1400 LST. At this time the majority of the convective systems and rain cells have a small size (Figures 6 and 7) and have the maximum area fraction increasing rate (Figure 2a). Figure 8 shows that the maximum precipitation occurs at this time.

[37] Initiations of convective systems and rain cells take place around the same time (1330 LST) of maximum precipitation. Maximum rain cell dissipation occurs one hour later at the time when the average precipitation rapidly decreases. Convective systems have longer and more variable lifetime durations. Convective system dissipation occurs 3 to 11 hours after the initiation, nevertheless, maximum dissipation occurs 5 hours after initiation. Rain cells present a secondary maximum of initiation, at 1830 LST, in agreement with a secondary maximum in precipitation. This secondary maximum in the initiation is associated with a peak of dissipation two-hour later. The nocturnal squall lines that crossed the LBA region are not present in the initiation and dissipation curves, probably because these convective systems are associated with a few long-lived convective systems that were generated earlier. As mentioned before, Figure 8 considers only the sponta-

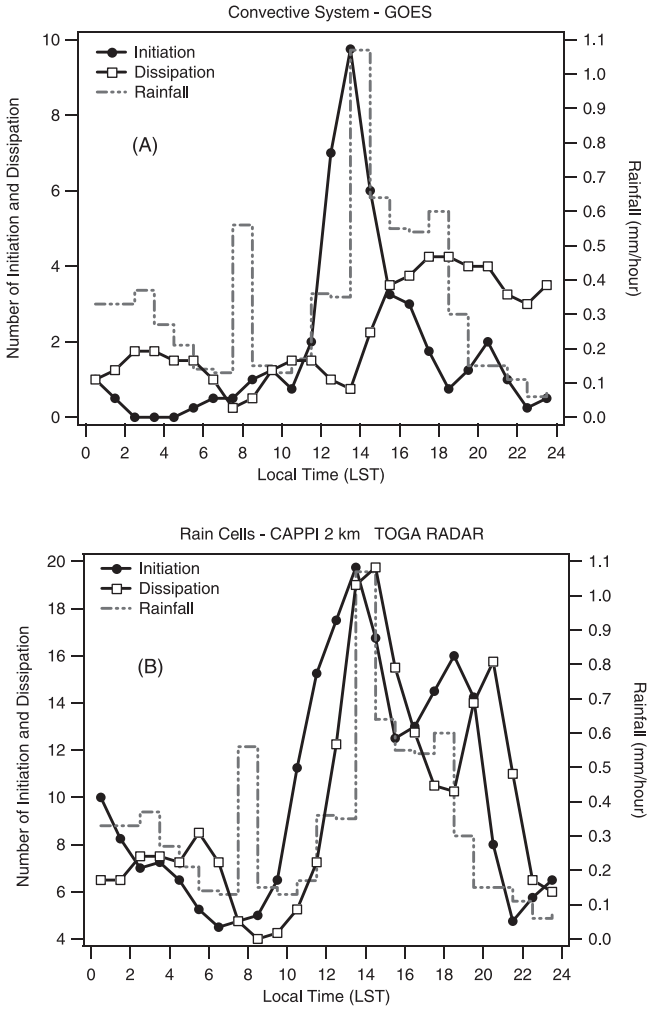


**Figure 8.** Hourly average precipitation for the 4 networks and the number of initiation and dissipation of the convective system (a) and rain cells (b).

neous initiation. The maximum merge occurred two hours after the maximum initiation at the time of the maximum high cloud fraction (figure not shown). It points to the fact that high cloud cover and convective system size increases are partially due to the merge of individual convective systems.

[38] As discussed before the variability is higher for the rain features than for the cloudiness. The time interval between initiation and dissipation is much larger for cloud systems than for rain cells. This result shows that the mesoscale cloudiness associated to the convective system has a longer life cycle than the rain feature within the convective system. *Machado et al.* [1998] showed that the size of convective systems increases somewhat more rapidly than it decreases. They also found that the size of the convective cells embedded inside the convective systems begin to decrease 3–6 hours before the whole convective system size begins to decrease.

## 5. Thermodynamic Structure

[39] Figure 9 shows an example of the time evolution of the ensemble of parameters described in the previous section over a 24 hours period. The sequence from 16 February 1200 LST to 17 February 1200 LST was chosen because it is well representative of the mean pattern. The minimum total cloud cover, for the day 16, occurs around 1300 LST; one hour later we observe an important increase in the convective rain and high cloud fraction, associated with a large amount of precipitation at about 1500 LST. Two hours later the high cloud cover reaches its maximum associated with weak precipitation. The total cloud cover presents a secondary maximum, 3 to 5 hours after the precipitation peak, followed by a decrease around 2300 LST. At this time the total cloud cover increases again and neither more rain fraction nor high cloud cover is observed. During the morning, cloud cover rapidly decreases to reach its minimum around 1200 LST.

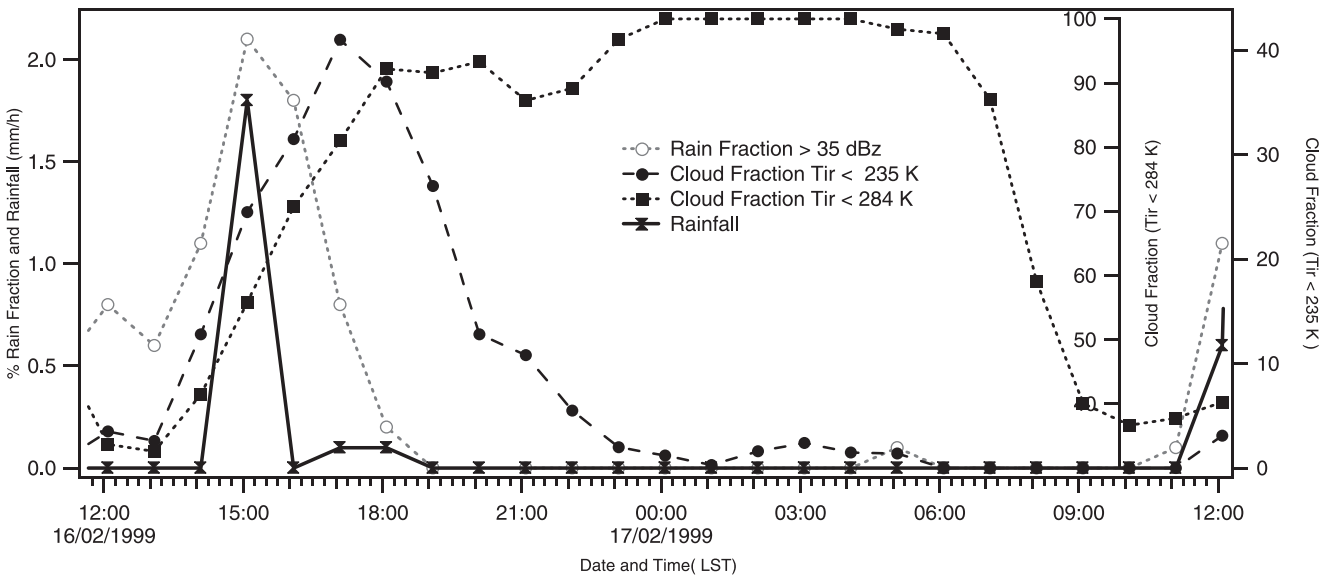


**Figure 9.** Evolution of the rain fraction (>35 dBZ), cloud fraction (<284 K), cold cloud fraction (<235 K), and rainfall (the average 4 networks) from 16 February at 1200 LST to 17 February at 1200 LST.

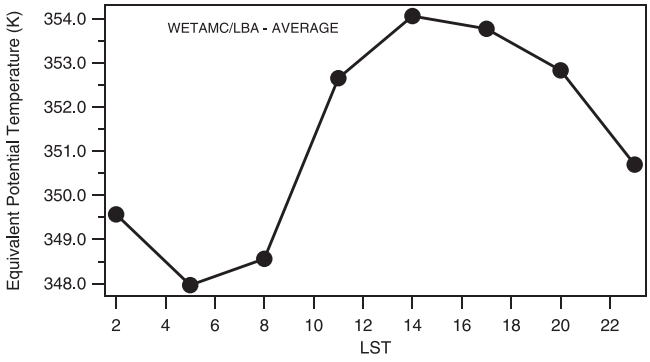


**Figure 10.** Hourly average for all radiosonde sites of the surface (the first 40 hPa layer) equivalent potential energy.

[40] As shown by radar and rain gauge data, precipitation occurs very rapidly in the early afternoon close to the time of minimum total cloud cover and at the time when high and convective clouds have the maximum area fraction increase rate and also when the initiation of convective systems and rain cells are the most numerous. The question that rises is why the maximum precipitation occurs just at the time of initiation when rain cells have a small size. It suggests that this explosive precipitation occurs because at this time the precipitating processes are very efficient; the large amount of water vapor advected in the convective towers is rapidly precipitated. Other studies [e.g., *McAnelly et al.*, 1997] have also observed the heaviest rainfall occurring near the time of convective initiation. At the early stage of convection, precipitation seems to be very efficient but later this efficiency decreases because part of the water vapor flux is advected to feed the stratiform anvil of the convective systems. *Gamache and Houze* [1983] studying GATE squall lines concluded that horizontal transfer of liquid water from convective towers into stratiform region of the cloud system created the majority of stratiform cloud.

[41] Another question that raise is why precipitation occurs in the early afternoon close to the time of minimum total cloud cover and why precipitation and high and convective cloud cover decreases in the end of the afternoon. The diurnal cycle of radiative forcing ultimately causes diurnal variations in the cloudiness. The large magnitude of the diurnal variation in insolation affects indirectly the surface radiation budget. The interaction of cloudiness and insolation depends on the thermodynamic characteristics of the atmosphere. To answer these questions this section discusses the thermodynamic characteristic observed during the experiment.

[42] The thermodynamic characteristics of the WETAMC/LBA are based on the analysis of the vertical profiles of temperature and humidity. Because surface measurements are very dependent on the local conditions and independent of the radiosonde measurements the first radiosonde level was computed as the average of the first 40 hPa layer (typical height of the mixed layer) to give an information not biased by surface observations and representative of the mean mixed layer conditions.

[43] Thermodynamic plays an important role in the energy exchanges in the atmosphere. The energy supplied for convection depends on the properties of the boundary layer and on the environment temperature. One of the most common parameters to analyze the energy available in the boundary layer to generate convection is the convective available potential energy (CAPE). The CAPE is useful to measure the amount of buoyancy in the atmosphere to drive updrafts. The CAPE was largely used to study deep convection [e.g., *Zipzer and LeMone*, 1980; *Jorgensen and LeMone*, 1989; *Mapes and Houze*, 1992; *Williams and Renno*, 1993].

[44] The present analysis was performed calculating the thermodynamic parameters for each site, based on work by *Bolton* [1980], *Emanuel* [1994], and *Wallace and Hobbs* [1977]. The CAPE was computed considering a pseudo-adiabatic process of an unmixed parcel ascending in the atmosphere (see equation (4)). Instability ($N^2$) was calculated as the Square of Brunt Vaisala frequency (see equation (5)). The thickness of the positive buoyancy layer [TPBL] was calculated as the difference between the LFC (Level of Free Convection), the first level when the parcel is warmer than the environment, and the LNB (Level of Neutral Buoyancy), the first level (after LFC) when the parcel is colder than the environment. The inhibition, the layer in which the parcel needs energy to move up because of the negative buoyancy, was computed as the difference between LCL (Lifting Condensation Level) and LFC.

$$CAPE = \int_{LFC}^{LNB} R_d\left(Tv_p - Tv_e\right) LnP \tag{4}$$

where, $Tv_p$ and $Tv_e$ are the virtual temperature of an air parcel lifted from the surface and the environment virtual temperature; $R_d$ is the dry air gas constant and P is the pressure.

$$N^2 = \frac{g}{\theta_v}\frac{\partial \theta_v}{\partial z} \tag{5}$$

where, $\theta_v$ is the equivalent virtual temperature and $\delta z$ corresponds to the difference between surface (the average of the first 40 hPa layer) and the level 40 hPa higher.

[45] The CAPE is very sensitive to small changes in the surface temperature, humidity, and pressure [*Mapes and Houze*, 1992]. However, the density profile of the upper troposphere, in the tropical regions, is more stable accounting for less significant variations and having a minor influence in the CAPE value [*Ye et al.*, 1998]. Large CAPE values are then mainly defined by surface parameters ($\theta_e$); surface parameters are strongly affected by surface fluxes (local processes) and advection (small scale downdraft or large scale subsidence).

[46] The hourly average $\theta_e$ for all radiosonde stations is presented in Figure 10. We can see that in the morning there is an important increase in the $\theta_e$ mainly at the time of the minimum total cloud cover, which corresponds also to the time when maximum solar radiation reaches the surface. Around 1400 LST, $\theta_e$ reaches the maximum value around 354 K, decreasing after 1700 LST. During the night the mean $\theta_e$ weakly changes with time, maintaining a value around 349 K. The diurnal variation of $\theta_e$, that rapidly increase with the solar insolation and reaches the maximum at the time of minimum total cloud cover is in good agreement with the convective activity and the time of the maximum precipitation.

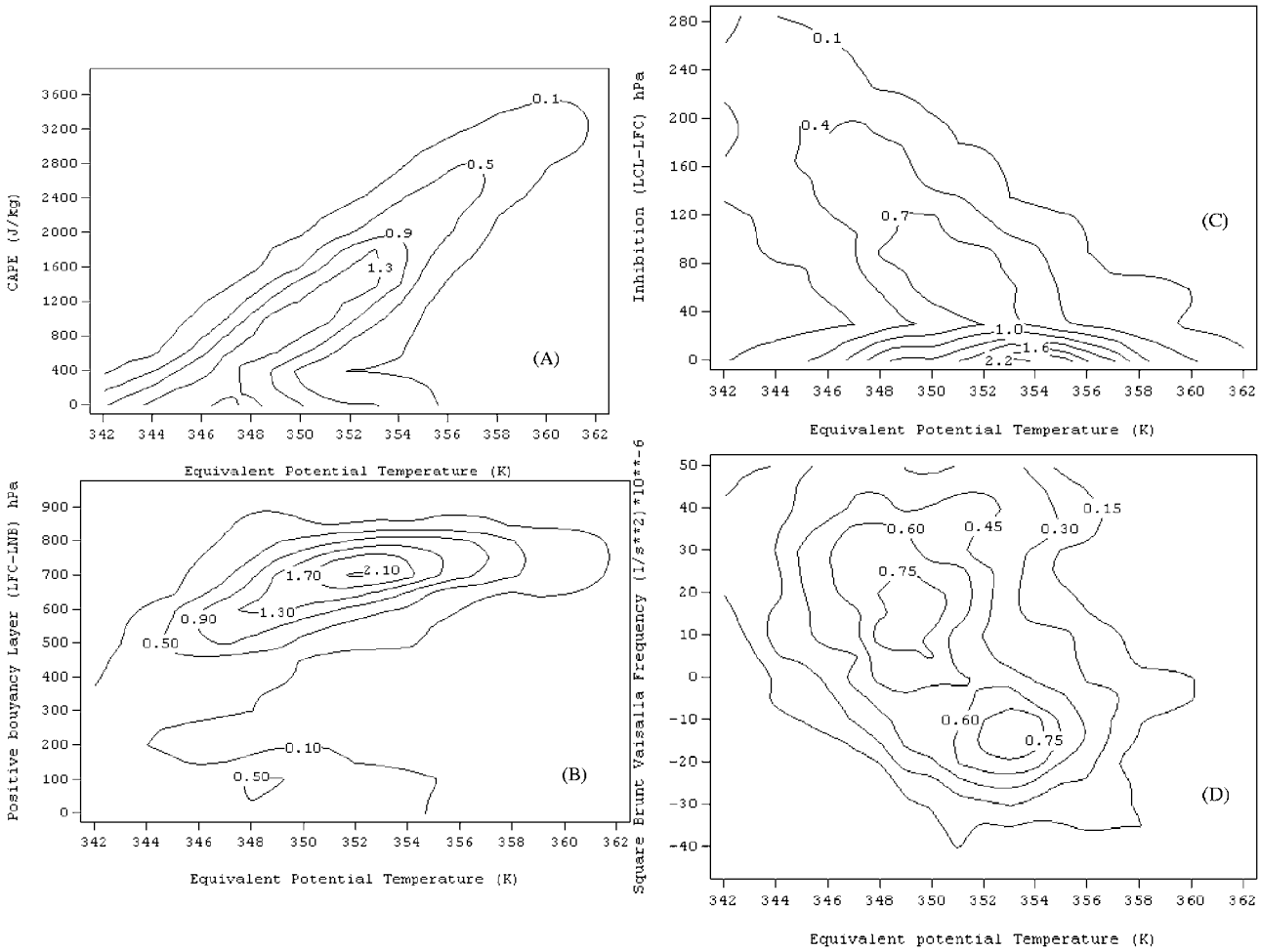


**Figure 11.** Relationship between surface (the first 40-hPa layer) equivalent potential energy, for all sites, and CAPE (a), the thickness of the layer between level of free convection and level of neutral buoyancy (b), the thickness of the layer between the lift condensation level and the level of free convection (c) and the Square of the Brunt Vaisalla Frequency (d). Values correspond to the probability of occurrence.

[47] Figure 11 shows the relationship between $\theta_e$ and CAPE (Figure 11a), TPBL (Figure 11b), Inhibition (Figure 11c) and the square of the Brunt Vaisala frequency (Figure 11d).

[48] A linear relationship between CAPE and surface $\theta_e$ or θw was proposed by *Mapes* [1993] and *Williams and Renno* [1993]. *Ye et al.* [1998] using GCM model showed that the almost perfect linear relationship between CAPE and wet-bulb potential temperature (θw) is primarily due to the surface evaporation. The analysis of our data is coherent with this quasi-linear relation between CAPE and $\theta_e$. However, we note that for $\theta_e$ values smaller than about 356 K two features can be identified: One is a linear relation between CAPE and $\theta_e$ and the other is CAPE close to zero independently of $\theta_e$. However, for larger $\theta_e$ values, larger than 356 K, a linear relation is well adapted and corresponds to the population of large CAPE. These large CAPE values mainly occur in the early afternoon in agreement with the hourly evolution of the $\theta_e$ as shown in Figure 10.

[49] Figure 11b shows $\theta_e$ as a function of the TPBL. As for Figure 11a, we can observe two different behaviors: For the TPBL between 150 and 800 hPa, the TPBL increases exponentially as a function of $\theta_e$. For TPBL smaller than 150 hPa $\theta_e$ is not function of the TPBL. Small values of CAPE are more associated to the TPBL than the $\theta_e$ (not shown). It seems that CAPE is a function of $\theta_e$ when the atmosphere is far from its equilibrium state; otherwise the CAPE strongly depends on the atmosphere temperature and humidity profiles. The population of TPBL smaller than 150 hPa is the same as the CAPE uncorrelated with $\theta_e$. It seems that the atmosphere first reaches the equilibrium state to decrease the surface $\theta_e$ later. These results suggest that the surface equivalent potential temperature increases due to the surface flux as a result of the large amount of solar energy reaching the surface in the morning and as a consequence TPBL and CAPE increase. The CAPE increases as $\theta_e$ increases by increasing the magnitude of the buoyancy in each pressure level. In the early afternoon when large CAPE ($\theta_e$) values are found, convection develops changing the environment, modifying the structure of the atmosphere toward the reference of quasi equilibrium state. Parcels rising in the atmosphere have less and less buoyancy

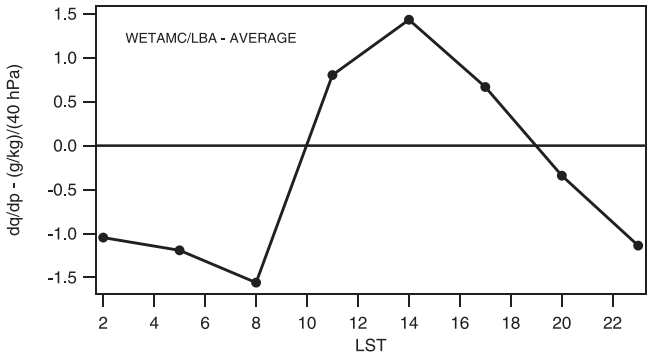


**Figure 12.** The diurnal cycle of the specific humidity gradient between the first 40-hPa layer and the subsequent layer 40 hPa higher, computed for all sites.

because the environment becomes nearly saturated, close to the equivalent potential temperature of saturation.

[50] The air close to the surface when rising adiabatically has negative buoyancy up to its LFC (except when the surface temperature reaches the convective temperature). This layer of negative buoyancy is essential to prevent spontaneous release of available potential energy and to accumulate potential buoyancy energy [*Emanuel et al.*, 1994]. If the existence of a negative buoyancy layer is substantial to the convection (mainly to the organization of the convection) it is an inhibition for the convective processes. The height of the LFC defines the degree of inhibition, i.e., the quantity of energy that needs to be supplied to the surface air parcels to reach the layer of positive buoyancy. Figure 11c shows the relationship between inhibition, computed as LCL-LFC, and $\theta_e$. We can observe a nearly linear relation; large $\theta_e$ values, especially those close to the early afternoon $\theta_e$ value (>356 K) are associated with a thin layer of negative buoyancy.

[51] The relationship between $\theta_e$ and the instability, here presented as the square of the Brunt Vaisalla frequency (Figure 11d) also shows a nearly linear relationship with $\theta_e$ although with a larger dispersion; however, $\theta_e$ values larger than 356 K are mainly associated with an unstable boundary layer.

[52] Results from Figure 11 show how the insolation after the sunrise modulates the thermodynamics. We can notice a positive feedback: In the morning insolation increases and cloud cover decreases increasing the energy reaching the surface, up to the time of the beginning of the convection; the higher the $\theta_e$ the lower the inhibition, the higher the CAPE and the more unstable the atmosphere, favoring the development of the convection.

[53] The relationship between $\theta_e$ and high cloud fraction (not shown) demonstrate that the majority of high values of $\theta_e$ are associated with small high cloud fraction. When the cloud cover is high, $\theta_e$ (CAPE) has already been used to move the atmosphere to the equilibrium state. *Reed and Recker* [1971] studying Easterly Waves during GATE and *Mapes and Houze* [1992] studying mesoscale convective systems during the EMEX also found low values of CAPE associated with high cloud cover. This behavior explains the difference of about two hours between the $\theta_e$ maximum and the maximum of high cloud cover described in the previous section. The time needed by the convection to adjust to the reference profile is discussed by *Betts and Miller* [1986].

[54] The net vertical flux of water vapor across the boundary layer is proportional to the specific humidity gradient. The rate of transfer of water vapor in the boundary layer (evaporation) depends on many factors as, for example, the surface roughness and the vertical gradient of specific humidity. *Peixoto and Oort* [1992] estimated the evaporation (E) as a gradient flux by the relation:

$$E = -\rho\alpha_w \frac{\partial q}{\partial z} \tag{6}$$

where $\alpha_W$ is the molecular diffusivity for water vapor, $\rho$ is the air density near surface, and q is the specific humidity of saturation in the boundary layer.

[55] Figure 12 shows the diurnal cycle of the specific humidity gradient (pressure coordinate). We can notice that the maximum water vapor flux in the boundary layer occurred in the early afternoon followed by a rapid decrease. After 1800 LST up to 1000 LST, in the next morning, we do not observe, in the average, water vapor flux from the surface to the atmosphere. When $\theta_e$ is higher the specific humidity gradient ($\delta q/\delta p$) is positive and a larger evaporation or a water vapor flux in the boundary layer is expected. For the conditions of low $\theta_e$ values $\delta q/\delta p$ is nearly zero or negative decreasing or extinguishing the water vapor flux to the atmosphere.

[56] For the majority of the cases, the convection is initiated by small-scale updrafts mainly during the time of minimum cloud cover, when values of $\theta_e$ are large (high CAPE, atmosphere unstable, deep layer of positive buoyancy and small layer of inhibition), initiating a large number of convective cells. When the cloud cover increases, the convection acts as a negative feedback damping the convection, saturating the boundary layer and extinguishing the water vapor flux. While the convective cloud cover is important the surface is nearly saturated and the lower atmosphere is strongly stable (not shown). The downdrafts stabilize the subcloud layer by cooling and drying the atmosphere. *Yano and Emanuel* [1991] improved the WISHE model [*Emanuel*, 1987] by explicitly taking into account this feature. After convection reached the maximum activity, the nearly saturated subcloud layer can be explained by three processes: (1) the evaporation of the precipitation in the subcloud layer, not taken into account in the WISHE model, is an important parameter in the moist entropy budget. (2) The effect of cooling by downdraft, decreasing the mixing ratio of saturation, is more important than the drying effect that decreases the sub cloud layer mixing ratio. (3) Surface flux of water vapor feeds the subcloud layer and this one feeds with water vapor the deep troposphere. When the specific humidity gradient in the lower atmosphere is nearly null, the boundary layer cannot export this water vapor and become saturated.

[57] Based on the discussion above, we propose the following hypothesis to describe the behavior of the local convection in the Amazon Basin: During the night the surface temperature decreases by radiative cooling building a low level inversion and decreasing the boundary layer height. However, the large amount of cloud cover observed at this time, limits the radiative cooling, which may explain the small differences between pasture and forest sites (Fisch

et al., submitted manuscript, 2001). The Amazon region receives more solar radiation than it loses by radiative cooling, and as the atmosphere is in statistical equilibrium, the atmosphere exports this excess of energy by convection. The high cloud cover during the night reduces the OLR (Outgoing Longwave Radiation) therefore the atmosphere needs more convection to export this excess of energy stored during the night. During the first hours of the day the heating of solar radiation breaks the low level inversion, and the boundary layer rapidly increases [*Fisch*, 1996]. Cloud cover decreases in the morning, which increases the solar flux reaching the surface, and consequently increases the equivalent potential energy. At this time, the boundary layer has the possibility to receive large amounts of water vapor by surface latent flux (it is essentially unsaturated and there is large gradient of specific humidity - Figure 12). If the surface reaches the convective temperature or if there is an orographic forcing (*Laurent et al.* [2001], show the importance of the orography in the convection generation during the TRMM-WETAMC/LBA) the air parcel can rise even without any large-scale forcing. Consequently the LFC decreases, the surface wind increases by boundary layer convergence which increase evaporation and convection rapidly develops. After the convection is developed, the atmosphere profile is modified to the nearly saturated state; the boundary layer becomes saturated and very stable, decreasing the surface flux and consequently extinguishing the convection.

## 6. Summary

[58] The TRMM-WETAMC/LBA experiment provides an opportunity to study the tropical convection in the Amazon Basin. The combination of different instrumentations such as radar, satellite images, rain gauge network, and radiosondes is a unique and robust database for fundamental studies of cloud and precipitation processes. This work studied the diurnal variation of the different types of clouds observed by satellite, intensities of rain cells observed by radar and precipitation and their relationships with thermodynamic parameters.

[59] High and convective cloud areas reach their maximum some hours after the maximum rainfall detected by rain gauge and radar 2 km CAPPI. The minimum cloud cover occurs only a few hours before the maximum of precipitation and the maximum cloud cover occurs during the night. The maximum rainfall takes place at the time of the maximum number of initiation of the convective systems observed by satellite and rain cells observed by radar. Rain cells have a typical lifetime of about one hour but for convective systems, dissipations take place from 3 to 11 hours after initiation with a dissipation maximum occurring about 5 hours later. At the time of maximum of precipitation (and rain fraction) the majority of the convective systems and rain cells are small sized and present the maximum increasing rate.

[60] The diurnal evolution of the equivalent potential temperature also presents a very clear diurnal variation with a maximum occurring in the early afternoon. The CAPE is well related to the $\theta_e$; when $\theta_e$ is high (above 356 K) CAPE values are high, the atmosphere is unstable, a deep layer of positive buoyancy is developed and the inhibition layer is very shallow. About four-five hours after the precipitation maximum, high-level cloud fraction reaches its maximum, $\theta_e$ decreases, and the atmosphere boundary layer reduces the water vapor flux to the atmosphere.

[61] The general description above, suggests the following mechanism controlling the diurnal cycle of convection: In the morning, the cloud cover decreases as the insolation and solar flux reaching the surface increases and consequently $\theta_e$ also increases. The boundary layer has the ability to receive a large amount of water vapor by surface latent flux because there is a large specific humidity gradient. In the early afternoon the convection develops rapidly, the high and convective cloud fraction increase rapidly, and the maximum of precipitation and initiation is observed. The large amount of water vapor advected in the convective towers is rapidly precipitated. It is suggested that the latent heat released by the convective towers in the middle atmosphere will contribute to a later development of large cloud clusters. These hypotheses explain the later maximum in convective and high cloud fraction and the large number of convective systems merge and the precipitation reduction. The precipitation efficiency decreases probably because part of the water vapor flux is advected to the anvil creating the stratiform parts of the convective systems. Between the initiation and the dissipation of the convective systems the atmosphere profile is modified to reach a nearly saturated state; the boundary layer becomes saturated and very stable, which inhibits the surface fluxes and consequently extinguishes the convection.

[62] **Acknowledgments.** This study was supported by Conselho Nacional de Desenvolvimento Cientifico e Tecnólogico (CNPq), Brazil/Institut de Recherche pour le Développement, France (IRD) cooperative project grant 910153/98-1. The work has also received financial support from the Fundação de Amparo à Pesquisa do Estado de São Paulo (FAPESP) grant 99/06045-7 and FAPESP grant 1997/9926-9. The authors especially thank Carlos Morales and Dirceu Herdies for the radar and satellite data process and all the participants of the LBA campaign, especially Maria Assunção F. Silva Dias for her effort and dedication in managing the Brazilian components of the experiment. We would like to thank William Rossow and the anonymous reviewers for their comments and suggestions to the manuscript.

## References

Betts, A. K., and M. J. Miller, A new convective adjustment scheme, part II, Single column tests using GATE wave, BOMEX, ATEX and arctic airmass data sets, *Q. J. R. Meteorol. Soc.*, *112*, 693–709, 1986.

Bolton, D., The computation of equivalent potential temperature, *Mon. Weather Rev.*, *108*, 1046–1053, 1980.

Chen, S. S., and R. A. Houze Jr., Diurnal variation and life-cycle of deep convective systems over the tropical Pacific warm pool, *Q. J. R. Meteorol. Soc.*, *123*, 357–388, 1997.

Cohen, J. C. P., M. A. F. Silva Dias, and C. A. Nobre, Environmental conditions associated with Amazonian squall lines: Case study, *Mon. Weather Rev.*, *123*, 3163–3174, 1995.

Cotton, W. R., and R. A. Anthes, *Storm and Cloud Dynamics*, 880 pp., Academic, San Diego, Calif., 1989.

Duvel, J. P., Convection over tropical Africa and the Atlantic Ocean during northern summer, part I, Interannual and diurnal variations, *Mon. Weather Rev.*, *117*, 2782–2799, 1989.

Duvel, J. P., and R. S. Kandel, Regional-scale diurnal variations of outgoing infrared observed by Meteosat, *J. Clim. Appl. Meteorol.*, *24*, 335–349, 1985.

Emanuel, K. A., An air-sea interaction model of intraseasonal oscillation in the tropics, *J. Atmos. Sci.*, *44*, 2324–2340, 1987.

Emanuel, K. A., *Atmospheric Convection*, 567 pp., Oxford Univ. Press, New York, 1994.

Emanuel, K. A., J. D. Neelin, and C. S. Bretherton, On large-scale circulations in convecting atmospheres, *Q. J. R. Meteorol. Soc.*, *120*, 1111–1143, 1994.

Fisch, G. F., *Amazon boundary layer: Observation and modeling aspects*, Ph.D. thesis (in Portuguese), Dep. of Atmos. Sci., Inst. Nac. de Pesquisas Esp., São José dos Campos, Brazil, 1996.

Gamache, J. F., and R. A. Houze Jr., Water budget of a mesoscale convective system in the Tropics, *J. Atmos. Sci.*, *40*, 1835–1850, 1983.

Garreaud, R. D., and J. M. Wallace, The diurnal march of convective cloudiness over the Americas, *Mon. Weather Rev.*, *125*, 3157–3171, 1997.

Garstang, M., H. L. Massie Jr., J. Halverson, S. Grego, and J. Scala, Amazon coastal squall lines, part I, Structure and kinematics, *Mon. Weather Rev.*, *122*, 608–622, 1994.

Guedes, R. L., and L. A. T. Machado, Characteristics of the cloud cover over the South America based in satellite images (in Portuguese), *Rev. Bras. Meteorol.*, *12*, 1–19, 1997.

Hendon, H. H., and K. Woodberry, The diurnal cycle of tropical convection, *J. Geophys. Res.*, *98*, 16,623–16,637, 1993.

Janowiak, J. E., P. A. Arkin, and M. Morrissey, An examination of the diurnal cycle in oceanic tropical rainfall using satellite and in situ data, *Mon. Weather Rev.*, *122*, 2296–2311, 1994.

Jorgensen, D. P., and M. A. LeMone, Vertical velocity characteristics of oceanic convection, *J. Atmos. Sci.*, *46*, 621–640, 1989.

Laurent, H., L. A. T. Machado, C. Morales, and L. Durieux, Characteristics of the amazonian mesoscale convective systems observed from satelite and radar during the WETAMC/LBA experiment., submitted to *J. Geophy. Res.*, *107*, 10.1029/2001JD000337, in press, 2002.

Machado, L. A. T., The Amazon energy budget using the ABLE-2B and FluAmazon data, *J. Atmos. Sci.*, *57*, 3131–3143, 2000.

Machado, L. A. T., and W. B. Rossow, Structural characteristics and radiative properties of tropical cloud clusters, *Mon. Weather Rev.*, *121*, 3234–3260, 1993.

Machado, L. A. T., M. Desbois, and J. P. Duvel, Structural characteristics of deep convective systems over tropical Africa and Atlantic Ocean, *Mon. Weather Rev.*, *120*, 392–406, 1992.

Machado, L. A. T., J. P. Duvel, and M. Desbois, Diurnal variations and modulation by easterly waves of the size distribution of convective cloud clusters over west Africa Ocean, *Mon. Weather Rev.*, *121*, 37–49, 1993.

Machado, L. A. T., W. B. Rossow, R. L. Guedes, and A. Walker, Life cycle variations of convective systems over the Americas, *Mon. Weather Rev.*, *126*, 1630–1654, 1998.

Maddox, R. A., Mesoscale convective complexes, *Bull. Am. Meteorol. Soc.*, *61*, 1374–1387, 1980.

Mapes, B. E., Gregarious tropical convection, *J. Atmos. Sci.*, *50*, 2026–2037, 1993.

Mapes, B. E., and R. A. Houze Jr., An integrated view of 1987 Australian monsoon and its mesoscale convective systems, part I, Horizontal structure, *Q. J. R. Meteorol. Soc.*, *118*, 927–963, 1992.

Mathon, V., and H. Laurent, Life cycle of the Sahelian mesoscale convective cloud systems, *Q. J. R. Meteorol. Soc.*, *127*, 377–406, 2001.

McAnelly, R. L., J. E. Nachamkin, W. Cotton, and M. E. Nicholls, Upscale evolution of MCSs: Doppler radar analysis and analytical investigation, *Mon. Weather Rev.*, *125*, 1083–1110, 1997.

Miller, D., and J. M. Fritsch, Mesoscale convective complexes in the Western Pacific region, *Mon. Weather Rev.*, *119*, 2978–2992, 1991.

Minnis, P., and E. F. Harrison, Diurnal variability of regional cloud and clear sky radiative parameters derived from GOES data, part II, November 1978. Cloud distributions, *J. Clim. Appl. Meteorol.*, *23*, 1032–1051, 1984.

Peixoto, J., and A. Oort, *Physics of Climate*, 520 pp., Am. Inst. of Phys., New York, 1992.

Reed, R. J., and E. E. Recker, Structure and properties of synoptic-scale wave disturbances in the equatorial western Pacific, *J. Atmos. Sci.*, *28*, 1117–1133, 1971.

Rickenbach, T. M., Cloud top evolution of tropical oceanic squall lines from radar reflectivity and infrared satellite data, *Mon. Weather Rev.*, *127*, 2951–2976, 1999.

Silva Dias, M. A. F., et al., Clouds and rain processes ina biosphere atmosphere interaction context in the Amazon region, submitted to *J. Geophys. Res.*, *107*, 10.1029/2001JD000355, in press, 2002.

Silva Dias, P. L., and J. P. Bonatti, A preliminary study of observed vertical mode structure of the summer over tropical South America, *Tellus, Ser. A*, *37*, 185–195, 1985.

Silva Dias, P. L., J. P. Bonatti, and V. E. Kousky, Diurnally forced tropical tropospheric circulation over South America, *Mon. Weather Rev.*, *115*, 1465–1478, 1987.

Wallace, J. M., and P. V. Hobbs, *Atmospheric Science. An Introductory Survey*, 465 pp., Academic, San Diego, Calif., 1977.

Williams, E., and N. Renno, An analysis of the conditional instability of the tropical atmosphere, *Mon. Weather Rev.*, *121*, 21–36, 1993.

Wu, X., and M. A. LeMone, Fine structure of cloud patterns within the intraseasonal oscillation during TOGA COARE, *Mon. Weather Rev.*, *127*, 2503–2513, 1999.

Yano, J. I., and K. Emanuel, Improved model of the equatorial troposphere and its coupling with stratosphere, *J. Atmos. Sci.*, *48*, 377–389, 1991.

Ye, B., A. D. Del Genio, and K. K. W. Lo, CAPE variations in the current climate and in a climate change, *J. Clim.*, *11*, 1997–2015, 1998.

Zipser, E. J., and M. A. LeMone, Cumulonimbus vertical velocity events in GATE, part II, Synthesis and model core structure, *J. Atmos. Sci.*, *37*, 2458–2469, 1980.

---

H. Laurent, A. A. Lima, and L. A. T. Machado, Divisão de Ciências Atmosféricas, Instituto de Aeronáutica e Espaço, Centro Técnico Aeroespacial, São José dos Campos, SP, Brazil.

JOURNAL OF GEOPHYSICAL RESEARCH, VOL. 107, NO. D20, 8054, doi:10.1029/2001JD000337, 2002

# Characteristics of the Amazonian mesoscale convective systems observed from satellite and radar during the WETAMC/LBA experiment

Henri Laurent[1] and Luiz A. T. Machado
Divisão de Ciências Atmosféricas, Instituto de Aeronáutica, Centro Técnico Aeroespacial, São José dos Campos, Brazil

Carlos A. Morales
Department of Atmospheric Science, Colorado State University, Fort Collins, Colorado, USA

Laurent Durieux[1]
Divisão de Ciências Atmosféricas, Instituto de Aeronáutica, Centro Técnico Aeroespacial, São José dos Campos, Brazil

Received 8 January 2001; revised 16 July 2001; accepted 11 September 2001; published 4 September 2002.

[1] An objective tracking of mesoscale convective systems (MCSs) observed in full-resolution Geostationary Operational Environmental Satellite (GOES) satellite images has been applied during the Wet Season Atmospheric Mesoscale Campaign/Large-Scale Biosphere–Atmosphere (WETAMC/LBA) experiment in Amazonia from January to February 1999 to document the characteristics of the convective cloud organization in the southwestern Amazon region. The same tracking methodology was also applied to the National Aeronautical Space Administration (NASA) Tropical Ocean Global Atmosphere (TOGA) C-Band radar data in order to estimate the propagation of the convective rain cells from constant altitude plan position indicators (CAPPI) at a height of 2 km. The convective activity showed two different patterns named Easterly and Westerly regimes according to the wind flow in the 700–850-hPa layer. During the Easterly regime, MCSs and rain cells had closely related propagations. MCS as well as rain cell propagations were associated mostly to the midlevel mean flow. During the Westerly regime, the propagations of both MCSs and rain cells were much more disorganized, there was no clear relationship with the mean atmospheric flow at any level, although the rain cells have a slight tendency to propagate eastward, and the low-level rain cells propagated quite independently of the high-level cloud cover. MCS initiations were mostly driven by topography, that is, high escarpment and relatively high elevation. *INDEX TERMS:* 3374 Meteorology and Atmospheric Dynamics: Tropical meteorology; 3314 Meteorology and Atmospheric Dynamics: Convective processes; 3329 Meteorology and Atmospheric Dynamics: Mesoscale meteorology

**Citation:** Laurent, H., L. A. T. Machado, C. A. Morales, and L. Durieux, Characteristics of the Amazonian mesoscale convective systems observed from satellite and radar during the WETAMC/LBA experiment, *J. Geophys. Res.*, *107*(D20), 8054, doi:10.1029/2001JD000337, 2002.

## 1. Introduction

[2] Tropical convection is mostly organized in cloud clusters also-called mesoscale convective systems [*Cotton and Anthes*, 1989; *Houze*, 1993]. These systems have their own organization, they are not passive components in the mean atmospheric flow but rather interact with the large-scale dynamic [*Maddox*, 1983; *Hartmann et al.*, 1984; *Chen et al.*, 1996]. Over tropical ocean, mesoscale convective cloud systems have been extensively studied from field experiments. The GARP (Global Atmospheric Research Program) Atlantic Tropical Experiment (GATE) and the Tropical Ocean Global Atmosphere-Coupled Ocean/Atmosphere Response Experiment (TOGA-COARE) are probably the most important experiments already conducted. GATE was conducted in the eastern Atlantic [*Martin and Schreiner*, 1981] and more recently TOGA COARE in the western Pacific [*Chen et al.*, 1996]. Observational evidence from TOGA COARE showed new features in the convective system organization such as superclusters originally identified by *Nakazawa* [1988] [*Mapes and Houze*, 1993] and the two-day oscillation [*Chen et al.*, 1996]. Less attention has been paid to the convective systems over tropical land. In South America, the Amazon region is recognized to be one of the main centers of convective activity in the global tropics. Two experiments including a large-scale component were recently conducted in the Amazon region: the Amazon

[1]Also at Institut de Recherche pour le Développement, LTHE, Grenoble, France.


0148-0227/02/2001JD000337$09.00

Boundary Layer Experiment (ABBLE-2B) [*Garstang et al.*, 1990; *Cohen et al.*, 1995] and the Amazon water vapor Flux (FluAmazon) [*Rocha*, 1991], which provided a better understanding of the oceanic water vapor flux [*Rocha*, 1991], of the Amazonian squall line development and propagation [*Garstang et al.*, 1994; *Greco et al.*, 1994] and of the Amazon energy budget during convective or nonconvective conditions [*Machado*, 2000].

[3] More recently, the Wet season Amazon Mesoscale Campaign (WET-AMC) held in January–February 1999 as part of the Large-Scale Biosphere–Atmosphere experiment (LBA) has provided an extensive set of observations of the physical climate in southwestern Amazon [*Silva Dias et al.*, 2002]. Several other instruments to measure precipitation as part of the ground validation of the Tropical Rainfall Measuring Mission (TRMM) satellite [*Simpson et al.*, 1998] were also set up with WETAMC [*Petersen et al.*, 2001]. This field campaign took place in the Rondônia state in Brazil during January and February 1999. The combined WETAMC/LBA and TRMM/LBA campaigns represent a major effort to understand the tropical convection in the Amazon and its relation to the underlying forested and deforested regions [*Silva Dias et al.*, 2000]. The knowledge of the convection in the Amazonian region should contribute to a better understanding of the continental tropical convection. Moreover, there is no physical, robust convective scheme available to represent properly in General Circulation Models (GCMs) the convection at various scales and for the different regions of the globe. Subsequently, observational studies are essential to better understand the organization of the convection viewing to improve the convective schemes used in atmospheric models, such as the representation of organized convection in GCMs [*Moncrieff and Klinker*, 1997; *Su et al.*, 2000].

[4] Throughout the globe, satellite measurements are extensively used to study convective systems, since weather radars are not available over a large scale. Infrared and visible sensors onboard geostationary satellites are commonly used because of their high temporal resolution that makes it possible to track the cloud systems along their life cycle [e.g., *Maddox*, 1980; *Mapes and Houze*, 1993; *Chen et al.*, 1996; *Hodges and Thorncroft*, 1997; *Machado et al.*, 1998; *Mathon and Laurent*, 2001]. Few studies were devoted to South America [*Velasco and Fritsch*, 1987; *Machado et al.*, 1998]. The most widely documented convective systems are the large mesoscale convective complexes [*Maddox*, 1980; *Laing and Fritsch*, 1997, 2000]. However, they represent only a small fraction of the total convective systems.

[5] The strength of the convection is related to the thermodynamic instability, but another fundamental parameter is the low-level vertical shear of the horizontal wind that controls the organization and propagation of the convective systems [*Moncrieff and Miller*, 1976; *Franck*, 1978].

[6] There is a good relationship between cold cloud top and precipitation when averaging over larger scale and time periods. However, the relationships between cold cloud top and the underlying precipitation are not straightforward when considering fine time and space resolution. *Rickenbach* [1999] showed that the propagation of satellite-observed cold cloud shield can be decoupled from the propagation of the underlying squall line observed from radar data during TOGA COARE. This was also found in a modeling study by *Wu and Lemone* [1999].

[7] This study documents the Amazonian mesoscale convective systems during the WETAMC campaign, analyzing their signature in the satellite-observed cloud structures as well as the radar-observed rain structures. Therefore this paper aims to address the issues related to the organization and propagation of convective cloud systems relative to the low-level wind shear, or the convective cloud system initiation relative to orography and vegetation. It also aims to compare the propagation and characteristics of the cloud clusters as seen by satellite with the precipitating areas as observed by weather radar.

[8] In section 2, we describe the data sets and tracking algorithms. Section 3 describes the convective system population observed by satellite and by radar, whereas in section 4 we analyze the propagation of these systems. Section 5 deals with the generation of satellite-observed convective systems. Discussion and conclusions are given in section 6.

## 2. Data and Tracking Methodology

[9] In our study, we used the Geostationary Operational Environmental Satellite (GOES-8) infrared images (channel 4, wavelength $\sim$11 mm) available every 30 min. The images were ingested and preprocessed by National Aeronautical Space Administration-Goddard Space Flight Center (NASA-GSFC) GOES project science. The horizontal resolution of these images is 4 $\times$ 4 km at nadir. Convective systems are commonly detected in the infrared channel images of geostationary satellites. The basic assumption is that low brightness temperatures are associated with deep convection. This assumption is valid for tracking tropical convective cloud systems over their whole life cycle, since in these regions thick cirrus are likely to be generated by deep convection. In this study, no attempt is made to distinguish between the convective and the stratiform regions of the convective cloud systems. However, the very deep convective areas that can be embedded in the convective shields are generally associated with high top clouds and therefore a colder brightness temperature [*Fu et al.*, 1990; *Machado and Rossow*, 1993]. We use the threshold 235 K to detect the mostly convective high level cloud cover (cold cloud hereafter) and the threshold 210 K to detect the mostly deep convective very high level cloud cover (very cold cloud hereafter). A discussion on the selection of these thresholds can be found in the work of *Machado et al.* [2002].

[10] The cloud cluster tracking method is detailed in the work of *Mathon and Laurent* [2001]. The main points can be summarized as follows:

- In a given image at time t every cluster of pixels with brightness temperature smaller than 235 K is identified and its morphological and radiative characteristics are calculated. The small cloud clusters are not considered for tracking because of the time interval between two successive images. The cut-off is set at 200 pixels, i. e., about 3500 km$^2$. The remaining cloud clusters are called Mesoscale Convective System (MCS). Note that the term MCS is used here to define the cold cloud structure, not the precipitating structure.

- The same is done in the following image at time t + Dt; the matching of the MCS between the two successive images is performed by an overlapping technique as in the work of

*Williams and Houze* [1987]. Every split and merge are recorded, therefore it would be possible to consider both parts of a split (or both parts of a merge) to be part of the same system, as in the work of *Williams and Houze* [1987]. Nevertheless, it was not done here because we distinguish between spontaneous generation and split generation, and between dissipation and merging end. *Mathon and Laurent* [2001] have shown that MCS splits are mostly (79% at 233 K, 93% at 213 K) due to weakening of convection and this information can be useful to analyze the variations of the convective activity. Besides, only spontaneous generations will be considered in section 5.

- In case of missing images (up to 5 h), the tracking is continued by extrapolating the missing images from the characteristics of each cluster at the previous time steps.

- We applied the same methodology using the brightness temperature threshold of 210 K, viewing to track the very cold cloud clusters larger than the size cut-off defined above.

[11] This objective tracking was performed over the whole tropical South America for the period from 11 January to 28 February 1999. The percentage of total missing images was about 8%. Most of the missing images were interpolated within the tracking routine. The tracking was not feasible during only two periods: 17 January from 0445 to 1745 UT and 21 January from 0445 to 1015 UT, representing less than 2% of the missing data.

[12] The same methodology was used to track low-level rain cells observed from meteorological surface radar. We used a data set from the NASA C-Band Doppler weather radar, known as the TOGA radar. This radar has a wavelength of 5.4 cm (5.6–5.65 GHz), a beam width of 1.65 degrees and a peak power of 250 kW. It operated with a pulse width of 2.0 ms and a gate width of 250 m. The position of the TOGA radar and the 150 km radius coverage is shown in Figure 1. Complete volume scans were performed at 10-min intervals accomplishing 11 elevations from 0.5–6.2 degrees. In our study, we used the 2-km constant altitude plan position indicator (CAPPI) based on weighted beam volumes [*Anagnostou and Krajewski*, 1997]. This methodology accounts for beam propagation, refraction and widening, according to a specified radar sampling geometry and mean refractive index profile [*Battan*, 1973]. Refractive index profiles for this study were determined using the 4/3rd earth radius model [*Doviac and Zrnic*, 1993]. The weight and the 3-D position are precomputed, based on elevation and range lookup tables for the TOGA radar scan strategy. We used CAPPIs with horizontal resolution of 5 km × 5 km limited to a range of 150 km to be consistent with the horizontal resolution obtained in the GOES IR images. Additionally, we used the final calibrated version of the TOGA radar, which removed the 4 dB calibration offset when compared with the TRMM precipitation radar [*Anagnostou and Morales*, 2002].

[13] The tracking methodology used in the satellite data was adapted to track the large echoes identified in the radar images. The size cut-off was set to 40 pixels, i. e., about 1000 $km^2$, in order to account for the radar time step (mostly 10 min, sometimes more). The maximum time interval allowed between two successive images was set to 1 h. The interpolation of missing images was not employed.

[14] We selected the reflectivity thresholds 20 dBZ and 35 dBZ that can be associated very roughly to rainfall rates of 0.5 mm $h^{-1}$ and 5 mm $h^{-1}$ respectively [*Marshall and Palmer*, 1948]. The application of a proper radar reflectivity factor and rainfall rate relationship is not so straightforward. Thus, it would be more reasonable to assume that the 20-dBZ isopleths delineate the weak precipitation, while the 35-dBZ pixels define the strong precipitating areas observed by the TOGA radar. Moreover, we simplify our radar analyses to distinguish from the satellite-observed cloud systems, and define rain cells as radar echoes (2-km CAPPI) above 20 dBZ and 35 dBZ larger than the size cut-off (1000 $km^2$). The tracking of the rain cells was performed over the period 7 January–27 February 1999. For each 20-dBZ rain cell we computed the morphological parameters as in the case of the MCS tracking, including the area of reflectivity larger than 35 dBZ. Additionally, we computed the tracking of the 35-dBZ threshold rain cells.

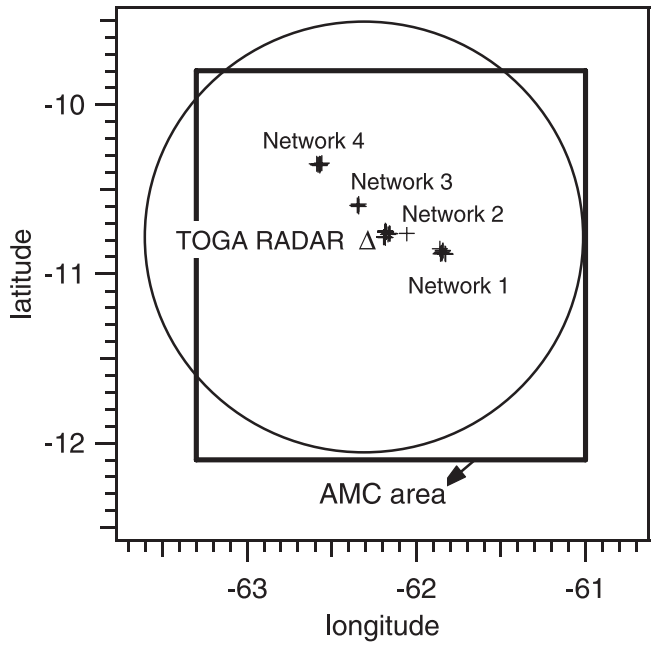


**Figure 1.** Location of the TOGA radar (Δ) and of the rain gauges (+) clustered in four networks. 150 km range of the radar (circle) and AMC area (square) as defined in this study are also indicated.

[15] This study also uses precipitation measurements from a rain gauge network of 40 tipping buckets. The spatial distribution of the LBA rain gauge network is shown in Figure 1. The gauges were distributed on four clusters to improve the radar rainfall estimation. These tipping buckets have a rainfall sampling resolution of 0.1 inches (0.254 mm). The maximum temporal resolution is of 10 s, whenever it rains. The NASA-GSFC Distributed Active Archive Center (DAAC) provided the raw precipitation measurements for each rain gauge. This data set can be accessed at http://daac.gsfc.nasa.gov. Afterward, we applied a quality control based on a cross-correlation among the closest gauges and number of tips observed in a 10 s time interval. Finally, intervals of 15 min and hourly accumulations were computed for each gauge during the entire experiment. For this study, we only used the hourly average of the entire rain gauge network.

[16] The analyses were performed over the period from 11 January through 27 February 1999 when both satellite

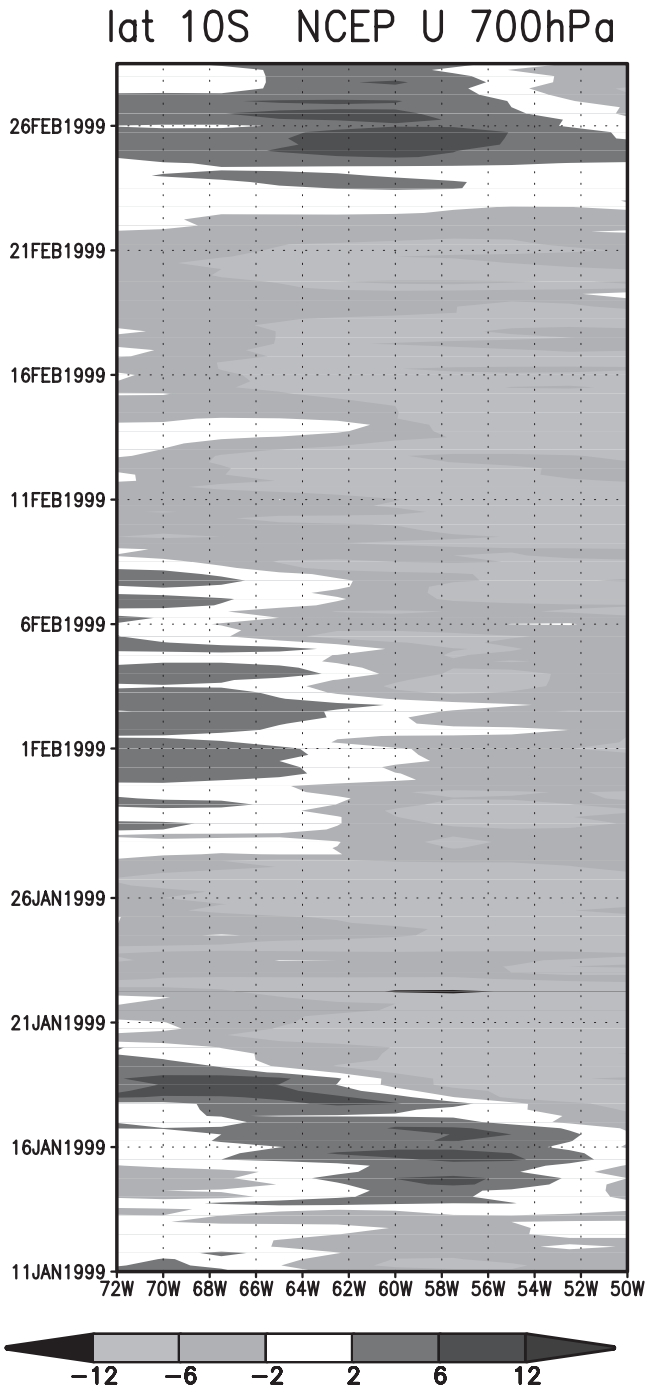


**Figure 2.** Time–longitude diagram of the zonal component of the wind ($ms^{-1}$) at 700 hPa from the NCEP reanalysis, latitude 10 S.

and radar data were available. During the WETAMC/LBA campaign, two main regimes in the convective activity were observed [*Rickenbach et al.*, 2000a]. These two regimes are closely associated with the zonal wind component in the low tropospheric layer at 850–700 hPa; hence they were named as Westerly and Easterly regimes. The Westerly regime is characterized by weaker vertical development of the convective radar echoes, large coverage of stratiform rain, and lower mean rainfall rate for both convective and stratiform rain fractions as compared to the Easterly regime [*Rickenbach et al.*, 2000a; *Halverson et al.*, 2001; *Anagnostou and Morales*, 2002]. The Easterly regime is characterized by a stronger convective activity. The convective systems are smaller with higher rain intensities [*Rickenbach et al.*, 2000a; *Anagnostou and Morales*, 2002]. As a whole the difference in the rainfall rate between the two regimes is compensated by the difference in the rain area, which produced comparable total rain amounts [*Rickenbach et al.*, 2000a].

[17] Figure 2 presents a Hovmoller diagram of the zonal wind at 700 hPa, taken from the NCEP (National Centers for Environmental Predictions) reanalysis, during the period of the study at the latitude of the experiment area. There were two clear periods of Westerlies, between 13 January and 19 January, and between 22 February and 27 February. There was also a period of weak Westerlies between 28 January and 9 February. From the zonal wind, and more importantly, from the radar observations [*Rickenbach et al.*, 2000b; *Rutledge et al.*, 2000] one can distinguish the following regime sequences for the period of 11 January–27 February:

- Westerly regime: 11–18 January; 27 January–7 February; 22–27 February; total: 26 days;
- Easterly regime: 19–26 January; 8–21 February; total: 22 days.

[18] Figure 3 shows the time evolution over the WET/AMC area of the zonal wind in a vertical section of the troposphere. During the Westerly and Easterly periods the wind pattern extends from 850 hPa to 400 hPa, except for the second Westerly period that is weakly established. At 200 hPa the wind is generally easterly with the exception of Westerlies between 22 and 25 January.

## 3. Convective System Distributions During WETAMC/LBA

### 3.1. Overview of the Convective Cloud Cover Over Tropical South America

[19] Figure 4 shows the occurrences of cold cloud top, colder than 235 K, over the window used to compute the MCS tracking. The region of the WETAMC/LBA experiment is represented by two squares. The smaller box is the AMC area defined here as a 2.3 × 2.3 degree square (9.8S–12.1S; 61W–63.3W), where the in-situ observations such as radar, precipitation and radiosondes were concentrated. The larger box is the extended AMC area, a 5-degree square used in the next section to compute the MCS statistics during the experiment. The Inter Tropical Convergence Zone (ITCZ) is noticeable over the ocean. As expected in this season, cold cloud cover is very important over the whole Amazon, from the equator to 15S. The AMC area is very far from the coast; in this region the monsoon moisture flux that comes from the tropical North Atlantic has undergone several cycles of precipitation/evaporation. Also, the Amazonian squall lines that form near the coast would generally not reach the AMC area.

[20] The mean propagation of the 235 K MCSs is shown in Figure 5 (details of the calculation can be found in the work of *Mathon and Laurent* [2001]). MCSs propagate mostly westward at 5 to 10 $ms^{-1}$ typically. According to the NCEP reanalysis data set, this propagation is consistent with the mean atmospheric flow in midlevels (around 700 hPa) rather than in low or high levels of the troposphere. Over the

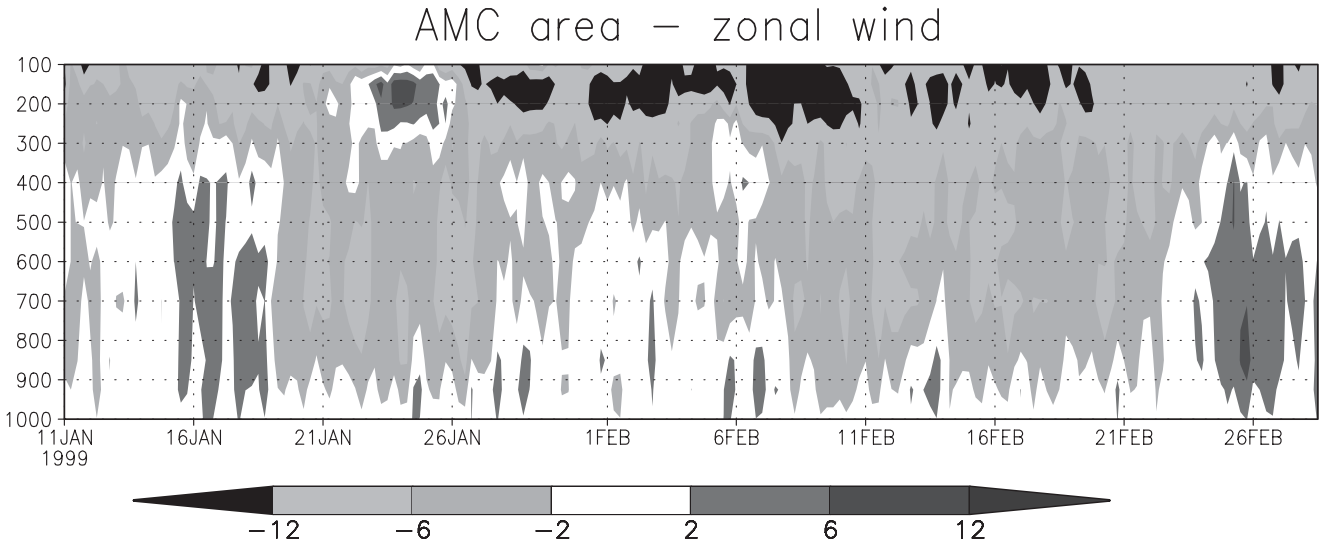


**Figure 3.** Vertical cross-section of the NCEP zonal component wind ($ms^{-1}$) over the AMC area.

AMC area in Rondônia, there is a slight decrease of the mean propagation speed. This will be further investigated in section 4.

### 3.2. MCS Distributions in the AMC Region

[21] In this section we consider only the MCSs that crossed the 5 × 5 degree region centered on the AMC area: 8 S–13 S and 59.5 W–64.5 W. They were 551 (respectively 200) for the threshold 235 K (210 K), among them 44% (12%) were split-generated and 42% (14%) ended by merging. As already mentioned most of the splits are not associated with split of distinct convective systems but rather with the weakening of the convective activity of a single system. Symmetrically most of the merges are associated with increase of the convective activity, although the actual merging of distinct convective systems is not a negligible process [*Mathon and Laurent*, 2001]. Over West Africa, the total number of splits is about 33% at 233 K and 19% at 213 K. The comparatively large number of splits found for 235 K in the AMC region is likely to be a consequence of a strong diurnal variability of the convection.

[22] MCS distributions have been computed as a function of their life duration or as a function of their size (radius). It is well known that the average size of the convective cloud clusters is closely related to their life duration and vice versa. This relationship is more or less linear as shown by *Chen and Houze* [1997] over the Pacific, *Machado et al.* [1998] over the Americas, or *Mathon and Laurent* [2001] over West Africa. In our analyses, we found that the mean radius increases by 7.5 km per hour of duration for 235 K, which is not very different from the 6 km $h^{-1}$ found by *Machado et al.* [1998] over the Americas with a threshold of 245 K and a lower resolution data set. However, the variability is very large hence a linear extrapolation cannot be used, particularly in our study due to the small sample

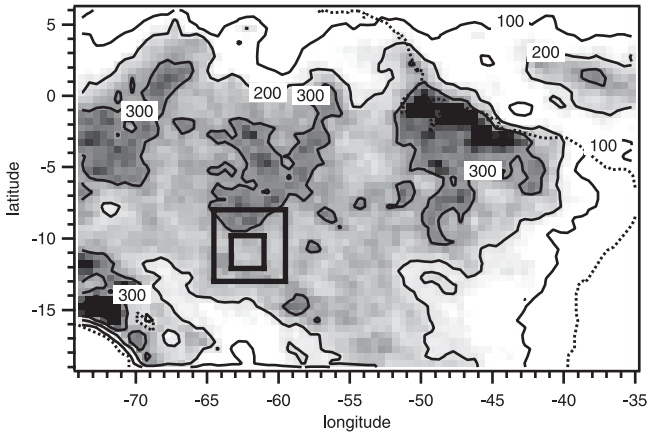


**Figure 4.** Cold cloud occurrences for brightness temperature threshold 235 K from 11 January to 27 February 1999. The AMC area and the extended 5 × 5 degree area (see text) are indicated.

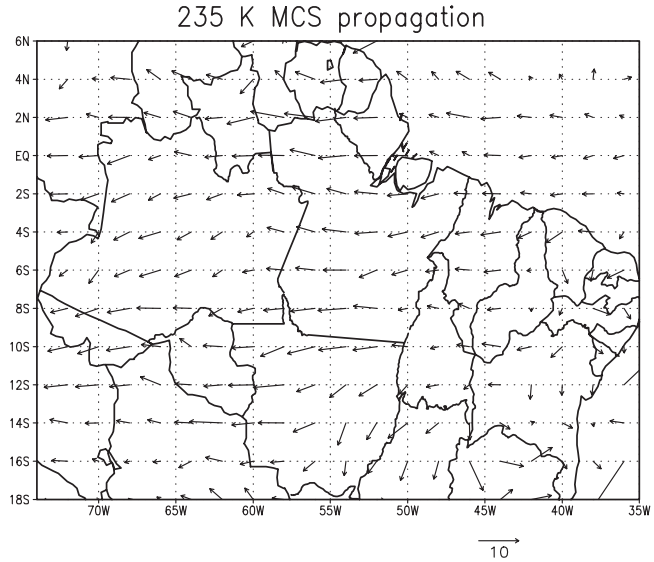


**Figure 5.** Mean MCS propagation ($ms^{-1}$) for threshold 235 K, period of 11 January–27 February 1999. Solid line indicates the state boundaries.

size. Besides it can be useful to think either in terms of life duration or size. Therefore the two sets of distributions are presented in Figure 6, as a function of the life duration on the left side, and as a function of the size on the right side. Although there are only a few hundred MCSs that does not allow for satisfying statistics, we plotted the results with logarithmic axis to facilitate comparisons with statistical results obtained over other regions of the world [*Machado et al.*, 1992; *Mapes and Houze*, 1993; *Roca and Ramanathan*, 2000; *Mathon and Laurent*, 2001].

[23] Figures 6a and 6b show the distributions of the MCS number. For the 235 K threshold the variation of the MCS number as a function of the size or the lifetime is similar to what is observed in other regions of the world. The main difference is that there are only a few long-lived clusters, with duration of more than one day. Figures 6c and 6d show the area coverage of each MCS class, expressed in $km^2$ per image, for the different ranges of duration or size. The cumulative coverage distributions integrated and normalized from Figures 6c and 6d are plotted in Figures 6e and 6f, showing the contribution of the clusters to the total cloud cover. *Machado and Rossow* [1993] have shown that for different regions the coverage of the convective cloud cluster as a function of the cluster size is almost constant up to a critical radius. Similar behavior has been observed for the cloud coverage as a function of the cloud duration [*Mathon and Laurent*, 2001]. We do observe the same effects, although the results are quite noisy due to the limited period of observation. A few long-lived clusters, with a lifetime larger than 24 h, give a noticeable contribution of about 20% to the total convective cover. However, the contribution of long-lived systems to the total cloud coverage is smaller in the AMC region than in other regions. This will be discussed in section 6.

[24] The MCS coverage as a function of the cluster size (Figures 6d and 6f) is not constant but rather increases between 40 km and 100 km, then decreases between 150 km and 200 km. There is also a noticeable contribution of 30% of the total cold cloud cover from the MCSs larger than 200 km that are likely to be associated with the fronts described by *Rickenbach et al.* [2002]. Note that the very small sized clouds are not taken into account due to the size cut-off, however this contribution is small as shown by *Mathon and Laurent* [2001].

[25] The results presented in Figure 6 can be used for the validation of models since it describes the distributions of cold cloudiness as a function of lifetime and size of the convective systems. As an example, 80% of the total cold cloud cover comes from systems having a lifetime smaller than 24 h or having a size smaller than 220 km. It is important to state that the size in Figure 6 is the mean radius along the MCS life cycle. The results would be different if we compute the distributions of cold cloud cover according to the instantaneous cluster radius, as it can be done without tracking. For example, Figure 6f shows that 50% of the cold cloudiness is in clusters with mean radii larger than 130 km; we computed that 50% of the cold cloudiness is in clusters with instantaneous radii larger than about 180 km.

[26] The total area of very cold pixels ($T < 210$ K) embedded in the 235 K MCSs (not shown) is very similar to the distribution of cold cloud in Figures 6c or 6d. The total 210 K cloud area represents about 10% of the 235 K cloud cover, whatever the lifetime or the size. This result is in agreement with the findings of *Machado and Rossow* [1993]. However, the distribution from the tracked MCSs at 210 K as shown in Figure 6 is quite different because the size cut-off inherent to the tracking methodology has a large impact at that temperature threshold. From Figures 6a, 6c, and 6e it can be seen that the 210 K MCSs with a lifetime between 2 h and 6 h are the most important in terms of very cold cloud cover, bearing 70% of the total coverage. The maximum lifetime is about 12 h. This result is quite different from what can be observed over ocean and over other continental regions and has implications for the parameterization in GCMs of convective processes in Amazonia.

[27] The 235-K and 210-K distributions are not significantly different during the Westerly and Easterly regimes. The main difference observed between the two regimes is in the very cold cloud cover. Figure 7 shows that the 210-K cloud coverage per image was about 30% larger for the Easterly regime compared to the Westerly one. This is consistent with the higher convective activity observed during the Easterly regime.

[28] We also computed the MCS speed as the mean displacement between the beginning and the end of the MCS (figure not shown). The main feature is that for all lifetime up to 10 h or size up to 150 km, the mean speed is uniform at about 10 m $s^{-1}$ for both 235 K and 210 K. The zonal component is about $-6$ m $s^{-1}$ (westward propagation); the meridian component is close to zero on average. The variability is large for long-lived and large systems when the number of systems is small, however, there is a tendency for the zonal speed intensity to be reduced for long-lived or large MCSs. This is because these large and long-lived systems were mostly associated with the fronts already mentioned. These results differ from what was found over West Africa by *Mathon and Laurent* [2001], i.e., higher speed for coldest temperature thresholds and higher speed for largest life durations. The MCS propagation will be further investigated in section 4.1.

### 3.3. Distributions of Radar-Observed Rain Cells

[29] During the period of 11 January–27 February 1999 we tracked 517 rain cells at 20 dBZ. Among these rain cells about 70% of them had a spontaneous generation, 25% a split generation and 5% unknown generation because the tracking began after a large time interval of missing data. Similar values were observed for the end of the cells as dissipation, merge or unknown end, respectively. At 35 dBZ only 44 rain cells were tracked with a small number of split or merge, about 4%, and very few unknown generation or end.

[30] The size of the rain cells increases with their life duration. A linear adjustment gives a slope of about 3.5 km $h^{-1}$, which is quite different from the value of 7.5 km $h^{-1}$ found for the 235 K MCSs. One might question what is the impact of the limited window of observation of the radar that constrains both the lifetime and the size of the rain cells on the edge of the window. Therefore we calculated the statistics excluding the rain cells that initiated or ended near the observation disk edge (i.e., more than 120 km from the radar), the split-generated and merge-ended rain cells as well as the cells that initiate or end in association with an interval of missing data, in order to select only the "pure life cycle" rain cells. The cell number

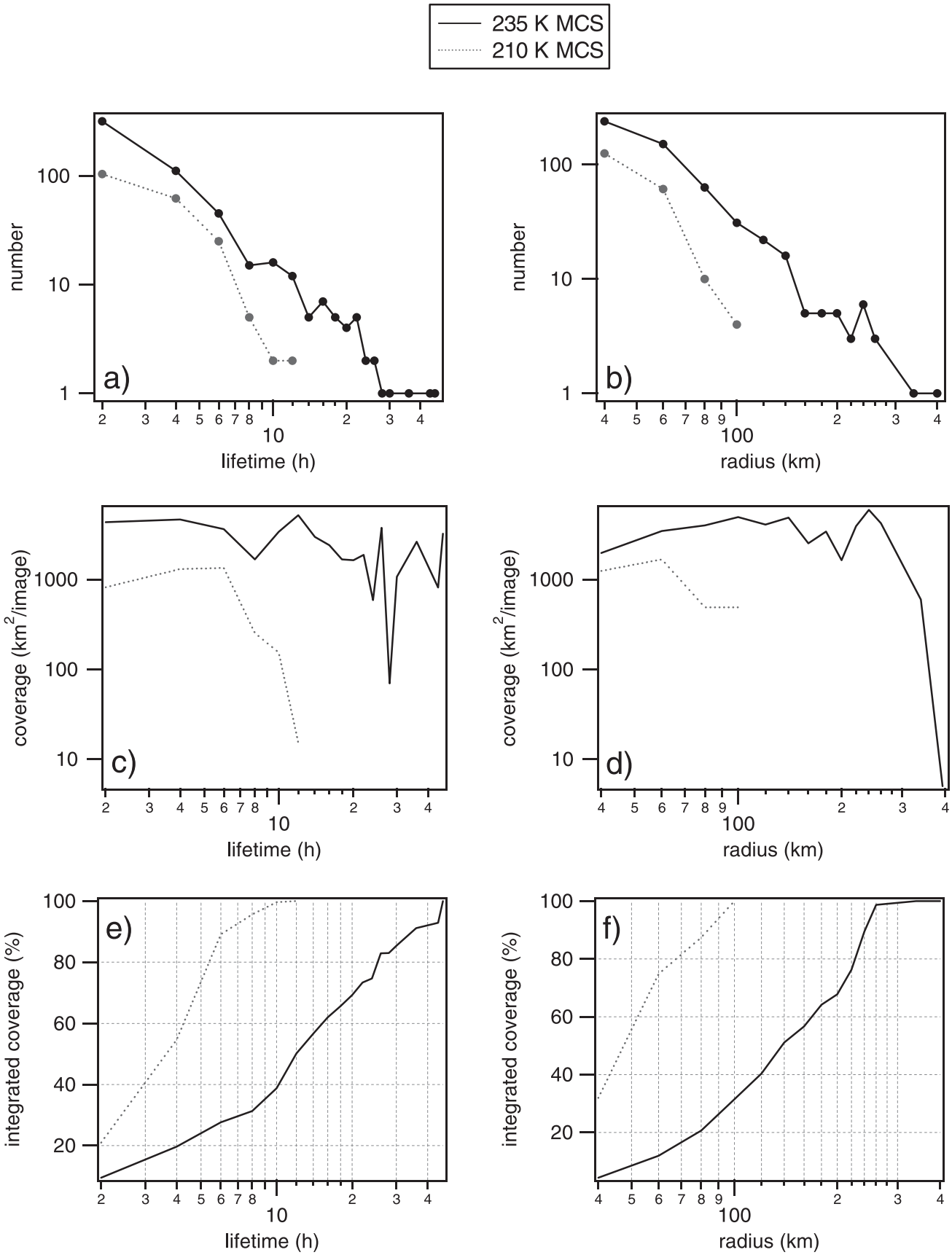


**Figure 6.** MCS distributions versus lifetime (left side) and versus mean radius (right side) for thresholds 235 K (solid line) and 210 K (dotted line). a) and b) Number of MCS. c) and d) MCS coverage ($km^2$ per image). e) and f) Integrated MCS coverage fraction (%).

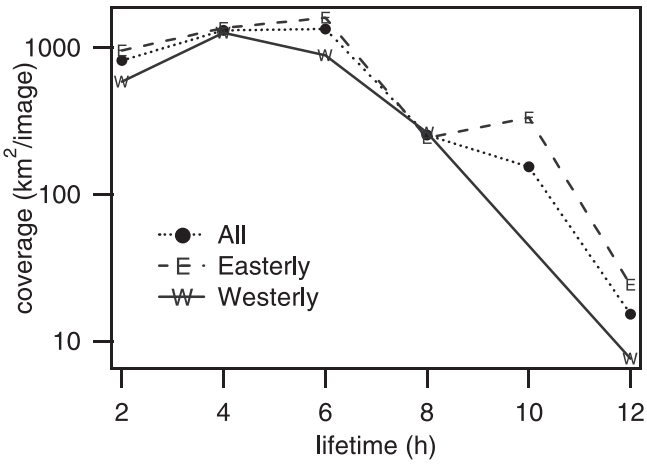


**Figure 7.** 210 K MCS coverage (km$^2$ per image) versus lifetime (h) for Easterly regime (dashed line), Westerly regime (solid line) and total period of 11 January–27 February 1999 (dotted line).

was reduced by a factor of four, however, the distributions remained similar. Figure 8 shows the radius versus lifetime for both radar-observed rain cells and satellite-observed MCSs. In this plot, only "pure life cycle" MCSs and rain cells have been taken into account. This figure shows clearly the two distinct populations of rain cells and MCSs. The slope of the linear adjustment is 3 km h$^{-1}$ for rain cells and 7.8 km h$^{-1}$ for MCSs. The behavior of the rain cell life cycle differs from that of the MCSs, as the rain cell spatial extension remains limited even in case of long duration, as already observed in other regions [e.g., *Stout et al.*, 1979]. This result has implication for the downscaling of MCSs into precipitation fields [*Guillot and Lebel*, 1999].

[31] Figure 9 shows the distributions of the rain cells tracked during the two regimes (Westerly and Easterly) and for the whole period, as a function of the cell lifetime (on the left side) and cell size (on the right side). We only present the results for the 20-dBZ rain cells because of the limited number of rain cells tracked at 35 dBZ. The number of cells (Figures 9a and 9b) is larger during the Westerly regime than during the Easterly one, however, the number of Westerly days was also larger. The number of rain cells per day is very close for the two regimes. The maximum lifetime was 14 h during the Easterly and 20 h during the Westerly where 8 cells persisted for more than 10 h.

[32] Figures 9c and 9d show the radar cell coverage, expressed in km$^2$ per image, for the different ranges of duration and size, respectively. For number of cells larger than 10, the radar cell coverage is roughly constant, as in the case of satellite-observed MCS. The coverage of the 20 dBZ rain cells is similar during the two regimes and somewhat larger during the Westerly regime as confirmed by the statistics obtained excluding the cells close to the observation disk edge (not shown). Additionally, on Figures 9c and 9d we plotted the coverage of the 35 dBZ pixels embedded into the 20-dBZ rain cells. In a first approximation, the 35 dBZ pixel coverage is about 10% of the 20-dBZ rain cell coverage for all the lifetime or the radius cells. However, differently from the 20-dBZ threshold, the 35-dBZ surface per image is two times larger during the Easterly regime than during the Westerly regime, in agreement with the higher convective activity of the Easterly regime. This is quite similar to what is observed in Figure 7 giving some consistency to the association between very cold clouds and high rain rates. The cumulative coverage distributions integrated and normalized from Figures 9c and 9d are presented in Figures 9e and 9f. About 50% of the rain cover comes from cells with duration larger than 5.5 h or radius larger than 35 km. No significant differences are observed during the two regimes.

## 4. Convective System Propagation

### 4.1. MCS Propagation

[33] In this section, we consider the propagation of the MCSs that crossed the AMC area (2.3 × 2.3 degree square). In order to filter out the systems that covered only a very small fraction of the area, the MCSs must have covered at least 3500 km$^2$ (i.e., 5%) of the AMC area or 50% of the MCS area at the corresponding time step. With this selection we found 237 MCSs at 235 K and 47 at 210 K.

[34] Figures 10a and 10b show the trajectories of the centers of the MCSs crossing the AMC area in a longitude-time diagram for 235 K and 210 K, respectively. At that scale, the main features are given by the long-lived systems, especially in the case of the 235 K MCSs (Figure 10a). They generally propagate westward at about 7 to 8 degrees per day ($\sim$ 9 m s$^{-1}$) except during the two periods of strong Westerlies: day 11 to 18 and day 53 to 58. Note that the propagation keeps on westward during the period of weak Westerly: day 27 to 38. Continuous lines in Figures 10a and 10b show when the MCS is reaching the AMC area following the in-zone criterion described above. It was observed that the AMC area was covered by cold cloud belonging to a huge convective shield whose center was very far away. This was the case at the end of day 29 and at the end of day 57.

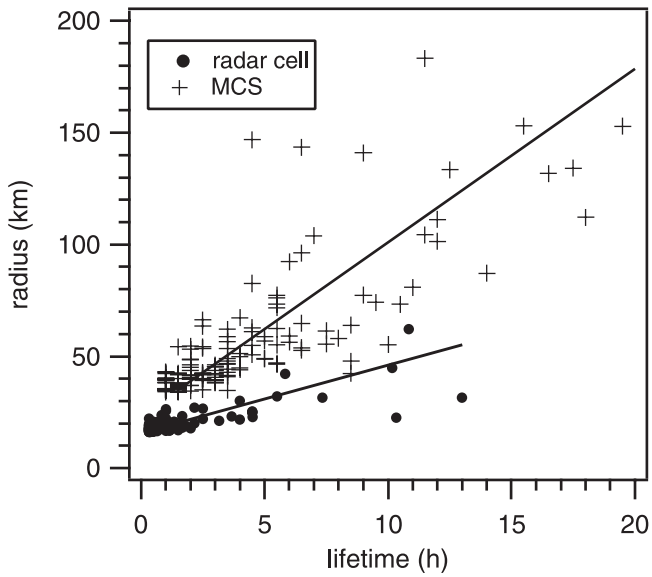


**Figure 8.** Mean radius (km) versus life duration (h) for 20-dBZ rain cells (●) and 235-K MCS (+) with spontaneous generation and dissipation. Solid lines indicate linear fitting.

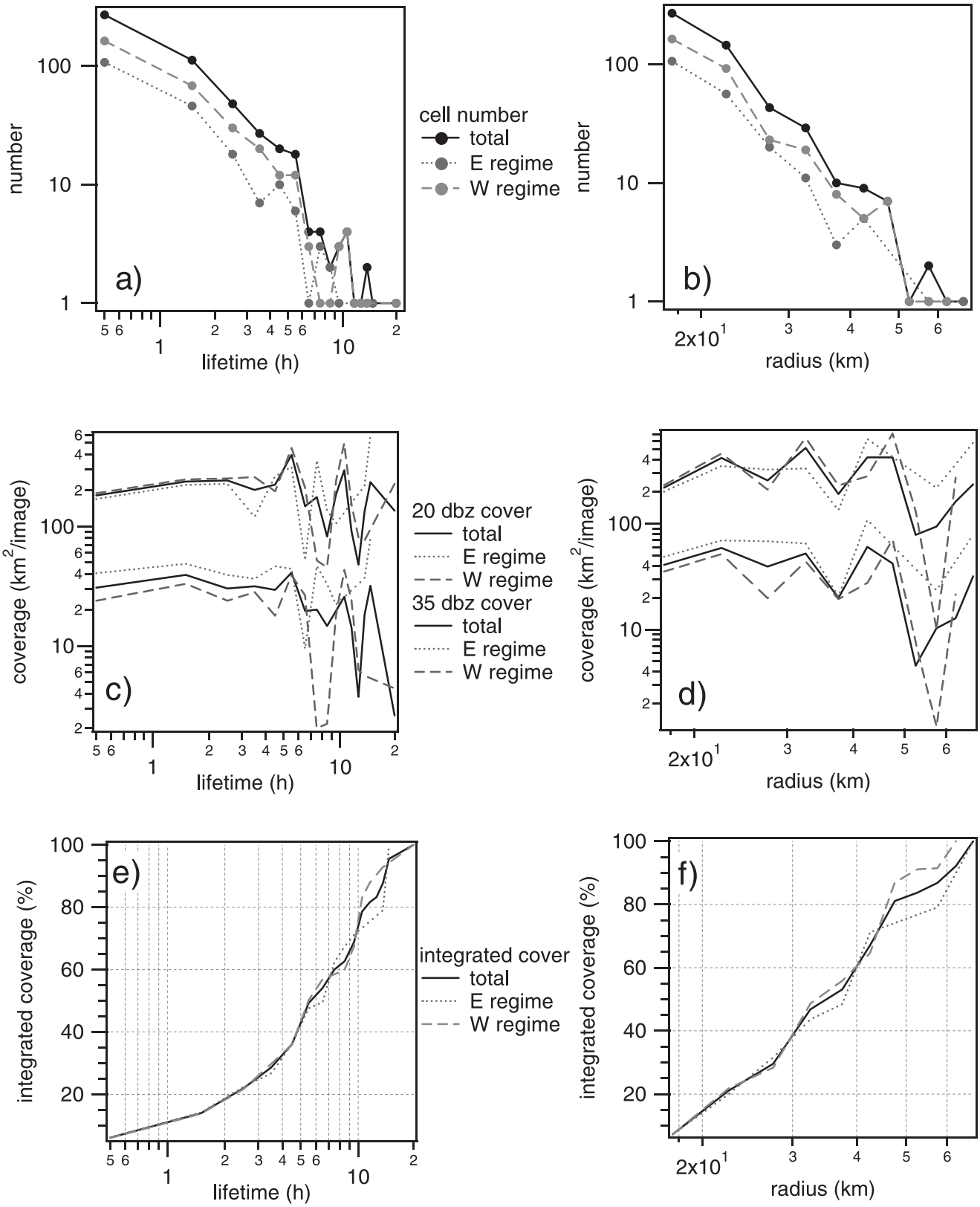


**Figure 9.** Radar-observed 20-dBZ rain cell distributions versus lifetime (left side) and versus mean radius (right side), for Easterly regime (dotted line), Westerly regime (dashed line) and total period of 11 January–27 February 1999 (solid line).

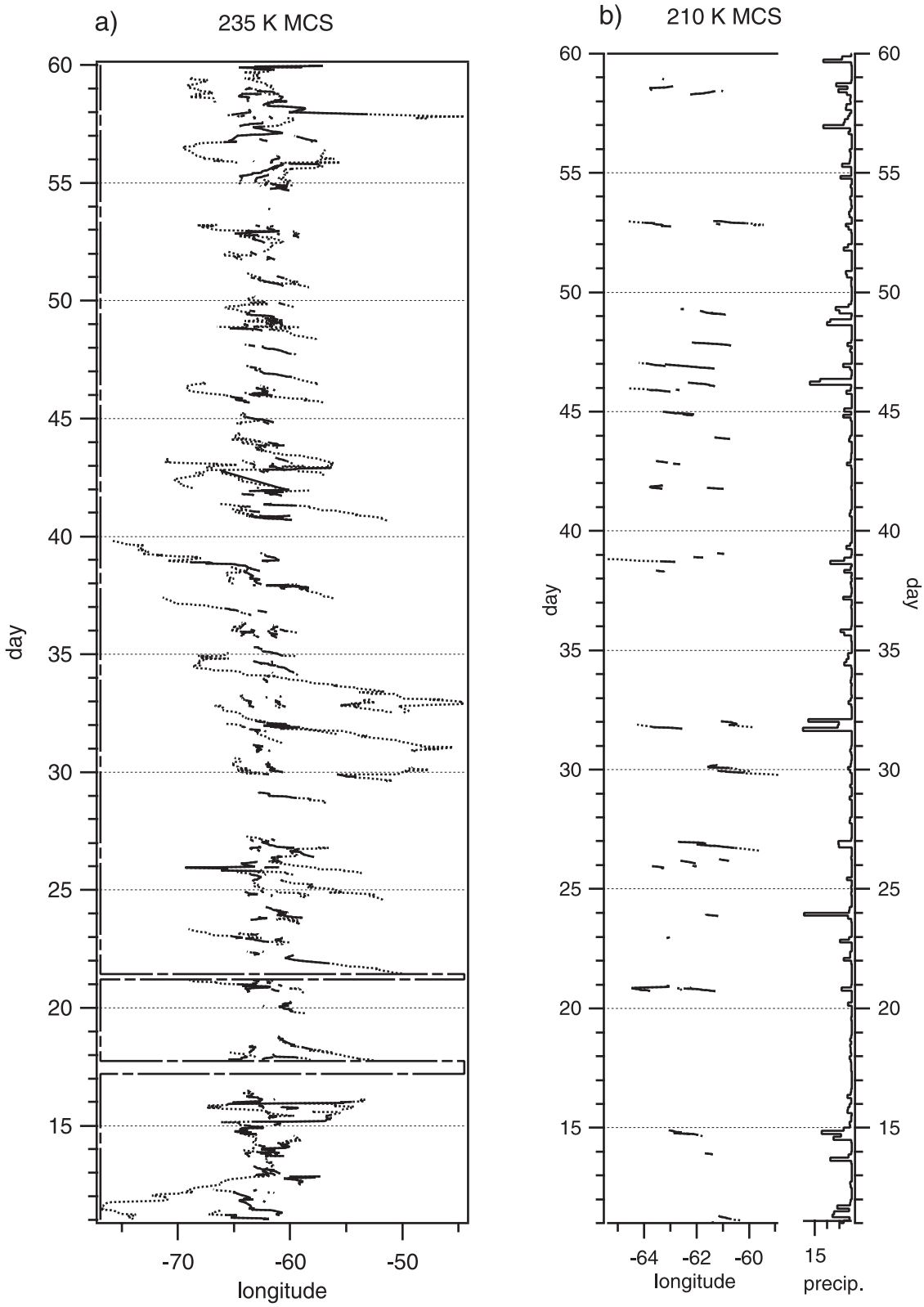


**Figure 10.** Time-longitude trajectories of the MCS crossing the AMC area between 11 January and 27 February 1999, for thresholds 235 K a) and 210 K b). The trajectory is drawn when the MCS is covering the AMC area (solid line) or not (dotted line). The interrupted line indicates when the tracking was not possible because of a large time interval of missing images. The observed 3-hourly cumulated precipitation (mm) is also plotted on the right side.

[35] The MCSs defined at 235 K generally have at least one pixel with a brightness temperature lower than 210 K. However, the clusters at 210 K with the minimum size needed for the tracking are much less numerous. Their life cycle is also much shorter, as shown in Figure 10b. The propagation of the 210 K MCSs is mostly westward, even during the first Westerly regime. Only during the last Westerly regime can an eastward propagation (day 58) be observed. In Figure 10b we also plotted the mean three hourly rainfall computed from the network of about 40 rain gauges in the AMC area. Almost every 210 K MCS is associated with rainfall, in a large range of intensity, whereas many rainfall events are not associated with any 210 K MCS.

[36] In order to analyze better the displacement of the convective clouds, the mean speed of the cloudy pixels has been estimated with the same methodology as in Figure 5. Figure 11a shows that the 235 K MCS mean propagation is mostly from east to west, with a module of about 7 m $s^{-1}$. At 210 K (Figure 11b) the mean speed is larger, about 9 m $s^{-1}$, with a larger variability due to a smaller number of MCSs. Figures 11c and 11d show the mean propagation for 235 K during Westerly and Easterly regimes, respectively. Note that both regimes display different patterns in magnitude and direction. During the Easterly regime, the cloud systems propagate uniformly westward with a speed of about 8 m $s^{-1}$. During the Westerly regime there is a large spatial variability. In the eastern part of the area, the propagation is westward at about 6 m $s^{-1}$ whereas in the western part the mean propagation is almost null.

[37] One might question whether the MCS propagation does or does not reflect the propagation of passive cirrus advected in the high tropospheric flow. Indeed the 200-hPa wind as described in the NCEP reanalysis is generally from west-southwest over the region of study, which is controlled by the Bolivian High. However, between 21 and 26 January there was a dramatic change in the high-level circulation and the wind became southeasterly. The zonal component of the 200-hPa wind was larger than +6 m $s^{-1}$ over the AMC area between 22 and 25 January, as can be seen in Figure 3. The trajectories in Figure 10 do not show any clear change during this period. The MCSs propagate mostly westward, which is more consistent with mid to low-level flow than with high levels. Actually, the midlevel flow is important because it induces a vertical shear in the low troposphere. However, during the Westerly regimes the MCS trajectories are not totally consistent with the midlevel flow but rather tend to keep on westward. For example, on days 14 to 16 the 235 K MCSs do not show preferential direction of propagation and a 210 K MCS propagates westward, opposite to the midlevel flow. This can be related to a weak low-level wind shear. To summarize, during Easterly regime the MCS propagation seems associated with the midlevel flow with a best fit at 700 hPa (and with the vertical wind shear between 700 hPa and 925 hPa) even in the case of opposite 200-hPa flow. During Westerly regime the MCS propagation is not clearly defined and therefore not associated with any mean flow. In that case, it is possible that part of the MCS could be cirrus advected in the high-level flow.

### 4.2. Radar Cell Propagation

[38] The rain cells tracked from radar data propagate westward during the Easterly regime, with a mean speed of 6 to 10 m $s^{-1}$ on average. During the Westerly regime, the zonal mean speed is weak because the cells propagate either eastward or westward. The rain cell trajectories are presented in Figure 12 for the five successive regime sequences during the period of study. The color in the trajectories allows us to distinguish whether the tracked rain cell contains at least one pixel with radar reflectivity factor larger than 35 dBZ (in red) or not (in black). The periods without radar data during more than one hour and therefore without tracking, are indicated in the figure. The mean hourly rainfall observed from the rain gauge network is also plotted.

[39] The first Westerly regime period (from day 11 to 18 included) is characterized by a large number of rain cells with rather confusing propagations. This is partly due to merging of cells resulting in very abrupt changes that appear as horizontal segments in the figure. This is also due to a mixing of westward and eastward propagations in a same day, which can be explained by the very weak vertical wind shear between low and midlevels during the Westerly periods (see Figure 3). Much of the rain cells have a long duration and a moderate intensity, i.e., their reflectivity never reaches the 35-dBZ threshold. Some of these weak reflectivity systems have produced large amounts of rainfall (e.g., day 11) and/or rainfall over a long period of time (e.g., day 15 and 16), because they have a large spatial extension. The second Westerly regime period (from day 27 to 38) also shows disorganized rain cell propagations and many cells have a short lifetime. Sometimes propagation seems to be more organized, showing a marked propagation eastward (day 33) or westward (day 34). The rainfall events are generally of moderate intensity and long duration (e.g., day 34) but a very strong rainfall is also observed on day 31/32. The third Westerly regime period (day 53 to 58) is very similar to the first one. The rain cells have generally a moderate reflectivity; their propagation is not very marked but preferentially westward. The rainfall events are generally moderate but last very long, especially on days 56 to 58.

[40] In contrast to the Westerly regime, during the two Easterly regime periods (from day 19 to 26 and from day 39 to 52) the rain cells have a well-pronounced propagation from east to west with a typical speed of 9 m $s^{-1}$. This is related to a strong wind shear between low and midlevels, as can be seen in Figure 3. Rain cells still exist with moderate intensity (reflectivity always inferior to 35 dBZ) but they are not as frequent as during the Westerly regime. The rainfall events are generally brief with a high intensity.

### 4.3. Comparison Between MCSs and Radar Cells

[41] In Figure 13, the trajectories of the radar-observed rain cells are superimposed to the areas covered by the satellite-observed MCS at 235 K and 210 K. The 210 K MCSs are always associated with low-level rain according to the radar cells (when there is no missing data). This result confirms that over the Amazon the cloud clusters, with a very cold top (i.e., thick cloud with top between 12 km and the tropopause), are associated with deep convection. The same result applies most of the time to the 235 K MCSs, with some exceptions: day 12 in the morning, day 12 at night, day 13 in the morning, and day 31 in the morning. The convective systems are generally generated in the early afternoon but the cold cloud cover reaches its maximum in

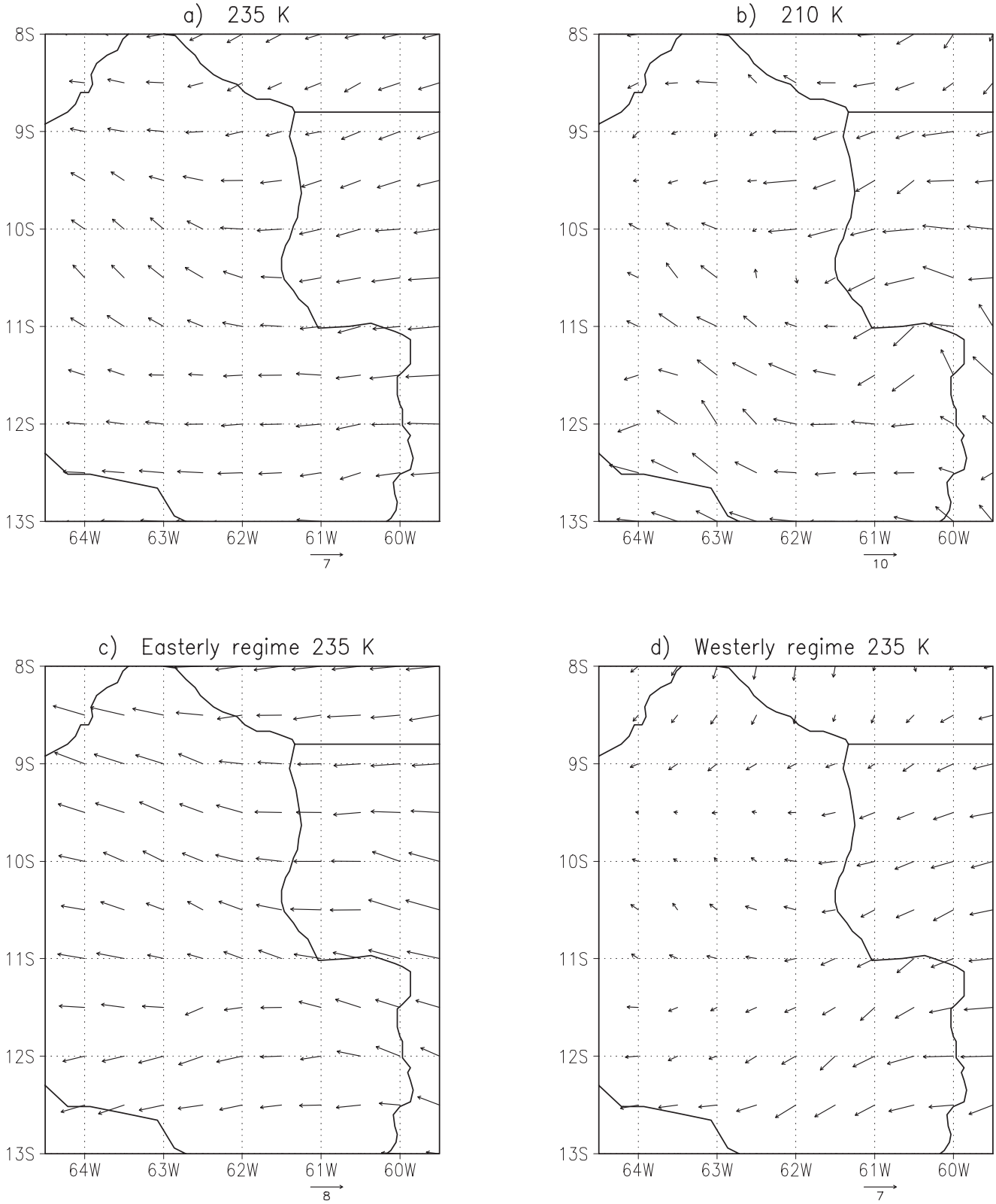


**Figure 11.** Mean MCS propagation ($ms^{-1}$) between 11 January and 27 February 1999 for a) threshold 235 K and b) threshold 210 K. c) Same as a) but for the Easterly regime. d) same as a) but for the Westerly regime. The solid line indicates the state boundaries.

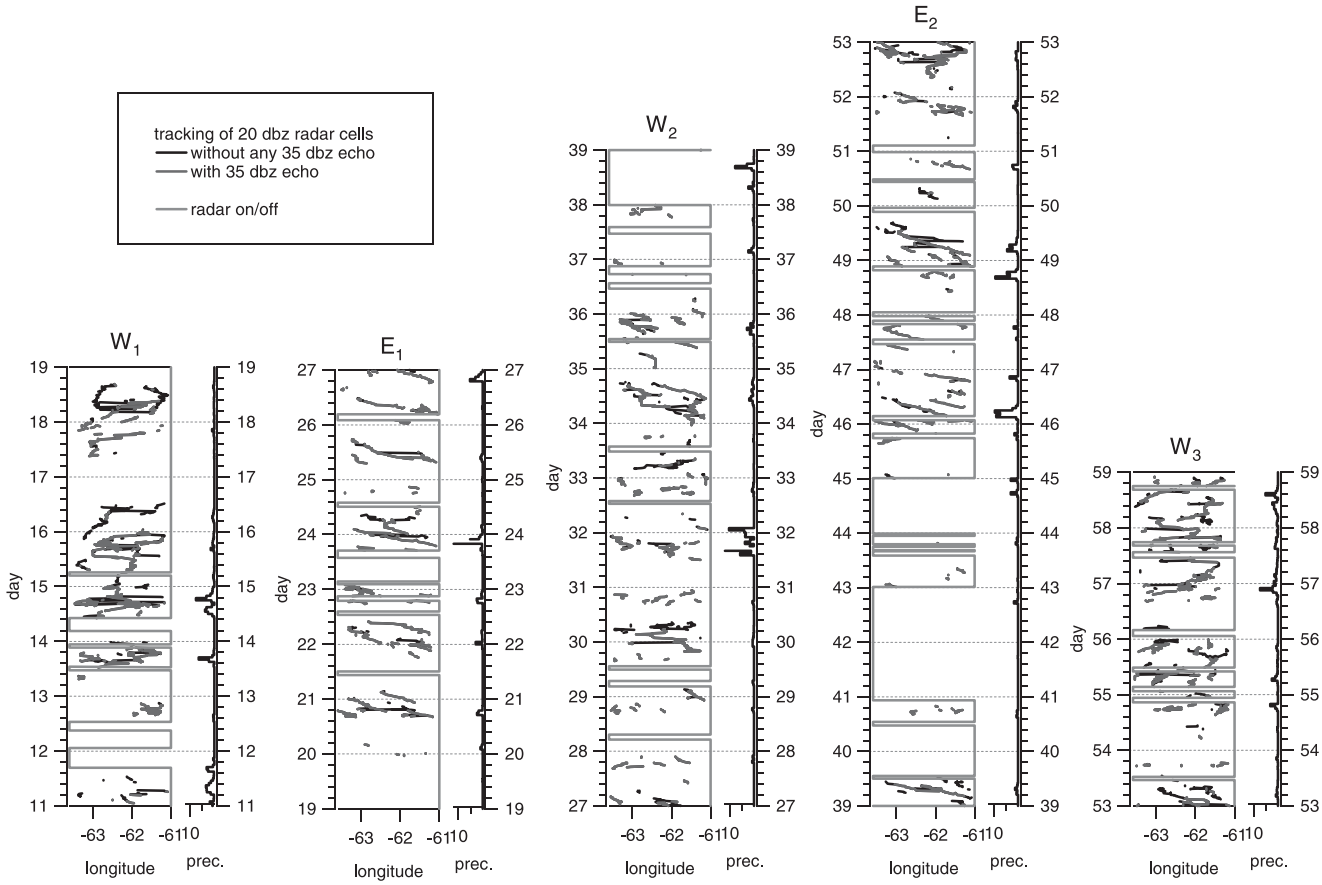


**Figure 12.** Time-longitude trajectories of the rain cells for the five subperiod of Westerly and Easterly regimes between 11 January and 27 February 1999. Rain cells defined at 20 dBZ contains at least one 35 dBZ pixel (red) or not (black). The solid line in green indicates when the tracking was not possible due to a large time interval of missing radar data. The rain gauge average hourly precipitation (mm) is also plotted. See color version of this figure at back of this issue.

the late afternoon. More details can be found in the work of *Machado et al.* [2002] who investigated the diurnal cycle of the convection during the WETAMC/LBA.

[42] The rain cells are not always lying under MCSs. This can be observed mainly during Westerly regime on days 18, 27, 28, 29, 30, 33, 34, 53, and 54. This also occurred, but rarely, during the Easterly regime, on days 21 and 22. In some cases, there was some cloud cover at 235 K or 210 K but not enough to pass the cut-off selection, especially in case of interpolated missing satellite images. However, in other cases there was simply no cold top cloud. The 2-km rain cells were associated with low- or midlevel clouds.

[43] The trajectories in Figure 13 show that during Easterly regime radar cells and MCSs propagate in close association. This is particularly obvious for the 210-K MCSs during days 20 and 46. During the first and the third Westerly periods, rain cells propagate independently of the upperlying 235 K MCSs. For the second Westerly period the MCS coverage is more intermittent. There are also many rain cells that are not associated with any MCS. The tracking of radar cells using the 35-dBZ threshold produced only a few trajectories, most of them associated with MCSs at 210 K.

[44] The results presented in the previous section showed that the distributions of convective systems (size and lifetime) are similar between the two regimes. As shown in Figure 13, the main differences appear in the organization of the convection. In Easterly regime, cloud cluster and rain cells are closely associated and show an organized propagation westward. During Westerly regime, cloud cluster and rain cells are much less linked and rain cells propagation is disorganized.

## 5. Generation of the MCSs

[45] This section attempts to describe the relationship between surface characteristics and localization of the MCS initiations (Figures 14 and 15). Only MCSs that crossed the AMC area are taken into account. Among them only 116 spontaneous initiations will be considered at 235 K, as we excluded split-generations. In 45 cases, the 235 K MCSs developed an area colder than 210 K reaching a sufficient size to be tracked as 210 K MCS. Forty-two percent of the 210 K MCS initiations occurred less than 3 h later than the corresponding 235 K initiation, and 70% less than 6 h later.

[46] The AMC area is located in a transition area in terms of geomorphologic characteristics, in the border between the Amazon basin and the Central Plateau. In this region, elevation and slope vary from the flat low lands of the

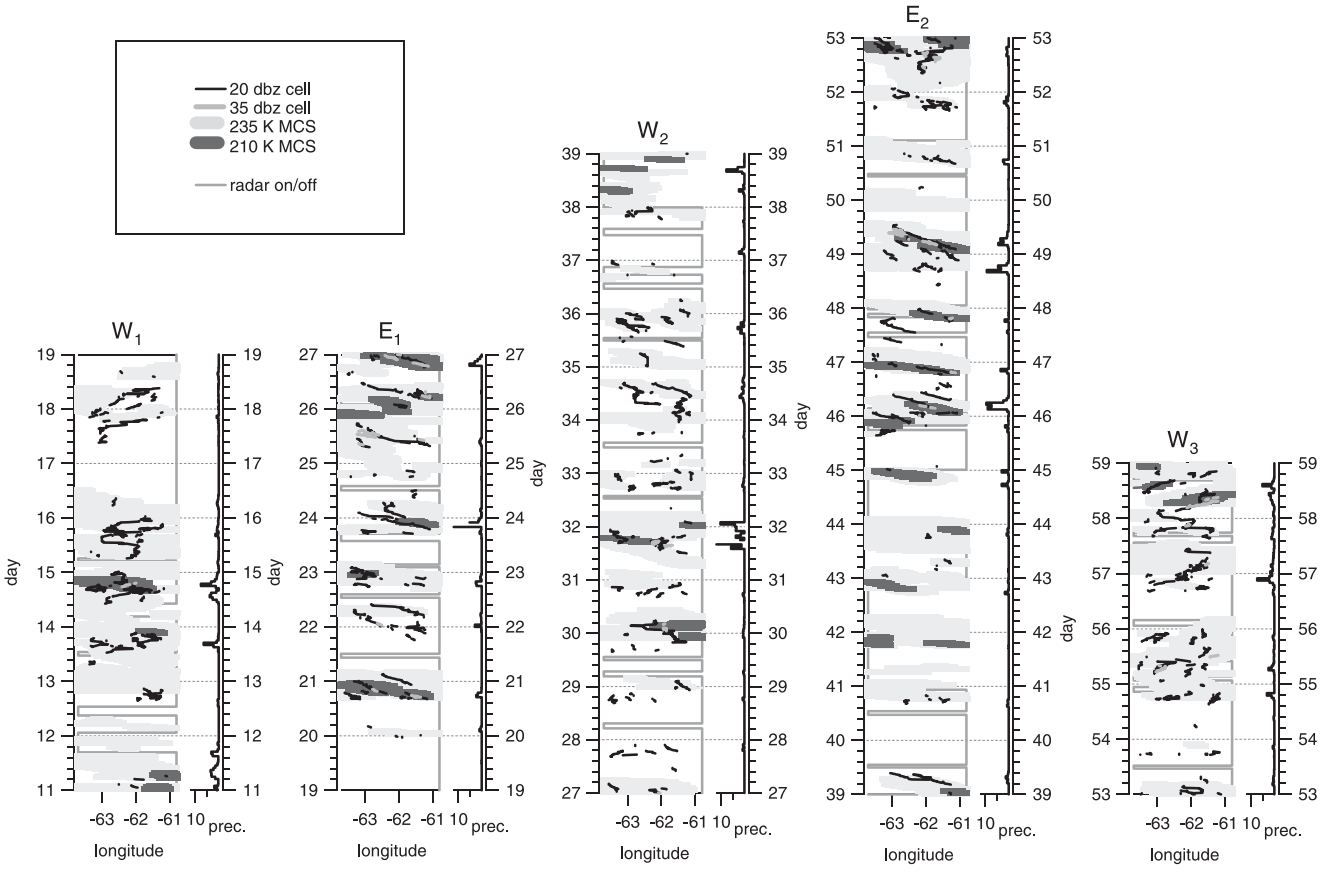


**Figure 13.** Time-longitude trajectories of radar-observed 20-dBZ rain cells (black) and 35-dBZ rain cells (yellow) superimposed with the satellite-observed MCS cloud cover at thresholds 235 K (blue) and 210 K (red), for the five subperiod of Westerly and Easterly regimes between 11 January and 27 February 1999. The solid line in green indicates when the rain cell tracking was not possible due to missing data. The average rain gauge hourly precipitation (mm) is also plotted. See color version of this figure at back of this issue.

Amazon basin to the higher and steeper regions of the Chapadas Mountains. Some of the MCSs that crossed the AMC area were generated in the lower elevation (low lands) of the Amazon basin but the majority of them were generated over the Central Plateau. The MCS initiations at 210 K are all in the vicinity of the AMC area whereas for the 235-K MCSs the initiations can be really far away. One MCS was generated in the Amazon delta, 1700 km from the AMC area. Eight MCSs came from the Tocantins, Araguaia and Xingu valleys traveling more than 1000 km before entering the study area; one came from north of the Amazon basin, one from Pantanal wetlands and two from the

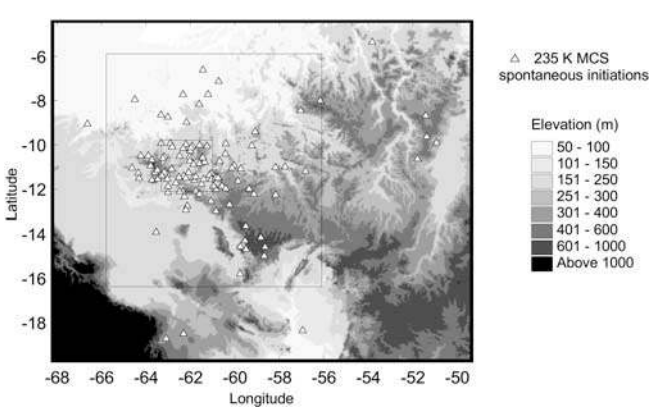


**Figure 14.** Spontaneous initiations of 235K MCS superimposed to the orography. Boxes show the AMC area and the 10 × 10 degree area used in the analysis.

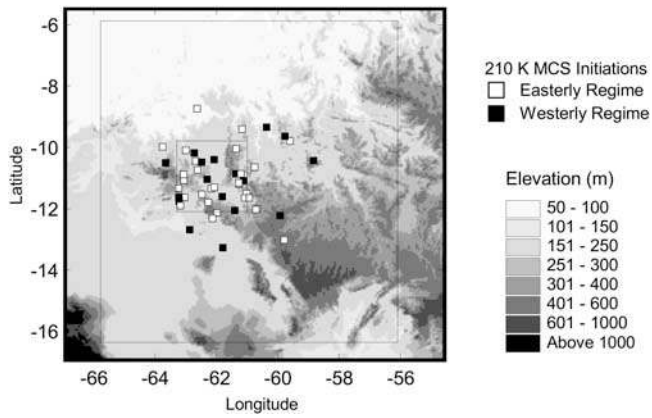


**Figure 15.** Same as Figure 14 but for the 210 K MCS initiations. The color of the marker indicates the regime at the date of the initiation.

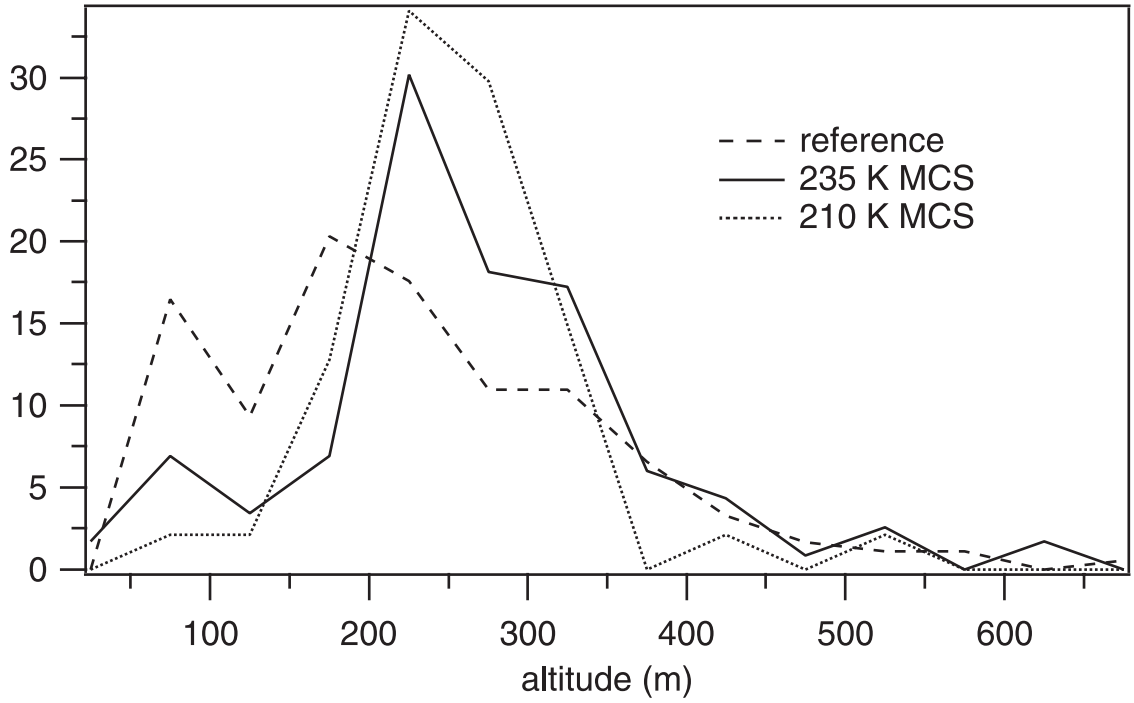


**Figure 16.** Number (%) of MCS initiations as a function of the mean altitude of the area of initiation.

Bolivian Andes borders. However, most of the MCSs were originated from less than 500 km of the AMC area. To study the relationship between MCS initiations and topography, we have focused on a restricted area of 10-degree square (see Figure 14). This area was chosen to fit to the majority of the total spontaneous initiations (90% at 235 K and 100% at 210 K) of the MCSs that crossed the AMC area. It is shifted to the east because MCS initiations were more numerous (28 initiations) and more distant east of the AMC area than in the west (12 initiations).

[47] In order to retrieve the surface characteristics, MCS initiations are approximated to disks with the same area as the MCS area at the initiation time. The surface elevation of the MCS initiation area was analyzed using a 30″ resolution digital elevation model in terms of mean, maximum and minimum elevation, standard deviation and escarpment defined as the difference between maximum and minimum elevation within each initiation disk. We compared these values with a reference based on a regular sampling of the $10 \times 10$ degree area by 182 disks of 5280 $km^2$, corresponding to the average MCS initiation disk. Distributions of the mean altitude of reference and MCS initiations at 235 K and 210 K are presented in Figure 16. For the 235 K MCS initiations, the mean elevation is generally between 200 m and 350 m. This value is higher than the mean elevation for the reference centered around 200 m. Initiations also occur in areas of relatively steep slope with an escarpment generally between 150 m and 400 m (250 m on average) whereas this value varies between 0 and 400 m (190 m on average) for the reference. For the 210 K MCS initiations, we observe almost the same dependence on ground elevation although they are concentrated in a smaller area. As a whole, it was observed that 235 K MCS initiations (and to a lesser extend 210 K MCS initiations) occurred preferentially over nonflat regions and near high elevation. Using 6-hourly NCEP wind data at 925 hPa, we estimated that 53% of the 235 K MCSs formed upwind of topography whereas 29% formed lee-side, and the remaining 18% corresponds to weak wind conditions (<2 m $s^{-1}$) or regions without significant topography. This result suggests that upstream or upslope triggering [*Houze*, 1993] are preferential mechanisms for 235 K MCS generation. A comparison between Westerly and Easterly regimes did not show significant differences in the behavior of the MCS initiations relative to ground elevation.

[48] We have also made a first attempt to study the relationships between vegetation and localizations of the MCS initiations. We used the vegetation map of Brazil produced by *Instituto Brasileiro de Geografia e Estatística-Instituto Brasileiro do Meio Ambiente e dos Recursos Naturais Renováveis* (IBGE–IBAMA) (1988) and the deforestation data of the PROjeto de monitoramento do DESfloramento (PRODES) monitoring [*Instituto Nacional de Pesquisas Espaciais* (*INPE*), 1999]. The study area is a critical area of deforestation. A main road crosses the middle of the AMC area. This road had started the deforestation process in the last twenty years: more than 35% of the AMC area is deforested. In the $10 \times 10$ degree square region, only 7% of the area is deforested. The remaining vegetation is characterized by dense and open evergreen forest in the north (53% of the total area), savanna and contact vegetation (defined as transition between forest and savanna) on the Central Plateau (35%), and Pantanal wetlands and seasonal forest (5%) in the south. The organization of the MCS initiations does not show any clear relationship with the vegetation and deforestation maps. Most of the initiations (47%) are over the evergreen forest, 31% over savanna and contact vegetation, 19% over deforested area and 3% over Pantanal wetlands and seasonal forest. However, the short period of the study does not allow us to reach any definite conclusion. More clear results on the relationships between vegetation and MCS initiations

could appear in the dry and transition season, when there is a noticeable difference in the structure of the planetary boundary layer and in the fluxes of sensible heat at the surface (G. Fisch et al., The convective boundary layer over pasture and forest in Amazonia, submitted to *Journal of Geophysical Research*, 2002).

## 6. Discussion and Conclusions

[49] A methodology for automatic, objective tracking of mesoscale convective systems has been applied to full resolution satellite images during the WETAMC/LBA experiment. It aims to document the convective cloud organization characteristics. Moreover, the same tracking methodology was applied to radar data in order to estimate the propagation of the convective rain cells on the 2-km CAPPI height.

[50] The MCS distributions quantified the importance of the large and long-lived MCSs to the total convective cloudiness. For the threshold 235 K, half of the cold cloud cover comes from MCSs with lifetime greater than 12 h or radius larger than 130 km (i.e., area larger than 50,000 km$^2$). Over West Africa half of the 233 K cloudiness is in clusters with lifetime greater than 24 h or radius larger than 190 km (area larger than 110,000 km$^2$) [*Mathon and Laurent*, 2001]. For the 210 K cloud cover, the lifetime and size of contribution to half of the total cloudiness are 4 h or 50 km (area larger than 7800 km$^2$) in this study, while they are 12 h and 110 km (area larger than 40,000 km$^2$) at 213 K over West Africa. It can then be concluded that large and long-lived convective cloud clusters were much less frequent over southwestern Amazon during the WETAMC/LBA experiment than over continental West Africa. It is important to state that these findings are only valid for the AMC region. For instance, we computed that the typical lifetime of the MCSs that are mostly responsible for the cold cloud cover is 12 h in the AMC region (state of Rondônia), almost 24 h over the state of Amazonas and more than 24 h in the eastern part of the Amazon region (coastal region), which is probably linked to the Amazonian squall lines. However, it was beyond the scope of this paper to study the convective cloudiness in the different regions of the whole Amazon region.

[51] During the WET AMC/LBA experiment two different regimes of convective activity were observed, forced by large-scale circulation. The structural characteristics of the convective systems as depicted by the distributions of size and lifetime are similar between the two regimes whereas large differences appear in the organization of the convection. During Easterly regime MCSs and rain cells propagate in close association. This is particularly visible for the 210 K MCSs, confirming that very cold cloud clusters (i.e., high-level top clouds and high emissivity) are well correlated to the deep convection. MCS propagation as well as rain cell propagation are associated mostly to the midlevel flow around 700 hPa rather than the high-level flow. During Westerly regime the propagations of both MCSs and rain cells are more disorganized. There is no clear relationship with the mean atmospheric flow at any level, which is probably due to the weakness of the low-level vertical shear. The low-level rain cells propagate quite independently of the upperlying cloud cover; it might even have an opposite propagation, which is quite similar to what was observed over the ocean during TOGA COARE [*Rickenbach*, 1999]. Over West Africa, the midlevel African Easterly Jet (AEJ) is an essential element in the organization of convection into squall lines [*Lafore and Moncrieff*, 1989]. The different behaviors observed between the two regimes suggest that, despite its moderate magnitude, the 700 hPa westerly "jet", through the vertical wind shear it induces, is a key element in the organization of the convection over the southwestern Amazonian region.

[52] The results presented here can be used to improve the parameterization of subgrid convective processes relative to the regime that depends on the large-scale flow resolved in the GCMs. Indeed cold cloud deck is well associated to the rain features during Easterly regime; however, it is decoupled during Westerly regime, this difference being probably due to the low-level jet and the associated wind shear.

[53] The initiations of the MCSs that crossed the AMC area are mostly driven by orography. Initiations generally do not occur in flat land but rather in areas with relatively high escarpment and relatively high elevation. From the preliminary results presented here, the effect of the vegetation cover on the MCS generation would be of second order compared to orographic effects.

[54] This same tracking methodology was originally employed over West Africa during the rainy season [*Mathon and Laurent*, 2001]. Therefore a first limited comparison between these two continental regions can be addressed. As already mentioned large- and long-lived MCSs are more important over the Sahel than over the WETAMC/LBA region. MCSs propagate westward with a higher speed over the Sahel than over the AMC region. The speed is higher for cold brightness temperature threshold, which is not observed here. Also the life duration of the coldest MCSs can be larger than 24 h whereas over the AMC region it is shorter than 12 h (however, as already mentioned, results would be probably different over other parts of the Amazon region). The diurnal march of the convection [*Machado et al.*, 2002] appears to be the key element of the convective systems in the Southwestern Amazon in contrast to the Sahel where squall lines and other long-lived MCSs play the main role. This suggestion is also supported by the high number of splits at 235 K found in this study because they are likely to be associated with a large variability of the diurnal convective activity. The behaviors of the MCSs during Easterly regime present large similarities with that of the Sahelian MCSs. They are much more different during Westerly regime.

[55] **Acknowledgments.** This study is part of a cooperative framework between the CNPq (Conselho Nacional de Desenvolvimento Cientifico e Tecnólogico, Brasil) and the IRD (Institut de Recherche pour le Développement, France), support number 910153/98-1. This work has also received financial support from the FAPESP (Fundação de Amparo à Pesquisa do Estado de São Paulo) grant 99/06045-7 and FAPESP grant 1997/9926-9. Thanks to Dirceu Herdies for his help in processing radar and satellite data.

## References

Anagnostou, E. N., and W. F. Krajewski, Simulation of radar reflectivity fields: Algorithm formulation and evaluation, *Water Resour. Res.*, *33*(6), 1419–1428, 1997.

Anagnostou, A. N., and C. A. Morales, Rainfall estimation from TOGA

radar observations during LBA field campaign, *J. Geophys. Res.*, *107*, 10.1029/2000JD000337, in press, 2002.
Battan, L. J., *Radar Observation of the Atmosphere*, 324 pp., Univ. of Chicago Press, Chicago, Ill., 1973.
Chen, S. S., and R. A. Houze, Diurnal variation and life-cycle of deep convective systems over the tropical Pacific warm pool, *Q. J. R. Meteorol. Soc.*, *123*, 357–388, 1997.
Chen, S. S., R. A. Houze, and B. E. Mapes, Multiscale variability of deep convection in relation to large-scale circulation in TOGA COARE, *J. Atmos. Sci.*, *53*, 1380–1409, 1996.
Cohen, J. C. P., M. A. Silva Dias, and C. A. Nobre, Environmental conditions associated with Amazonian squall lines: Case study, *Mon. Weather Rev.*, *123*, 3163–3174, 1995.
Cotton, W. R., and R. A. Anthes, *Storm and Cloud Dynamics*, 880 pp., Academic, San Diego, Calif., 1989.
Doviak, R. J., and D. S. Zrnic, *Doppler Radar and Weather Observations*, 2nd ed., 562 pp., Academic, San Diego, Calif., 1993.
Frank, W. M., The life cycles of GATES convective systems, *J. Atmos. Sci.*, *35*, 1256–1264, 1978.
Fu, R., A. D. Del Genio, and W. B. Rossow, Behavior of deep convective clouds in the tropical Pacific deduced from ISCCP radiances, *J. Clim.*, *3*, 1129–1152, 1990.
Garstang, M., et al., The Amazon Boundary Layer Experiment (ABLE 2B): A meteorological perspective, *Bull. Am. Meteorol. Soc.*, *71*, 19–32, 1990.
Garstang, M., H. L. Massie Jr., J. Halverson, S. Grego, and J. Scala, Amazon coastal squall lines, Part 1, Structure and kinematics, *Mon. Weather Rev.*, *122*, 608–622, 1994.
Grego, S., J. Scala, J. Halverson, H. L. Massie Jr., W. K. Tao, and M. Garstang, Amazon coastal squall lines, Part II, Heat and moisture transports, *Mon. Weather Rev.*, *122*, 623–635, 1994.
Guillot, G., and T. Lebel, Disaggregation of Sahelian mesoscale convective system rain fields: Further developments and validation, *J. Geophys. Res.*, *104*, 31,533–31,551, 1999.
Halverson, J. B., T. Rickenbach, B. Roy, H. Pierce, and E. Williams, Environmental characteristics of convective systems during TRMM–LBA, *Mon. Weather Rev.*, in press, 2001.
Hartmann, D. L., H. H. Hendon, and R. A. Houze, Some implications of the mesoscale circulations in tropical cloud clusters for large-scale dynamics and climate, *J. Atmos. Sci.*, *41*, 113–121, 1984.
Hodges, K. I., and C. D. Thorncroft, Distribution and statistics of African mesoscale convective weather systems based on the ISCCP METEOSAT imagery, *Mon. Weather Rev.*, *125*, 2821–2837, 1997.
Houze, *Cloud Dynamics*, 573 pp., Academic Press, San Diego, Calif., 1993.
Instituto Brasileiro de Geografia e Estatística–Instituto Brasileiro do Meio Ambiente e dos Recursos Naturais Renováveis (IBGEI–BAMA), Mapa de vegetação do Brasil, Escala 1:5,000,000, 1988.
Instituto Nacional de Pesquisas Espaciais (INPE), PRODESLevantamento do Desflorestamento da Amazônia, Internal Rep., 1999.
Lafore, J. P., and M. W. Moncrieff, A numerical investigation of the organization and interaction of the convective and stratiform regions of tropical squall lines, *J. Atmos. Sci.*, *46*, 521–544, 1989.
Laing, A. G., and J. M. Fritsch, The global population of mesoscale convective complexes, *Q. J. R. Meteorol. Soc.*, *123*, 389–405, 1997.
Laing, A. G., and J. M. Fritsch, The large-scale environments of the global populations of mesoscale convective complexes, *Mon. Weather Rev.*, *128*, 2756–2776, 2000.
Machado, L. A. T., The Amazon energy budget using the ABBLE-2B and FluAmazon data, *J. Atmos. Sci.*, *57*, 3131–3144, 2000.
Machado, L. A. T., and W. B. Rossow, Structural characteristics and radiative properties of tropical cloud clusters, *Mon. Weather Rev.*, *121*, 3234–3260, 1993.
Machado, L. A. T., M. Desbois, and J. P. Duvel, Structural characteristics of deep convective systems over tropical Africa and the Atlantic Ocean, *Mon. Weather Rev.*, *120*, 392–406, 1992.
Machado, L. A. T., W. B. Rossow, R. L. Guedes, and A. W. Walker, Life cycle variations of mesoscale convective systems over the Americas, *Mon. Weather Rev.*, *126*, 1630–1654, 1998.
Machado, L. A. T., H. Laurent, and A. A. Lima, The diurnal march of the convection observed during the TRMM/WETAMC/LBA, *J. Geophys. Res.*, *107*, 10.1029/2001JD000338, in press, 2002.
Maddox, R. A., Mesoscale convective complexes, *Bull. Am. Meteorol. Soc.*, *61*, 1374–1387, 1980.
Maddox, R. A., Large-scale meteorological conditions associated with midlatitude mesoscale convective complexes, *Mon. Weather Rev.*, *111*, 1475–1493, 1983.
Mapes, B. E., and R. A. Houze, Cloud clusters and superclusters over the oceanic warm pool, *Mon. Weather Rev.*, *121*, 1398–1415, 1993.
Marshall, J. S., and W. M. K. Palmer, The distribution of raindrops with size, *J. Meteorol.*, *5*, 165–166, 1948.
Martin, D. W., and A. J. Schreiner, Characteristics of West African and East Atlantic cloud clusters: A survey from GATE, *Mon. Weather Rev.*, *109*, 1671–1688, 1981.
Mathon, V., and H. Laurent, Life cycle of the Sahelian mesoscale convective cloud systems, *Q. J. R. Meteorol. Soc.*, *127*, 377–406, 2001.
Moncrieff, M. W., and E. Klinker, Organized convective systems in the tropical western Pacific as a process in general circulation models: A TOGA COARE case-study, *Q. J. R. Meteorol. Soc.*, *123*, 805–827, 1997.
Moncrieff, M. W., and M. J. Miller, The dynamics and simulation of tropical cumulonimbus and squall lines, *Q. J. R. Meteorol. Soc.*, *102*, 373–394, 1976.
Nakazawa, T., Tropical superclusters within intraseasonal variations over the western Pacific, *J. Meteorol. Soc. Jpn.*, *66*, 823–839, 1988.
Peterson, W. A., S. W. Nesbitt, R. J. Blakeslee, R. Cifelli, P. Hein, and S. A. Rutledge, TRMM observations of convective regimes in the Amazon, *J. Clim.*, in press, 2001.
Rickenbach, T. M., Cloud-top evolution of tropical oceanic squall lines from radar reflectivity and infrared satellite data, *Mon. Weather Rev.*, *127*, 2951–2976, 1999.
Rickenbach, T. M., R. Cifelli, J. Halverson, P. Kucera, and O. Thiele, Convective systems in contrasting regimes during TRMMLBA in Rondônia, Brazil, *15th Hydrology Conference*, Long Beach, Calif., USA, AMS Publ., 329–332, 2000a.
Rickenbach, T. M., R. N. Ferreira, and J. Halverson, Relationship between mesoscale properties of convection and large-scale regimes during TRMM–LBA in Rondônia, Brazil, *6th International Conference on Southern Hemisphere Meteorology and Oceanography*, 3–7 April 2000, Santiago, Chile, AMS Publ., 324–325, 2000b.
Rickenbach, T. M., R. N. Ferreira, J. Halverson, and M. A. Silva Dias, Modulation of convection in the Southwestern Amazon basin by extratropical stationary fronts, *J. Geophys. Res.*, *107*, 10.1029/2001JD000263, in press, 2002.
Roca, R., and V. Ramanathan, Scale dependance of monsoonal convective systems over the Indian ocean, *J. Clim.*, *13*, 1286–1298, 2000.
Rocha, E. J. P., Amazon Humidity budget in Amazon Basin during FluAmazon Experiment (in Portuguese), M. S. thesis, 92 pp., São Paulo University USP/IAG/DCA, 1991.
Rutledge, S. A., L. D. Carey, W. A. Petersen, M. A. Silva Dias, and E. J. Zipser, Early results from TRMM/LBA, *6th International Conference on Southern Hemisphere Meteorology and Oceanography*, 3–7 April 2000, Santiago, Chile, AMS Publ., 286–287, 2000.
Silva Dias, M. A., A. J. Dolman, P. L. Silva Dias, S. Rutledge, E. J. Zipser, G. Fisch, P. Artaxo, A. Manzi, J. Marengo, C. Nobre, and P. Kabat, Rainfall and surface processes in Amazonia during the WETAMC/LBAAn overview, *6th International Conference on Southern Hemisphere Meteorology and Oceanography*, 3–7 April 2000, Santiago, Chile, AMS Publ., 249–250, 2000.
Silva Dias, M. A., et al., Clouds and rain processes in a biosphere atmosphere interaction context in the Amazon region, *J. Geophys. Res.*, *107*, 10.1029/2001JD000335, in press, 2002.
Simpson, J., R. F. Adler, and G. R. North, A proposed Tropical Rainfall Measuring Mission (TRMM) satellite, *Bull. Am. Meteorol. Soc.*, *69*, 278–285, 1998.
Stout, J. E., D. W. Martin, and D. N. Sikdar, Estimating GATE rainfall with geosynchronous satellite images, *Mon. Weather Rev.*, *107*, 585–598, 1979.
Su, H., C. S. Bretherton, and S. S. Chen, Self-aggregation and large-scale control of tropical deep convection: A modeling study, *J. Atmos. Sci.*, *57*, 1797–1816, 2000.
Velasco, I., and J. M. Fritsch, Mesoscale convective complexes in the Americas, *J. Geophys. Res.*, *92*, 9591–9613, 1987.
Williams, M., and R. A. Houze, Satellite-observed characteristics of winter monsoon cloud clusters, *Mon. Weather Rev.*, *115*, 505–519, 1987.
Wu, X., and M. A. LeMone, Fine structure of cloud patterns within the intraseasonal oscillation during TOGA COARE, *Mon. Weather Rev.*, *127*, 2503–2513, 1999.

L. Durieux, H. Laurent, and L. Machado, IEA/ACA, CTA, 12228-904, São José dos Campos, SP, Brazil. (hlaurent@iae.cta.br)
C. Morales, Department of Atmospheric Science, Colorado State University, Fort Collins, CO 80523, USA.

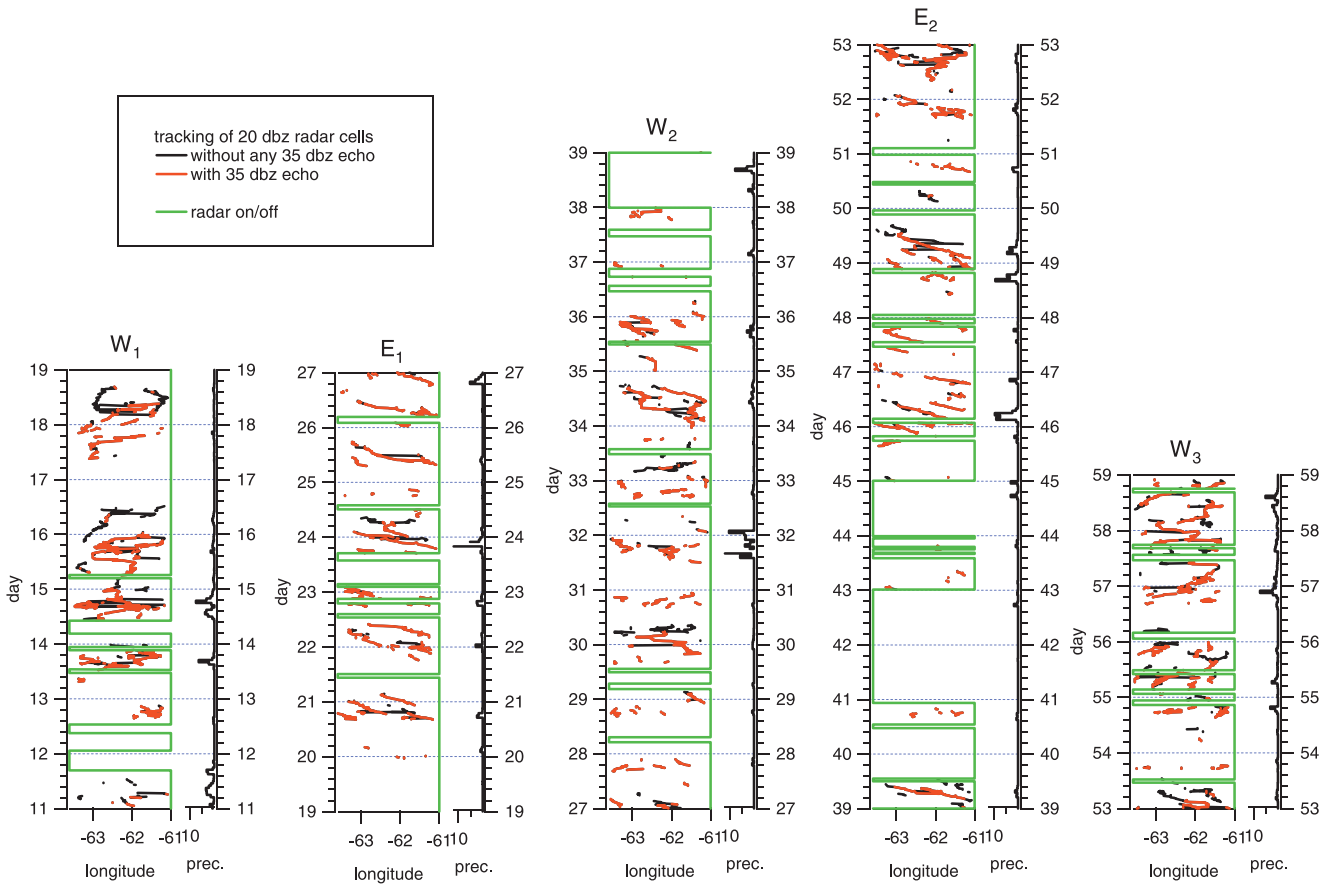


**Figure 12.** Time-longitude trajectories of the rain cells for the five subperiod of Westerly and Easterly regimes between 11 January and 27 February 1999. Rain cells defined at 20 dBZ contains at least one 35 dBZ pixel (red) or not (black). The solid line in green indicates when the tracking was not possible due to a large time interval of missing radar data. The rain gauge average hourly precipitation (mm) is also plotted.

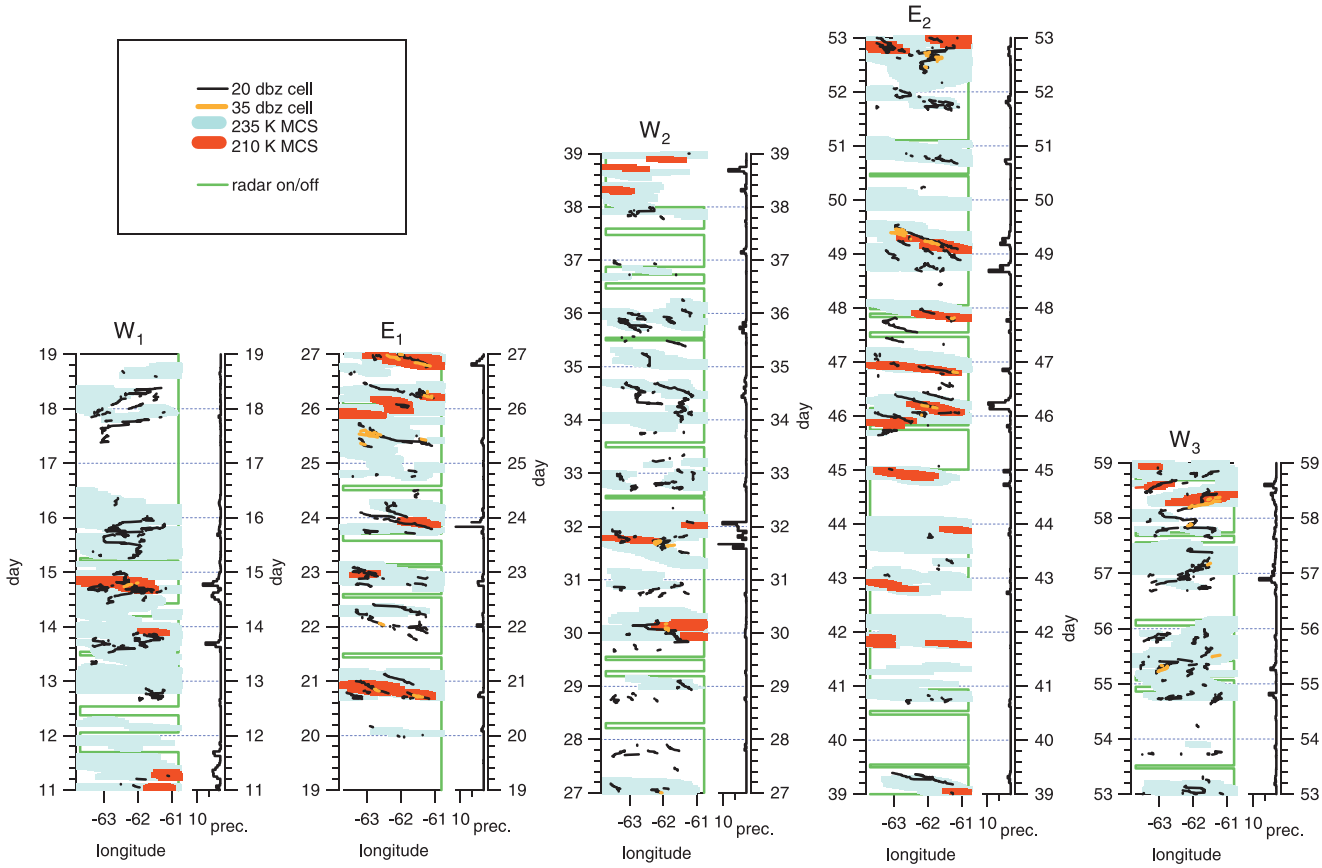


**Figure 13.** Time-longitude trajectories of radar-observed 20-dBZ rain cells (black) and 35-dBZ rain cells (yellow) superimposed with the satellite-observed MCS cloud cover at thresholds 235 K (blue) and 210 K (red), for the five subperiod of Westerly and Easterly regimes between 11 January and 27 February 1999. The solid line in green indicates when the rain cell tracking was not possible due to missing data. The average rain gauge hourly precipitation (mm) is also plotted.

# Mesoscale Convective System Rainfall in the Sahel

VINCENT MATHON, HENRI LAURENT, AND THIERRY LEBEL

*LTHE, IRD, Grenoble, France*

(Manuscript received 15 June 2001, in final form 20 May 2002)

ABSTRACT

Based on a full-resolution Meteosat dataset, an extensive climatological study of the mesoscale convective systems (MCSs) observed by satellite over the Sahel leads to the definition of a subpopulation of MCSs—called organized convective systems (OCSs)—that represents only 12% of the total number of MCSs observed during 9 yr over the central Sahel while accounting for almost 80% of the total convective cloud cover defined at the 233-K threshold. Using a high-resolution rainfall dataset, it is shown that these OCSs are also the main source of rain in this region, accounting for about 90% of the seasonal rainfall, with a mean areal rainfall of 14.7 mm per system. All of the OCSs are associated with a rain event, and more than 90% of the major rain events are associated with an OCS. These figures are compared with those obtained for mesoscale convective complexes (MCCs). Each MCC produces more rainfall on average (19 mm per system) but there are only a few of them (1.2% of the total number of MCSs), and they consequently produce only 19% of the seasonal rainfall. The interannual rainfall variability is first determined by the year-to-year fluctuation of the number of events defined from satellite rather than by the fluctuations of their mean rain efficiency. In fact, the total rain yield of an OCS appears to be linked primarily to its duration (which itself is largely determined by its spatial extension) rather than to its average rain rate. The diurnal cycle over the region is also studied, and it is shown that it is largely conditioned by the propagative nature of the OCSs associated with orography-driven generations located a few hundred kilometers to the east of the validation area.

## 1. Introduction

Tropical convective clouds often evolve into organized clusters with anvils merging into a single mesoscale cloud shield (Houze 1993). This configuration is commonly referred to as a mesoscale convective system (MCS). Since the end of the 1970s, geostationary satellite data have made possible a precise identification and tracking of MCSs. Because of the availability of large datasets of infrared images, several studies were conducted in the 1980s and 1990s to characterize the life cycle of large MCSs in various regions of the world.

In his pioneering work, Maddox (1980) was the first to define a subset of large and well-organized MCSs, widely known since as mesoscale convective complexes (MCCs). Many ensuing studies have focused on the MCCs because they are only few in number but account for a significant share of cloud coverage (e.g., Miller and Fritsch 1991; Laing and Fritsch 1993).

Even though it has long been recognized that tropical convective clouds account for most of the tropical precipitation (e.g., Houze 1981), there are relatively few studies that are aimed at a precise estimation of the rainfall associated with either MCSs or MCCs in the tropical regions. In recent studies carried out over Africa, Laing et al. (1999) estimated that 22% of Sahelian rainfall was produced by MCCs, whereas Mathon and Laurent (2001), using a different definition, estimated that MCCs contribute only about 15% of the convective cloud cover. Laurent et al. (1997) previously found that, over the region of Niamey, Niger, most of the intense rain events producing 80% of the annual rainfall were associated with large cloud clusters easily identified from infrared imagery.

The various studies cited above illustrate the need to define as precisely and objectively as possible what a rain-efficient MCS is in the Sahel and which subpopulation of MCS should be monitored to account for the largest possible share of the total rainfall. This paper therefore intends to provide reliable statistics on the rainfall associated with the Sahelian MCSs based on the combination of two datasets covering 9 yr (1990–94 and 1996–99): a high-resolution satellite imagery database and the Etudes des Précipitations par Satellite (EPSAT)-Niger (EN) ground rainfall dataset (Lebel et al. 1992). The central issue of this paper, discussed in section 2, is to define as objectively as possible a population of rain events from in situ observations and a subpopulation of rain-efficient convective systems from satellite imagery. Sections 3 and 4 describe how these definitions are applied to the EN dataset and to the Meteosat dataset, respectively. In section 5, a climatological description of rainfall from Sahelian MCSs is given, based on statistics computed for two different subpopulations of MCSs. Section 6 focuses on analyzing some

*Corresponding author address:* Thierry Lebel, LTHE, BP 53, 38041 Grenoble Cedex 9, France.
E-mail: thierry.lebel@inpg.fr

TABLE 1. Criteria commonly used to define populations of rain events and convective systems.

| | Rain events | Convective systems |
|---|---|---|
| Sensor | Recording rain gauges | Satellite radiometers |
| Data | Accumulated rain depth | IR brightness temperature |
| Intensity (magnitude) criterion | Min rain depth at one or several gauges | Threshold temperature |
| Space (size) criterion | Proportion of rain gauges recording rain | Continuous area above threshold temperature |
| Time criterion | Min duration with no rainfall between two consecutive events | Min life duration of the cluster |

aspects of the interannual variability of these statistics. A final section is devoted to the discussion of the results presented in sections 5 and 6.

## 2. Mesoscale convective systems and rain events

A rainfall regime may be crudely defined by the average occurrence rate of rain events and by the average magnitude of these events. These two parameters vary from region to region and, within a region, display a seasonal cycle. Detecting whether one, or both, parameters are changing—and in what sense—during dry years may provide clues regarding the atmospheric causes of droughts in the Sahel. However, defining a rain event is not straightforward. Indeed, the definition is conditioned by the sensor or combination of sensors used. On the one hand, cloud clusters are observed well from a geostationary satellite, but not all of these clusters are producing significant rain. Imposing thresholds in temperature, duration, and size is the common way to select the supposedly most efficient cloud clusters in terms of rainfall. On the other hand, it is possible to define directly from a rain gauge network a sample of important rain events. This approach leads to defining rain events as space–time ground rain structures. However, the characteristics of the population so defined are network dependent; that is, they may change with the spatial coverage of the network and with the sampling properties of the gauges. Given this, obtaining two coincidental populations of cloud clusters and rain events is not easy. It may be seen from Table 1 that the criteria used to define these two entities are both similar and distinct. One major reason for this is the difference in nature of the sensors used for identifying cloud systems or rain events. Infrared satellite images provide a global view of the convective systems but their rainfall quantification is very inaccurate. Rain gauge networks give precise quantitative information but at given points only, and the identification of rain events requires ad hoc hypotheses and specific algorithms.

In the Sahel, where operational ground networks are sparse and composed of daily reading gauges only, the EN dataset is the only one to cover several years and to allow for a precise identification of rain events. Combined with full-resolution geostationary satellite images, the EN observations thus provide a unique opportunity to establish a climatological rainfall description of the Sahelian MCSs.

## 3. Rain-event climatological description in the Sahel

### a. Dataset

To produce a consistent climatological description, including interannual variability, it is necessary to use rainfall observations sampled at a time interval smaller than one day because the typical duration of a rain event in the Sahel is on the order of a few hours. One motivation of the EPSAT-Niger experiment (Lebel et al. 1992) was precisely to provide such observations that are lacking in operational networks, which report daily readings of rain. The experiment started in 1990 with 100 recording rain gauges (minimum recording threshold of 0.5 mm) covering a $160 \times 110$ km$^2$ area, hereinafter referred to as the EN area (Fig. 1). In 1994, the network was reduced to 30 gauges. Lebel and Amani (1999) have shown that such a network was able to estimate accurately the average rainfall over the EN area from the event level to seasonal scales and beyond. The data used in this work are event rainfall accumulations obtained at each station from the original series of 5-min rainfall recorded by the 30-gauge network over 1990–94 and 1996–99.

### b. EPSAT-Niger rain events

The criteria listed in Table 1 to define a rain event from rain gauge measurements can be computed either for a single gauge or for an ensemble of gauges. When using a single gauge, there is great sensitivity to the time parameter used to separate two consecutive events. In this respect, one important advantage of the EN network is the ability to use an ensemble of gauges to define a rainfall event. Because the area covered by the network and the area covered by an MCS are of comparable size, the probability of observing two different systems at the same time over the EN area is relatively low. Therefore, it was decided to define a rain event in the following way:

1) At least 30% of the gauges (ground space criterion: $\alpha_g$) must record an event rain depth equal to or greater than 1 mm (ground intensity criterion: $i_g$).
2) There should not be a rainfall interruption of more than 30 min (ground time criterion: $\tau_g$) over the whole network. If all gauges do not report any rain during a continuous 30-min period, then it is the end of the rain event.

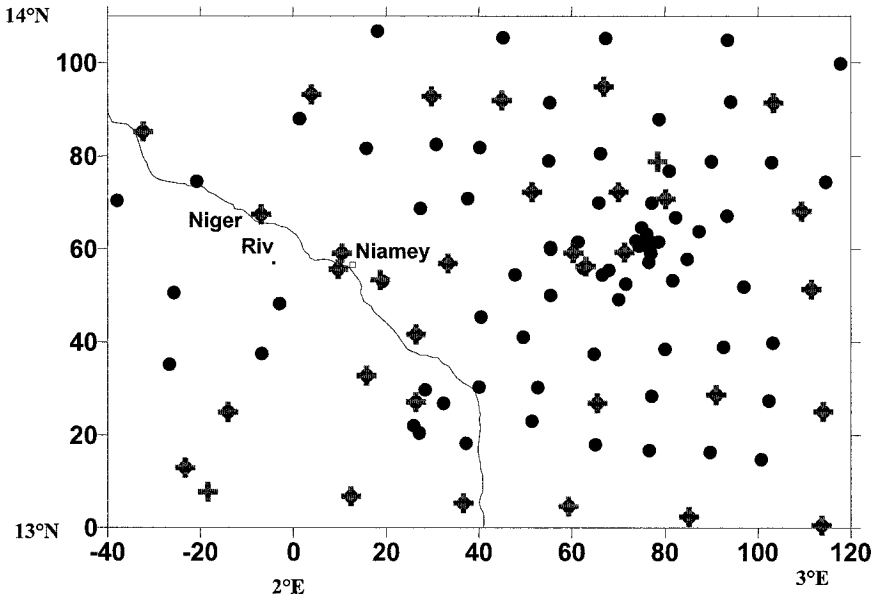


FIG. 1. The EN recording network. Coordinates are in kilometers with the origin at 13°N, 2°E. Black circles are the stations of the dense network in operation from 1990 to 1993. Crosses are the stations of the long-term monitoring network in operation from 1990 to 1999.

An extensive study of the sensitivity of the number of events to the value of $\tau_g$ and $i_g$ showed some stability around the values chosen above. In fact, reducing $\tau_g$ to 15 min or increasing $i_g$ to 2 mm produces only minor variations in the number of events (on the order of 1%–2%).

With these criteria (i.e., $\alpha_g = 30\%$, $i_g = 1$ mm, and $\tau_g = 30$ min), the total number of rain events observed over the EN area in 9 yr is 387, with an average rain depth per event of 10.2 mm. The average proportion of gauges recording no rainfall during an EN rain event is 26%, so the average point rain depth, conditional to rain being observed at a station, is 13.8 mm.

### c. Rain-event classification

D'Amato and Lebel (1998) proposed a simple classification of the EN rain events based on the proportion of gauges recording rainfall ($\alpha_g > 30\%$). They also showed that rain events with at least 80% of the gauges recording rainfall ($\alpha_g > 80\%$) explain more than 70% of the total rainfall while accounting for approximately 50% of the total number of rain events. Henceforth, rain events satisfying the ground space criterion $\alpha_g > 80\%$ are called "major rain events." For the 9 yr covered by this study, a total of 253 rain events were recorded by the EN network during the core of the rainy season (1 July–15 September), 144 of which are major rain events. Table 2 shows that 72% of the rain (or 361 out of 499 mm) falls during the core of the rainy season. This proportion has decreased in recent years. In the 1950s and 1960s, the mean annual rainfall in the Niamey area was about 650 mm, with about 510 mm falling during the period 1 July–15 September, that is, about 78%. From Table 2 it is also seen that both the EN events and the EN major events account for a slightly larger share of rain during the core of the rainy season (91% and 73%, respectively, against 88% and 70%, respectively, over the whole rainy season).

TABLE 2. Rainfall statistics over the EN area. The statistics are computed for 1990–99 (1995 excluded) for the whole rainy season in the first line and for the core of the rainy season (1 Jul–15 Sep) in the second line.

| | Total (mm) | EN rain events (mm) | Major EN rain events (mm) |
|---|---|---|---|
| Annual rainfall | 499 | 439 (88%) | 349 (70%) |
| 1 Jul–15 Sep | 361 | 328 (91%) | 263 (73%) |

## 4. MCS identification from satellite imagery

### a. MCS tracking

Ten years (1990–99) of full-resolution (30 min; $5 \times 5$ km$^2$) Meteosat infrared channel (10.5–12.5 $\mu$m) images covering the 1 July–15 September period were archived for this study. However, 1995 is not used because 10 days of data are lacking in July. The statistics presented here were thus computed over a period of 9 yr: 1990–94 and 1996–99. Over this period the proportion of time with no data is 8%. From year to year, this proportion fluctuates between 1% and 14% (Table 3). As explained below, the final proportion of time with no tracking was significantly reduced by a linear interpolation scheme.

MCS identification was carried out through a tracking algorithm based on an areal overlap method, similar to

TABLE 3. Fraction of total missing images and fraction of missing images that cannot be interpolated (gaps larger than five consecutive hours).

| Year | Missing images (%) | Gaps > 5 h (%) |
|---|---|---|
| 1990 | 8 | 5 |
| 1991 | 7 | 5 |
| 1992 | 6 | 0 |
| 1993 | 13 | 0 |
| 1994 | 14 | 0 |
| 1996 | 12 | 2.5 |
| 1997 | 12 | 0 |
| 1998 | 1 | 0 |
| 1999 | 2 | 0 |

those described by Williams and Houze (1987). The method and the quality of the results it produces are discussed in detail in Mathon and Laurent (2001). Thus, only its main features are recalled below.

Convective clouds are delineated in Meteosat infrared images using two different brightness temperature thresholds: 233 and 213 K. The 233-K threshold is in the range of the most commonly used thresholds for identifying deep convection (Duvel 1989) and accumulated convective precipitation in the Tropics (Arkin 1979). The 213-K threshold targets the most active part of the convective systems. Moreover, the 213-K threshold was found by some authors as an optimum for correlating cloud occurrences and rainfall during the core of the rainy season over the central Sahel (Jobard and Desbois 1992).

The tracking method is only applied to convective clouds larger than 5000 km$^2$. Below this value, tracking is difficult to implement because the cloud number increases strongly, whereas the overlapping surface tends to be limited. Mathon and Laurent (2001) have shown that, despite the 5000-km$^2$ size cutoff, the cloud life cycles obtained are very close to what could be produced by a manual method. Moreover, they calculated that only 7% (9%) of the total cloud cover at the 233-K (213 K) threshold are lost because of the filtering of small clouds.

The effect of missing data on the tracking results is limited by using an interpolation scheme. It basically consists of generating virtual images and running the tracking process as if there were no missing images. These virtual images are generated by extrapolating the displacement of each cloud present in the last actual image. It has been shown that this interpolation scheme generates cloud occurrences very close to the actual ones, and that this process is of particular interest to estimate the actual number of convective clouds (Mathon and Laurent 2001). However, when more than 10 successive images are missing, the tracking is not carried out. Table 3 gives the fraction of missing images for each year. There were only a few cases in 1990, 1991, and 1996 when the interval of missing images was larger than 5 h. The interpolation scheme allows reduction of the proportion of missing hours over the whole period of study from 8% to 1.4%.

Mesoscale convective systems are defined as convective clouds larger than 5000 km$^2$ at the 233-K threshold. There are several reasons for the choice of this temperature threshold:

- The 233-K threshold is in the range of the most common thresholds used to define MCS (Machado et al. 1992, 1998) and MCS subpopulations, such as MCCs (Laing and Fritsch 1993) or squall lines (Rowell and Milford 1993).
- As already mentioned, 233 K is in the range of the temperature thresholds used in satellite-derived rainfall estimation algorithms (Arkin 1979).

MCSs as defined above contribute to 93% of the total Sahelian cloud coverage at the 233-K threshold for the core of the Sahelian rainy season (1 July–15 September).

### *b. Classification of the Sahelian mesoscale convective systems*

At the early stage of MCS studies from satellites it was found that very deep convection associated with the heaviest rainfall was most likely to be found in large MCSs displaying some specific structure. Such systems are noticeably characterized by large trailing anvils and by the presence of intense convective cells imbedded in mesoscale clusters. Maddox (1980) was the first to define numerical criteria allowing for an objective identification of a particular set of such systems that were called MCCs. In the Sahel, however, MCCs account for a small fraction of either rainfall or cloud cover, as mentioned in section 1. There is thus a need to identify a larger subsample of MCSs so as to include most of the rain-producing systems.

Based on the radar data acquired during field experiments, such as the Global Atmospheric Research Program (GARP) Atlantic Tropical Experiment (GATE) and the Convection Profonde Tropicale (COPT) experiment (e.g., Zipser 1977; Houze 1977; Roux 1988), Houze (1981) divided the tropical cloud clusters into squall and nonsquall clusters. First described by Hamilton and Archbold (1945) for West Africa, squall lines produce heavy rainfall and are characterized by a unique and well-defined structure, documented in radar data and simulated in numerical studies (e.g., Redelsperger and Lafore 1988; Lafore and Moncrieff 1989). Squall lines are likely to contribute to a large share of the Sahelian precipitation, but it is not easy to find objective criteria to identify them in a population of MCSs. In their studies over West Africa, Desbois et al. (1988) and Rowell and Milford (1993) used a sharp-leading-edge criterion. However, cases of MCSs that do not present a well-defined leading edge on satellite images may prove to present a typical squall line structure on radar images, as shown by Smull and Houze (1985) and by Lebel et al. (1997).

The most obvious way to establish a comprehensive

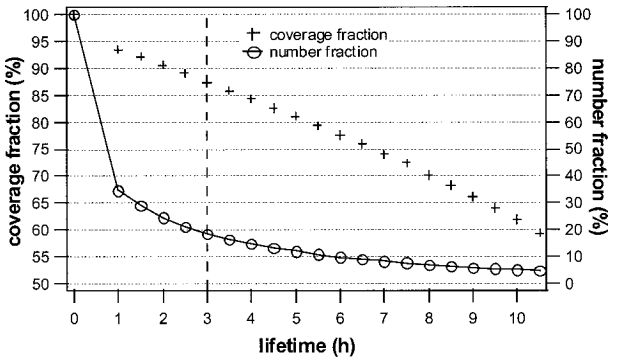


FIG. 2. The 233-K MCS coverage fraction (crosses) and number fraction (line and circles) vs lifetime of the 213-K clusters embedded in the 233-K MCS cloud shield. The first selection criterion is indicated as a vertical line at lifetime = 3 h.

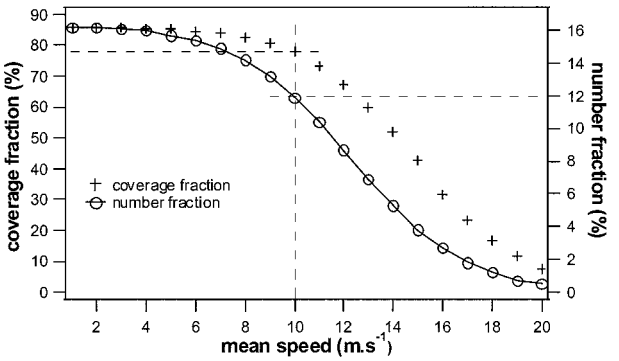


FIG. 3. The 233-K MCS coverage fraction (crosses) and number fraction (line and circles) vs mean speed of the embedded 213-K clusters. Only MCSs passing the first selection criterion have been considered here. The second criterion is indicated as a vertical line at speed = 10 m $s^{-1}$.

climatological description of rainfall from satellite data is to relax the criteria commonly used to define MCCs. The selection proposed here is based on two temperature thresholds: 233 and 213 K. When studying the life cycle of 213-K clusters (i.e., continuous 213-K areas larger than 5000 $km^2$), it appears that using two numerical criteria allows us to select a small number of MCSs associated with a large proportion of the total cloud cover at 233 K. The first criterion is related to the lifetime of the 213-K clusters. Figure 2 shows the number fraction and coverage fraction of the 233-K MCSs as a function of the lifetime of their 213-K clusters. The first class (0 h) corresponds to 233-K MCSs, which do not contain any cluster at 213 K tracked by the algorithm. Note that most systems are located in this first class. The two distributions appear markedly different, which shows that a small number of systems account for most of the total cloud coverage. The 3-h threshold was chosen as a compromise to select potentially rain-efficient MCSs. Systems with a 213-K cluster lasting for more than 3 h are 18% in number but account for 87% of the total 233-K cloud coverage.

In a second step, the selection is refined by using a mean speed criterion. Houze (1981) states that squall clusters are notable by their rapid propagation. These systems might be expected to be the most rain-efficient producers because of their well-defined and organized mesoscale up- and downdrafts. Houze et al. (1990) also found that springtime major rain events in Oklahoma are associated with rapidly moving squall lines. Applying a mean speed criterion to refine a preselection based on cloud extension at 213 K is thus a logical step. The mean speed calculation is based on the mean displacement of the cloud geometric center between initiation and dissipation of the 213-K cluster. Similar to Fig. 2, Fig. 3 presents the number fraction and cloud coverage fraction at 233 K as a function of the mean speed at 213 K. One-third of the MCSs retained in the first step (6% of the total population of MCSs) have a mean speed below 10 m $s^{-1}$, and two-thirds (12% of the total population of MCSs) have a mean speed larger than 10 m $s^{-1}$. The coverage fraction decreases slightly (from 87% to 78%) when the mean speed increases from 0 to 10 m $s^{-1}$. The speed threshold of 10 m $s^{-1}$ was thus retained to eliminate slow-moving MCSs that are associated with a moderate 233-K cloud coverage. In summary, the new stratification procedure proposed here is as follows:

1) In a population of MCSs defined at the 233-K threshold, only those containing at least one 213-K cluster lasting for 3 h or more are kept. They represent 18% in number and 87% in 233-K cloud coverage.
2) In a second step, the selected systems without any 213-K clusters moving faster than 10 m $s^{-1}$ are discarded.

The selected systems are called organized convective systems (OCSs). They account for 78% of the total 233-K cloud cover while representing only 12% of the total MCSs number. Based on the above-mentioned papers of Houze (1981) and Houze et al. (1990), there are good reasons to assume that the fast-moving large MCSs are the organized systems such as squall lines. Even though it is not possible with the data available to us to confirm this inference rigorously, the label ''organized'' seems appropriate for the classification proposed here.

### *c. Cloud-cover climatological description of MCSs, OCSs, and MCCs in the Sahel*

The cloud-cover climatological description of the Sahelian MCSs has been studied in detail by Mathon and Laurent (2001). This section compares some statistics of the MCC and OCS subpopulations with those computed for the whole MCS population. MCCs are identified using the Maddox criteria adapted to our temperature thresholds by linear extrapolation:

1) area >80 000 $km^2$ at the 233-K threshold,
2) area >30 000 $km^2$ at the 213-K threshold,
3) criteria 1 and 2 during at least six consecutive hours, and

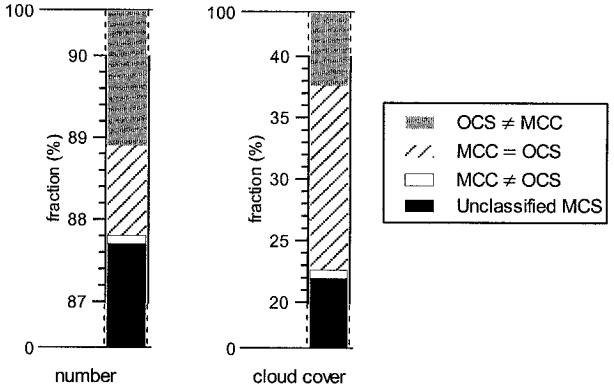


FIG. 4. Contribution of OCSs, MCCs, and unclassified MCSs in term of (left) number and (right) 233-K cloud cover.

4) eccentricity (minor axis/major axis) >0.7 at time of maximum extent at 233-K threshold.

There are, on average, 1947 MCSs, 217 OCSs, and 23 MCCs per year over the Sahel. MCC and OCS contributions to the total MCS number and cloud cover are presented in Fig. 4. As already mentioned, OCSs account for 78% of the 233-K cloud cover and represent 12% of the total MCS number. In comparison, MCCs represent 16% of the cloud cover and 1.2% of the MCS number. As one might suspect, MCC and OCS subsets overlap. Indeed only 8% of the MCC population do not satisfy the OCS criteria. Figure 5 shows the mean annual number (Fig. 5a) and cloud cover (Fig. 5b) of OCSs, MCCs, and MCSs versus their life span for 2-h classes. Every long-lived MCS (lifetime longer than 24 h) is classified as OCS, which means that all long-lived MCC also satisfy OCS criteria.

The above MCC statistics confirm that MCCs represent a too-small share of the cloud cover in the perspective of a comprehensive climatological study. A similar result will be found below (see section 5) regarding rainfall. Note that, in their study carried out over the whole of Africa with 3-h temporal-resolution Meteosat images, Laing and Fritsch (1993) identified 195 MCCs in 2 yr. They show a map on which about 60 MCCs are positioned over the Sahel, which is an average of 30 per year. Given the fact that they worked at a warmer threshold (240 K) and over the whole year, this statistic compares well with our figure of 23 MCCs per year, which applies to the core of the rainy season only.

The spatial distributions of OCS and MCC cover are summarized in Fig. 6 as their contributions to the total MCS coverage. The two populations have a similar spatial distribution with a maximum contribution between approximately 10° and 15°N. This figure shows clearly that the central Sahel is a privileged location for large organized convection extending from 11°–12°N to 15°–16°N and from 10°W to 15°E. This is related to the presence of a midlevel jet (the African easterly jet) that provides a vertical wind shear favoring the development of large convective systems, such as squall lines (e.g., Lafore and Moncrieff 1989). To the south of 10°N, MCCs explain less than 10% of the MCS coverage, and the share of OCSs drops down to less than 40%.

The mean annual spatial distribution of OCS and MCC occurrences at initiation and dissipation time are plotted in Fig. 7. Only OCSs and MCCs that cross the

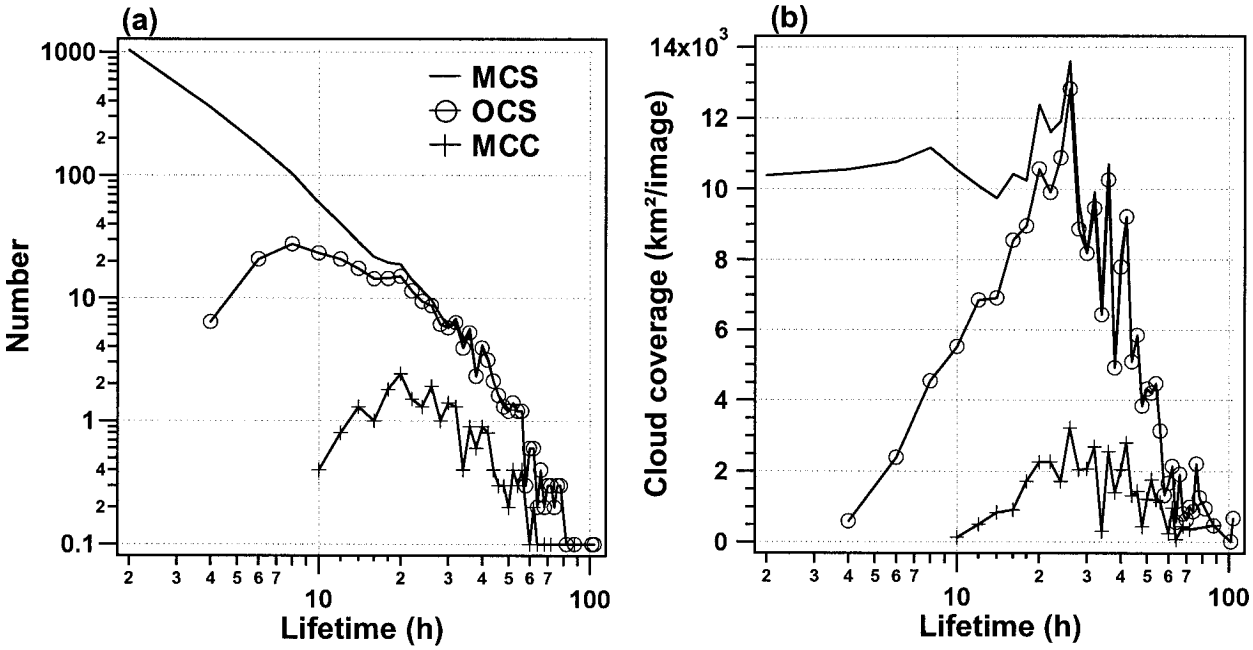


FIG. 5. Mean annual distributions of MCS, OCS, and MCC (a) number and (b) 233-K cloud cover (square kilometers per image) vs lifetime. Results were obtained over the central Sahel area during nine summers.

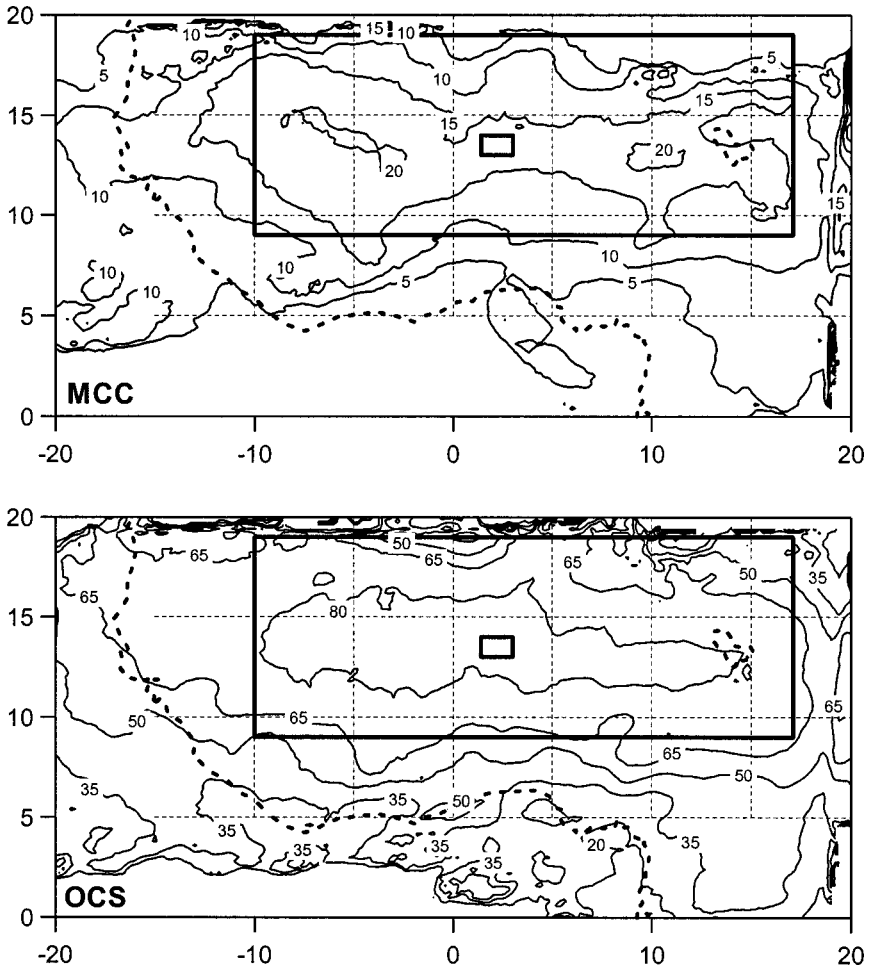


FIG. 6. Spatial distributions of MCC and OCS contribution (%) to the total MCS cloud coverage. Results were obtained over nine summers at a threshold of 233 K. The central Sahel area and the EN area are enclosed. The dashed contours delineate the continent.

central Sahel area, delineated as the large boldface rectangle, are taken into account. Most of the OCSs or MCCs that cross the central Sahel are initiated within the area itself. Some of them are initiated to the east of the area; the maximum observed on the right-hand side of the map is an artifact corresponding to the edge of the satellite images used.

Although the MCC initiation map does not display any clear preferential location of initiation, the effect of orography appears clearly when looking at OCS initiation. For instance, the Jos Plateau (9°N, 8°E) and the Air massif (18°N, 8°E) are places of maximum generation occurrence. Both MCC and OCS dissipations are shifted westward and southward in relation to their initiations. Dissipation can occur far to the west of the Sahel zone (as far as 30°W). Most of OCS dissipations occur in the 10°–15°N belt and about one-half of the MCC population dissipates outside of the Sahel area.

## 5. Rainfall climatological description of the Sahelian MCSs

To evaluate the rainfall characteristics of the satellite-observed MCSs, it was necessary to build a population of events comparable to that defined from rainfall data as defined in section 3b. This consisted of selecting MCSs according to their overlapping surface with the EN area. Both the temperature threshold and the overlapping surface threshold were investigated so as to explain most of the major rain events (see section 3c) while eliminating most of the other cases. The best compromise was obtained when 80% of the EN area is covered by a cluster at a threshold of 233 K. Note that this overlapping ratio is very similar in magnitude to the ground-based criterion used to select major rain events.

The MCSs that are potentially important in terms of rainfall over the EN study area are defined at 233 K as follows:

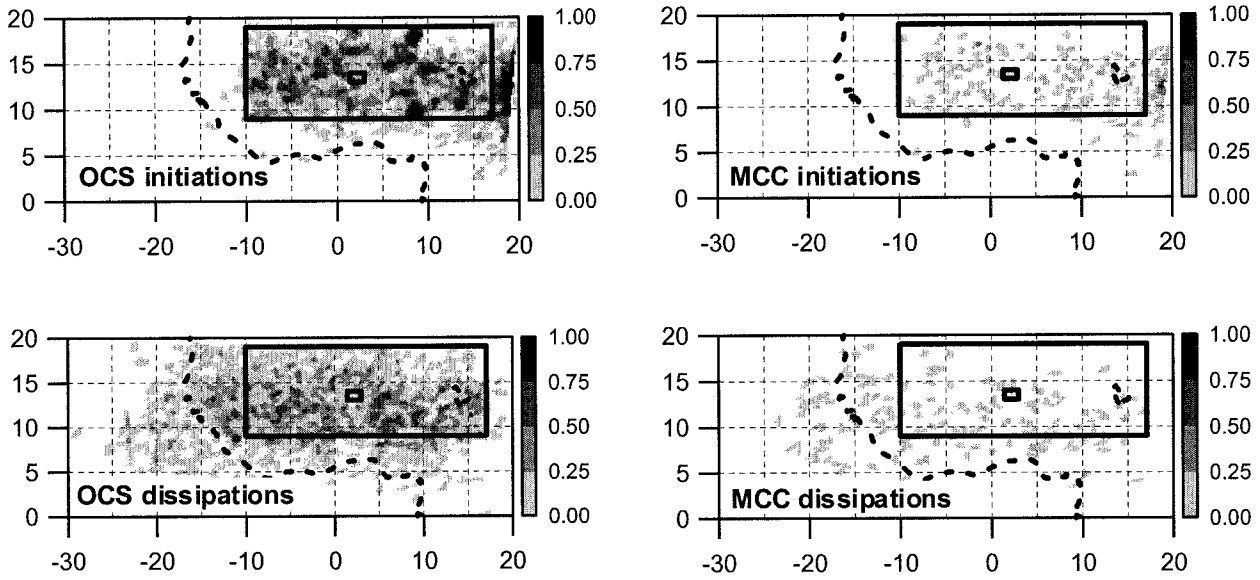


FIG. 7. Mean annual occurrences of MCCs and OCSs at initiation time and dissipation time. Only MCCs or OCSs that have crossed the central Sahel area have been taken into account. Results were obtained over nine summers at 233 K. Boxes and dashed contours are the same as in Fig. 6.

1) t0 is the time at which the MCS first covers at least 1 pixel belonging to the study area,
2) the event ends at t1, which is when the system has totally left the EN area, and
3) between t0 and t1, there must be at least one image in which 80% of the EN area is covered by the system.

Most of these events are associated with a single MCS. However, in 25% of the cases several MCSs are involved. This may be a problem for an objective estimation of the contribution of each MCS type. A calculation based on interpolated rainfall data (with comparable time–space resolution between satellite and rainfall information) indicates that in such cases 83% of rainfall can be attributed to the leading MCS. Thus, one can reasonably and objectively associate a rain event, as defined in section 3b, to a single MCS.

### *a. Total rainfall*

Over the 9 yr of this study, and for the period 1 July–15 September, a total of 530 MCSs covered at least 25 $km^2$ of the EN study area (i.e., 1 pixel in Meteosat images) at any moment of their life cycle. However, only 186 of these 530 MCSs satisfy the criterion for overlapping as defined above. Referring to these events as ''EN MCSs,'' it is calculated that, on average, 21 of them are observed each year, producing 301 mm (83% of the total rainfall observed on the ground).

TABLE 4. Annual statistics of the EN convective systems for 1 Jul–15 Sep.

| | Total | EN MCS | EN OCS | EN MCC |
|---|---|---|---|---|
| Number | | 21 | 19 | 3 |
| Cumulative rainfall (mm) | 361 | 301 (83%) | 280 (78%) | 57 (16%) |

OCS and MCC contributions to the total rainfall have been investigated. It is seen in Table 4 that there are, on average, 19 EN OCSs per year, against 3 EN MCCs per year (EN OCSs and EN MCCs refer to the subpopulations of the EN MCSs satisfying, respectively, the OCS and MCC criteria). The subpopulations of EN OCSs and EN MCCs represent roughly 10% of the corresponding total populations of Sahelian systems: over the 9 yr of our study, 171 EN OCSs were recorded, as compared with 1949 OCSs over the whole Sahel (9%), and 26 EN MCCs, as compared with 211 MCCs over the whole Sahel (12%). The OCSs produce 280 mm (78% of the total rainfall observed on the ground), that is, 14.7 mm per event, on average. The EN MCCs are more efficient because they produce 57 mm (16% of the total rainfall observed on the ground), that is, 19 mm per event. All the statistics given above are nonconditional area averages over the EN study area, that is, they integrate rainy and nonrainy areas. Again, they apply to the core of the rainy season—D'Amato and Lebel (1998) have shown that convective systems tend to be less rain efficient during the margins of the rainy season.

One can wonder to what extent the subpopulation of EN rain events defined from the gauge network matches the subpopulation of EN OCSs. In comparing the statistics of Table 2 with those of Table 4, it is seen that the EN rainfall share of the EN OCSs (78%) is in between the share of all of the EN rain events (91%) and that of the EN major rain events (73%). At the same time, the contingency statistics of Table 5 show that

TABLE 5. Contingency table of EN rain events vs EN convective systems. The MCS line corresponds to MCS for which at least 1 pixel overlapped the EN study area. EN MCS (EN OCS) is MCS (OCS) overlapping 80% of the EN study area during at least 0.5 h (one image).

| | Isolated or no rain (a) | EN rain events (253 in total over the period of study) (b) | Major EN rain events (144 in total over the period of study) | Total (a) + (b) |
|---|---|---|---|---|
| MCS | 277 | 253 | 144 | 530 |
| EN MCS | 14 | 172 | 136 | 186 |
| EN OCS | 0 | 171 | 134 | 171 |

there are more EN OCSs than EN major rain events. This deserves a few comments: (i) EN major rain events produce 16.5 mm of rain on average, whereas OCSs produce 14.7 mm on average; (ii) most *major* rain events (93% in number, accounting for 83% of the cumulative rainfall produced by the major events) are associated with an EN OCS; (iii) however, when considering *all* EN rain events, 100% of the EN OCSs are associated with an EN rain event; (iv) 92% of the EN MCSs are associated with an EN rain event (this accounts for 85% of the cumulative rainfall produced by the EN rain events). In addition, it was found that all of the EN MCCs are EN OCSs (it is only in the south of the Sahel that a few MCCs are not OCSs). The differences between the population of EN OCSs and the population of *major* rain events is linked to the 233-K cloud shield being larger than the precipitating area. Despite this, it is seen that the EN OCSs constitute a good proxy of the major rain events.

There is a last point to consider regarding the computation of these seasonal rainfall statistics. The raw computation of the OCS seasonal rainfall share certainly underestimates the real statistics. By considering only those convective systems that overlap more than 80% of the EN area, one eliminates small systems of little rain productivity but also eliminates OCSs with an unfavorable trajectory. Recall that such a selection procedure is needed to obtain a robust and objective method to be used in the absence of ground validation. When such a ground validation is available, as in the case here, one can systematically evaluate the marginal rain produced by the OCSs eliminated in the selection procedure. For instance, considering all the OCSs with at least 1 pixel overlapping the EN study area at any time of their life leads to the computation that an additional 15% of the seasonal rain is associated with the OCSs, increasing their total share to 93%. A realistic estimate of the total share of OCS rainfall during the core of the rainy season over the central Sahel thus may be around 90%.

### *b. Diurnal cycle*

To characterize the diurnal cycle of a convective system, one would like to have an EN validation area ''traveling'' with the convective system. Here it is only possible to study the diurnal cycle of rainfall over a fixed area and relate it to the overpassage of convective systems at various stages of their life cycle. As seen from Fig. 8a, the diurnal cycle of the rain yield associated with the EN OCSs is very similar to the diurnal cycle of the total rainfall over the EN area. A large share of rainfall occurs between 0100 and 1000 LST. Such a feature is atypical because over land the convective activity is at a maximum during the evening rather than at night or early morning. It is obvious that the geo-

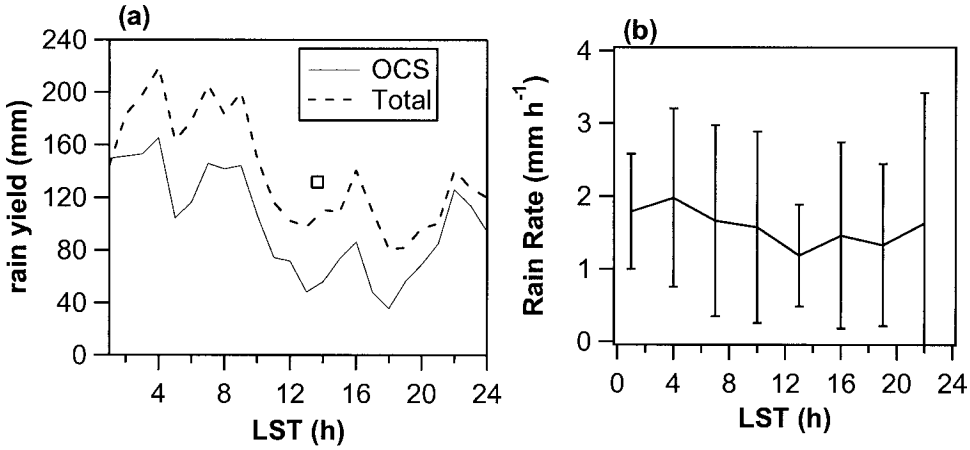


FIG. 8. (a) Diurnal variations of the total rain yield obtained from EN data (mm) and the rain yield associated with OCSs. (b) Averaged OCS mean rain rate vs mean time of first occurrence over the EN area. Associated standard deviations are also plotted. Results are obtained for nine summers.

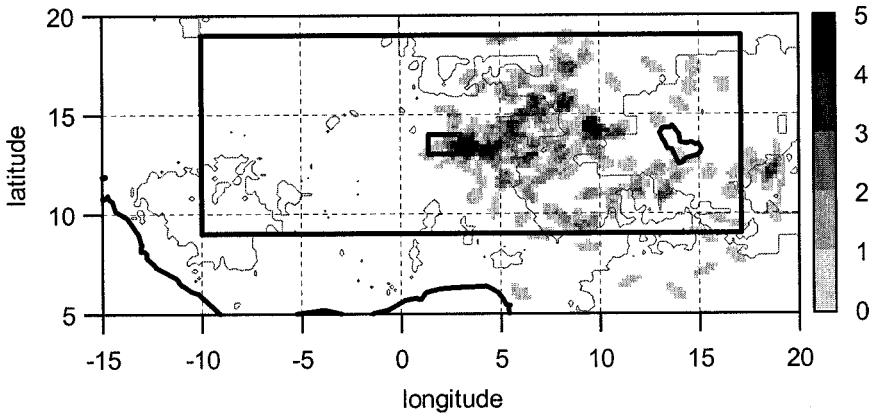


FIG. 9. Map of the mean annual number of initiations of the EN OCSs. The light contours indicate regions of elevation greater than 400 m. Indicated boxes are the same as in Fig. 6.

graphical location of the validation area must partly explain this result.

Figure 8b shows the mean rain rate of the EN OCSs versus the mean time of their occurrence over the EN area. The mean rain rate is calculated by dividing the rain yield of an event by its duration. It is seen that the OCSs tend to be slightly more rain efficient when they reach the EN area during nighttime. However, as indicated by standard deviations, there is a large scattering around the mean values. Thus, no clear modulation explaining the atypical diurnal cycle of Fig. 8a can be identified. This leads us to conclude that the nocturnal/early morning predominance of rainfall over the EN area is primarily due to the fact that OCSs occur more frequently over the study area during the night, because of their propagative nature, as already suggested by Shinoda et al. (1999). To check this finding, the location of generation of the EN OCSs is plotted in Fig. 9 along with the areas with an elevation above 400 m. Most of the events come from regions far from the EN area, and most of the initiations occur in areas above 400 m in altitude. The distances separating the validation area from the initiations are generally greater than 250 km. Because OCS initiations occur mostly in the afternoon over the Sahel (Mathon and Laurent 2001) and because the OCSs propagate mainly westward at 10–15 m $s^{-1}$, the probability of observing nocturnal occurrences over the EN area is enhanced. These results demonstrate that, in the EN area, the diurnal cycle of rainfall is significantly influenced by the orography located to the east.

## 6. Interannual variability

As shown by Le Barbé and Lebel (1997) at the regional and decadal scales, there is a relationship between the number of rain events (derived from daily rain gauge readings) and the corresponding rain yield in the Sahel. In the current paper, the use of two sources of data led to the definition of two populations of events with respect to the EN window of observation: (i) EN convective systems, observed from Meteosat, have a subpopulation of more efficient systems, the EN OCSs; and (ii) EN rain events, observed from the EN rain gauges, have a subpopulation of more efficient systems, referred to as the EN major rain events (see section 3c).

The question addressed here is whether the conclusions of Le Barbé and Lebel (1997) hold when looking at the interannual variability and whether the number of convective systems and the number of rain events display the same kind of relationship with the seasonal rainfall. Figure 10a shows that there is indeed a significant cofluctuation between the total rain yield over the period considered and the number of major events observed during that period, whether these events are satellite-defined (EN OCSs) or ground-defined (EN major rain events). Note that 1996 was the only year with more major rain events than OCSs. Note also that 1998 and 1999 are two untypical years (at least as can be ascertained from our limited sample of 9 yr); relative to the seasonal rainfall there are fewer EN rain events than expected in 1998, and in 1999 there are more EN OCSs than expected. One peculiarity of 1999 is that, while the number of EN major rain events is normal, the number of all the EN ground events is above normal (not shown), meaning that in this year an unexpectedly large number of smaller ground events were observed. This also means that the mean rain yield per event was smaller in 1999 and that a larger frequency of deep convective cloud occurrences may not correspond to a larger rain yield. Note that 1999 was the most cloudy year (threshold of 233 K, not shown) over the central Sahel during the last 10 yr and that, as a consequence, satellite rainfall estimates based on the counting of deep convective clouds occurrences [e.g., the global precipitation index method; Arkin (1979)] would predict a large seasonal total. According to the validation provided by the EN network, the rainfall would have been largely overestimated over the central Sahel that year.

It is clear that the good cofluctuation between the total seasonal rainfall and the number of events implies

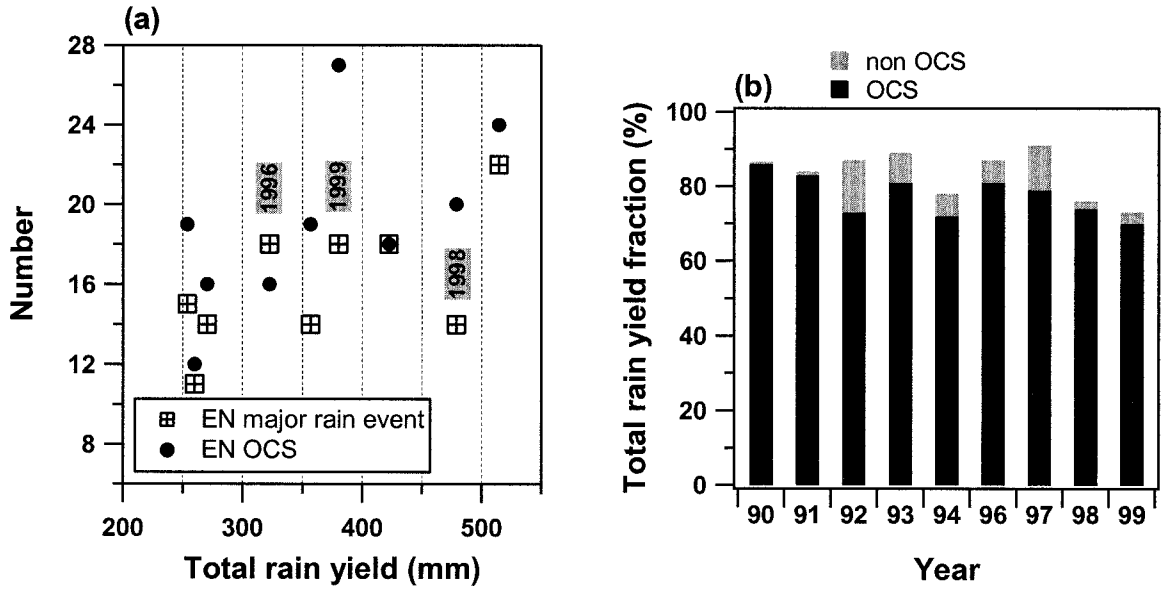


FIG. 10. (a) Number of EN major rain events and number of EN OCSs vs total rain yield between the 1 Jul and 15 Sep. (b) Contribution of the EN MCSs to the seasonal rain yield (the respective contributions of the EN OCSs and of the non-OCSs are shown).

that the fraction of total rain produced by these events is somewhat stable. This is confirmed by Fig. 10b, with the proportion of rain produced by the EN OCSs varying from 70% to 85%. It is striking that the years with the lowest share of OCS rainfall are the wet years: 1994, 1998, and 1999. Only in 1992, a moderately dry year, do we observe a similarly low share of the EN OCS rainfall. Despite some variability from year to year, it is well established from Fig. 10 that the number of OCSs is a good indicator of the abundance of the rainy season, always producing more than 70% of the total rain yield (and even more if one considers the correction applied to the seasonal statistics of the OCS rainfall at the end of section 5a). Keeping in mind the spatial distribution of the OCSs shown in Fig. 6, it can be concluded that the OCSs constitute a key element for understanding the interannual variability of rainfall over the Sahel.

## 7. Conclusions

The work presented here has two main objectives. One is to obtain reliable statistics for the rainfall produced by mesoscale convective systems over the Sahel, depending on their extension and degree of organization. The other is to identify the factors influencing the variability of these statistics. To reach these goals, two high-resolution datasets were used: full-resolution infrared images collected by Meteosat that cover the whole of the Sahel and direct rainfalls recorded by the dense EPSAT-Niger network of digitized rain gauges covering a 16 000-km$^2$ area in the region of Niamey. Both datasets span a common period of 9 yr, thus allowing for the computation of reliable statistics regarding the core of the rainy season (1 July–15 September).

For the period considered, it has been found that 90% of the total rainfall over the 16 000-km$^2$ EN area is produced by a small population of organized convective systems characterized by a 213-K cluster lasting for 3 h or more and moving at a speed of more than 10 m s$^{-1}$. This population of OCSs represents only 12% of the total population of MCSs—defined as 5000-km$^2$ cloud clusters at 233 K. The OCSs are also responsible for about 78% of the cloud cover at 233 K, which is a confirmation that, statistically, the 233-K cloud cover is a good proxy of ground rainfall. The average rain production of one OCS is 14.7 mm. This amount is less than the average rain produced by an MCC (defined from Maddox criteria), which is 19 mm. Hence, MCCs are more rain efficient than OCSs, but their frequency is much smaller (on average, 3 MCCs vs 19 OCSs are recorded during one rainy season over the 16 000-km$^2$ area) and they account for only 16% of the seasonal rainfall over the central Sahel.

Over the EN validation area, the comparison between the population of convective systems and the population of rain events shows that all of the OCSs are associated with a rain event identified from the rain gauge network. In fact, the share of the seasonal rainfall was computed to be 91% for the so-called EN rain events and was estimated to be around 90% for the OCSs. It is thus possible to build a coherent climatologic description of rain events based on the identification of OCSs from infrared imagery. To summarize, OCSs are large and fast-moving systems—this, as found in previous studies, implies some degree of organization—that account for most of the rain over the Sahel during the core of the rainy season.

The variability of the rainfall produced by MCSs is

determined by two factors: (i) their rate of occurrence and (ii) their intensity. In this paper, it has been shown that the interannual variability of rainfall in the region is mostly determined by the year-to-year fluctuation of the number of OCSs, which confirms results obtained previously from ground measurements (see e.g., D'Amato and Lebel 1998).

Beyond the initial goals of the study, the demonstration that it is possible to associate a single cloud system to a rain event at the mesoscale has important consequences for rainfall studies over a limited region. For instance, the hypothesis of Shinoda et al. (1999) on the origin of the nocturnal and early-morning peak of precipitation observed over the region of Niamey was confirmed. This is due to the propagative nature of the OCSs associated with orography-driven generations located a few hundred kilometers to the east of the validation area. Another application of this study is in the area of satellite rainfall estimation. It is known that a simple counting of cloud cover at 233 K may provide good rainfall estimates when a sufficiently large averaging is carried out in space and time. This may be related to our result showing that 233-K cloud cover is correlated well with the number of OCSs, which is itself correlated well with rainfall. At the same time, there is a random and significant variability of the average rain rate from one OCS to another. Algorithms that combine a satellite-based identification and tracking of the OCSs with a few ground measurements to enable an estimation of their average rain rate should, therefore, produce more robust rain estimates than a simple counting of the number of 233-K pixels.

*Acknowledgments*. We are grateful to Direction de la Météorologie du Niger, and especially to its director, Dr. A. Also, for our close collaboration in the operation of the EPSAT-Niger network. Special thanks are given to three anonymous reviewers for detailed comments and suggestions on the paper and to Nick Hall for helping to put it in proper English. This research was funded by IRD.

## REFERENCES

Arkin, P. A., 1979: The relationship between fractional coverage of high cloud and rainfall accumulations during GATE over the B-scale array. *Mon. Wea. Rev.*, **107,** 1382–1387.

D'Amato, N., and T. Lebel, 1998: On the characteristics of the rainfall events in the Sahel with a view to the analysis of climatic variability. *Int. J. Climatol.*, **18,** 955–974.

Desbois, M., T. Kayiranga, B. Gnamien, S. Guessous, and L. Picon, 1988: Characterization of some elements of the Sahelian climate and their interannual variations for July 1983, 1984 and 1985 from the analysis of Meteosat ISCCP data. *J. Climate*, **1,** 867–904.

Duvel, J. P., 1989: Convection over tropical Africa and the Atlantic Ocean during northern summer. Part I: Interannual and diurnal variations. *Mon. Wea. Rev.*, **117,** 2782–2799.

Hamilton, R. A., and J. W. Archbold, 1945: Meteorology of Nigeria and adjacent territories. *Quart. J. Roy. Meteor. Soc.*, **71,** 231–235.

Houze, R. A., 1977: Structure and dynamics of a tropical squall line system observed during GATE. *Mon. Wea. Rev.*, **105,** 1540–1567.

——, 1981: Structure of atmospheric precipitation systems: A global survey. *Radio Sci.*, **16,** 671–689.

——, 1993: *Cloud Dynamics*. Academic Press, 573 pp.

——, B. F. Smull, and P. Dodge, 1990: Mesoscale organization of springtime rainstorms in Oklahoma. *Mon. Wea. Rev.*, **118,** 613–654.

Jobard, I., and M. Desbois, 1992: Remote sensing of rainfall over tropical Africa using Meteosat infrared imagery: Sensitivity to time and space averaging. *Int. J. Remote Sens.*, **13–14,** 2683–2700.

Lafore, J.-P., and M. W. Moncrieff, 1989: A numerical investigation of organization and interaction of the convective and mesoscale region of a tropical squall line. *J. Atmos. Sci.*, **46,** 521–544.

Laing, A. G., and J. M. Fritsch, 1993: Mesoscale convective complexes in Africa. *Mon. Wea. Rev.*, **121,** 2254–2263.

——, ——, and A. J. Negri, 1999: Contribution of mesoscale convective complexes to rainfall in Sahelian Africa: Estimates from geostationary infrared and passive microwave data. *J. Appl. Meteor.*, **38,** 957–964.

Laurent, H., T. Lebel, and J. Polcher, 1997: Rainfall variability in Soudano-Sahelian Africa studied from raingauges, satellite and GCM. Preprints, *13th Conf. on Hydrology*, Long Beach, CA, Amer. Meteor. Soc., 17–20.

Le Barbé, L., and T. Lebel, 1997: Rainfall climatology of the HAPEX-Sahel region during the years 1950–1990. *J. Hydrol.*, **188–189,** 43–73.

Lebel, T., and A. Amani, 1999: Rainfall estimation in the Sahel: What is the ground truth? *J. Appl. Meteor.*, **38,** 555–568.

——, H. Sauvageot, M. Hoepffner, M. Desbois, B. Guillot, and P. Hubert, 1992: Rainfall estimation in the Sahel: The EPSAT-Niger experiment. *Hydrol. Sci. J.*, **37,** 201–215.

——, J. D. Taupin, and N. D'Amato, 1997: Rainfall monitoring during HAPEX-Sahel: 1. General rainfall conditions and climatology. *J. Hydrol.*, **188–189,** 74–96.

Machado, L. A. T., M. Desbois, and J.-P. Duvel, 1992: Structural characteristics of deep convective systems over tropical Africa and the Atlantic Ocean. *Mon. Wea. Rev.*, **120,** 392–406.

——, W. B. Rossow, R. L. Guedes, and A. W. Walker, 1998: Life cycle variations of mesoscale convective systems over the Americas. *Mon. Wea. Rev.*, **126,** 1630–1654.

Maddox, R. A., 1980: Mesoscale convective complexes. *Bull. Amer. Meteor. Soc.*, **61,** 1374–1387.

Mathon, V., and H. Laurent, 2001: Life cycle of the Sahelian mesoscale convective cloud systems. *Quart. J. Roy. Meteor. Soc.*, **127,** 377–406.

Miller, D., and J. M. Fritsch, 1991: Mesoscale convective complexes in the western Pacific region. *Mon. Wea. Rev.*, **119,** 2978–2992.

Redelsperger, J.-L., and J.-P. Lafore, 1988: A three-dimensional simulation of a tropical squall line: Convection, organization and thermodynamic vertical transport. *J. Atmos. Sci.*, **45,** 1334–1356.

Roux, F., 1988: The West African squall line observed on 23 June 1981 during COPT 81: Kinematics and thermodynamics of the convective region. *J. Atmos. Sci.*, **45,** 406–426.

Rowell, D. P., and J. R. Milford, 1993: On the generation of African squall lines. *J. Climate*, **6,** 1181–1193.

Shinoda, M., T. Okatani, and M. Saloum, 1999: Diurnal variations of rainfall over Niger in the West African Sahel: A comparison between wet and drought years. *Int. J. Climatol.*, **19,** 81–94.

Smull, B. F., and R. A. Houze, 1985: A midlatitude squall line with a trailing region of stratiform rain: Radar and satellite observations. *Mon. Wea. Rev.*, **113,** 117–133.

Williams, M., and R. A. Houze, 1987: Satellite-observed characteristics of winter monsoon cloud clusters. *Mon. Wea. Rev.*, **115,** 505–519.

Zipser, E. J., 1977: Mesoscale and convective-scale downdrafts as distinct components of squall-line structure. *Mon. Wea. Rev.*, **105,** 1568–1589.

# The Convective System Area Expansion over Amazonia and Its Relationships with Convective System Life Duration and High-Level Wind Divergence

LUIZ AUGUSTO T. MACHADO* AND HENRI LAURENT+

*Divisão de Ciências Atmosféricas, Centro Técnico Aeroespacial, Instituto de Aeronáutica e Espaço São José dos Campos, São Paulo, Brazil*

(Manuscript received 4 November 2002, in final form 2 September 2003)

ABSTRACT

The relationships between the initial area expansion rate of tropical convective systems and their total life duration are analyzed during the period of the Wet Season Amazon Mesoscale Campaign/Large-Scale Biosphere–Atmosphere (WETAMC/LBA) experiment over tropical South America, using an objective tracking of convective systems during their life cycle from infrared Geostationary Operational Environmental Satellite (GOES) images. The results show that it is possible to estimate the probable lifetime of a convective system, within certain error bars, considering only its initial area expansion. This result shows that the initial area expansion could be used as a predictor of the life cycle of convective systems. The area expansion is also a good indicator of convective activity such as the diurnal cycle of convection. Over the southwest Amazon, the maximum area expansion occurs close to the time of maximum precipitation and about 4 h before the maximum cold cloud fraction at the same threshold (235 K).

Also, the hypothesis that the area expansion, and hence the convective activity, impacts the high-level wind divergence has been investigated using satellite wind observations. It is found that the wind divergence fields derived are able to describe the large-scale patterns but are not able to capture the small-scale features. The diurnal cycle of the high-level wind divergence generally shows a flat response over tropical South America, although a coherent but not significant signal is observed over the WETAMC/LBA area. It is shown that the area of the cloud shield of convective systems varies not only in association with the upper-level wind divergence but also with the condensation–evaporation process. The increase of area in this initial stage is mainly due to the condensation process. During the ensuing mature stage, the upper-air wind divergence also contributes to the expansion.

## 1. Introduction

Convective systems are responsible for most of the rainfall in tropical regions as well as in temperate latitudes during the warm season, and they are also responsible for some extreme weather conditions in various regions of the earth. Knowledge of convective system evolution is of fundamental importance for understanding weather and climate, particularly in the Tropics, and it is essential for improving forecasting of these systems to reduce vulnerability to extreme weather damage. The identification of predictor parameters for the evolution of a convective system, based on its previous evolution, could make a significative contribution to a nowcasting scheme and provide important information for mesoscale model initialization.

Machado et al. (1998), using a methodology able to track convective systems during their life cycle, suggested that the surface expansion of a convective system could be associated with the high-level wind divergence and the length of the life cycle. They showed that large initial growth rates characterize large and long-lived convective systems and suggest a large updraft inside the convective towers consistent with high cloud tops and large upper-level divergence. Knowledge of the divergence field is important for understanding the tropical atmospheric circulation. Cumulus-scale convection supplies the energy needed to force large-scale disturbances that will in turn produce the low-level moisture convergence needed to drive the convection, resulting in ascending motions in the convective systems and divergence at high levels due to mass continuity (Holton 1979). Unfortunately, conventional observations are very few in tropical and oceanic regions; therefore, satellite data must be used to study convective atmospheric circulations. Wind vectors estimated from successive water vapor channel satellite images are numerous, provide consistent wind fields at high levels (Laurent 1993; Velden et al. 1997), and can be used for climatological

* Current affiliation: CPTEC/INPE, Cachoeira-Paulista, São Paulo, Brazil.
+ Current affiliation: LTHE, IRD, Grenoble, France.

*Corresponding author address:* Dr. Henri Laurent, LTHE/IRD, BP 53, 38041 Grenoble Cedex 9, France.
E-mail: Henri.Laurent@ird.fr

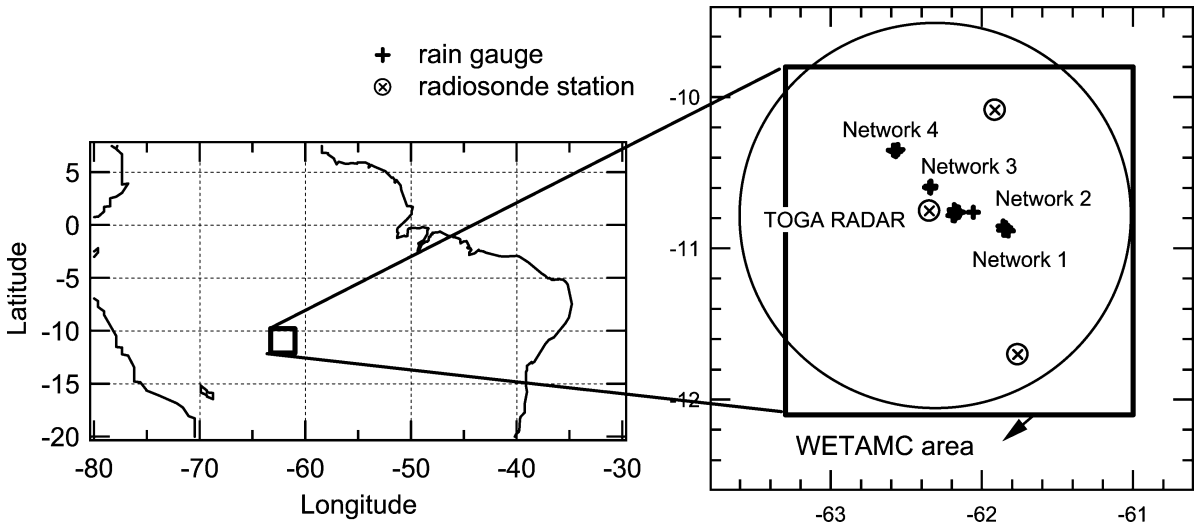


FIG. 1. (left) Region used to track the convective systems from GOES images and the location of the WETAMC/LBA area. (right) Location of the 150-km range of the TOGA radar (circle), the WETAMC area (square), the rain gauges clustered in four networks, and the radiosounding stations.

studies (Schmetz et al. 1995) or to monitor convective systems. Laurent and Sakamoto (1998) calculated the high-level wind divergence from water vapor wind fields. They showed that the areas with low brightness temperature, corresponding to convective systems, are well correlated with large divergence values.

Scofield (1987) presented a technique to estimate precipitation using image satellite based on the time evolution of the convective cloud area. Estimates of convective rainfall are computed by comparing the changes in cloud characteristics that are observed between two consecutive images of enhanced infrared and visible images. This technique and others of similar nature have shown that the area evolution of a convective system can be associated with the intensity of the precipitation.

This study utilizes the dataset collected during the Wet Season Amazon Mesoscale Campaign (WETAMC) held in January–February 1999, in the Rondônia state in Brazil, as part of the Large-Scale Biosphere Atmosphere (LBA) experiment (Silva Dias et al. 2002). Several instruments for measuring precipitation as part of the ground validation of the Tropical Rainfall Measuring Mission (TRMM) satellite were also included in WETAMC (Petersen et al. 2002). The TRMM–WETAMC/LBA experiment presents a unique opportunity to analyze the convective processes in the Amazon, enabling study of convective systems by combining different measurements such as satellite, radar, radiosonde, and rain gauge.

The growth rate of the convective systems can be deduced from their area expansion, which is easily observed from successive satellite images. This area expansion is expected to be associated with the high-level wind divergence and with the rate of condensation/evaporation that is directly related to the mass flux inside the convective system. The objective of this study is to investigate these hypotheses to examine if the rate of change of area of a convective system can be associated with its lifetime and if this rate can indicate the level of convective activity.

In section 2 the in situ and satellite data used in this study are presented. Section 3 presents the initial area expansion of the convective systems and its relationship with the system duration. The diurnal cycle of the area expansion is shown in section 4 and compared with precipitation and high-level wind divergence in the WETAMC region. The relationships between area expansion and high-level wind divergence are analyzed in section 5. Section 6 summarizes the main conclusions.

## 2. Data

### *a. Rain gauge, radar, and radiosonde data*

The WETAMC/LBA allows us to study the three-dimensional structure of convective systems and their associated precipitation using a combination of meteorological radars, rain gauge network, TRMM active and passive sensors, and radiosonde data. Figure 1 shows the location of the experiment and the many instruments used in this study.

The rain gauge network was distributed in four clusters. The rain gauge tipping buckets have a sampling resolution of 0.254 mm and maximum temporal resolution of 10 s. In this study we used the hourly accumulated rain gauge data from the Goddard Distributed Active Archive Center (DAAC). An average over the four networks was applied to describe the average hourly rainfall over the TRMM–WETAMC region (see Fig. 1 for location).

Three radiosonde stations performed 3-hourly soundings during the experiment: Rebio Jaru (RJ: 10°, 5′S,

61°, 55′W; altitude, 120 m); Abracos (AB: 10°, 45′S, 62°, 21′W; altitude, 290 m); Rolim de Moura (RM: 11°, 42′S, 61°, 46′W; altitude, 225 m). These three stations form a triangle, allowing for the computation of horizontal wind divergence using the Kelvin and Green theorem. Machado (2000) used this method to compute the fields of mass and energy divergence in the Amazon region. In this study we will focus on the 200-hPa wind divergence.

Data from the National Aeronautics and Space Administration (NASA) C-band radar (wavelength of 5.4 cm) known as the Tropical Ocean and Global Atmosphere Program (TOGA) radar were used to track the displacements of the rain cell echoes. During the experiment, complete volume scans were performed at 10-min intervals, from which was calculated the 2-km constant altitude plan position indicator (CAPPI), following Anagnostou and Krajewski (1997). We used CAPPIs with a horizontal resolution of 5 km × 5 km limited to a range of 150 km to be consistent with the horizontal resolution obtained in the Geostationary Operational Environmental Satellite (GOES) IR images. The TOGA radar calibration was also adjusted using the TRMM precipitation radar (Anagnostou and Morales 2002). With the same methodology as described for the satellite data in section 2b, the rain cells observed in the CAPPI 2-km data were tracked throughout their life cycle, considering only the cells that initiated and dissipated spontaneously inside the 150-km disk. The rain cells delimited with the 20-dB*Z* threshold include weak to strong rainfall. More details on the methodology can be found in Laurent et al. (2002).

### *b. Satellite data processing*

The *GOES-8* satellite images were preprocessed by NASA Goddard Space Flight Center (GSFC) for the entire duration of the experiment at full resolution (every 30 min; pixel size of ~4 km for the infrared channels). The convective systems are detected using the thermal infrared channel (~11 $\mu$m) assuming that the convective clouds that are high and thick are those with a small brightness temperature. A convective system is here defined as an area of at least 200 pixels (i.e., an area larger than about 3500 km$^2$) that falls below the temperature threshold. Two thresholds were used: 235 K to identify the whole convective system including the thick cirrus shield and 210 K to identify the areas of very intense convection that may exist embedded in the convective system. The systems are tracked during their life cycle using the method described by Mathon and Laurent (2001) that determines whether the system initiates spontaneously or from a split, and whether it ends by dissipation or by merging into another system. This objective tracking was performed for the period 11 January–27 February over a window covering tropical South America approximately from 7.5°N to 20°S and from 80° to 30°W. The total number of systems tracked was 13 409 at 235 K and 3867 at 210 K. For comparison with the WETAMC/LBA observations, we use a window defined by 12°–8°S and 64°–60°W (see Fig. 1). A more detailed description of the methodology is given in Laurent et al. (2002).

According to the average radiosonde profile, the 235-K (210 K) level is located around 260 hPa (160 hPa). Indeed, as the temperatures of the convective system pixels are lower than 235 K, the system top level is somewhere above the 260 hPa level. To estimate the wind divergence associated with the system top, we will therefore consider the slice from 250 to 150 hPa.

## 3. Area expansion of the convective systems

### *a. Definition of the area expansion*

The convective system area is calculated from the number of pixels with a brightness temperature smaller than the given threshold (235 or 210 K). The area expansion rate is simply the normalized difference of the system area between two successive images (Machado et al. 1998). The area expansion is closely linked to the phase of the convective system life. At the beginning of its life the convective system presents a large positive area expansion. The area expansion is close 0 during the mature phase of the system and negative during the dissipative phase. The magnitude of the area expansion may be a good indicator to monitor the convective activity of the convective system, acting as a proxy to quantify the mass flux or the condensation rate inside the convective system.

Machado et al. (1998) discuss the possibility of associating the area expansion of the convective systems with the high-level wind divergence, if condensation and evaporation are neglected, with the following equation:

$$A_e = \frac{1}{A}\frac{\partial A}{\partial t} \approx \nabla \cdot \mathbf{V}, \tag{1}$$

where $A$ is the convective system area, and $\mathbf{V}$ is the horizontal wind vector. In this paper, $A_e$ is the normalized area time rate of expansion called area expansion. A negative area expansion corresponds to contraction. Rapid area expansion would correspond to large upper-level wind divergence (e.g., Wallace and Hobbs 1979).

Machado et al. (1998) suggest that the magnitude of the area expansion at the initial time may be related to the total duration of the convective system. They found that the area expansion is systematically larger at the initiation stage for long-lived convective systems. There are two possible reasons for this: (i) the environmental conditions that are needed for vigorous development of convection, such as low-level moisture convergence and vertical conditional instability, are likely to persist during the following hours; and (ii) a strong area expansion indicates a strong internal dynamic (strong mass flux) of the convective system that will transport energy to

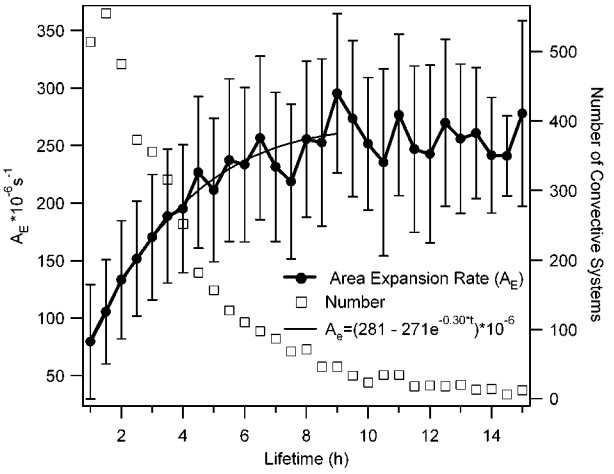


FIG. 2. Area expansion ($A_e$; $10^{-6}$ s$^{-1}$) and associated std dev as a function of the convective system lifetime (h). The number of cases is also plotted (right axis).

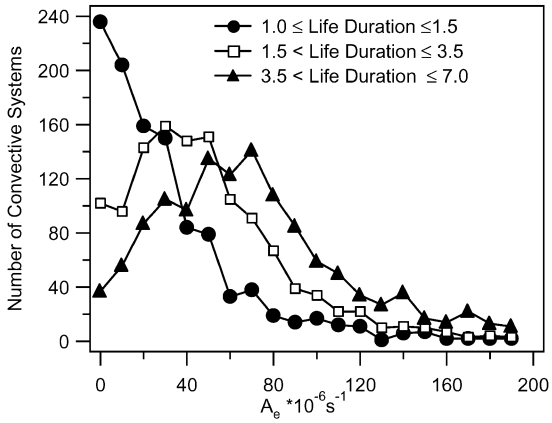


FIG. 3. Histogram of the area expansion ($10^{-6}$ s$^{-1}$) for three classes of convective system lifetime.

the middle to high troposphere, modifying the atmospheric circulation and favoring the low-level moisture convergence that will in turn prolong the life of the convective system. This feedback is likely to be activated if the convective system has a strong internal mass flux in the initial stage. Note that as the convective systems have a size larger than 3500 km$^2$, they include various convective towers, and the satellite analysis is an integration of all small-scale features.

### *b. Relationship between area expansion and lifetime*

The work of Machado et al. (1998) was based on a low-resolution dataset and did not consider the different situations of splitting and merging of convective systems. This study aims to test the hypotheses mentioned using high-resolution data from various sources. In order to analyze the relationship between the area expansion of a convective system and its lifetime, we only consider here the systems that initiate spontaneously (i.e., not as a result of a split of a former system) and end by dissipation (i.e., not by merging into another system). This ensures that the initial growth of the system is due to its internal dynamics and that the lifetime is representative of a complete life cycle. The tracking method allows for such a selection; the number of systems is thus reduced to 4240 at 235 K and 2569 at 210 K.

The average relationship between area expansion at the initial time (between t0 and t0 + 30 min) and total lifetime is shown in Fig. 2. The plot gives the mean area expansion observed for each life duration and the associated standard deviation. The number of observed convective systems is also indicated. On average, the convective systems with a weak area expansion during the initial phase have a short lifetime. The convective system duration increases as its initial area expansion increases. The fitted curve shows that there is a nearly exponential relationship. For life duration larger than 8 h the function could be asymptotic; however, the small number of cases leads to a very noisy and inconclusive relationship. For most cases (lifetime smaller than 8 h) the results show that the area expansion is a good indicator of the lifetime, within error bars, and that the relationship can be approximated by an exponential function.

The relationship shown in Fig. 2 is valid on average, but there is considerable variability. Figure 3 shows the histogram of the area expansion values for three classes of convective systems: lifetime of 1 and 1.5 h, from 2 to 3.5 h, and from 4 to 7 h. Each class has approximately the same population. The three histograms are different, showing that there is a larger probability that a small area expansion is associated with a short lifetime than with a long one. However, it can also be seen that there is quite a large dispersion; in other words, a given area expansion value can be associated with different life durations. In fact it is not only the initial conditions but also other factors that can impact the growth and duration of convective systems, for instance, the topography, breeze effect, or any change of forcing during the life of the system. However, it is beyond the scope of this paper to reach a full understanding of these different cases.

To analyze the impact of the threshold used to define the convective systems and hence their area expansion and lifetime, the same calculations were performed for a threshold of 210 K. Figure 4 shows the area expansion at the initial time versus lifetime for convective systems defined at 210 and 235 K. There is a similar relationship for both cases. For the convective systems defined with the colder threshold, the coefficient of the exponential fitting is $-0.5$ instead of $-0.3$. According to Eq. (1), this means that the high-level wind divergence associated with the convection is larger when the convective system has a very cold top, consistent with the idea that in a given location the higher the convective cloud top, the more intense the convective activity. On the one

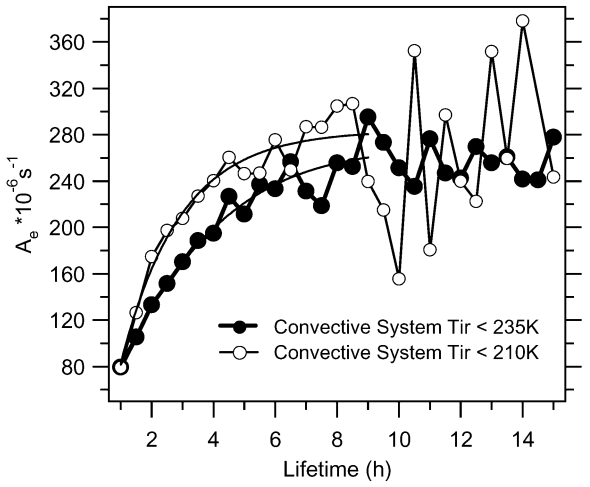


FIG. 4. Area expansion ($10^{-6}$ s$^{-1}$) vs lifetime (h) for the convective systems defined at 235 or 210 K.

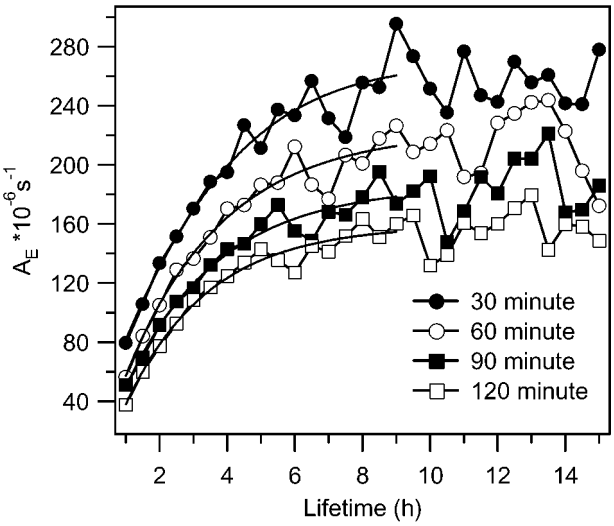


FIG. 5. Area expansion ($10^{-6}$ s$^{-1}$) vs lifetime (h) of the convective systems for area expansion calculated with a time interval of 30, 60, 90, or 120 min.

hand, the relationship between initial area expansion and lifetime seems sharper with the 210-K threshold than with the 235-K threshold. This is likely to be due to the shorter lifetime of the convective cells (convective systems defined by 210 K) merged inside the convective system. On the other hand, the number of 210-K convective cells is smaller, and the area expansion variability is very large for lifetimes larger than 5 h. The initial time of the convective cells comes after the initial time of the convective system at a warmer threshold. Therefore, considering a possible application of the present study in nowcasting, it is preferable to focus on the earlier-detected, 235-K convective systems. Another parameter that needs to be analyzed is the time interval used to calculate the area expansion. In the previous results the minimum interval was used: 30 min between the first and the second image containing the convective system considered. However a larger time interval can be used. Figure 5 shows the area expansion versus lifetime relationship when computing the area expansion over an initial time interval of 30, 60, 90, or 120 min. The relationship remains very similar but the values of the area expansion vary by a factor of 1.7. Nevertheless, it should be noted that a shorter time interval is much more useful for nowcasting. Note that the wind divergence is also very dependent on the time interval over which it is computed. Based on these results, an empirical relationship between area expansion and life cycle duration can be established. This relationship will depend on the threshold and the time interval between two successive images.

The results indicate that a mean relationship exists between the area expansion at the initial time and the lifetime of the convective systems. This relationship depends on the definition of a convective system and the time interval considered. The main point is that it is possible to estimate the highest probability duration of a convective system, within certain error bars, considering only its growth rate during its initiation phase. The same is true for the size of the convective system, as there is a good relationship between size and lifetime (Machado et al. 1998; Mathon and Laurent 2001). Figure 6 presents a simplified representation of the convective system life cycle. The faster the initial growth rate, the larger the size and the duration of the system.

Using the CAPPI 2-km data from the TOGA radar, the area expansion can be computed in the same way as for the satellite data. The area expansion of the rain cells is closely linked to the water condensed at 2-km height, resulting from low-level moisture convergence. Figure 7 shows the area expansion of the rain cell as a function of the rain cell duration. The number of cases is quite small because of the rejection of every case of splitting or merging and also because of the small area covered by the radar. It can be seen, however, that the

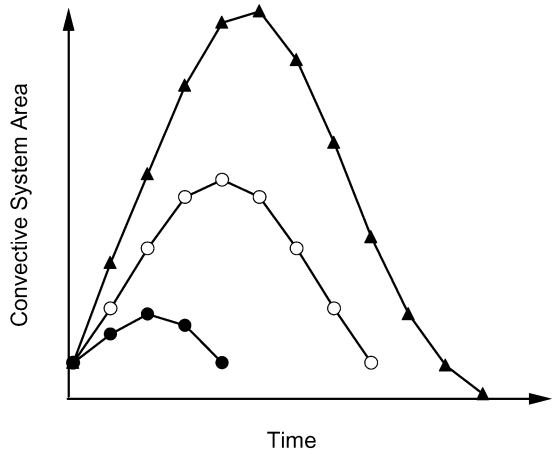


FIG. 6. Schematic diagram of the convective system size evolution for different initial area expansions.

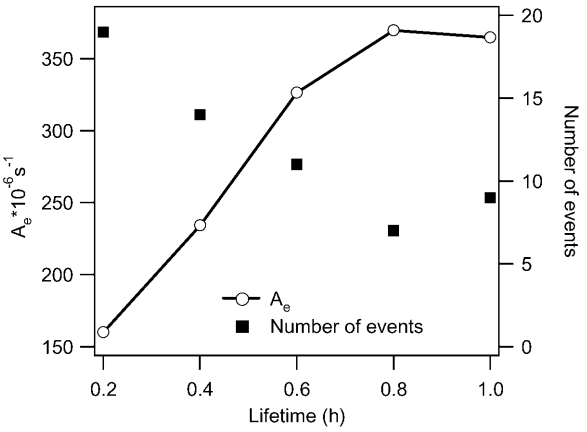


FIG. 7. Area expansion ($10^{-6}$ s$^{-1}$) vs rain cell lifetime (h), using CAPPI 2-km data with the 20-dB*Z* threshold. The number of cases is also indicated (right axis).

relationship is similar to what is observed for the convective systems (Fig. 2). Note the difference in time scale between the rain cells (typically 1 h) and the convective systems (typically 10 h). In the latter case the rapid increase of area of liquid water in the initiation stage can be linked with the vigor of the dynamics associated with the convective system. The radar data observations suggest that the area expansion can be closely associated with the low-level humidity convergence, and the effect of the condensation probably cannot be neglected, as will be discussed in section 5.

## 4. The diurnal cycle of the area expansion, precipitation, and wind divergence

One of the main difficulties in comparing the convective system area expansion with the high-level wind divergence arises from the different time and space scales involved. As was mentioned before, the wind divergence depends strongly on the space–time scale. In order to investigate how Eq. (1) can be used to relate the cloud shield expansion with the wind divergence, we need to make some simplifications:

- The area expansion is considered as uniform for the whole convective system area (threshold, 235 K), which is reasonable when considering the mean behavior. Actually, as seen in Fig. 4 the coldest parts of the system are associated with larger values of area expansion and therefore divergence. We do not attempt to detail here the internal structure of the systems but rather try to understand their mean behavior.
- The pressure level corresponding to 235 K is about 250 hPa in the region of the experiment; however, a large fraction of the cloud system top is at higher levels. We consider here a slice of 200 hPa $\pm$ 50 hPa as representative of the whole convective system top.

The area expansion has been computed for every convective system for each 30-min interval. The values obtained over each system have then been interpolated on a regular $1° \times 1°$ grid using the Barnes (1964) methodology. The average 3-hourly fields computed over the period 10 January–29 February 1999 are presented in Fig. 8. This figure shows that the area expansion describes very clearly the diurnal cycle of the convection. The large convective activity develops over the Amazon region at about 1300 LST, that is, 1600 UTC at 45°W and 1700 UTC at 60°W. During nighttime the convective systems dissipate (negative area expansion) in agreement with the diurnal cycle described by Machado et al. (2002).

To compare the area expansion with the high-level wind divergence, we have used high-level wind measurements obtained from successive water vapor (WV) channel GOES images (Velden at al. 1997). These so-called WV winds have been computed every 3 h for the entire WETAMC/LBA experiment by National Oceanic and Atmospheric Administration/National Environmental Satellite, Data, and Information Service (NOAA/NESDIS). The wind vectors in the 150–250-hPa layer are here interpolated onto a $1° \times 1°$ grid using the same method as applied to the area expansion. The divergence is then calculated by finite differences. The mean divergence computed from the WV winds is presented in Fig. 9. The WV wind mainly describes the large-scale field. The divergence field in Fig. 9 is very close to the cold cloud occurrences for a brightness temperature threshold of 235 K (not shown). The 200-hPa WV wind vectors are derived from the motions of high-level clouds, whereas the water vapor structure motions derived in regions free of high-level clouds are assigned to lower levels than 250 hPa. Therefore the regions of subsidence are not considered in the 200-hPa field. The variability of divergence time series is large (standard deviation of almost $2 \times 10^{-5}$ s$^{-1}$), which can explain that the mean diurnal variation of the 200-hPa WV wind divergence over the whole region is quite noisy and does not show a clear diurnal cycle (not shown).

In order to compare the area expansion, the wind divergence from radiosonde and the WV wind divergence, we focus on the WETAMC/LBA area defined by the region from 12° to 8°S and 64° to 60°W. To compute the area expansion and the water vapor wind, only the convective systems and the wind vectors inside these areas are considered. The divergence computed from radiosonde is obtained from the three radiosonde sites, and the methodology is described in section 2a.

Figure 10 shows the average diurnal variation for the 200-hPa level of the wind divergence from radiosonde, the WV wind divergence, and the area expansion. There is a coherent phase variation among these parameters, exhibiting a maximum in the beginning of the afternoon close to the time of maximum precipitation (see Fig. 11). During nighttime, according to the radiosonde data, there is a secondary maximum, barely visible with the water vapor wind divergence and the area expansion. Machado et al. (2002) have shown that the convective

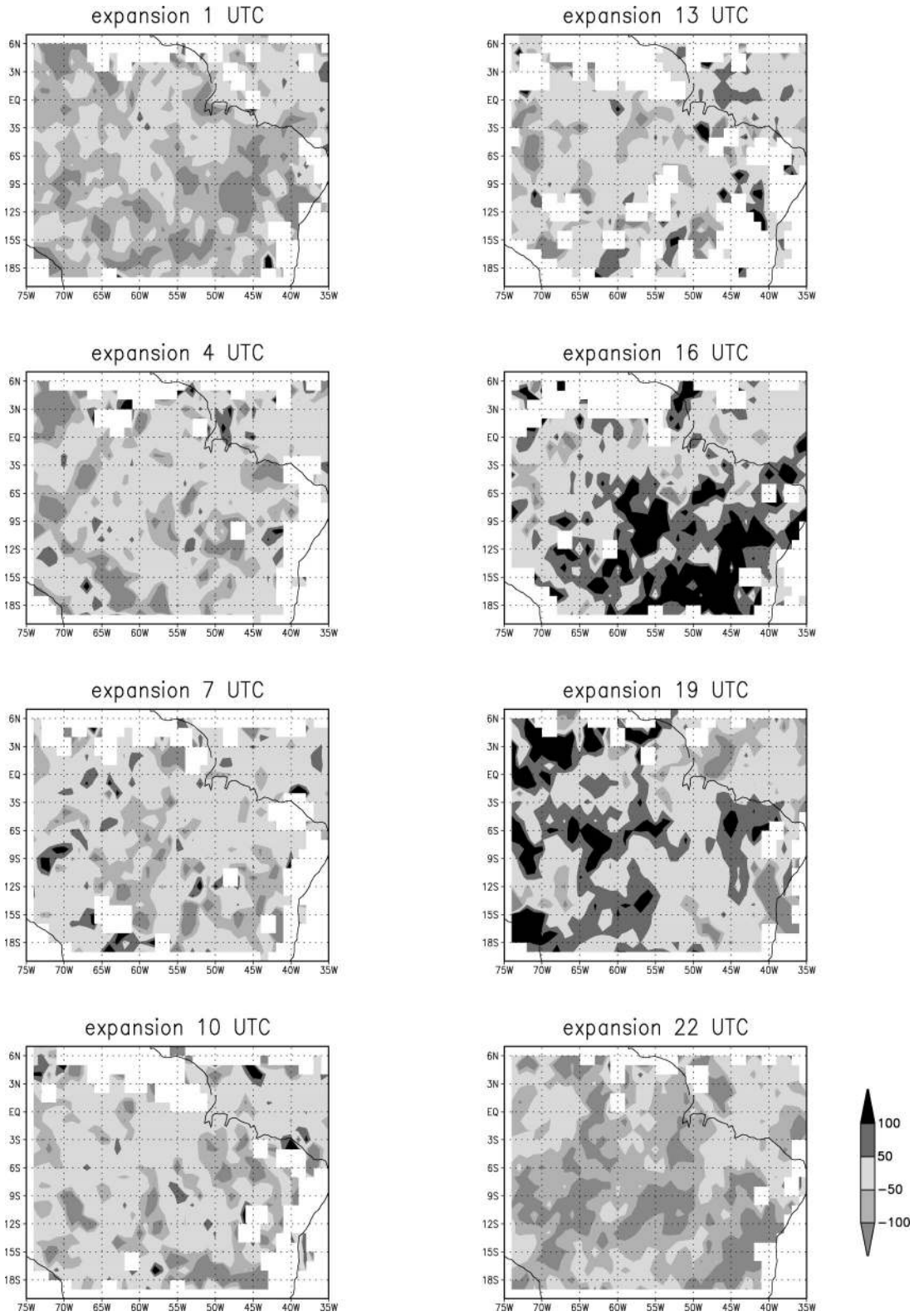


FIG. 8. Mean area expansion ($10^{-6}$ $s^{-1}$) over the period 10 Jan–28 Feb 1999 for different hours (UTC).

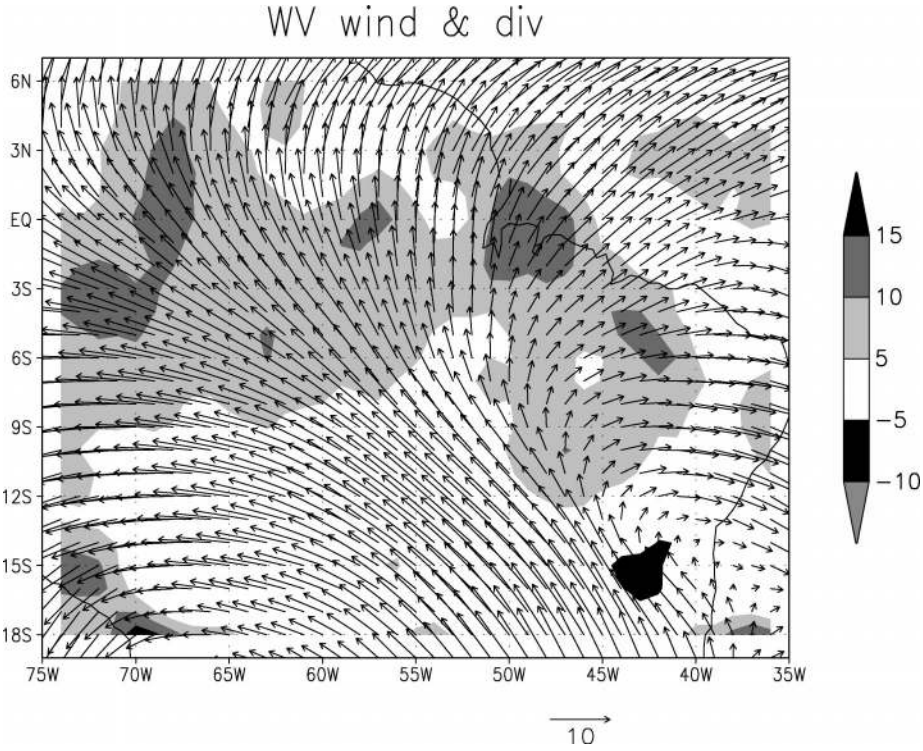


FIG. 9. Mean wind (m $s^{-1}$) and wind divergence ($10^{-6}$ $s^{-1}$) over the period 10 Jan–28 Feb 1999 computed from the NOAA/NESDIS water vapor winds in the slice 150–250 hPa.

cloud fraction was very small during the night during the WETAMC/LBA period. Therefore the secondary maximum of divergence is probably not related to the convective systems, but rather to the large-scale field. There is a small time lag between the maxima: the area expansion peaks 1 h earlier than the wind divergence from radiosonde and 2 h earlier than the water vapor wind divergence; this feature will be discussed in the next section. It should also be noted that the number of WV wind vectors in the level considered is drastically reduced during the morning because of the small cold cloud amount at that time. The values of the wind divergence are very different depending on the different calculations. This is probably due to the fact that the wind divergence is a parameter very sensitive to the spatial and time scales considered and to the different smoothness of the wind field from different sources. The WV winds are computed by tracking large-scale clouds

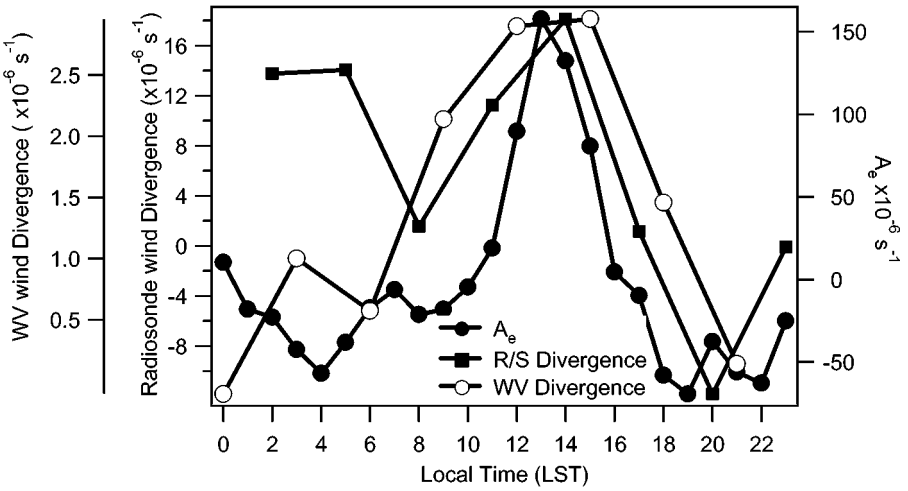


FIG. 10. Mean hourly area expansion, water vapor wind divergence, and radiosonde-derived wind divergence ($10^{-6}$ $s^{-1}$) for the 200-hPa level in the WETAMC/LBA region.

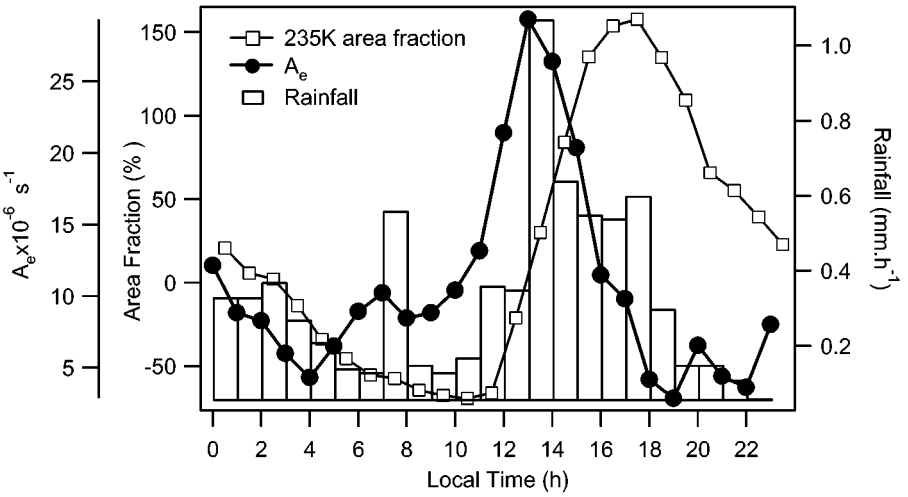


FIG. 11. Mean hourly area expansion ($10^{-6}$ s$^{-1}$), rainfall (mm h$^{-1}$), and 235-K area fraction (%) for the WETAMC/LBA region.

and water vapor structures using windows of about 130-km width in three successive images, that is, over 1 h. The flow of these structures is smoothed in comparison with the local wind as measured with radiosondes. Over the WETAMC/LBA area, the values of divergence calculated from the radiosondes are typically 4 times larger than those calculated from the WV winds and 8 times smaller than the area expansion. As already mentioned, the diurnal cycle of upper-level divergence is generally not observed elsewhere from the WV wind divergence, and the WV divergence signal observed over the WETAMC/LBA area is not significant according to the large standard deviation of this measurement. Radiosonde observations in other areas or other periods would be necessary to check the validity of the WV wind divergence diurnal cycle observed here.

Figure 11 shows the average diurnal cycle of the area expansion, rainfall, and 235-K area fraction. It can be seen that the maximum area expansion occurs close to the time of maximum precipitation and around 4 h before the maximum cold cloud fraction defined with the same threshold (235 K). This means that, for this region, the area expansion captures the moment of maximum precipitation, whereas a traditional approach to estimate the rainfall using brightness temperature would be biased by about 4 h. As discussed by Machado et al. (2002), precipitation occurs very rapidly in the beginning of the afternoon close to the time of minimum total cloud cover. It is also the time when high and convective clouds have the maximum area fraction increase rate and when the initiation of convective systems and rain cells are the most numerous. These are the characteristics of the convection in the WETAMC/LBA region. However, other investigations are needed to determine whether the nearly simultaneous time of maximum precipitation, wind divergence, and area expansion could be verified in others regions of Amazonia.

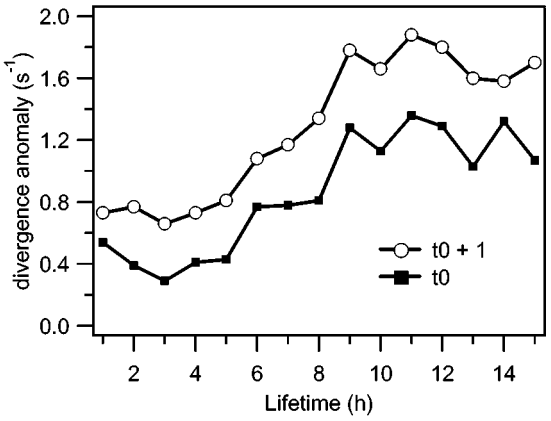


FIG. 12. Water vapor wind divergence anomaly ($10^{-6}$ s$^{-1}$) associated with the convective systems vs convective system lifetime (h) at the time of system initiation (t0) or 1 h after the system initiation (t0 + 1).

## 5. Area expansion and high-level wind divergence

The relationships between convective system area expansion and high-level wind divergence have been further investigated by analyzing how the divergence varies over the convective system life cycle.

Figure 12 shows the high-level wind divergence anomaly observed over convective systems as a function of the lifetime of the systems. In order to remove the large-scale variation of the mean field (see Fig. 9), the divergence anomaly was computed in each grid point as the WV wind divergence minus the local mean. Then for each occurrence of a convective system, the divergence anomaly was considered at the system initiation time (t0) or at a time lag (t0 + 1 h). The divergence anomaly is weak but always positive, and it increases with the system duration. The variability is large (stan-

dard deviation of about $2 \times 10^{-6}$ s$^{-1}$) and the signal is weak, but the mean signal is consistent with the behavior obtained with the area expansion (Fig. 2). Also, the divergence is larger when considering a time lag after the system initiation, with an optimum lag of 1 or 2 h. We should remember the convective system initiation is defined here as the time when the cloud-top area colder than 235 K is larger than 3500 km$^2$. This leads to an initiation time shifted with respect to the very beginning of the convection. This time lag between convective system initiation and high-level wind divergence is not surprising. Frank (1978) found large-scale convergence precedes by several hours the formation of convective systems observed in the Global Atmospheric Research Program's Atlantic Tropical Experiment (GATE). Tollerud and Esbensen (1985) performed a composite analysis of the wind divergence vertical profile for the large convective systems occurring during GATE. They concluded that the maximum low-level convergence is observed during the initiation stage, and the maximum upper-level divergence occurs during the mature stage.

The scale dependence of divergence estimation is not sufficient to explain the observed inconsistencies between wind divergence and area expansion. The cloud growing due to condensation cannot be neglected, as the area expansion depends on it and not only on the divergence. The area expansion reaches its maximum value in the initiation stage, and the upper-level wind divergence reaches the maximum later, at or just before the mature stage. The rate of increase of the total liquid water of the convective system cannot be neglected during the initiation stage, when the maximum area expansion occurs, and therefore Eq. (1) is not sufficient to describe the convective system size change. Time changes of the convective system area is a function of wind divergence (div) and condensation–evaporation process (cond) as follows:

$$\frac{1}{A}\frac{\partial A(\text{div, cond})}{\partial t} = \frac{1}{A}\frac{\partial A(\text{div})}{\partial t}\bigg|_{\text{cond=cte}} + \frac{1}{A}\frac{\partial A(\text{cond})}{\partial t}\bigg|_{\text{div=cte}}, \quad (2)$$

$$\frac{1}{A}\frac{\partial A(\text{div})}{\partial t}\bigg|_{\text{cond=cte}} = \boldsymbol{\nabla}\cdot\mathbf{V}, \quad (3)$$

where $A$ is the area of the convective system and cte is a constant. Combining Eqs. (2) and (3) gives

$$\frac{1}{A}\frac{\partial A(\text{div, cond})}{\partial t} = \boldsymbol{\nabla}\cdot\mathbf{V} + \frac{1}{A}\frac{\partial A(\text{cond})}{\partial t}\bigg|_{\text{div=cte}}. \quad (4)$$

The liquid water content of the convective system ($Q_1$) can be described as

$$Q_l = \rho_l A H \quad \text{and} \quad (5)$$

$$\frac{\partial Q_l}{\partial t} = \rho_l A\frac{\partial H}{\partial t} + \rho_l H\frac{\partial A(\text{cond})}{\partial t} \approx \rho_l H\frac{\partial A(\text{cond})}{\partial t}, \quad (6)$$

where $\rho l$ is the liquid water density, and $H$ is the convective system height. The top of the convective system, detected using a cold threshold, is close to the tropopause, and therefore $H$ variations are relatively small and can be neglected. Combining Eqs. (5) and (6), we obtain

$$\frac{1}{A}\frac{\partial A(\text{cond})}{\partial t} = \frac{1}{AH\rho_l}\frac{\partial Q_l}{\partial t} = \frac{1}{Q_l}\frac{\partial Q_l}{\partial t}. \quad (7)$$

Combining Eqs. (4) and (7) gives

$$\frac{1}{A}\frac{\partial A}{\partial t} = \boldsymbol{\nabla}\cdot\mathbf{V} + \frac{1}{Q_l}\frac{\partial Q_l}{\partial t}. \quad (8)$$

To characterize and understand the evolution of the terms in Eq. (8) during the life cycle of the convective system, we have applied the following methodology. The life cycle is divided into five classes: initiation (class 1); intermediary between initiation and maximum size (class 2); maximum size, the mature stage (class 3); intermediary between maximum size and dissipation (class 4); and dissipation (class 5). Only systems with a lifetime longer than 3.5 h are considered in order to simplify the classification, and the few systems that last longer than 10 h are discarded to reduce the possibility of multiple growing phases. Also, the convective systems associated with splits or merges are discarded. Based on this classification we have done a composite study for each life stage, for the area expansion and the water vapor wind divergence, for the whole of tropical South America. The results of these calculations show that the area expansion ranges from $2 \times 10^{-4}$ to $-2 \times 10^{-4}$ s$^{-1}$, whereas the divergence anomaly varies between $7 \times 10^{-7}$ and $6 \times 10^{-6}$ s$^{-1}$. As already mentioned, the divergence is strongly scale dependent, and it is not possible to compare the absolute values of WV wind divergence with the area expansion for a large range of convective sizes. As we are here interested in the relative variations during the convective system life cycle, we plot in Fig. 13 the relative variations of the area expansion and divergence, that is, each parameter is normalized using its mean and standard deviation obtained from the composite analysis. As shown in Fig. 13, the normalized area expansion decreases linearly during the convective system life cycle in agreement with the results of Machado et al. (1998). Hence the evolution of the convective system area can be parameterized by

$$\frac{1}{A}\frac{\partial A}{\partial t} = at + b, \quad (9)$$

which leads to

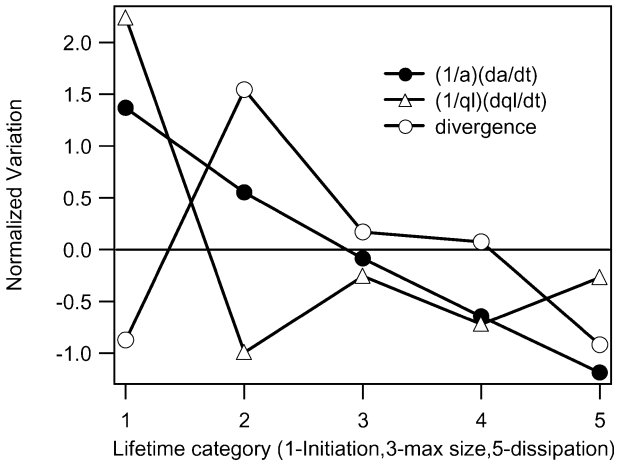


FIG. 13. Average variation of the normalized area fraction for convective systems having a duration between 3.5 and 10 h, associated normalized anomalies of wind divergence, and calculated condensation/evaporation rate, as a function of the lifetime categories 1 (initiation), 2 (intermediary stage between initiation and mature stage), 3 [maximum area stage (mature stage)], 4 (intermediary stage between the mature and the dissipation stage), and 5 (dissipation stage). Values are normalized by their std dev.

$$A = \exp\left(\frac{at^2}{2} + bt + c\right), \tag{10}$$

where $t$ is the time from the initiation.

The upper-level wind divergence is positive, on average, throughout the entire convective system life cycle. The normalized values show that the minimum is observed at the initiation time, and the maximum is reached during the growing phase of the system (class 2 in Fig. 13), close to the mature stage, and then decreases slowly in the dissipation phase.

Considering Eq. (8), the relative variation of the condensation term can be deduced from the difference between area expansion and horizontal wind divergence, using only the normalized terms. The following behavior can be seen in Fig. 13: at the initiation of the convective system the area expansion is very large, due mainly to a very strong condensation rate. Then the divergence increases during the growing phase. At the mature phase (maximum size), all terms are close to their mean value. During the dissipative phase, the negative area expansion is associated with both a small divergence and evaporation (Fig. 13 presents the relative variation). Based on this result the area expansion in the initiation stage is mainly due to the condensation rate and can provide important information for assimilation in mesoscale models to describe the vigor of the convection during the model spinup.

## 6. Conclusions

The WETAMC/LBA makes it possible to study convective systems and their associated precipitation from the combination of satellite images, meteorological radars and rain gauges, and radiosonde data for dynamic and thermodynamic analysis.

The full-resolution *GOES-8* satellite images were used to detect and track the convective systems during their life cycle. This objective tracking was performed for 48 days during the WETAMC/LBA over a window covering tropical South America.

The convective system area is calculated from the number of pixels with a brightness temperature smaller than the threshold considered (235 or 210 K). The area expansion is defined as the system area difference between two successive images, normalized by the mean area. The area expansion is closely linked to the phase of the convective system's life. At the beginning of its life, the convective system presents a large positive area expansion. The area expansion becomes close to zero during the mature stage of the convective system and negative in the dissipation stage.

The results demonstrate the ability to predict the probable lifetime of a convective system from its initial area expansion. The physical explanation for this result is founded on the principle that this parameter measures the vigor of the convective forcing indicating the time–space scale of the convective cloud organization. The area of the cloud shield of the convective system changes in association with the upper-level wind divergence and with the condensation/evaporation process. A rapidly growing convective system is a cloud cluster with strong liquid water condensation and strong vertical mass flux. The area increase in the initial stage is mainly due to the condensation process, then afterward, in the mature stage, the upper-air wind divergence increases. The upper-air divergence is a signature of the mass flux inside the convective towers that had previously contributed to the condensation process. The average area expansion at the initial stage varies exponentially with the life cycle duration. For short to medium lifetimes (less than 8 h) the relationship between initial area expansion and total lifetime is very clear; however, for longer lifetimes all that can be predicted is that the convective system will live for longer than 8 h. Very long lifetimes cannot be predicted from the signature of the vigor of the convection at the initial stage, probably because of the diurnal cycle, the large-scale forcing, and other external forcing. This time scale of 8 h applies to the cloud shield defined at 235 K. For the colder cloud area of 210 K this time scale is around 5–6 h and for the liquid water at 2 km (using the CAPPI 2-km radar data) this time scale is only of a couple of hours.

The maximum area expansion occurs close to the time of maximum precipitation and about 4 h before the maximum cold cloud fraction at the same threshold (235 K). It can be concluded that the area expansion could be used to determine the time of maximum precipitation.

The analysis of the area expansion showed that this parameter could be very useful for short-range forecasts, convection diagnostics, and perhaps to help improve the

precipitation estimation from geostationary meteorological satellites. Also, the area expansion can be used to determine the convective system life stage and to supply information about the condensation processes and the upper-level divergence.

Future work might include seeing if the parameterized relationship in equation 10 has predictive value anywhere else, particularly the midlatitudes.

*Acknowledgments.* This study was done in a cooperative framework between the CNPq (Conselho Nacional de Desenvolvimento Cientifico e Tecnólogico, Brazil) and the IRD (Institut de Recherche pour le Développement, France), support number 690089/01-5. The work has received financial support from the CNPq Grant 47210/2001-4.

## REFERENCES

Anagnostou, E. N., and W. F. Krajewski, 1997: Simulation of radar reflectivity fields: Algorithm formulation and evaluation. *Water Resour. Res.,* **33,** 1419–1428.

——, and C. A. Morales, 2002: Rainfall estimation from TOGA radar observations during LBA field campaign. *J. Geophys. Res.,* **107**, 8068, doi:10.1029/2001JD000377.

Barnes, S. L., 1964: A technique for maximizing details in numerical weather map analysis. *J. Appl. Meteor.,* **3,** 396–409.

Frank, W. M., 1978: The life cycles of GATE convective systems. *J. Atmos. Sci.,* **35,** 1256–1264.

Holton, J. R., 1979: *An Introduction to Dynamic Meteorology.* Academic Press, 394 pp.

Laurent, H., 1993: Wind extraction from METEOSAT water vapor channel image data. *J. Appl. Meteor.,* **32,** 1124–1133.

——, and M. Sakamoto, 1998: Measure of divergence at the top of tropical convective systems from water vapor winds. *Proc. Fourth Int. Winds Workshop,* Saanenmoser, Switzerland, EUMETSAT, 155–161.

——, L. A. T. Machado, C. A. Morales, and L. Durieux, 2002: Characteristics of the Amazonian mesoscale convective systems observed from satellite and radar during the WETAMC/LBA experiment. *J. Geophys. Res.,* **107**, 8054, doi:10.1029/2001JD000337.

Machado, L. A. T., 2000: The Amazon energy budget using the ABLE-2B and FluAmazon data. *J. Atmos. Sci.,* **57,** 3131–3144.

——, W. B. Rossow, R. L. Guedes, and A. W. Walker, 1998: Life cycle variations of mesoscale convective systems over the Americas. *Mon. Wea. Rev.,* **126,** 1630–1654.

——, H. Laurent, and A. A. Lima, 2002: Diurnal march of the convection observed during TRMM-WETAMC/LBA. *J. Geophys. Res.,* **107**, 8064, doi:10.1029/2001JD000338.

Mathon, V., and H. Laurent, 2001: Life cycle of the Sahelian mesoscale convective cloud systems. *Quart. J. Roy. Meteor. Soc.,* **127,** 377–406.

Petersen, W. A., S. W. Nesbitt, R. J. Blakeslee, R. Cifelli, P. Hein, and S. A. Rutledge, 2002: TRMM observations of intraseasonal variability in convective regimes over the Amazon. *J. Climate,* **15,** 1278–1294.

Schmetz, J., and Coauthors, 1995: Monthly mean large-scale analyses of upper-tropospheric humidity and wind field divergence derived from three geostationary satellites. *Bull. Amer. Meteor. Soc.,* **76,** 1578–1584.

Scofield, R. A., 1987: The NESDIS operational convective precipitation estimation technique. *Mon. Wea. Rev.,* **115,** 1773–1792.

Silva Dias, M. A., and Coauthors, 2002: Cloud and rain processes in a biosphere–atmosphere interaction context in the Amazon region. *J. Geophys. Res.,* **107**, 8072, doi:10.1029/2001JD000335.

Tollerud, E. I., and S. K. Esbensen, 1985: A composite life cycle of nonsquall mesoscale convective systems over the tropical ocean. Part I: Kinematic fields. *J. Atmos. Sci.,* **42,** 823–837.

Velden, C., C. M. Hayden, S. J. Nieman, W. P. Menzel, S. Wanzong, and J. S. Goerss, 1997: Upper-tropospheric winds derived from geostationary satellite water vapor observations. *Bull. Amer. Meteor. Soc.,* **78,** 173–195.

Wallace, J. M., and P. V. Hobbs, 1979: *Atmospheric Science: An Introductory Survey.* Academic Press, 467 pp.